UNIVERSITY OF OKLAHOMA

GRADUATE COLLEGE

DIGITAL PREDISTORTION OF PSEUDO-ORTHOGONAL WIDEBAND WAVEFORMS FOR DUAL-POLARIMETRIC PHASED ARRAY RADARS

A DISSERTATION

SUBMITTED TO THE GRADUATE FACULTY

in partial fulfillment of the requirements for the

Degree of

DOCTOR OF PHILOSOPHY

By

ZACHARY THOMAS DUNN

Norman, Oklahoma

2016

Downloaded from SHAREOK. Persistent Handle URL: https://hdl.handle.net/11244/34587

DIGITAL PREDISTORTION OF PSEUDO-ORTHOGONAL WIDEBAND WAVEFORMS FOR DUAL-POLARIMETRIC PHASED ARRAY RADARS

A DISSERTATION APPROVED FOR THE
SCHOOL OF ELECTRICAL AND COMPUTER ENGINEERING

BY

Dr. Mark Yeary, Chair

Dr. Caleb Fulton

Dr. Nathan Goodman

Dr. Jessica Ruyle

Dr. Michael Biggerstaff

© Copyright by ZACHARY THOMAS DUNN 2016
All Rights Reserved.

To our gracious and compassionate God "in whom are hidden all the treasures of wisdom and knowledge," to my grandfather Charles who inspired me to become an engineer in the first place, and to my wonderful, intelligent, and selfless wife Deana.

Acknowledgments

First, I would like to sincerely thank my research advisor Professor Mark Yeary for the guidance, wisdom, and support he has imparted throughout my time at the University of Oklahoma.

I would also like to thank the remainder of my ECE research committee, Professor Caleb Fulton, Professor Nathan Goodman, and Professor Jessica Ruyle for their guidance and help. I am truly thankful for the time and effort that the committee in its entirety has invested into me and my research.

Again, I would like to thank God for the countless blessings He has imparted, and for the opportunity He has given me to pursue this research.

Finally, I would like to thank my family, especially my wife Deana, for their seemingly unending support, sacrifices, selflessness, and patience while I pursued this degree.

Table of Contents

Acknowledgments **iv**

Abstract **xv**

1 Introduction **1**

2 Mathematical Basis for Dual-Polarimetric Operation **7**

2.1 Introduction 7

2.2 Dual-Polarimetric Radar Operation 8

2.3 Cross-Correlation and Pulse Compression 20

2.4 Orthogonality and Waveform Pseudo-Orthogonality 28

2.4.1 Pseudo-Orthogonality of a Linear Frequency Modulated Waveform Pair 33

2.5 Example of Orthogonal Waveform Separability in a Dual-Polarized Radar System 38

2.6 Analysis of Common Pulse Compression Waveforms and Their Utility as Pseudo-Orthogonal Waveform Sets 48

2.7 Low Sidelobe Pseudo-Orthogonal Code Sets Through Particle Swarm Optimization 67

2.7.1 Particle Swarm Optimization Background 67

2.7.2 Determining a Fitness Function 70

2.7.3 Optimized Polyphase Coded Pseudo-Orthogonal Waveform Sets . . . 71
2.7.4 Non-Linear Frequency Modulated Waveform Set 73
2.7.5 Particle Swarm Conclusion 77
2.8 Analysis of Range Resolution and Range Sidelobe Characteristics as a Function of Orthogonality Degradation 79
2.9 Orthogonal Polarization Basis Transformation 96
2.10 Conclusion 110

3 Modeling and Digital Predistortion of Broadband Solid-State High Power Amplifiers 111

3.1 Introduction 111
3.2 Technical Approach to Modeling Amplifier and Predistorter 115
3.2.1 Conceptual Approach to Digital Predistortion 115
3.2.2 Volterra Series and MP Model 119
3.2.3 Weighting for Numerical Stability of Least-Squares Model Solution 127
3.2.4 Bayesian Analysis for Model Parameter Refinement and Slowly Changing Systems 129
3.3 Predistortion of Digitally Coded Waveforms 135
3.3.1 P4 Waveform Simulation 137
3.3.2 P4 Waveform Test in Hardware 138
3.3.3 Non-Constant Modulus Waveform Simulation 139
3.3.4 Non-Constant Modulus Waveform Test in Hardware 141

3.4 Conclusion 144

4 An Impedance Dependent Memory Polynomial Model for Wideband Digital Predistortion of Solid-State Radar Amplifiers 146

4.1 Introduction 146

4.2 Technical Approach to Modeling Amplifier and Predistorter 150

4.2.1 Mutual Coupling and Scan Impedance in Phased Arrays 150

4.2.2 Conceptual Approach to Impedance Dependent Digital Predistortion 152

4.2.3 Memory Polynomial Model and Impedance Dependent Memory Polynomial Model 154

4.3 Predistortion of Digitally Coded Waveforms 167

4.4 Conclusion 174

5 Conclusion 177

References 182

Appendix A Moore-Penrose Pseudoinverse as Least-Squares Solution 191

Appendix B Matlab Code for Digital Predistortion 194

B.1 Digital Predistortion Utilizing Memory Polynomial Model . . 194

B.2 Memory Polynomial Delay Matrix Formation Function 197

B.3 Digital Predistortion Utilizing Impedance Dependent Memory Polynomial Model 199

B.4 Impedance Dependent Memory Polynomial Delay Matrix Formation Function 207

Appendix C Author's Previous Publications 212

List of Tables

2.1 Γ Parameter Separability Through Ratio of Desired Γ Parameter to Sum of Other Γ Parameters for Example Alternating Transmit and Simultaneous Transmit Cases 47

List of Figures

2.1 *Example of Pulse Compressed vs. Simple Waveform Receiver Output: 10 MHz Bandwidth LFM Case* 26

2.2 *Example of Pulse Compressed vs. Simple Waveform Receiver Output: 13 bit Biphase Barker Coded Case* 26

2.3 *Receiver Filter Response of Upchirp and Downchirp with an Upchirp Matched Filter vs Time* 37

2.4 *Magnified Receiver Filter Response of Upchirp and Downchirp with an Upchirp Matched Filter vs Time* 38

2.5 *Normalized Cross-Correlation Polyphase Barker Sequences* . . 54

2.6 *Normalized Convolution of Time-Reversed Polyphase Barker Sequences* 55

2.7 *Normalized Convolution of Complex Conjugated Polyphase Barker Sequences* 56

2.8 *Normalized Convolution of Polyphase Barker Sequences* . . . 57

2.9 *Matching Autocorrelations for and Frank, P1, and P2 and Matching Autocorrelations for P3 and P4* 60

2.10 *Normalized Convolution of Polyphase Barker Sequences* . . . 61

2.11 *Normalized Cross-Correlation of P1 Upchirp with P1, P2, and P4 Codes* 63

2.12 *Normalized Cross-Correlation of P2 Downchirp with P1, P2, and P4 Codes* 64
2.13 *Normalized Cross-Correlation of P4 Upchirp with P1, P2, and P4 Codes* 64
2.14 *Normalized Autocorrelations and Cross-Correlation of P2 Downchirp with P1, P2, and P4 Codes* 65
2.15 *Normalized Autocorrelations and Cross-Correlation of P4 Upchirp with P1, P2, and P4 Codes* 66
2.16 *Auto-Correlation and Cross-Correlation Results from Polyphase Coded Pseudo-Orthogonal Waveform Set, Reprinted from Dunn et al. (2016) © 2016 IEEE* 73
2.17 *Auto-Correlation and Cross-Correlation Results from NLFM Pseudo-Orthogonal Waveform Set Compared with LFM Waveform Set. a) Full View, b) Magnified View. Reprinted from Dunn et al. (2016) © 2016 IEEE* 78
2.18 *Pulse Compression Output: LFM Waveform Orthogonal Polarization Degradation of Return from 2 Separated Point Targets* 86
2.19 *Pulse Compression Output: P2 Coded Waveform Orthogonal Polarization Degradation of Return from 2 Separated Point Targets* 86
2.20 *Pulse Compression Output: LFM Waveform Orthogonal Coding Degradation of Return from 2 Separated Point Targets* 87
2.21 *Pulse Compression Output: P2 Coded Waveform Orthogonal Coding Degradation of Return from 2 Separated Point Targets* 88

2.22 *Pulse Compression Output: LFM Waveform Orthogonal Polarization Degradation of Return from 2 Separated 60m Long Extended Targets* 89
2.23 *Pulse Compression Output: P2 Coded Waveform Orthogonal Polarization Degradation of Return from 2 Separated 60m Long Extended Targets* 90
2.24 *Pulse Compression Output: LFM Waveform Orthogonal Coding Degradation of Return from 2 Separated 60m Long Extended Targets* 91
2.25 *Pulse Compression Output: P2 Coded Waveform Orthogonal Coding Degradation of Return from 2 Separated 60m Long Extended Targets* 92
2.26 *Pulse Compression Output: LFM Waveform Orthogonal Polarization and Coding Degradation of Return from 2 Separated Point Targets* 94
2.27 *Pulse Compression Output: P2 Coded Waveform Orthogonal Polarization and Coding Degradation of Return from 2 Separated Point Targets* 94
2.28 *Pulse Compression Output: LFM Waveform Orthogonal Polarization and Coding Degradation of Return from 2 Separated 60m Long Extended Targets* 95
2.29 *Pulse Compression Output: P2 Coded Waveform Orthogonal Polarization and Coding Degradation of Return from 2 Separated 60m Long Extended Targets* 95
2.30 *Transformation from H and V Basis to H and V Basis* 101
2.31 *Transformation from H and V Basis to Slant-45 Basis* 103

2.32 *Transformation from H and V Basis to Circular Basis* 105
2.33 *Transformation from H and V Basis to Elliptical Basis* 107
2.34 *Transformation from H and V Basis to Slant-Elliptical Basis* . 109

3.1 *Example of Non-Constant Modulus Waveform Single Channel Output of Wideband Beamforming Algorithm As Shown In [7], Reprinted from Dunn et al. (2016) © 2016 IEEE* 115
3.2 *Example of Power Out vs. Power In of Well-Behaved Narrowband and Ideal Amplified Signals, Reprinted from Dunn et al. (2016) © 2016 IEEE* 117
3.3 *Example of Power Out vs. Power In of Measured Wideband and Ideal Amplified Signals, Reprinted from Dunn et al. (2016) © 2016 IEEE* 119
3.4 *Flow Chart Summary of Digital Predistortion Process, Reprinted from Dunn et al. (2016) © 2016 IEEE* 126
3.5 *Delay Matrix Condition Number for Amplifier and DPD MP Models As a Function of Number of Model Terms. Note that the condition numbers resulting from the weighted approach are more stable regardless of scaling. Reprinted from Dunn et al. (2016) © 2016 IEEE* 130
3.6 *Measured Amplifier Data versus Least-Squares and Bayesian Model Results, Reprinted from Dunn et al. (2016) © 2016 IEEE* 133
3.7 *Power Spectral Density of Simulated Predistorted and Non-Predistorted P4 Coded Waveforms after HPA Distortion, Reprinted from Dunn et al. (2016) © 2016 IEEE* 138

3.8 *Power Spectral Density of Measured Predistorted and Non-Predistorted P4 Coded Waveforms after HPA Distortion, Reprinted from Dunn et al. (2016) © 2016 IEEE* 139
3.9 *Power Spectral Density of Simulated Predistorted and Non-Predistorted Signals after HPA Distortion, Reprinted from Dunn et al. (2016) © 2016 IEEE* 140
3.10 *Power Spectral Density of Measured Predistorted and Non-Predistorted Signals after HPA Distortion, Reprinted from Dunn et al. (2016) © 2016 IEEE* 141
3.11 *Power Out vs. Power In of Measured Predistorted and Non-Predistorted Signals after HPA Distortion, Reprinted from Dunn et al. (2016) © 2016 IEEE* 142
3.12 *Passband Group Delay of Measured Predistorted and Non-Predistorted Signals after HPA Distortion, Reprinted from Dunn et al. (2016) © 2016 IEEE* 143

4.1 *Various Perspectives of Mean of Top 5% Maximum Magnitudes per Load Impedance vs. Complex Reflection Coefficient, Reprinted from Dunn et al. (2017) © 2017 IEEE* 155
4.2 *Visualization of Volterra Series Post-Inverse A) to Pre-Inverse B) Equivalency Property, Reprinted from Dunn et al. (2017) © 2017 IEEE* 161
4.3 *Visualization of Calibration Post-Inverse A) to Calibration Pre-Inverse B) and Implemented Pre-Inverse C) Equivalency Property in Black-Box Linear Amplifier Method, Reprinted from Dunn et al. (2017) © 2017 IEEE* 162

4.4 *Flowchart Summary of Impedance Dependent Digital Predistortion Process, Reprinted from Dunn et al. (2017) © 2017 IEEE* 164
4.5 *Flowchart of Experimental Testbed Utilized, Reprinted from Dunn et al. (2017) © 2017 IEEE* 168
4.6 *Photograph of Experimental Testbed Utilized, Reprinted from Dunn et al. (2017) © 2017 IEEE* 169
4.7 *Calibration Dataset and Evaluation Dataset Impedance Test Points, Reprinted from Dunn et al. (2017) © 2017 IEEE* 171
4.8 *Power Spectral Density of Measured Non-Predistorted, Predistorted, and Ideal Waveforms, Reprinted from Dunn et al. (2017) © 2017 IEEE* 173
4.9 *Output Power Versus Input Power of Measured Non-Predistorted, Predistorted, and Ideal Waveforms, Reprinted from Dunn et al. (2017) © 2017 IEEE* 174
4.10 *Ideal, Measured, and Calculated Errors for Measured Non-Predistorted and Predistorted Waveforms, Reprinted from Dunn et al. (2017) © 2017 IEEE* 175
4.11 *Voltage Errors per Point Calculated on Point-by-Point Basis a) and Versus Maximum Measured Magnitude Basis b) for All Samples over Normalized Input Signal Power Threshold, Reprinted from Dunn et al. (2017) © 2017 IEEE* 176

Abstract

Many new and interesting radar operational modes and techniques are being explored to maximize the efficiency and utility of next-generation radar systems while complying with increasingly stringent operational and budgeting requirements. This dissertation's aim is to analyze and present possible techniques to help maximize the scientific value of measurements while complying with operational requirements through methods of physical transmission and exciting the target area, methods of processing the received waveforms, and methods of designing waveforms for a given system.

In regard to methods of physical transmission and exciting the target area, this dissertation addresses unique problems that will be faced by next-generation radar systems utilizing simultaneous transmit and simultaneous receive operational modes in polarimetric active phased array architectures. This is accomplished through establishing mathematical representations of the received complex baseband waveforms for dual-polarimetric radar operation and analyzing the predicted behavior versus traditional polarimetric radar alternating transmit and simultaneous receive operation.

In regard to methods of processing the received waveforms, pulse compression will undoubtedly be widely utilized in future radar systems due to the

increase in range resolution that it provides for a given pulse length. Additionally, matched filtering allows the realization of simultaneously transmitted pseudo-orthogonal waveforms occupying the same spectral region that would be otherwise impossible. As a result, the mathematical basis of pulse compression is provided, and pulse compression effects are taken into account in all relevant system analyses in this manuscript.

This dissertation arguably provides the most attention in regard to methods for designing and modifying waveforms for application in a given system. An analysis of common pulse compression waveforms for suitability in pseudo-orthogonal waveform sets is provided in addition to a novel method for designing polyphase coded waveform and non-linear frequency modulated waveform based pseudo-orthogonal waveform sets utilizing particle swarm optimization. Additionally, for the first time, research is presented on the full design and application methods for digital predistortion of wideband solid state radar amplifiers. Digital predistortion methods and results are presented for both the impedance matched high power amplifier case and for the varying load impedance case that can be expected to be encountered in radar systems utilizing electronic beamsteering in active phased array architectures.

Overall, this dissertation's aim is to provide relevant results from conducted research in the form of analysis and novel design methods that can be applied in both the design and operation of next-generation radar systems to maximize utility and scientific data quality while operating within given system and environmental specifications.

Chapter 1

Introduction

Since its beginnings in the early 1900s, radar systems have proved to be of great worth and valuable for a multitude of uses in tracking, mapping, navigation, and imaging [1]. However, growing expectations of future radar systems' capabilities are at odds with increasingly stringent operational and budgeting requirements [2]. As a result, many new and interesting radar operational modes and techniques are being explored to maximize the efficiency and utility of next-generation radar systems. Possible techniques to help maximize the scientific value of the measurements while complying with operational requirements include methods of physical transmission and exciting the target area, methods of processing the received waveforms, and methods of designing waveforms for a given system.

The method of physical transmission plays a pivotal role in the type of scientific data a radar system can acquire. While radar systems can use any type of electromagnetic radiating element, modern and next-generation radar systems are becoming increasingly dependent upon the use of active phased array antennas. A phased array antenna consists of multiple radiating elements working together so that the transmitted electromagnetic waves constructively

interference at the intended angle relative to the array (the beamsteering angle) and mostly destructively interfere at all other angles. Phased array antennas offer multiple benefits over antennas consisting of a single radiating element. These benefits include linear scalability in system power and cost, graceful degradation, and rapid beamsteering [1]. Active phased array architectures differ from traditional phased arrays in that every antenna element has a unique transmit/receive chain, allowing for the execution of advanced operational modes such as multi-beam transmit and receive, the use of designed wideband waveform sets that result in frequency-invariant beampatterns, and simultaneous multi-mode operation that are desired in next-generation systems [3]–[8]. Traditional radar systems only physically transmit a single polarization of electromagnetic waves. With increased interest in the second-order moments of the polarization scattering matrix and the unique information they can provide about radar targets that can only be derived from examining the effects of different polarizations' excitations of a target, future radar systems will undoubtedly utilize orthogonally polarized waveforms during transmission [9]. While some existing radar systems utilizing orthogonally polarized waveforms exist that can capture the "full" polarization scattering matrix, these systems tend to operate in an alternating transmit and simultaneous receive mode. Future radar systems will likely operate in a simultaneous transmit and simultaneous receive mode while retaining the capture of the full polarization scattering matrix. The mathematical framework of a dual-polarization system is outlined in Section 2.6.

The method in which received waveforms are processed can have a drastic effect on the overall quality of the scientific data recovered. Pulse compression

of wideband waveforms through the application of a matched filter is becoming a common method for increasing the range resolution for a given pulse length [10]. After matched filtering, this effectively allows for the transmitted energy of a long pulse while concentrating the energy into a much shorter duration than the length of the pulse, giving a drastic improvement in performance versus an unmodulated waveform. Pulse compression is becoming widespread in modern radar systems and will undoubtedly be widely utilized in future radar systems. The mathematical basis for pulse compression and its reliance on cross-correlation is outlined in Section 2.3.

Designing the transmit waveform for a next-generation radar system is crucial to the ultimate operational effectiveness and scientific quality of the received data. Indeed, the majority of this dissertation is devoted to designing or intelligently modifying the transmitted waveform to maximize its implemented effectiveness in a given radar system. While many pulse compression waveforms are already known, and several, such as linear frequency modulated chirps, have been in widespread use for many years, choosing a waveform for a next-generation simultaneous transmit and simultaneous receive radar system is more complicated than simply choosing a desired time-bandwidth product. For a simultaneous transmit and simultaneous receive operational mode to be realized without sacrificing range resolution or increasing the necessary system bandwidth (conflicting with strict spectral transmission requirements), the waveforms being transmitted on the differing polarizations require that another dimension of orthogonality be introduced in addition to polarization orthogonality. This extra dimension of orthogonality is accomplished through the use of specifically designed modulated waveform sets, referred to as pseudo-

orthogonal waveform sets. Pseudo-orthogonal waveform sets must be carefully designed so that all individual waveforms within a set display desirable pulse compression characteristics when processed with their own matched filter, but display very low and uniform pulse compression responses when processed with any other waveform's matched filter in the set [11]. Pseudo-orthogonal waveform sets are relatively difficult to create, but will be necessary as strictly maintained orthogonality in both polarization and waveform modulation are required in order to recover the polarization scattering matrix with high fidelity from a single measurement, as shown in Sections 2.2, 2.5, and 2.8. A collection of common pulse compression waveforms are analyzed for their suitability as pseudo-orthogonal waveform sets in Section 2.6, and a novel method of generating pseudo-orthogonal waveform sets within a given set of operational bounds through particle swarm optimization is presented in Section 2.7.

While designing and choosing an adequate pseudo-orthogonal waveform set for a radar system is crucial to the system's ultimate operational effectiveness, it must be addressed that there always lies a difference between the theoretical data fidelity of the system and the actual data fidelity of the physical system. While thermal noise does play a role in this degradation, a significant amount of the variation is due to a difference between the ideal transmitted waveform and the actual transmitted and received waveform. The disparity between the ideal transmitted waveform and the physically transmitted waveform is primarily due to non-linear behavior of the transmit chain, namely the high power amplifier. Nearly all amplifiers experience non-linearities over their input power range with the most drastic effects near the upper limit of output power, which coincidentally is also the region of operation coinciding with the

amplifier's highest power added efficiency [12]–[14]. Additionally, this non-linear behavior changes as a function of frequency. The non-linearities in high power amplifiers not only alter the expected behavior of the waveforms during matched filtering, but also introduce spectral spreading where the transmitted waveforms occupy more bandwidth than intended. While the transmit chain of the amplifier can be made to exhibit more linear behavior by reducing the input power for a given high power amplifier, the reduction in output power results in a sub-optimal power added efficiency. For the first time, Chapters 3 and 4 present research toward methods for intelligently modifying an ideal wideband radar transmit waveform so that the physically transmitted waveform is linearly reproduced by the system while still operating at the peak power added efficiency, thus maximizing the utility of a system's given hardware while complying with strict spectral requirements. These methods are referred to as digital predistortion. Chapter 3 presents a conceptual approach to wideband digital predistortion, a generalized method for executing wideband digital predistortion utilizing the memory polynomial model for a single high power amplifier, and simulated and measured results verifying the effectiveness of the approach.

While the digital predistortion method in Chapter 3 effectively predistorts a single channel, in practice many next-generation radar systems will be implemented with active array architectures. One of the main advantages of phased array antennas is rapid electronic beamsteering, but changing the beamsteering angle in a phased array antenna alters the coupling between antenna elements which changes each antenna element's apparent impedance as seen by the amplifier [1], [15]. The non-linear behavior of high power ampli-

fiers also vary with the amplifiers' load impedance, therefore the non-linear behavior of each high power amplifier in an active array architecture depends not only on the desired waveform, but also on the desired beamsteering angle and its intrinsically related effective load impedance. Chapter 4 expands upon Chapter 3 by presenting a modified wideband digital predistortion method that also accounts for the variations in a high power amplifier's non-linearities as a function of the amplifier's experienced load impedance. This digital predistortion is accomplished through application of the impedance dependent memory polynomial model, which was developed through this research. A short description of mutual coupling and scan impedance effects is given, followed by a conceptual approach to impedance dependent digital predistortion, the mathematical framework for the impedance dependent memory polynomial model, and measured results verifying the effectiveness of the approach.

Altogether, this dissertation's aim is to help provide some of the necessary framework for next-generation radar systems so that they can maximize their potential impact by providing high fidelity scientific data while operating within strict operational and budgetary guidelines. This is accomplished through the mathematical analysis of expected operational modes and through processes for helping analyze, design, and intelligently modify potential wideband waveform sets.

Chapter 2

Mathematical Basis for Dual-Polarimetric Operation

2.1 Introduction

From a scientific perspective, high resolution measurements of a target's range, velocity, and four-element polarimetric scattering matrix are desirable. In order to support these kind of measurements, a wideband dual-polarimetric radar system will need to implement several advanced operational, processing, and design techniques, including simultaneous transmit and simultaneous receive operation utilizing pseudo-orthogonal waveforms, pulse compression, interferometry, and wideband beamforming. The following sections will aim to establish the definitions and mathematical basis of several techniques in order to verify their feasibility, to compare their operation with traditional techniques (where applicable), and to present a novel design method utilizing particle swarm optimization for the creation of pseudo-orthogonal waveform sets.

2.2 Dual-Polarimetric Radar Operation

From a science perspective, the desired measurements from a dual-polarimetric system are the co-polar and cross-polar signal return characteristics from both polarizations in regards to a target, preferably separable and measured at the same instance in time. A dual-polarimetric radar has independent amplifiers for each of the two antenna polarization ports. For true dual-polarimetric operation, the radar system must effectively have two transmit-receive chains, one for each antenna polarization port. This definition of "dual-pol" (similar to Raney's definition of "Full-Polarization" in [16]) will be used throughout this document. For the proposed orthogonal coding use with simultaneous transmit and simultaneous receive on both polarizations, it must be shown that a dual-pol system is capable of discerning the desired signals from the received signal.

In order to give the matrix-based mathematical formulation for a received generic dual-pol signal, some assumptions and unit conventions must be stated. The radar system is assumed to be a monostatic with coherent operation. When in regards to signals handled inside the radar architecture, "Horizontal" and "Vertical," denoted by the subscripts $_H$ and $_V$ respectively, will refer to the the transmit-receive chain connected to the antenna polarization feed of the same name. When in regards to signals propagating to the target and back, H and V will refer to the orthonormal basis describing the polarization of transmitted fields, where H and V are aligned with the fixed antenna polarizations, and the plane formed by the orthonormal basis is perpendicular to the direction of field propagation in the far-field. It is also assumed for

this problem that the physical antenna's polarization elements are perfectly physically orthogonal to one another. Co-pol gain mismatch and cross-pol contamination at the antenna will still be taken into effect, though it will be assumed that the cross-pol contamination (ignoring additional co-pol gain mismatch factor) is the same between channels, and antenna effects will be the same upon transmit and recieve. Finally, because these equations are framed with the purpose of researching the feasibility of recovering signal information rather than computing power losses, signal amplitude effects (due to antenna gain, target range, system losses, etc...) that affect the H and V channels equally will not be included in the equations.

The ideal transmit signal $\mathbf{T}_{\text{ideal}}(t)$ can be shown as

$$\mathbf{T}_{\text{ideal}}(t) = \begin{bmatrix} |a_1(t)|\, cos(2\pi f_0 t \, + \, \theta_1(t))\ \hat{\text{H}} \\ |a_2(t)|\, cos(2\pi f_0 t \, + \, \theta_2(t))\ \hat{\text{V}} \end{bmatrix} \tag{2.1}$$

where $a_1(t),\ a_2(t)\ \in \mathbb{C}$ are the complex baseband modulation waveforms of the H and V channels, respectively, $a_1(t) = |a_1(t)|e^{j\,\theta_1(t)}$, $a_2(t) = |a_2(t)|e^{j\,\theta_2(t)}$, f_0 is the carrier frequency, and $\hat{\text{H}}$ and $\hat{\text{V}}$ are the basis vectors representing the independent channels. The process of the antenna converting the signals on each channel to transmitted signals (and back upon reception) contaminates the signal, due primarily to co-pol gain mismatch and cross-pol contamination. Using the horizontal channel to horizontally polarized transmitted signal conversion as a reference (with a conversion factor equal to 1), the unitless factors α and β can be used to represent the relative magnitude of cross-pol contamination and co-pol gain mismatch effects, respectively. The contamination

factors α and β are defined as

$$\alpha = \frac{\text{magnitude of horizontal channel's signal converted to vertical polarization}}{\text{magnitude of horizontal channel's signal converted to horizontal polarization}} \tag{2.2}$$

and

$$\beta = \frac{\text{magnitude of vertical channel's signal converted to vertical polarization}}{\text{magnitude of horizontal channel's signal converted to horizontal polarization}} \tag{2.3}$$

where α, $\beta \in \mathbb{R}$. Using these terms the unitless antenna contamination vector $\mathbf{C}_{\text{ant}}$ can be shown as

$$\mathbf{C}_{\text{ant}} = \begin{bmatrix} 1 & \alpha\,\beta \\ \alpha & \beta \end{bmatrix} \tag{2.4}$$

For correctly working antennas $|\alpha| < 1$, and for antennas with high cross-pol isolation $|\alpha| << 1$. For antennas with low co-pol gain mismatch, $\beta \approx 1$. Therefore, the actual transmitted signal $\mathbf{T}_{\text{trans}}(t)$ can be shown as

$$\begin{aligned} &\mathbf{T}_{\text{trans}}(t) = \mathbf{C}_{\text{ant}}\mathbf{T}_{\text{ideal}}(t) = \\ &= \begin{bmatrix} |a_1(t)|\,cos(2\pi f_0 t + \theta_1(t)) + \alpha\,\beta\,|a_2(t)|\,cos(2\pi f_0 t + \theta_2(t))\ \hat{\mathrm{H}} \\ \alpha\,|a_1(t)|\,cos(2\pi f_0 t + \theta_1(t)) + \beta\,|a_2(t)|\,cos(2\pi f_0 t + \theta_2(t))\ \hat{\mathrm{V}} \end{bmatrix} \end{aligned} \tag{2.5}$$

where $\hat{\mathrm{H}}$ and $\hat{\mathrm{V}}$ are the polarization basis vectors.

For a given static line-of-sight target centered at range R, the unitless matrix $\mathbf{\Gamma}$ represents the polarimetric shifts as well as the phase shifts due to the transmitted fields' reactions with the target. The accurate acquisition of this matrix for further analysis of the target is one of the main scientific

measurements of a dual-pol system (see pg. 239-242 of [9]). The matrix $\mathbf{\Gamma}$ can be expanded as

$$\mathbf{\Gamma} = \begin{bmatrix} \Gamma_{\mathrm{HH}} & \Gamma_{\mathrm{HV}} \\ \Gamma_{\mathrm{VH}} & \Gamma_{\mathrm{VV}} \end{bmatrix} \tag{2.6}$$

where $\Gamma_{\mathrm{HH}}, \Gamma_{\mathrm{HV}}, \Gamma_{\mathrm{VH}}, \Gamma_{\mathrm{VV}} \in \mathbb{C}$, and the two subscripts denote the reflected and incident polarizations, respectively. Additionally, $\Gamma_{\mathrm{HH}} = |\Gamma_{\mathrm{HH}}|e^{j\,\theta_{HH}}$, $\Gamma_{\mathrm{HV}} = |\Gamma_{\mathrm{HV}}|e^{j\,\theta_{HV}}$, $\Gamma_{\mathrm{VH}} = |\Gamma_{\mathrm{VH}}|e^{j\,\theta_{VH}}$, and $\Gamma_{\mathrm{VV}} = |\Gamma_{\mathrm{VV}}|e^{j\,\theta_{VV}}$. The reflected signals are also dependent upon the target's distribution in range, such that the reflected signal can be represented as a convolution of the transmitted signal with an envelope representing the magnitude of reflection at range. Assuming a point target at range R, the reflected signal due to target range distribution is shown as

$$\mathbf{R}_{\mathrm{refl}}(t) \;=\; \mathbf{T}_{\mathrm{trans}}(t) \otimes \delta(t - \frac{2R}{c}) \;=\; \mathbf{T}_{\mathrm{trans}}(t - \frac{2R}{c}) \;=\; \mathbf{T}_{\mathrm{trans}}(t') \tag{2.7}$$

where $\otimes$ is the convolution operator (when a single function is convolved with a matrix, the single function is independently convolved with each element in the matrix to form a new matrix), $t' = (t - \frac{2R}{c})$, c is the speed of light, and $(\frac{2R}{c})$ is the round trip time delay between the monostatic radar and the point target. Therefore, the returned signal $\mathbf{R}_{\mathrm{surf}}(t)$ at the surface of the antenna immediately before reception is shown as

$$\mathbf{R}_{\text{surf}}(t) = \mathbf{\Gamma}\mathbf{R}_{\text{refl}}(t) = \mathbf{\Gamma}(\mathbf{T}_{\text{trans}}(t) \otimes \delta(t - \frac{2R}{c})) = \mathbf{\Gamma}\mathbf{T}_{\text{trans}}(t - \frac{2R}{c}) = \mathbf{\Gamma}\mathbf{T}_{\text{trans}}(t') =$$

$$\begin{bmatrix} \Gamma_{\text{HH}} & \Gamma_{\text{HV}} \\ \Gamma_{\text{VH}} & \Gamma_{\text{VV}} \end{bmatrix} \begin{bmatrix} |a_1(t')|\, cos(2\pi f_0 t' + \theta_1(t')) + \alpha\, \beta\, |a_2(t')|\, cos(2\pi f_0 t' + \theta_2(t'))\ \hat{\text{H}} \\ \alpha\, |a_1(t')|\, cos(2\pi f_0 t' + \theta_1(t')) + \beta\, |a_2(t')|\, cos(2\pi f_0 t' + \theta_2(t'))\ \hat{\text{V}} \end{bmatrix} =$$

$$= \begin{bmatrix} |\Gamma_{\text{HH}}|\, [|a_1(t')|\, cos(2\pi f_0 t' + \theta_1(t') + \theta_{HH}) + \alpha\, \beta\, |a_2(t')|\, cos(2\pi f_0 t' + \theta_2(t') + \theta_{HH})] + \\ |\Gamma_{\text{VH}}|\, [|a_1(t')|\, cos(2\pi f_0 t' + \theta_1(t') + \theta_{VH}) + \alpha\, \beta\, |a_2(t')|\, cos(2\pi f_0 t' + \theta_2(t') + \theta_{VH})] + \\ + |\Gamma_{\text{HV}}|\, [\alpha\, |a_1(t')|\, cos(2\pi f_0 t' + \theta_1(t') + \theta_{HV}) + \beta\, |a_2(t')|\, cos(2\pi f_0 t' + \theta_2(t') + \theta_{HV})]\, \hat{\text{H}} \\ + |\Gamma_{\text{VV}}|\, [\alpha\, |a_1(t')|\, cos(2\pi f_0 t' + \theta_1(t') + \theta_{VV}) + \beta\, |a_2(t')|\, cos(2\pi f_0 t' + \theta_2(t') + \theta_{VV})]\, \hat{\text{V}} \end{bmatrix} \tag{2.8}$$

where $\hat{\text{H}}$ and $\hat{\text{V}}$ are the polarization basis vectors. Upon reception by the antenna, co-pol gain mismatch and cross-pol contamination affects the signals again, leading to an actual measured signal $\mathbf{R}_{\text{meas}}(t)$ that can be shown as

$$\mathbf{R}_{\text{meas}}(t) = \mathbf{C}_{\text{ant}}^{\text{T}}\mathbf{R}_{\text{surf}}(t) = \mathbf{C}_{\text{ant}}^{\text{T}}\mathbf{\Gamma}\mathbf{C}_{\text{ant}}\mathbf{T}_{\text{ideal}}(t') =$$

$$\begin{bmatrix} R_{\text{meas,H}}(t) \\ R_{\text{meas,V}}(t) \end{bmatrix} = \begin{bmatrix} 1 & \alpha \\ \alpha\,\beta & \beta \end{bmatrix} \begin{bmatrix} \Gamma_{\text{HH}} & \Gamma_{\text{HV}} \\ \Gamma_{\text{VH}} & \Gamma_{\text{VV}} \end{bmatrix} \begin{bmatrix} 1 & \alpha\,\beta \\ \alpha & \beta \end{bmatrix} \begin{bmatrix} |a_1(t')|\,cos(2\pi f_0 t' + \theta_1(t'))\ \hat{\text{H}} \\ |a_2(t')|\,cos(2\pi f_0 t' + \theta_2(t'))\ \hat{\text{V}} \end{bmatrix} =$$

$$\begin{bmatrix} |\Gamma_{\text{HH}}|\,[|a_1(t')|\,cos(2\pi f_0 t' + \theta_1(t') + \theta_{HH}) + \alpha\,\beta\,|a_2(t')|\,cos(2\pi f_0 t' + \theta_2(t') + \theta_{HH})] + \\ \alpha\,\beta\,|\Gamma_{\text{HH}}|\,[|a_1(t')|\,cos(2\pi f_0 t' + \theta_1(t') + \theta_{HH}) + \alpha\,\beta\,|a_2(t')|\,cos(2\pi f_0 t' + \theta_2(t') + \theta_{HH})] + \end{bmatrix}$$

$$+ \quad |\Gamma_{\text{HV}}|\,[\alpha\,|a_1(t')|\,cos(2\pi f_0 t' + \theta_1(t') + \theta_{HV}) + \beta\,|a_2(t')|\,cos(2\pi f_0 t' + \theta_2(t') + \theta_{HV})] +$$

$$+ \ \alpha\,\beta\,|\Gamma_{\text{HV}}|\,[\alpha\,|a_1(t')|\,cos(2\pi f_0 t' + \theta_1(t') + \theta_{HV}) + \beta\,|a_2(t')|\,cos(2\pi f_0 t' + \theta_2(t') + \theta_{HV})] +$$

$$+ \ \alpha|\Gamma_{\text{VH}}|\,[|a_1(t')|\,cos(2\pi f_0 t' + \theta_1(t') + \theta_{VH}) + \alpha\,\beta\,|a_2(t')|\,cos(2\pi f_0 t' + \theta_2(t') + \theta_{VH})] +$$

$$+ \ \beta\,|\Gamma_{\text{VH}}|\,[|a_1(t')|\,cos(2\pi f_0 t' + \theta_1(t') + \theta_{VH}) + \alpha\,\beta\,|a_2(t')|\,cos(2\pi f_0 t' + \theta_2(t') + \theta_{VH})] +$$

$$\begin{bmatrix} + \ \alpha|\Gamma_{\text{VV}}|\,[\alpha\,|a_1(t')|\,cos(2\pi f_0 t' + \theta_1(t') + \theta_{VV}) + \beta\,|a_2(t')|\,cos(2\pi f_0 t' + \theta_2(t') + \theta_{VV})]\ \hat{\text{H}} \\ + \ \beta\,|\Gamma_{\text{VV}}|\,[\alpha\,|a_1(t')|\,cos(2\pi f_0 t' + \theta_1(t') + \theta_{VV}) + \beta\,|a_2(t')|\,cos(2\pi f_0 t' + \theta_2(t') + \theta_{VV})]\ \hat{\text{V}} \end{bmatrix} \tag{2.9}$$

where $[\,\cdot\,]^{\text{T}}$ denotes the transpose, and $\hat{\text{H}}$ and $\hat{\text{V}}$ are the basis vectors representing the independent channels.

Once the signals have been received by the antenna, the channel corresponding with each polarization goes to its respective quadrature receiver chain, where each signal is split and mixed with a copy of the carrier in-phase (I) and in quadrature (Q). It is assumed that there is no phase error in the carrier, and that the carriers mixed in the I and Q channels for both polarization channels have magnitude equal to twice the magnitude of the original carrier that was mixed with the complex baseband modulating signals during transmission. This can be shown by forming two new matrices representing

the mixed received signals for the H and V channels, $\mathbf{R}_{\mathrm{M,H}}(t)$ and $\mathbf{R}_{\mathrm{M,V}}(t)$ respectively, shown as

$$\mathbf{R}_{\mathrm{M,H}}(t) = R_{\mathrm{meas,H}}(t) \begin{bmatrix} 2\,cos(2\pi f_0 t)\ \hat{\mathrm{I}} \\ -2\,sin(2\pi f_0 t)\ \hat{\mathrm{Q}} \end{bmatrix} \tag{2.10}$$

and

$$\mathbf{R}_{\mathrm{M,V}}(t) = R_{\mathrm{meas,V}}(t) \begin{bmatrix} 2\,cos(2\pi f_0 t)\ \hat{\mathrm{I}} \\ -2\,sin(2\pi f_0 t)\ \hat{\mathrm{Q}} \end{bmatrix} \tag{2.11}$$

where $\hat{\mathrm{I}}$ and $\hat{\mathrm{Q}}$ are the basis vectors representing the in-phase and quadrature channels, respectively. Low-pass filters can then be used to remove the high frequency components of the signals, leaving the baseband signals to be digitized by ADCs. These baseband signals, contained within the vectors $\mathbf{R}_{\mathrm{BB,H}}(t)$ and $\mathbf{R}_{\mathrm{BB,V}}(t)$, can be expanded to be shown as

$$
\begin{aligned}
&\mathbf{R}_{\mathrm{BB,H}}(t) = \\
&\left[\begin{array}{l}
\quad |\Gamma_{\mathrm{HH}}|\left[|a_1(t')|\,cos(4\pi f_0\tfrac{R}{c} - \theta_1(t') - \theta_{HH}) + \alpha\,\beta\,|a_2(t')|\,cos(4\pi f_0\tfrac{R}{c} - \theta_2(t') - \theta_{HH})\right] + \\
-|\Gamma_{\mathrm{HH}}|\left[|a_1(t')|\,sin(4\pi f_0\tfrac{R}{c} - \theta_1(t') - \theta_{HH}) + \alpha\,\beta\,|a_2(t')|\,sin(4\pi f_0\tfrac{R}{c} - \theta_2(t') - \theta_{HH})\right] +
\end{array}\right. \\
&\quad + |\Gamma_{\mathrm{HV}}|\left[\alpha\,|a_1(t')|\,cos(4\pi f_0\tfrac{R}{c} - \theta_1(t') - \theta_{HV}) + \beta\,|a_2(t')|\,cos(4\pi f_0\tfrac{R}{c} - \theta_2(t') - \theta_{HV})\right] + \\
&\quad - |\Gamma_{\mathrm{HV}}|\left[\alpha\,|a_1(t')|\,sin(4\pi f_0\tfrac{R}{c} - \theta_1(t') - \theta_{HV}) + \beta\,|a_2(t')|\,sin(4\pi f_0\tfrac{R}{c} - \theta_2(t') - \theta_{HV})\right] + \\
&\quad + \alpha|\Gamma_{\mathrm{VH}}|\left[|a_1(t')|\,cos(4\pi f_0\tfrac{R}{c} - \theta_1(t') - \theta_{VH}) + \alpha\,\beta\,|a_2(t')|\,cos(4\pi f_0\tfrac{R}{c} - \theta_2(t') - \theta_{VH})\right] + \\
&\quad - \alpha|\Gamma_{\mathrm{VH}}|\left[|a_1(t')|\,sin(4\pi f_0\tfrac{R}{c} - \theta_1(t') - \theta_{VH}) + \alpha\,\beta\,|a_2(t')|\,sin(4\pi f_0\tfrac{R}{c} - \theta_2(t') - \theta_{VH})\right] + \\
&\left.\begin{array}{l}
\quad + \alpha|\Gamma_{\mathrm{VV}}|\left[\alpha\,|a_1(t')|\,cos(4\pi f_0\tfrac{R}{c} - \theta_1(t') - \theta_{VV}) + \beta\,|a_2(t')|\,cos(4\pi f_0\tfrac{R}{c} - \theta_2(t') - \theta_{VV})\right]\ \hat{\mathrm{I}} \\
- \alpha|\Gamma_{\mathrm{VV}}|\left[\alpha\,|a_1(t')|\,sin(4\pi f_0\tfrac{R}{c} - \theta_1(t') - \theta_{VV}) + \beta\,|a_2(t')|\,sin(4\pi f_0\tfrac{R}{c} - \theta_2(t') - \theta_{VV})\right]\ \hat{\mathrm{Q}}
\end{array}\right] = \\
&= \left[\begin{array}{l}
\quad |\Gamma_{\mathrm{HH}}|\left[|a_1(t')|\,cos(-4\pi f_0\tfrac{R}{c} + \theta_1(t') + \theta_{HH}) + \alpha\,\beta\,|a_2(t')|\,cos(-4\pi f_0\tfrac{R}{c} + \theta_2(t') + \theta_{HH})\right] + \\
\quad |\Gamma_{\mathrm{HH}}|\left[|a_1(t')|\,sin(-4\pi f_0\tfrac{R}{c} + \theta_1(t') + \theta_{HH}) + \alpha\,\beta\,|a_2(t')|\,sin(-4\pi f_0\tfrac{R}{c} + \theta_2(t') + \theta_{HH})\right] +
\end{array}\right. \\
&\quad + |\Gamma_{\mathrm{HV}}|\left[\alpha\,|a_1(t')|\,cos(-4\pi f_0\tfrac{R}{c} + \theta_1(t') + \theta_{HV}) + \beta\,|a_2(t')|\,cos(-4\pi f_0\tfrac{R}{c} + \theta_2(t') + \theta_{HV})\right] + \\
&\quad + |\Gamma_{\mathrm{HV}}|\left[\alpha\,|a_1(t')|\,sin(-4\pi f_0\tfrac{R}{c} + \theta_1(t') + \theta_{HV}) + \beta\,|a_2(t')|\,sin(-4\pi f_0\tfrac{R}{c} + \theta_2(t') + \theta_{HV})\right] + \\
&\quad + \alpha|\Gamma_{\mathrm{VH}}|\left[|a_1(t')|\,cos(-4\pi f_0\tfrac{R}{c} + \theta_1(t') + \theta_{VH}) + \alpha\,\beta\,|a_2(t')|\,cos(-4\pi f_0\tfrac{R}{c} + \theta_2(t') + \theta_{VH})\right] + \\
&\quad + \alpha|\Gamma_{\mathrm{VH}}|\left[|a_1(t')|\,sin(-4\pi f_0\tfrac{R}{c} + \theta_1(t') + \theta_{VH}) + \alpha\,\beta\,|a_2(t')|\,sin(-4\pi f_0\tfrac{R}{c} + \theta_2(t') + \theta_{VH})\right] + \\
&\left.\begin{array}{l}
\quad + \alpha|\Gamma_{\mathrm{VV}}|\left[\alpha\,|a_1(t')|\,cos(-4\pi f_0\tfrac{R}{c} + \theta_1(t') + \theta_{VV}) + \beta\,|a_2(t')|\,cos(-4\pi f_0\tfrac{R}{c} + \theta_2(t') + \theta_{VV})\right]\ \hat{\mathrm{I}} \\
+ \alpha|\Gamma_{\mathrm{VV}}|\left[\alpha\,|a_1(t')|\,sin(-4\pi f_0\tfrac{R}{c} + \theta_1(t') + \theta_{VV}) + \beta\,|a_2(t')|\,sin(-4\pi f_0\tfrac{R}{c} + \theta_2(t') + \theta_{VV})\right]\ \hat{\mathrm{Q}}
\end{array}\right]
\end{aligned}
\tag{2.12}
$$

and

$$
\begin{aligned}
&\mathbf{R}_{\mathrm{BB,V}}(t) = \\
&\left[\begin{array}{l}
\alpha\,\beta\,|\Gamma_{\mathrm{HH}}|\left[|a_1(t')|\,cos(4\pi f_0\tfrac{R}{c} - \theta_1(t') - \theta_{HH}) + \alpha\,\beta\,|a_2(t')|\,cos(4\pi f_0\tfrac{R}{c} - \theta_2(t') - \theta_{HH})\right] + \\
-\alpha\,\beta\,|\Gamma_{\mathrm{HH}}|\left[|a_1(t')|\,sin(4\pi f_0\tfrac{R}{c} - \theta_1(t') - \theta_{HH}) + \alpha\,\beta\,|a_2(t')|\,sin(4\pi f_0\tfrac{R}{c} - \theta_2(t') - \theta_{HH})\right] +
\end{array}\right. \\
&+ \alpha\,\beta\,|\Gamma_{\mathrm{HV}}|\left[\alpha\,|a_1(t')|\,cos(4\pi f_0\tfrac{R}{c} - \theta_1(t') - \theta_{HV}) + \beta\,|a_2(t')|\,cos(4\pi f_0\tfrac{R}{c} - \theta_2(t') - \theta_{HV})\right] + \\
&- \alpha\,\beta\,|\Gamma_{\mathrm{HV}}|\left[\alpha\,|a_1(t')|\,sin(4\pi f_0\tfrac{R}{c} - \theta_1(t') - \theta_{HV}) + \beta\,|a_2(t')|\,sin(4\pi f_0\tfrac{R}{c} - \theta_2(t') - \theta_{HV})\right] + \\
&+ \beta\,|\Gamma_{\mathrm{VH}}|\left[|a_1(t')|\,cos(4\pi f_0\tfrac{R}{c} - \theta_1(t') - \theta_{VH}) + \alpha\,\beta\,|a_2(t')|\,cos(4\pi f_0\tfrac{R}{c} - \theta_2(t') - \theta_{VH})\right] + \\
&- \beta\,|\Gamma_{\mathrm{VH}}|\left[|a_1(t')|\,sin(4\pi f_0\tfrac{R}{c} - \theta_1(t') - \theta_{VH}) + \alpha\,\beta\,|a_2(t')|\,sin(4\pi f_0\tfrac{R}{c} - \theta_2(t') - \theta_{VH})\right] + \\
&\left.\begin{array}{l}
+ \beta\,|\Gamma_{\mathrm{VV}}|\left[\alpha\,|a_1(t')|\,cos(4\pi f_0\tfrac{R}{c} - \theta_1(t') - \theta_{VV}) + \beta\,|a_2(t')|\,cos(4\pi f_0\tfrac{R}{c} - \theta_2(t') - \theta_{VV})\right]\ \hat{\mathrm{I}} \\
- \beta\,|\Gamma_{\mathrm{VV}}|\left[\alpha\,|a_1(t')|\,sin(4\pi f_0\tfrac{R}{c} - \theta_1(t') - \theta_{VV}) + \beta\,|a_2(t')|\,sin(4\pi f_0\tfrac{R}{c} - \theta_2(t') - \theta_{VV})\right]\ \hat{\mathrm{Q}}
\end{array}\right] = \\
&= \left[\begin{array}{l}
\alpha\,\beta\,|\Gamma_{\mathrm{HH}}|\left[|a_1(t')|\,cos(-4\pi f_0\tfrac{R}{c} + \theta_1(t') + \theta_{HH}) + \alpha\,\beta\,|a_2(t')|\,cos(-4\pi f_0\tfrac{R}{c} + \theta_2(t') + \theta_{HH})\right] + \\
\alpha\,\beta\,|\Gamma_{\mathrm{HH}}|\left[|a_1(t')|\,sin(-4\pi f_0\tfrac{R}{c} + \theta_1(t') + \theta_{HH}) + \alpha\,\beta\,|a_2(t')|\,sin(-4\pi f_0\tfrac{R}{c} + \theta_2(t') + \theta_{HH})\right] +
\end{array}\right. \\
&+ \alpha\,\beta\,|\Gamma_{\mathrm{HV}}|\left[\alpha\,|a_1(t')|\,cos(-4\pi f_0\tfrac{R}{c} + \theta_1(t') + \theta_{HV}) + \beta\,|a_2(t')|\,cos(-4\pi f_0\tfrac{R}{c} + \theta_2(t') + \theta_{HV})\right] + \\
&+ \alpha\,\beta\,|\Gamma_{\mathrm{HV}}|\left[\alpha\,|a_1(t')|\,sin(-4\pi f_0\tfrac{R}{c} + \theta_1(t') + \theta_{HV}) + \beta\,|a_2(t')|\,sin(-4\pi f_0\tfrac{R}{c} + \theta_2(t') + \theta_{HV})\right] + \\
&+ \beta\,|\Gamma_{\mathrm{VH}}|\left[|a_1(t')|\,cos(-4\pi f_0\tfrac{R}{c} + \theta_1(t') + \theta_{VH}) + \alpha\,\beta\,|a_2(t')|\,cos(-4\pi f_0\tfrac{R}{c} + \theta_2(t') + \theta_{VH})\right] + \\
&+ \beta\,|\Gamma_{\mathrm{VH}}|\left[|a_1(t')|\,sin(-4\pi f_0\tfrac{R}{c} + \theta_1(t') + \theta_{VH}) + \alpha\,\beta\,|a_2(t')|\,sin(-4\pi f_0\tfrac{R}{c} + \theta_2(t') + \theta_{VH})\right] + \\
&\left.\begin{array}{l}
+ \beta\,|\Gamma_{\mathrm{VV}}|\left[\alpha\,|a_1(t')|\,cos(-4\pi f_0\tfrac{R}{c} + \theta_1(t') + \theta_{VV}) + \beta\,|a_2(t')|\,cos(-4\pi f_0\tfrac{R}{c} + \theta_2(t') + \theta_{VV})\right]\ \hat{\mathrm{I}} \\
+ \beta\,|\Gamma_{\mathrm{VV}}|\left[\alpha\,|a_1(t')|\,sin(-4\pi f_0\tfrac{R}{c} + \theta_1(t') + \theta_{VV}) + \beta\,|a_2(t')|\,sin(-4\pi f_0\tfrac{R}{c} + \theta_2(t') + \theta_{VV})\right]\ \hat{\mathrm{Q}}
\end{array}\right]
\end{aligned}
\tag{2.13}
$$

Using Euler's formula, $cos(\theta) + jsin(\theta) = e^{j\,\theta}$, the $\hat{\mathrm{I}}$ and $\hat{\mathrm{Q}}$ components of $\mathbf{R}_{\mathrm{BB,H}}(t)$ and $\mathbf{R}_{\mathrm{CBB,V}}(t)$ can be used as the real and imaginary components, respectively, to form the complex baseband signals, contained in the matrix $\mathbf{R}_{\mathrm{CBB}}(t)$ with terms $R_{\mathrm{CBB,H}}(t)$ and $R_{\mathrm{BB,V}}(t)$ for the H and V channels, respec-

tively. This is shown as

$$\mathbf{R}_{\mathrm{CBB}}(t) \;=\; \begin{bmatrix} R_{\mathrm{CBB,H}}(t)\;\hat{\mathrm{H}} \\ R_{\mathrm{CBB,V}}(t)\;\hat{\mathrm{V}} \end{bmatrix} \tag{2.14}$$

Due to the length of $R_{\mathrm{CBB,H}}(t)$ and $R_{\mathrm{CBB,V}}(t)$, they are shown below individually as

$$\begin{aligned}
R_{\mathrm{CBB,H}}(t) = \\
&= \;|\Gamma_{\mathrm{HH}}|\left[|a_1(t')|\,e^{j(-4\pi f_0\frac{R}{c}+\theta_1(t')+\theta_{HH})} \;+\; \alpha\,\beta\,|a_2(t')|\,e^{j(-4\pi f_0\frac{R}{c}+\theta_2(t')+\theta_{HH})}\right] \;+ \\
&+\; |\Gamma_{\mathrm{HV}}|\left[\alpha\,|a_1(t')|\,e^{j(-4\pi f_0\frac{R}{c}+\theta_1(t')+\theta_{HV})} \;+\; \beta\,|a_2(t')|\,e^{j(-4\pi f_0\frac{R}{c}+\theta_2(t')+\theta_{HV})}\right] \;+ \\
&+\; \alpha|\Gamma_{\mathrm{VH}}|\left[|a_1(t')|\,e^{j(-4\pi f_0\frac{R}{c}+\theta_1(t')+\theta_{VH})} \;+\; \alpha\,\beta\,|a_2(t')|\,e^{j(-4\pi f_0\frac{R}{c}+\theta_2(t')+\theta_{VH})}\right] \;+ \\
&+\; \alpha|\Gamma_{\mathrm{VV}}|\left[\alpha\,|a_1(t')|\,e^{j(-4\pi f_0\frac{R}{c}+\theta_1(t')+\theta_{VV})} \;+\; \beta\,|a_2(t')|\,e^{j(-4\pi f_0\frac{R}{c}+\theta_2(t')+\theta_{VV})}\right] = \\
&= \Gamma_{\mathrm{HH}}\left[a_1(t')\,e^{-j4\pi f_0\frac{R}{c}} \;+\; \alpha\,\beta\,a_2(t')\,e^{-j4\pi f_0\frac{R}{c}}\right] \;+ \\
&+\; \Gamma_{\mathrm{HV}}\left[\alpha\,a_1(t')\,e^{-j4\pi f_0\frac{R}{c}} \;+\; \beta\,a_2(t')\,e^{-j4\pi f_0\frac{R}{c}}\right] \;+ \\
&+\; \alpha\Gamma_{\mathrm{VH}}\left[a_1(t')\,e^{-j4\pi f_0\frac{R}{c}} \;+\; \alpha\,\beta\,a_2(t')\,e^{-j4\pi f_0\frac{R}{c}}\right] \;+ \\
&+\; \alpha\Gamma_{\mathrm{VV}}\left[\alpha\,a_1(t')\,e^{-j4\pi f_0\frac{R}{c}} \;+\; \beta\,a_2(t')\,e^{-j4\pi f_0\frac{R}{c}}\right] = \\
&= \left[\Gamma_{\mathrm{HH}}\,a_1(t') \;+\; \beta\,\Gamma_{\mathrm{HV}}\,a_2(t')\right]e^{-j4\pi f_0\frac{R}{c}} \;+ \\
&+\; \alpha\left[\beta\,\Gamma_{\mathrm{HH}}\,a_2(t') \;+\; \Gamma_{\mathrm{HV}}\,a_1(t') \;+\; \Gamma_{\mathrm{VH}}\,a_1(t') \;+\; \beta\,\Gamma_{\mathrm{VV}}\,a_2(t')\right]e^{-j4\pi f_0\frac{R}{c}} \;+ \\
&+\; \alpha^2\left[\beta\,\Gamma_{\mathrm{VH}}\,a_2(t') \;+\; \Gamma_{\mathrm{VV}}\,a_1(t')\right]e^{-j4\pi f_0\frac{R}{c}}
\end{aligned} \tag{2.15}$$

and

$$
\begin{aligned}
&R_{\mathrm{CBB,V}}(t) = \\
&= \alpha\,\beta|\Gamma_{\mathrm{HH}}|\left[|a_1(t')|\,e^{j(-4\pi f_0\frac{R}{c}+\theta_1(t')+\theta_{HH})} + \alpha\,\beta\,|a_2(t')|\,e^{j(-4\pi f_0\frac{R}{c}+\theta_2(t')+\theta_{HH})}\right] + \\
&+ \alpha\,\beta|\Gamma_{\mathrm{HV}}|\left[\alpha\,|a_1(t')|\,e^{j(-4\pi f_0\frac{R}{c}+\theta_1(t')+\theta_{HV})} + \beta|a_2(t')|\,e^{j(-4\pi f_0\frac{R}{c}+\theta_2(t')+\theta_{HV})}\right] + \\
&+ \beta|\Gamma_{\mathrm{VH}}|\left[|a_1(t')|\,e^{j(-4\pi f_0\frac{R}{c}+\theta_1(t')+\theta_{VH})} + \alpha\,\beta\,|a_2(t')|\,e^{j(-4\pi f_0\frac{R}{c}+\theta_2(t')+\theta_{VH})}\right] + \\
&+ \beta|\Gamma_{\mathrm{VV}}|\left[\alpha\,|a_1(t')|\,e^{j(-4\pi f_0\frac{R}{c}+\theta_1(t')+\theta_{VV})} + \beta\,|a_2(t')|\,e^{j(-4\pi f_0\frac{R}{c}+\theta_2(t')+\theta_{VV})}\right] = \\
&= \alpha\,\beta\Gamma_{\mathrm{HH}}\left[a_1(t')\,e^{-j4\pi f_0\frac{R}{c}} + \alpha\,\beta\,a_2(t')\,e^{-j4\pi f_0\frac{R}{c}}\right] + \\
&+ \alpha\,\beta\Gamma_{\mathrm{HV}}\left[\alpha\,a_1(t')\,e^{-j4\pi f_0\frac{R}{c}} + \beta\,a_2(t')\,e^{-j4\pi f_0\frac{R}{c}}\right] + \\
&+ \beta\Gamma_{\mathrm{VH}}\left[a_1(t')\,e^{-j4\pi f_0\frac{R}{c}} + \alpha\,\beta\,a_2(t')\,e^{-j4\pi f_0\frac{R}{c}}\right] + \\
&+ \beta\Gamma_{\mathrm{VV}}\left[\alpha\,a_1(t')\,e^{-j4\pi f_0\frac{R}{c}} + \beta\,a_2(t')\,e^{-j4\pi f_0\frac{R}{c}}\right] = \\
&= \left[\beta\,\Gamma_{\mathrm{VH}}\,a_1(t') + \beta^2\,\Gamma_{\mathrm{VV}}\,a_2(t')\right]\,e^{-j4\pi f_0\frac{R}{c}} + \\
&+ \alpha\left[\beta\,\Gamma_{\mathrm{HH}}\,a_1(t') + \beta^2\,\Gamma_{\mathrm{HV}}\,a_2(t') + \beta^2\,\Gamma_{\mathrm{VH}}\,a_2(t') + \beta\,\Gamma_{\mathrm{VV}}\,a_1(t')\right]\,e^{-j4\pi f_0\frac{R}{c}} + \\
&+ \alpha^2\left[\beta^2\,\Gamma_{\mathrm{HH}}\,a_2(t') + \beta\,\Gamma_{\mathrm{HV}}\,a_1(t')\right]\,e^{-j4\pi f_0\frac{R}{c}} \qquad (2.16)
\end{aligned}
$$

The resulting signals from equations 2.15 and 2.16 clearly show the necessity of high cross-pol isolation as a large cross-pol contamination, reflected in a large α value, removes the ability to accurately extract the $\mathbf{\Gamma}$ parameter values with pulse compression or other forms of waveform control on $a_1(t)$ and $a_2(t)$. As the cross-pol isolation is increased and the co-pol gain mismatch is decreased, the ideal return signal is approached, shown as

$$\lim_{\alpha\to 0}\lim_{\beta\to 1}\mathbf{R}_{\mathrm{CBB}}(t) = \mathbf{R}_{\mathrm{CBB,ideal}}(t) \qquad (2.17)$$

where

$$\mathbf{R}_{\mathrm{CBB,ideal}}(t) = \begin{bmatrix} [\Gamma_{\mathrm{HH}}\, a_1(t') \;+\; \Gamma_{\mathrm{HV}}\, a_2(t')]\; e^{-j4\pi f_0 \frac{R}{c}}\; \hat{\mathrm{H}} \\ [\Gamma_{\mathrm{VH}}\, a_1(t') \;+\; \Gamma_{\mathrm{VV}}\, a_2(t')]\; e^{-j4\pi f_0 \frac{R}{c}}\; \hat{\mathrm{V}} \end{bmatrix} \tag{2.18}$$

Now it can be easily seen that for very high cross-pol isolation and low co-pol gain mismatch where $\mathbf{R}_{\mathrm{CBB}}(t) \approx \mathbf{R}_{\mathrm{CBB,ideal}}(t)$, the individual terms of $\mathbf{\Gamma}$ can be recovered. This is relatively simple for the alternating H and V transmit mode because for any given instance of $\mathbf{R}_{\mathrm{CBB}}(t)$ resulting from a single measured pulse, either $a_1(t') = 0$ or $a_2(t') = 0$, leaving a single $\mathbf{\Gamma}$ parameter in both H and V channels, and once a measurement from both broadcast polarizations has been made, the full $\mathbf{\Gamma}$ matrix can be assembled. The downside of the alternating transmit approach is that the $\mathbf{\Gamma}$ matrix is assumed to be for the target at an instantaneous moment in time, but the $\mathbf{\Gamma}$ matrix is actually assembled from different measurements taken at minimum one Pulse Repetition Time (PRT) apart. This is why the simultaneous H and V transmit mode is more desired from a scientific standpoint, as the $\mathbf{\Gamma}$ matrix is assembled from measurements truly taken at the same instance. The difficulty of the simultaneous transmit mode is that the separation of individual $\mathbf{\Gamma}$ terms is achieved completely through signal processing dependent on the modulating waveforms $a_1(t)$ and $a_2(t)$. Therefore, $a_1(t)$ and $a_2(t)$ must be chosen so that after pulse compression with one of the selected waveforms, there is a single instantaneous high cross-correlation on the component multiplied by the same waveform, and an extremely low cross-correlation at all time delays with the component multiplied by the other waveform. Basically, $a_1(t)$ and $a_2(t)$ must each have pulse compression outputs with low range sidelobes (see Section 2.3) as well as together form a pseudo-orthogonal set (see Sec. 2.4), which presents

its own challenges, but is needed to achieve the desired scientific measurements. Therefore, by processing the matched filters for $a_1(t)$ and $a_2(t)$ on both H and V channels, the four elements of the $\mathbf{\Gamma}$ matrix can be obtained (Γ_{HH} and Γ_{HV} from the H channel, and Γ_{VH} and Γ_{VV} on the V channel) to the degree that the co-pol gain imbalance, cross-pol contamination, and pseudo-orthogonality of the waveform set allows. The measured values of the $\mathbf{\Gamma}$ matrix, $\mathbf{\Gamma}_{Meas}$, can be shown as

$$\mathbf{\Gamma}_{Meas} = \begin{bmatrix} \Gamma_{\mathrm{HH},Meas} \\ \Gamma_{\mathrm{HV},Meas} \\ \Gamma_{\mathrm{VH},Meas} \\ \Gamma_{\mathrm{VV},Meas} \end{bmatrix} = \begin{bmatrix} \max\left(R_{\mathrm{CBB,H}}(t) \otimes h_1(t)\right) \\ \max\left(R_{\mathrm{CBB,H}}(t) \otimes h_2(t)\right) \\ \max\left(R_{\mathrm{CBB,V}}(t) \otimes h_1(t)\right) \\ \max\left(R_{\mathrm{CBB,V}}(t) \otimes h_2(t)\right) \end{bmatrix} \tag{2.19}$$

where $h_1(t)$ is the matched filter for waveform $a_1(t)$, $h_2(t)$ is the matched filter for waveform $a_2(t)$, $\otimes$ is the convolution operator, $\max(\,\cdot\,)$ gives the value of the point with the maximum magnitude in its argument, and $\mathbf{\Gamma}_{Meas}$ is rearranged from the intuitive $[2 \times 2]$ format into a $[4 \times 1]$ format for ease of display due to the length of each expanded individual term.

2.3 Cross-Correlation and Pulse Compression

In order to understand the basis of pseudo-orthogonal waveform sets, the definitions and meanings of cross-correlation, matched filters, and pulse compression must be established.

The mathematical formula for continuous domain cross-correlation of $x(t)$ with $y(t)$ is defined as

$$s_{xy}(\tau) \;=\; \mathrm{E}\{x(t)y^*(t+\tau)\} \;=\; \int_{-\infty}^{+\infty} x(t)y^*(t+\tau)\,\mathrm{d}t \quad -\infty < \tau < +\infty \quad (2.20)$$

where $\mathrm{E}\{\cdot\}$ denotes the "expected value" as seen on pg 533 of [17], $s_{xy}(\tau)$, $x(t)$, $y(t) \in \mathbb{C}$, and t, $\tau \in \mathbb{R}$ (and t and τ are commonly in units of seconds), $s_{\mathrm{xy}}(\tau)$ is the continuous domain cross-correlation as a function of offset τ, $x(t)$ is a continuous signal as a function of t, and $y^*(t+\tau)$ is the complex conjugate of $y(t)$ with a difference in continuous variable by τ.

The mathematical formula for discrete domain cross-correlation of $x[n]$ with $y[n]$ is defined as

$$s_{\mathrm{xy}}[k] \;=\; \mathrm{E}\{x[n]y^*[n+k]\} \;=\; \sum_{n=-\infty}^{+\infty} x[n]y^*[n+k] \quad -\infty < k < +\infty \quad (2.21)$$

where $s_{xy}[k]$, $x[n]$, $y[n] \in \mathbb{C}$, and n, $k \in \mathbb{Z}$ (and n and k are commonly unitless), $s_{\mathrm{xy}}[k]$ is the discrete domain cross-correlation as a function of index offset k, $x[n]$ is a discrete signal with indexing n, and $y^*[n+k]$ is the complex conjugate of $y[n]$ with indexing offset k.

It should be noted that if $x(t) = y(t)$ in Eq. 2.20 or if $x[n] = y[n]$ in Eq. 2.21, then the resulting cross-correlation would be more aptly referred to as the autocorrelation. It should also be noted that the cross-correlation of $x[n]$ and $y[n]$ is equal to the convolution of $x[n]$ and $y^*[-n]$ as shown on pg 35 of [10].

Cross-correlation is crucial from a signal processing perspective, as it forms the basis of matched filtering and pulse compression.

Pulse compression is defined by Richards [10] as "the process of designing a waveform and its corresponding matched filter so that the matched filter output in response to the echo from a single point scatterer concentrates most of its energy in a very short duration, thus providing good range resolution while still allowing the high transmitted energy of a long pulse."

A traditional unmodulated fixed frequency radar transmits a constant modulus waveform for duration τ. This results in a minimum resolution in time of τ seconds, while increasing the tradeoff between probability of detection and probability of false alarm is directly related to increasing the Signal to Noise Ratio (SNR), which is also directly related to increasing the pulse length τ. This is because the SNR measured at a time T_M is given by

$$SNR == \frac{|y(T_M)|^2}{n_p} = \frac{\left|\frac{1}{2\pi}\int_{-\infty}^{+\infty} X(\Omega)H(\Omega)e^{j\Omega T_M}\,\mathrm{d}\Omega\right|^2}{\frac{N_0}{4\pi}\int_{-\infty}^{+\infty}|H(\Omega)|^2\,\mathrm{d}\Omega} \tag{2.22}$$

where the spectrum of the receiver output $y(T_M)$ is $Y(\Omega) = H(\Omega)X(\Omega)$, $X(\Omega)$ is the spectrum of the waveform, $H(\Omega)$ is the receiver frequency response, N_0 is the power spectral density of white noise in the receiver, and n_p is the total output noise power. By applying the Cauchy Schwarz inequality on the numerator with the intention of finding the receiver frequency response that maximizes the SNR, it is seen that it is necessary for $H(\Omega) = \alpha X^*(\Omega)e^{-j\Omega T_M}$ (or $h(t) = \alpha x^*(T_M - t)$ in the time domain) where α is an arbitrary scaling factor. As an aside, the receiver frequency response that maximizes the SNR for a given waveform is known as the matched filter, because it is specifically matched to the used waveform. Using the matched filter leads to a simplified

equation for SNR, shown as

$$SNR \;=\; \frac{1}{\pi N_0} \int_{-\infty}^{+\infty} |X(\Omega)|^2 \, \mathrm{d}\Omega \tag{2.23}$$

Applying Parseval's theorem $\int_{-\infty}^{+\infty} |x(t)|^2 \, \mathrm{d}t \;=\; \int_{-\infty}^{+\infty} |X(\Omega)|^2 \, \mathrm{d}\Omega$ and the assumption that $x(t)$ has a fixed amplitude, it can be seen that the only way to increase SNR, and thus the tradeoff between probability of detection and probability of false alarm, is to increase the pulse length time τ, which decreases the possible range resolution for the unmodulated constant modulus waveform [10]. The output of the matched filter $y(t)$ is given by the convolution of the matched filter with the received signal $x'(t)$, shown as

$$y(t) \;=\; \int_{-\infty}^{+\infty} x'(s) h(t-s) \, \mathrm{d}s \;=\; \alpha \int_{-\infty}^{+\infty} x'(s) x^*(s \,+\, T_M \,-\, t) \, \mathrm{d}s \tag{2.24}$$

Note that the equation for calculating the matched filter output (Eq. 2.24) is actually the cross-correlation (see Eq. 2.20) of the received signal $x'(t)$ with the transmitted signal $x(t)$. If the received signal were a perfect copy of the transmitted signal, the matched filter output would be the autocorrelation of the waveform. This is why cross-correlation is related to matched filtering, and since matched filtering is needed to maximize the SNR of the receiver output, matched filtering is needed to optimize the results of pulse compression.

Another way of examining the inverse relation between the range resolution and the possible SNR is by examining the time-bandwidth product, which is given by $TB \;=\; \beta \, \tau$, where TB is the time-bandwidth product, β is the Rayleigh bandwidth (minimum resolvable bandwidth), and τ is the minimum resolution in time at the matched filter output. For the simple unmodulated

waveform the Rayleigh bandwidth is $\frac{1}{\tau}$ and the minimum resolution in time is τ, which gives $TB = 1$. This relation between resolution and received power can be mitigated to an extent, improving the receive characteristics and filter output of the system by using a pulse compression waveform, which causes the decoupling of energy (more specifically, the pulse length due to the assumption of a constant modulus waveform) and resolution, which is accomplished through mindful waveform design and the use of a matched filter. As a result, a pulse compression waveform has $TB >> 1$ [10].

Pulse compression is well summarized by Skolnik on pg. 341 of [18], where pulse compression is "described as the use of a long pulse of width T to obtain the resolution of a short pulse by modulating the long pulse to achieve a bandwidth $B >> \frac{1}{T}$, and processing the modulated long pulse in a matched filter to obtain a pulse width $\tau \approx \frac{1}{B}$. Pulse compression allows a radar to simultaneously achieve the energy of a long pulse and the resolution of a short pulse without the high peak power required of a high-energy short-duration pulse."

Since the receiver output is the time convolution of the matched filter and received signal, this is equivalent to the cross-correlation of the received signal with the transmitted signal (which should be very close to one another, resulting in a maximum cross-correlation output at a delay of zero, similar to the true autocorrelation case). While the effect of Doppler shift, amplitude and phase errors, noise, and other received signal corruptions can and should be taken into account in waveform development, pulse compression signals are usually designed and analyzed initially with an ideal received signal, so that

the matched filter output actually is the autocorrelation of the transmitted signal.

Intuitively, this means that the autocorrelation of the waveform should destructively interfere as much as possible at all delays except for delay zero (which will already be the maximum as an inherrent property of the autocorrelation function). This is accomplished through clever assignment of phase shifts in the phase coding case, and is accomplished naturally in the frequency modulation case (it is assumed the frequency modulated waveform changes frequency monotonically) as different frequencies will increasingly destructively interfere with one another as the difference in frequencies increases. Examples of Linear Frequency Modulated (LFM) and biphase coded pulse compression results versus equal length unmodulated waveform receiver outputs are shown below in Figure 2.1 and Figure 2.2, respectively. A 13 bit Barker code was chosen for the biphase coded waveform example (See Sec. 2.6). Note that the peak autocorrelation of the unmodulated case is the same as the pulse compression signal case for both examples, but in both examples the sidelobes of the autocorrelation function are suppressed much lower for the modulated waveforms than for the unmodulated case.

Frequency modulation based pulse compression, more specifically LFM based pulse compression, has the benefits of easy generation and architecture implementation, the option of easy analog or digital implementation of the matched filter, and is very Doppler tolerant (meaning that the same matched filter can be used for target detection, even when the received signal has a large Doppler shift present). In addition, if stretch processing is utilized (where the

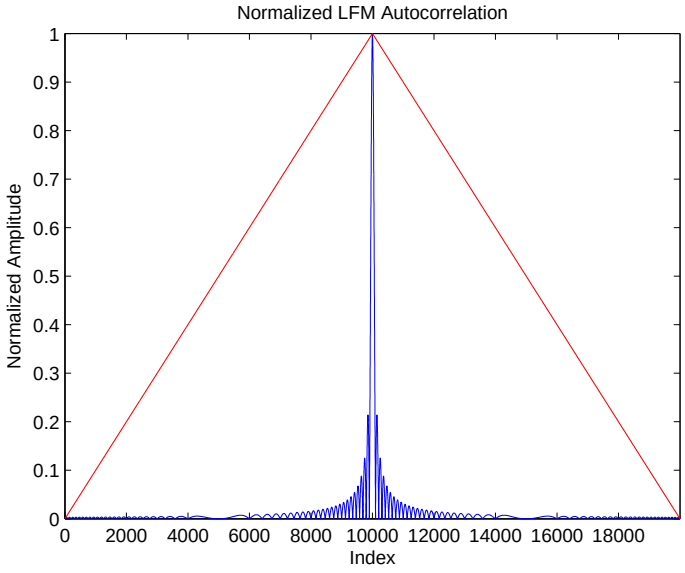


Figure 2.1: *Example of Pulse Compressed vs. Simple Waveform Receiver Output: 10 MHz Bandwidth LFM Case*

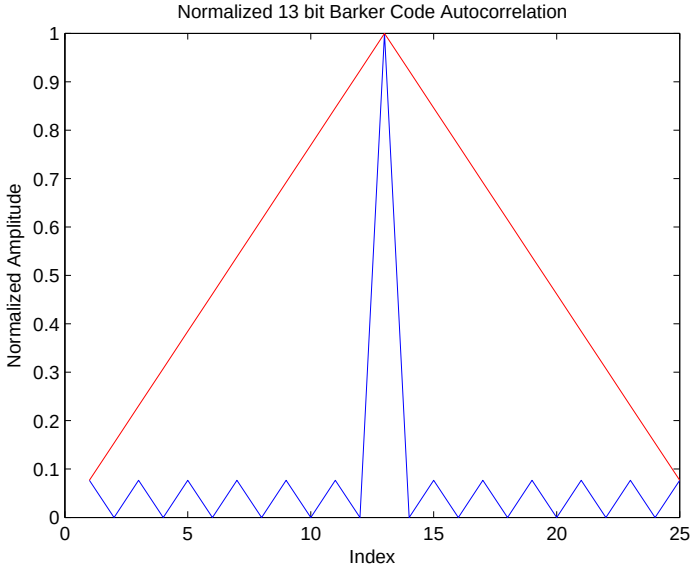


Figure 2.2: *Example of Pulse Compressed vs. Simple Waveform Receiver Output: 13 bit Biphase Barker Coded Case*

downconverted received signal is mixed with chirp based around a reference position), then high resolution detection can be made, possibly even able to

utilize an Analog to Digital Converter (ADC) with a more narrow bandwidth than the originally transmitted signal. However, LFM waveforms, with a sinc shaped autocorrelation output proportional to $\frac{sin\,\pi Bt}{\pi Bt}$, have relatively high peak sidelobes present which are only 13.2 dB lower than the autocorrelation peak, however these can be lowered with windowing to 30 dB lower than the autocorrelation peak if a loss of 1 dB can be tolerated [18]. Unwindowed Non-Linear Frequency Modulated (NLFM) waveforms can lead to autocorrelation function outputs with very low peak sidelobes, but this is usually at the expense of doppler tolerance.

Phase coding based pulse compression is usually divided into either biphase codes or polyphase codes. Biphase codes are limited to two phase states that are π radians out of phase. Arguably the most important biphase codes are Barker codes and Minimum Peak Sidelobe (MPS) codes (see Sec. 2.6). In general, biphase codes exhibit low, predictable sidelobe levels, and some biphase codes result in the minimum peak sidelobe for a given code length [17]. However, biphase codes are very Doppler intolerant, and filter banks utilizing matched filters with preset Doppler offsets must be utilized to detect substantially Doppler shifted targets in the received signal. Polyphase codes are not limited to two phase states, and in general polyphase codes can produce lower autocorrelation sidelobe levels and are more Doppler tolerant than equal length biphase codes (see Sec. 2.6). While polyphase codes can have much lower autocorrelation sidelobe levels than unwindowed (and also realistically windowed) LFM waveforms as well as be more Doppler tolerant than biphase codes, LFM waveforms are usually more applicable when detection of targets with very large Doppler shifts may be present [1].

2.4 Orthogonality and Waveform Pseudo-Orthogonality

As shown in Section 2.2, dual-polarized radar systems must utilize orthogonality in both polarization and in waveform coding. From a linear algebra perspective, the definition of orthogonal is given as Definition 5.4 by Kolman in [19], stating "Let V be an inner product space. Two vectors $\mathbf{u}$ and $\mathbf{v}$ in V are **orthogonal** if $(\mathbf{u}, \mathbf{v}) = 0$" where $(\cdot)$ denotes the inner product. Definition 5.5 in [19] states "Let V be an inner product space. A set S of vectors in V is called **orthogonal** if any two distinct vectors in S are orthogonal. If, in addition, each vector in S is of unit length, then S is called **orthonormal**."

From a signal processing perspective, Oppenheim [20] states on pg. 273 that "Two functions $u(t)$ and $v(t)$ are said to be *orthogonal over the interval (a,b)* if

$$\int_a^b u(t)v^*(t)\,\mathrm{d}t = 0 \tag{2.25}$$

If, in addition,

$$\int_a^b |u(t)|^2\,\mathrm{d}t = 1 = \int_a^b |v(t)|^2\,\mathrm{d}t \tag{2.26}$$

the functions are said to be *normalized* and hence are called *orthonormal*. A set of functions $\{\phi_k(t)\}$ is called an *orthogonal (orthonormal) set* if each pair of functions in the set is orthogonal (orthonormal)."

From a radar signal processing perspective, Pace [11] states on pg. 361-362 that "An orthogonal waveform set is a group of waveforms in which each of

the waveforms has nearly ideal noise-like aperiodic autocorrelation property and any two of them have no cross-correlation."

The definitions given by Kolman and Oppenheim imply that the true definition of orthogonality only applies to the current simultaneous state of two vectors (or functions), and does not take into account indexing or time lags between the two. Notice the similarity between the condition of orthogonality Eq. 2.25 and the definition of cross-correlation in Eq. 2.20. The condition for orthogonality is basically the cross-correlation at zero delay, integrated over a finite interval, equating to zero.

The definition of an orthogonal waveform set given by Pace requires that "any two [codes] have no cross-correlation" as well be non-zero (implied by the requirement that "each of the waveforms has nearly ideal noise-like aperiodic autocorrelation"). Pace's definition has no implicit necessity that the orthogonality is only evaluated at a single (zero) time lag, therefore it is assumed to use the normal definition of cross-correlation, which as shown in Eq. 2.20 implies that all time delays must be taken into account. As an aside, it is technically impossible for finite length non-zero codes to have no cross-correlation, so it is interpreted to mean very low cross-correlation for all time delays. Therefore Pace's presented definition of orthogonality does not technically agree with the usual mathematical definition of orthogonality due to taking into account all offsets between waveforms, and it is actually closer to the understood definition of "nearly orthogonal," here used synonymously with "pseudo-orthogonal," than true mathematical orthogonality.

Using Pace's definition of orthogonality for the definition of pseudo-orthogonality, this means that a pseudo-orthogonal set of waveforms contains waveforms where each waveform exhibits desirable autocorrelation characteristics (approaching that of white noise), and any two waveforms have very low cross-correlation for any and all time or indexing delays between waveforms. White noise is defined by Mitra [21] on pg. 901 as a "zero-mean Wide Sense Stationary (WSS) random process [that] has an autocorrelation sequence $\phi_{XX}[l]$ that is an impulse sequence of amplitude σ_x^2," where σ_x^2 is defined to be the variance of random variable X, and a random process where any pair of two different samples from the process are uncorrelated. In order for the autocorrelation of white noise to equal an impulse function, the sequence must be infinitely long. This is not feasible in practice, and is why the approximation (rather than matching) of a delta function in the autocorrelation function is one of the criteria of the pseudo-orthogonal waveform set.

It should be noted that due to the the nature of radar operation, where the delay between signal transmission and reception is directly due to target range, where range is an unknown and continuous variable, a set of pseudo-orthogonal waveforms is much more practical in usage than a set of truly mathematically orthogonal waveforms. This is because orthogonal waveforms, while having zero cross-correlation at zero delay, do not have defined characteristics for all other delays. Pseudo-orthogonal waveforms, while they most likely have non-zero cross-correlation at zero delay, almost assuredly have flatter and more suppressed cross-correlation response across non-zero delays than the orthogonal waveform set. Due to the radar's inability to sync demodulation with the time delay due to the unknown target range, the overall cross-correlation

characteristics of the pseudo-orthogonal set is much more desirable than the zero-lag cross-correlation characteristic of the orthogonal set.

The white noise-like autocorrelation properties desired in the pseudo-orthogonal waveform set means that white noise generated signals themselves can be used as an example to show that a pseudo-orthogonal waveform set is possible. Consider two infinite sequences of white noise generated signal points. Due to the quality of the white noise generated sequence that any two different points are uncorrelated, because both infinite sequences are white noise generated this means that any point in the first sequence will also be uncorrelated with any point in the second sequence. This also means that the cross-correlation between the two sequences is zero at all time delays, effectively making the two sequences truly orthogonal at all time delays. Therefore, a set of two white noise generated infinite sequences meets both the requirements for pseudo-orthogonality as well as mathematical orthogonality (though $a = -\infty \; and \; b = +\infty$ in Eq. 2.25).

In the real world, infinite sequences are not possible, so finite sequences must be used. However, in practice a very long finite sequence of white noise will still result in an autocorrelation resembling a delta function, but with very small non-zero values at non-zero delays rather than actual zero values like in the ideal infinitely long sequence case. This means that as the length is increased of the white noise generated sequence, the sequence continues to approximate more closely the ideal infinitely long case, and the non-zero delay autocorrelation values are suppressed accordingly. Creating a very (very) long sequence of white noise could easily result in an autocorrelation function with

a peak 50 dB greater than all other points. This is important because, due to the quality of the white noise generated sequence that any two different points are uncorrelated, a second equal length independently generated white noise sequence will have an autocorrelation function with very similar overall characteristics to those of the first function, but any point in the second sequence will be completely uncorrelated with any point in the first sequence. The result is the cross-correlation of the two sequences at all points will resemble the non-zero delay points in the autocorrelation of either of the sequences. Therefore, if two independently generated white noise sequences each have autocorrelations with peaks 50 dB greater than all other points, then they should also have a cross-correlation that is 50 dB lower than the peak in the autocorrelation functions.

While using white noise based sequences may not be practical or optimal for most radar systems, it does show that it is possible for a set of finite sequences to be created where the cross-correlation (inner product at all time lags) is tens of decibels lower than the autocorrelation peak of the individual sequences. More elegantly created (and much shorter) waveform sets should be possible with other forms of coding, but the difficulty in generation of these sets led to the use of white noise as an example.

2.4.1 Pseudo-Orthogonality of a Linear Frequency Modulated Waveform Pair

A pair of linear frequency modulated (LFM) waveforms are commonly casually referred to as an orthogonal set. As shown in Eq. 2.25, two signals are orthogonal if the cross-correlation at zero delay of the two signals is equal to zero. Therefore, to determine if a pair of LFM waveforms with opposite chirp directions and otherwise identical parameters form an orthogonal set, the derivation of the matched filter result will be given for both the traditional case of an upchirp with its matched filter as well as a downchirp with the upchirp's matched filter [22]. It is assumed that the center frequency, bandwidth, pulse duration, and all other parameters (with the exception of the direction of changing frequency) are identical between the upchirp and downchirp. The magnitude of the two responses relative to one another is desired rather than the absolute magnitude, so equal normalization of both signals will take place throughout the derivation.

The upchirp $x_1(t)$ and downchirp $x_2(t)$ are defined as

$$x_1(t) \;=\; \text{rect}\left(\frac{t}{T}\right) e^{j2\pi(f_0 t + \frac{k}{2}t^2)} \tag{2.27}$$

and

$$x_2(t) \;=\; \text{rect}\left(\frac{t}{T}\right) e^{j2\pi(f_0 t - \frac{k}{2}t^2)} \tag{2.28}$$

where f_0 is the center frequency (or carrier) of the chirp, $k = \frac{B}{T}$ where B is the bandwidth of the chirp and T is the duration in time of the chirp, and

$$\text{rect}\,(x) \;=\; \begin{cases} 1 & |x| < \frac{1}{2} \\ 0 & \text{otherwise} \end{cases} \tag{2.29}$$

Therefore the upchirp matched filter $y_1(t)$ is given by

$$y_1(t) \;=\; \alpha\, x_1^*(-t) \;=\; \alpha\,\text{rect}\left(\frac{t}{T}\right) e^{j2\pi(f_0 t - \frac{k}{2}t^2)} \tag{2.30}$$

where α is an arbitrary scaling vector, that will be set as $\alpha = 1$ for simplification (and because it will scale both cases equally). As referenced in Sec. 2.3 and shown in Eq. 2.24, the matched filter output is given by the convolution of the received signal and the matched filter. Therefore, the matched filter output of the matched upchirp case $S_{11}(t)$ is given by

$$\begin{aligned}
S_{11}(t) \;&=\; \int_{-\infty}^{+\infty} x_1(t-\tau) y_1(\tau)\,\mathrm{d}\tau \;= \\
&= \int_{-\infty}^{+\infty} \text{rect}\left(\frac{(t-\tau)}{T}\right) e^{j2\pi(f_0(t-\tau)+\frac{k}{2}(t-\tau)^2)}\,\text{rect}\left(\frac{\tau}{T}\right) e^{j2\pi(f_0\tau-\frac{k}{2}\tau^2)}\,\mathrm{d}\tau \;= \\
&= \text{rect}\left(\frac{t}{2T}\right) e^{j2\pi(f_0 t+\frac{k}{2}t^2)} \int_{-\frac{T}{2}}^{+\frac{T}{2}} e^{-j2\pi k t\tau}\,\mathrm{d}\tau \;= \\
&= \text{rect}\left(\frac{t}{2T}\right) e^{j2\pi(f_0 t+\frac{k}{2}t^2)} \left[\frac{e^{-j2\pi k t\tau}}{-j2\pi k t}\right]_{-\frac{T}{2}}^{+\frac{T}{2}} \;= \\
&= \text{rect}\left(\frac{t}{2T}\right) e^{j2\pi(f_0 t+\frac{k}{2}t^2)}\,\frac{sin(\pi k t T)}{\pi k t} \;= \\
&= \text{rect}\left(\frac{t}{2T}\right) e^{j2\pi(f_0 t+\frac{k}{2}t^2)}\,T\,sinc(\pi k t T)
\end{aligned} \tag{2.31}$$

where $sinc(x) \;=\; \frac{sin(x)}{x}$. Similarly $S_{21}(t)$, the receiver filter output when a downchirp $x_2(t)$ is processed by the upchirp matched filter $y_1(t)$, can be computed as

$$
\begin{aligned}
S_{21}(t) \;&=\; \int_{-\infty}^{+\infty} x_2(t\,-\,\tau) y_1(\tau)\,\mathrm{d}\tau \;=\; \\
&=\; \int_{-\infty}^{+\infty} \mathrm{rect}\left(\frac{(t\,-\,\tau)}{T}\right) e^{j2\pi(f_0(t-\tau)-\frac{k}{2}(t-\tau)^2)}\,\mathrm{rect}\left(\frac{\tau}{T}\right) e^{j2\pi(f_0\tau-\frac{k}{2}\tau^2)}\,\mathrm{d}\tau \;=\; \\
&\qquad =\; \mathrm{rect}\left(\frac{t}{2T}\right) e^{j2\pi(f_0 t-\frac{k}{2}t^2)} \int_{-\frac{T}{2}}^{+\frac{T}{2}} e^{j2\pi(kt\tau-k\tau^2)}\,\mathrm{d}\tau \;=\; \\
&\qquad =\; \mathrm{rect}\left(\frac{t}{2T}\right) e^{j2\pi(f_0 t-\frac{k}{2}t^2)} \left[\frac{1}{\sqrt{k}}\left(\frac{1}{4}-\frac{j}{4}\right) e^{j\frac{k}{2}\pi t^2} \;\times\right. \\
&\times\; \left.\left(\mathrm{Erf}\left[\sqrt{k\pi}\left(\frac{1}{2}+\frac{j}{2}\right)(T-t)\right] \;+\; \mathrm{Erf}\left[\sqrt{k\pi}\left(\frac{1}{2}+\frac{j}{2}\right)(T+t)\right]\right)\right]
\end{aligned}
\tag{2.32}
$$

where $\mathrm{Erf}[\,\cdot\,]$ is the complex error function, of which there are multiple solution methods [23].

Using assumed values of $T = 20\,\mu\mathrm{s}$ and $B = 80\,\mathrm{MHz}$ for the purpose of arriving at example answers to compare, and assuming analysis of a complex baseband signal (therefore $f_0 = 0$), using Eq. 2.31 yields $|S_{11}(0)| = 2.0 \times 10^{-5}\,\mathrm{V}$ and using Eq. 2.32 yields $|S_{21}(0)| = 3.5 \times 10^{-7}\,\mathrm{V}$. Due to $S_{11}(0)$ being the peak value, it is chosen as the normalizing factor for the matched filter outputs to give the normalized correlation functions $S_{11,N}(t)$ and $S_{21,N}(t)$ (similar to pg. 36 in [10]), shown as

$$
S_{11,N}(t) \;=\; \frac{S_{11}(t)}{S_{11}(0)} \tag{2.33}
$$

and

$$
S_{21,N}(t) \;=\; \frac{S_{21}(t)}{S_{11}(0)} \tag{2.34}
$$

Using the normalized correlation function, it is seen that $|S_{11,N}(0)| = 1$, and $|S_{21,N}(0)| = 0.018$. Therefore, because the cross-correlation at zero delay of an upchirp and a downchirp is not zero, an upchirp and a downchirp do not form an orthogonal signal set in the mathematical sense.

The decorrelation of the two signals at the autocorrelation peak is desired in dB. Due to the signal, and ultimately matched filter output, being in units of Volts (and $P = \frac{V^2}{Impedance}$) [17], the ratio of instantaneous power of the two matched filter outputs can be computed as $P_{21,11,ratio}(t) = 20\,Log_{10}\left(\frac{|S_{21,N}(t)|}{|S_{11,N}(t)|}\right)$. Therefore, the matched filter output decorrelation of the given upchirp and downchirp at the autocorrelation peak (delay zero) is $P_{21,11,ratio}(0) = 20\,Log_{10}\left(\frac{|S_{21,N}(0)|}{|S_{11,N}(0)|}\right) = 20\,Log_{10}\left(\frac{0.018}{1}\right) = -35.1\text{dB}$.

The total energy of the resulting signals upon matched filtering can be computed by taking the integral with respect to time of the squared magnitude of the matched filter output divided by the system impedance, which is equivalent to examining the autocorrelation of each filtered signal at zero delay and then dividing by the system impedance. Using the given parameters and scaling (including assuming an impedance of $50\,\Omega$), E_{11} and E_{21}, the total energy of the upchirp using the upchirp matched filter output and the total energy of the downchirp using the upchirp matched filter output, respectively, were calculated as

$$E_{11} = \frac{1}{50}\int_{-\infty}^{+\infty} |S_{11}(t)|^2\,\mathrm{d}t = 1.0 \times 10^{-19}\ \text{Joules} \tag{2.35}$$

and

$$E_{21} \;=\; \frac{1}{50}\int_{-\infty}^{+\infty} |S_{21}(t)|^2\,\mathrm{d}t \;=\; 1.0\times 10^{-19}\ \text{Joules} \tag{2.36}$$

Notice that the total receiver filtered output energy is the same for both cases, giving a relative total energy of the mismatched case to the total energy of the matched case of 0 dB. These results (matched filter, decorrelation ratio, and total energy of matched filter results) were calculated and verified in the continuous domain using Mathematica, as well as in the discretized domain (using small time element spacing) in Matlab. All approaches resulted in agreeing output values. The normalized receiver filtered outputs are shown in Figure 2.3, and magnified view of the correlation peak of the same outputs is shown in Figure 2.4.

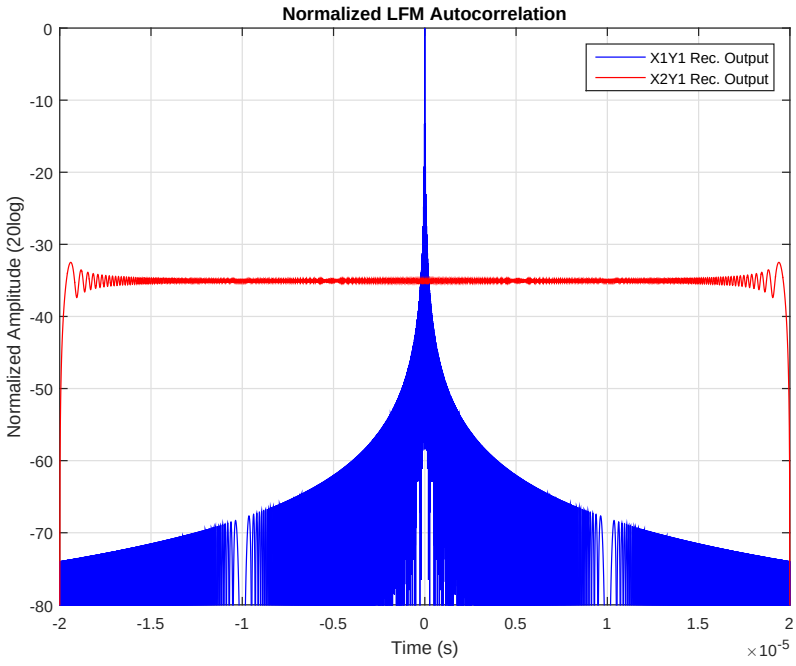


Figure 2.3: *Receiver Filter Response of Upchirp and Downchirp with an Upchirp Matched Filter vs Time*

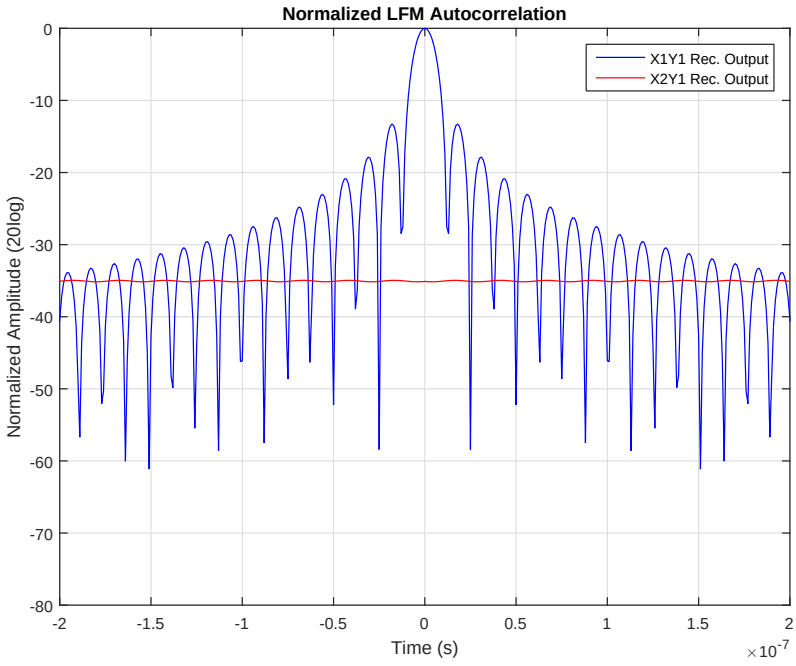


Figure 2.4: *Magnified Receiver Filter Response of Upchirp and Downchirp with an Upchirp Matched Filter vs Time*

2.5 Example of Orthogonal Waveform Separability in a Dual-Polarized Radar System

Given the matrix-based mathematical formulation for a received generic dual-polarized signal in sec. 2.2 and the definition of a pseudo-orthogonal waveform set in sec. 2.4, it is useful to examine the scientific impact of using orthogonal waveforms in a dual-polarized radar system. For the given example case the antenna cross-polarization isolation is set at 20 dB and the waveform set has a set orthogonality of 40 dB. Two cases are analyzed for system improvements through the use of pseudo-orthogonal waveforms, the first where the antenna co-pol gain mismatch is set to 0 dB and the second where the antenna co-pol gain mismatch is set to 0.5 dB.

Using Eq. 2.15 and Eq. 2.16 from sec. 2.2, the polarimetric received complex baseband signals for H and V channels (assuming no residual returns from previous transmit-receive cycles) are shown as

$$
\begin{aligned}
\mathbf{R}_{\mathrm{CBB}}(t) \;=\; & \begin{bmatrix} R_{\mathrm{CBB,H}}(t)\;\hat{\mathrm{H}} \\ R_{\mathrm{CBB,V}}(t)\;\hat{\mathrm{V}} \end{bmatrix} = \\
& = \begin{bmatrix} [\Gamma_{\mathrm{HH}}\, a_1(t') \;+\; \beta\,\Gamma_{\mathrm{HV}}\, a_2(t')] \;+ \\ [\beta\,\Gamma_{\mathrm{VH}}\, a_1(t') \;+\; \beta^2\,\Gamma_{\mathrm{VV}}\, a_2(t')] \;+ \end{bmatrix} \\
& + \alpha\,[\beta\,\Gamma_{\mathrm{HH}}\, a_2(t') \;+\; \Gamma_{\mathrm{HV}}\, a_1(t') \;+\; \Gamma_{\mathrm{VH}}\, a_1(t') \;+\; \beta\,\Gamma_{\mathrm{VV}}\, a_2(t')] \;+ \\
& + \alpha\,[\beta\,\Gamma_{\mathrm{HH}}\, a_1(t') \;+\; \beta^2\,\Gamma_{\mathrm{HV}}\, a_2(t') \;+\; \beta^2\,\Gamma_{\mathrm{VH}}\, a_2(t') \;+\; \beta\,\Gamma_{\mathrm{VV}}\, a_1(t')] \;+ \\
& \begin{bmatrix} + \alpha^2\,[\beta\,\Gamma_{\mathrm{VH}}\, a_2(t') \;+\; \Gamma_{\mathrm{VV}}\, a_1(t')]\;\hat{\mathrm{H}} \\ + \alpha^2\,[\beta^2\,\Gamma_{\mathrm{HH}}\, a_2(t') \;+\; \beta\,\Gamma_{\mathrm{HV}}\, a_1(t')]\;\hat{\mathrm{V}} \end{bmatrix} e^{-j4\pi f_0 \frac{R}{c}} \;= \\
= & \begin{bmatrix} \Gamma_{\mathrm{HH}}\,[a_1(t') \;+\; \alpha\,\beta\, a_2(t')] \;+\; \Gamma_{\mathrm{HV}}\,[\alpha\, a_1(t') \;+\; \beta\, a_2(t')] \;+ \\ \Gamma_{\mathrm{HH}}\,[\alpha\,\beta\, a_1(t') \;+\; \alpha^2\,\beta^2\, a_2(t')] \;+\; \Gamma_{\mathrm{HV}}\,[\alpha^2\,\beta\, a_1(t') \;+\; \alpha\,\beta^2\, a_2(t')] \;+ \\ + \Gamma_{\mathrm{VH}}\,[\alpha\, a_1(t') \;+\; \alpha^2\,\beta\, a_2(t')] \;+\; \Gamma_{\mathrm{VV}}\,[\alpha^2\, a_1(t') \;+\; \alpha\,\beta\, a_2(t')]\;\hat{\mathrm{H}} \\ + \Gamma_{\mathrm{VH}}\,[\beta\, a_1(t') \;+\; \alpha\,\beta^2\, a_2(t')] \;+\; \Gamma_{\mathrm{VV}}\,[\alpha\,\beta\, a_1(t') \;+\; \beta^2\, a_2(t')]\;\hat{\mathrm{V}} \end{bmatrix} e^{-j4\pi f_0 \frac{R}{c}}
\end{aligned}
\tag{2.37}
$$

A cross-pol isolation given in units of dB denotes the signal power transmitted on the intended polarization versus the signal power transmitted on the polarization orthogonal to the intended polarization. Therefore, a given cross-pol isolation of x dB corresponds with $\alpha = 10^{-x/20}$, and the given cross-pol isolation of 20 dB corresponds with $\alpha = 10^{-20/20} = \frac{1}{10}$. A waveform set with orthogonality of y dB denotes a waveform set where the highest point in cross-correlation output of any of the waveforms is $10^{-y/20}$ times smaller

than the peak autocorrelation output of any of the signals. Therefore, given a waveform set with orthogonality of 40 dB, the maximum receiver filtered outputs resulting from unmatched filters will be $10^{-40/20} = \frac{1}{100}$ times lower than the maximum receiver matched filter outputs. Relating the given values to Question #1 (sec. 2.2), specifically Eq 2.19, and assuming a co-pol gain mismatch of 0 dB (giving $\beta = 1$), $\mathbf{\Gamma}_{Meas}$ can be found for the alternating transmit case $\mathbf{\Gamma}_{Meas,Alt}$, the simultaneous transmit case $\mathbf{\Gamma}_{Meas,Sim}$ where the same waveform is transmitted on both polarizations, and the simultaneous transmit case $\mathbf{\Gamma}_{Meas,Orth}$ where nearly orthogonal waveforms are transmitted on each polarization. Due to the property of the convolution operator that $f \otimes (g \otimes h) = (f \otimes g) \otimes h$ and $a(f \otimes g) = (af) \otimes g$ for any $a \in \mathbb{C}$, the given values for α, β, and the maximum values for the cross-correlation and autocorrelation (both normalized, with autocorrelation peak equal to 1 and the cross-correlation peak value set equal to maximum ratio value dictated by the level of pseudo-orthogonality, giving the worst-case answer) can be directly substituted into the expanded form of Eq. 2.19 to find the appropriate $\mathbf{\Gamma}_{Meas}$ values. The equations for $\mathbf{\Gamma}_{Meas,Alt}$, $\mathbf{\Gamma}_{Meas,Sim}$, and $\mathbf{\Gamma}_{Meas,Orth}$ are shown below

as

$$\mathbf{\Gamma}_{Meas,Alt} = \begin{bmatrix} \Gamma_{\mathrm{HH},Meas,Alt} \\ \Gamma_{\mathrm{HV},Meas,Alt} \\ \Gamma_{\mathrm{VH},Meas,Alt} \\ \Gamma_{\mathrm{VV},Meas,Alt} \end{bmatrix} = \begin{bmatrix} \max\left(R_{\mathrm{CBB,H,Alt}}(t_1) \otimes h_1(t_1)\right) \\ \max\left(R_{\mathrm{CBB,H,Alt}}(t_2) \otimes h_2(t_2)\right) \\ \max\left(R_{\mathrm{CBB,V,Alt}}(t_1) \otimes h_1(t_1)\right) \\ \max\left(R_{\mathrm{CBB,V,Alt}}(t_2) \otimes h_2(t_2)\right) \end{bmatrix} =$$

$$= \begin{bmatrix} \Gamma_{\mathrm{HH}} + 0.1 \cdot \Gamma_{\mathrm{HV}} + 0.1 \cdot \Gamma_{\mathrm{VH}} + 0.01 \cdot \Gamma_{\mathrm{VV}} \\ 0.1 \cdot \Gamma_{\mathrm{HH}} + \Gamma_{\mathrm{HV}} + + 0.01 \cdot \Gamma_{\mathrm{VH}} + 0.1 \cdot \Gamma_{\mathrm{VV}} \\ 0.1 \cdot \Gamma_{\mathrm{HH}} + 0.01 \cdot \Gamma_{\mathrm{HV}} + \Gamma_{\mathrm{VH}} + 0.1 \cdot \Gamma_{\mathrm{VV}} \\ 0.01 \cdot \Gamma_{\mathrm{HH}} + 0.1 \cdot \Gamma_{\mathrm{HV}} + 0.1 \cdot \Gamma_{\mathrm{VH}} + \Gamma_{\mathrm{VV}} \end{bmatrix} \quad (2.38)$$

and

$$\mathbf{\Gamma}_{Meas,Sim} = \begin{bmatrix} \Gamma_{\mathrm{HH},Meas,Sim} \\ \Gamma_{\mathrm{HV},Meas,Sim} \\ \Gamma_{\mathrm{VH},Meas,Sim} \\ \Gamma_{\mathrm{VV},Meas,Sim} \end{bmatrix} = \begin{bmatrix} \max\left(R_{\mathrm{CBB,H,Sim}}(t_1) \otimes h_1(t_1)\right) \\ \max\left(R_{\mathrm{CBB,H,Sim}}(t_1) \otimes h_1(t_1)\right) \\ \max\left(R_{\mathrm{CBB,V,Sim}}(t_1) \otimes h_1(t_1)\right) \\ \max\left(R_{\mathrm{CBB,V,Sim}}(t_1) \otimes h_1(t_1)\right) \end{bmatrix} =$$

$$= \begin{bmatrix} \Gamma_{\mathrm{HH}}[1 + 0.1] + \Gamma_{\mathrm{HV}}[0.1 + 1] + \Gamma_{\mathrm{VH}}[0.1 + 0.01] + \Gamma_{\mathrm{VV}}[0.01 + 0.1] \\ \Gamma_{\mathrm{HH}}[1 + 0.1] + \Gamma_{\mathrm{HV}}[0.1 + 1] + \Gamma_{\mathrm{VH}}[0.1 + 0.01] + \Gamma_{\mathrm{VV}}[0.01 + 0.1] \\ \Gamma_{\mathrm{HH}}[0.1 + 0.01] + \Gamma_{\mathrm{HV}}[0.01 + 0.1] + \Gamma_{\mathrm{VH}}[1 + 0.1] + \Gamma_{\mathrm{VV}}[0.1 + 1] \\ \Gamma_{\mathrm{HH}}[0.1 + 0.01] + \Gamma_{\mathrm{HV}}[0.01 + 0.1] + \Gamma_{\mathrm{VH}}[1 + 0.1] + \Gamma_{\mathrm{VV}}[0.1 + 1] \end{bmatrix} =$$

$$= \begin{bmatrix} 1.1 \cdot \Gamma_{\mathrm{HH}} + 1.1 \cdot \Gamma_{\mathrm{HV}} + 0.11 \cdot \Gamma_{\mathrm{VH}} + 0.11 \cdot \Gamma_{\mathrm{VV}} \\ 1.1 \cdot \Gamma_{\mathrm{HH}} + 1.1 \cdot \Gamma_{\mathrm{HV}} + 0.11 \cdot \Gamma_{\mathrm{VH}} + 0.11 \cdot \Gamma_{\mathrm{VV}} \\ 0.11 \cdot \Gamma_{\mathrm{HH}} + 0.11 \cdot \Gamma_{\mathrm{HV}} + 1.1 \cdot \Gamma_{\mathrm{VH}} + 1.1 \cdot \Gamma_{\mathrm{VV}} \\ 0.11 \cdot \Gamma_{\mathrm{HH}} + 0.11 \cdot \Gamma_{\mathrm{HV}} + 1.1 \cdot \Gamma_{\mathrm{VH}} + 1.1 \cdot \Gamma_{\mathrm{VV}} \end{bmatrix} \quad (2.39)$$

and

$$\mathbf{\Gamma}_{Meas,Orth} = \begin{bmatrix} \Gamma_{\mathrm{HH},Meas,Orth} \\ \Gamma_{\mathrm{HV},Meas,Orth} \\ \Gamma_{\mathrm{VH},Meas,Orth} \\ \Gamma_{\mathrm{VV},Meas,Orth} \end{bmatrix} = \begin{bmatrix} \max\left(R_{\mathrm{CBB,H,Orth}}(t_1) \otimes h_1(t_1)\right) \\ \max\left(R_{\mathrm{CBB,H,Orth}}(t_1) \otimes h_2(t_1)\right) \\ \max\left(R_{\mathrm{CBB,V,Orth}}(t_1) \otimes h_1(t_1)\right) \\ \max\left(R_{\mathrm{CBB,V,Orth}}(t_1) \otimes h_2(t_1)\right) \end{bmatrix} =$$

$$= \begin{bmatrix} \Gamma_{\mathrm{HH}}[1 + 0.001] + \Gamma_{\mathrm{HV}}[0.1 + 0.01] + \Gamma_{\mathrm{VH}}[0.1 + 0.0001] + \Gamma_{\mathrm{VV}}[0.01 + 0.001] \\ \Gamma_{\mathrm{HH}}[0.01 + 0.1] + \Gamma_{\mathrm{HV}}[0.001 + 1] + \Gamma_{\mathrm{VH}}[0.001 + 0.01] + \Gamma_{\mathrm{VV}}[0.0001 + 0.1] \\ \Gamma_{\mathrm{HH}}[0.1 + 0.0001] + \Gamma_{\mathrm{HV}}[0.01 + 0.001] + \Gamma_{\mathrm{VH}}[1 + 0.001] + \Gamma_{\mathrm{VV}}[0.1 + 0.01] \\ \Gamma_{\mathrm{HH}}[0.001 + 0.01] + \Gamma_{\mathrm{HV}}[0.0001 + 0.1] + \Gamma_{\mathrm{VH}}[0.01 + 0.1] + \Gamma_{\mathrm{VV}}[0.001 + 1] \end{bmatrix} =$$

$$= \begin{bmatrix} 1.001 \cdot \Gamma_{\mathrm{HH}} + 0.11 \cdot \Gamma_{\mathrm{HV}} + 0.1001 \cdot \Gamma_{\mathrm{VH}} + 0.011 \cdot \Gamma_{\mathrm{VV}} \\ 0.11 \cdot \Gamma_{\mathrm{HH}} + 1.001 \cdot \Gamma_{\mathrm{HV}} + 0.011 \cdot \Gamma_{\mathrm{VH}} + 0.1001 \cdot \Gamma_{\mathrm{VV}} \\ 0.1001 \cdot \Gamma_{\mathrm{HH}} + 0.011 \cdot \Gamma_{\mathrm{HV}} + 1.001 \cdot \Gamma_{\mathrm{VH}} + 0.11 \cdot \Gamma_{\mathrm{VV}} \\ 0.011 \cdot \Gamma_{\mathrm{HH}} + 0.1001 \cdot \Gamma_{\mathrm{HV}} + 0.11 \cdot \Gamma_{\mathrm{VH}} + 1.001 \cdot \Gamma_{\mathrm{VV}} \end{bmatrix} \quad (2.40)$$

where the subscript $(\cdot)_{Alt}$ denotes the alternating transmit case, the subscript $(\cdot)_{Sim}$ denotes the simultaneous transmit case using identical waveforms, and the subscript $(\cdot)_{Orth}$ denotes the simultaneous transmit case using pseudo-orthogonal waveforms for the applicable variable, and t_1 and t_2 are separated by some non-zero multiple of the PRT. It is easily seen in Eq. 2.39 that the $\mathbf{\Gamma}_{Meas}$ values modifying the signals for a given receive polarization (the pair Γ_{HH} and Γ_{HV}, and the pair Γ_{VH} and Γ_{VV}) are inseparable when the same waveform is used on both transmit polarizations simultaneously. The introduction of waveforms with orthogonality of 40 dB is shown in Eq. 2.40 to improve the acquisition of science measurements $\mathbf{\Gamma}_{Meas}$ by lowering the relative amplitude of the effect of all other Γ parameters for a given channel/matched

filter combination. Using waveforms with orthogonality of 40 dB in a system with cross-pol isolation of 20 dB, the cross-pol contamination is the main contaminating effect present in $\mathbf{\Gamma}_{Meas}$. Comparing the results of the alternating transmit case in Eq. 2.38 with the simultaneous orthogonal transmit case in Eq. 2.40, it is seen that the alternating transmit case results in a slightly larger amplitude difference between the parameter of interest and all other parameters ($\frac{1}{0.1+0.1+0.01} = 4.7619$ versus $\frac{1.001}{0.11+0.1001+0.011} = 4.5274$). However, as mentioned in Sec. 2.2, it is desired from a scientific standpoint to assemble all four elements of $\mathbf{\Gamma}_{Meas}$ from measurements at the same instance in time, which by nature the alternating transmit case cannot accomplish, leaving simultaneous transmission of orthogonal waveforms as the most desirable method of operation for acquiring scientifically useful measurements.

A co-pol gain mismatch given in units of dB denotes the signal power transmitted by an antenna on one polarization versus the signal power transmitted by the other antenna on the orthogonal polarization. Using the horizontal channel to horizontally polarized transmitted signal conversion as a reference, and assuming that the gain on the H channel is larger than the V channel, a given co-pol mismatch of z dB corresponds with $\beta = 10^{-z/20}$, and the given co-pol mismatch of 0.5 dB corresponds with $\beta = 10^{-0.5/20} = 0.9441$. Using the same method as before, the equations for $\mathbf{\Gamma}_{Meas,Alt}$, $\mathbf{\Gamma}_{Meas,Sim}$, and $\mathbf{\Gamma}_{Meas,Orth}$ can be recalculated accounting for co-pol gain mismatch, shown below as

$$\mathbf{\Gamma}_{Meas,Alt} = \begin{bmatrix} \Gamma_{\mathrm{HH},Meas,Alt} \\ \Gamma_{\mathrm{HV},Meas,Alt} \\ \Gamma_{\mathrm{VH},Meas,Alt} \\ \Gamma_{\mathrm{VV},Meas,Alt} \end{bmatrix} = \begin{bmatrix} \max\left(R_{\mathrm{CBB,H,Alt}}(t_1) \otimes h_1(t_1)\right) \\ \max\left(R_{\mathrm{CBB,H,Alt}}(t_2) \otimes h_2(t_2)\right) \\ \max\left(R_{\mathrm{CBB,V,Alt}}(t_1) \otimes h_1(t_1)\right) \\ \max\left(R_{\mathrm{CBB,V,Alt}}(t_2) \otimes h_2(t_2)\right) \end{bmatrix} =$$

$$= \begin{bmatrix} 1 \cdot \Gamma_{\mathrm{HH}} + 0.1 \cdot \Gamma_{\mathrm{HV}} + 0.1 \cdot \Gamma_{\mathrm{VH}} + 0.01 \cdot \Gamma_{\mathrm{VV}} \\ 0.09441 \cdot \Gamma_{\mathrm{HH}} + 0.9441 \cdot \Gamma_{\mathrm{HV}} + 0.009441 \cdot \Gamma_{\mathrm{VH}} + 0.09441 \cdot \Gamma_{\mathrm{VV}} \\ 0.09441 \cdot \Gamma_{\mathrm{HH}} + 0.009441 \cdot \Gamma_{\mathrm{HV}} + 0.9441 \cdot \Gamma_{\mathrm{VH}} + 0.09441 \cdot \Gamma_{\mathrm{VV}} \\ 0.008913 \cdot \Gamma_{\mathrm{HH}} + 0.08913 \cdot \Gamma_{\mathrm{HV}} + 0.08913 \cdot \Gamma_{\mathrm{VH}} + 0.8913 \cdot \Gamma_{\mathrm{VV}} \end{bmatrix} \tag{2.41}$$

and

$$
\begin{aligned}
\mathbf{\Gamma}_{Meas,Sim} &= \begin{bmatrix} \Gamma_{\mathrm{HH},Meas,Sim} \\ \Gamma_{\mathrm{HV},Meas,Sim} \\ \Gamma_{\mathrm{VH},Meas,Sim} \\ \Gamma_{\mathrm{VV},Meas,Sim} \end{bmatrix} = \begin{bmatrix} \max\left(R_{\mathrm{CBB,H,Sim}}(t_1) \otimes h_1(t_1)\right) \\ \max\left(R_{\mathrm{CBB,H,Sim}}(t_1) \otimes h_1(t_1)\right) \\ \max\left(R_{\mathrm{CBB,V,Sim}}(t_1) \otimes h_1(t_1)\right) \\ \max\left(R_{\mathrm{CBB,V,Sim}}(t_1) \otimes h_1(t_1)\right) \end{bmatrix} = \\
&= \begin{bmatrix} \Gamma_{\mathrm{HH}}[1 + 0.09441] + \Gamma_{\mathrm{HV}}[0.1 + 0.9441] + \\ \Gamma_{\mathrm{HH}}[1 + 0.09441] + \Gamma_{\mathrm{HV}}[0.1 + 0.9441] + \\ \Gamma_{\mathrm{HH}}[0.09441 + 0.008913] + \Gamma_{\mathrm{HV}}[0.009441 + 0.08913] + \\ \Gamma_{\mathrm{HH}}[0.09441 + 0.008913] + \Gamma_{\mathrm{HV}}[0.009441 + 0.08913] + \end{bmatrix} \\
&\quad \begin{bmatrix} + \Gamma_{\mathrm{VH}}[0.1 + 0.009441] + \Gamma_{\mathrm{VV}}[0.01 + 0.09441] \\ + \Gamma_{\mathrm{VH}}[0.1 + 0.009441] + \Gamma_{\mathrm{VV}}[0.01 + 0.09441] \\ + \Gamma_{\mathrm{VH}}[0.9441 + 0.08913] + \Gamma_{\mathrm{VV}}[0.09441 + 0.8913] \\ + \Gamma_{\mathrm{VH}}[0.9441 + 0.08913] + \Gamma_{\mathrm{VV}}[0.09441 + 0.8913] \end{bmatrix} = \\
&= \begin{bmatrix} 1.09441 \cdot \Gamma_{\mathrm{HH}} + 1.0441 \cdot \Gamma_{\mathrm{HV}} + 0.109441 \cdot \Gamma_{\mathrm{VH}} + 0.10441 \cdot \Gamma_{\mathrm{VV}} \\ 1.09441 \cdot \Gamma_{\mathrm{HH}} + 1.0441 \cdot \Gamma_{\mathrm{HV}} + 0.109441 \cdot \Gamma_{\mathrm{VH}} + 0.10441 \cdot \Gamma_{\mathrm{VV}} \\ 0.103323 \cdot \Gamma_{\mathrm{HH}} + 0.098571 \cdot \Gamma_{\mathrm{HV}} + 1.03323 \cdot \Gamma_{\mathrm{VH}} + 0.98571 \cdot \Gamma_{\mathrm{VV}} \\ 0.103323 \cdot \Gamma_{\mathrm{HH}} + 0.098571 \cdot \Gamma_{\mathrm{HV}} + 1.03323 \cdot \Gamma_{\mathrm{VH}} + 0.98571 \cdot \Gamma_{\mathrm{VV}} \end{bmatrix}
\end{aligned} \tag{2.42}
$$

and

$$
\begin{aligned}
\mathbf{\Gamma}_{Meas,Orth} &= \begin{bmatrix} \Gamma_{\mathrm{HH},Meas,Orth} \\ \Gamma_{\mathrm{HV},Meas,Orth} \\ \Gamma_{\mathrm{VH},Meas,Orth} \\ \Gamma_{\mathrm{VV},Meas,Orth} \end{bmatrix} = \begin{bmatrix} \max\left(R_{\mathrm{CBB,H,Orth}}(t_1) \otimes h_1(t_1)\right) \\ \max\left(R_{\mathrm{CBB,H,Orth}}(t_1) \otimes h_2(t_1)\right) \\ \max\left(R_{\mathrm{CBB,V,Orth}}(t_1) \otimes h_1(t_1)\right) \\ \max\left(R_{\mathrm{CBB,V,Orth}}(t_1) \otimes h_2(t_1)\right) \end{bmatrix} = \\
&= \begin{bmatrix} \Gamma_{\mathrm{HH}}[1 + 0.0009441] + \Gamma_{\mathrm{HV}}[0.1 + 0.009441] + \\ \Gamma_{\mathrm{HH}}[0.01 + 0.09441] + \Gamma_{\mathrm{HV}}[0.001 + 0.9441] + \\ \Gamma_{\mathrm{HH}}[0.09441 + 0.00008913] + \Gamma_{\mathrm{HV}}[0.009441 + 0.0008913] + \\ \Gamma_{\mathrm{HH}}[0.0009441 + 0.008913] + \Gamma_{\mathrm{HV}}[0.00009441 + 0.08913] + \\ + \Gamma_{\mathrm{VH}}[0.1 + 0.00009441] + \Gamma_{\mathrm{VV}}[0.01 + 0.0009441] \\ + \Gamma_{\mathrm{VH}}[0.001 + 0.009441] + \Gamma_{\mathrm{VV}}[0.0001 + 0.09441] \\ + \Gamma_{\mathrm{VH}}[0.9441 + 0.0008913] + \Gamma_{\mathrm{VV}}[0.09441 + 0.008913] \\ + \Gamma_{\mathrm{VH}}[0.009441 + 0.08913] + \Gamma_{\mathrm{VV}}[0.0009441 + 0.8913] \end{bmatrix} = \\
&= \begin{bmatrix} 1.0009441 \cdot \Gamma_{\mathrm{HH}} + 0.109441 \cdot \Gamma_{\mathrm{HV}} + 0.10009441 \cdot \Gamma_{\mathrm{VH}} + 0.0109441 \cdot \Gamma_{\mathrm{VV}} \\ 0.10441 \cdot \Gamma_{\mathrm{HH}} + 0.9451 \cdot \Gamma_{\mathrm{HV}} + 0.010441 \cdot \Gamma_{\mathrm{VH}} + 0.09451 \cdot \Gamma_{\mathrm{VV}} \\ 0.09449913 \cdot \Gamma_{\mathrm{HH}} + 0.0103323 \cdot \Gamma_{\mathrm{HV}} + 0.9449913 \cdot \Gamma_{\mathrm{VH}} + 0.103323 \cdot \Gamma_{\mathrm{VV}} \\ 0.0098571 \cdot \Gamma_{\mathrm{HH}} + 0.08922441 \cdot \Gamma_{\mathrm{HV}} + 0.098571 \cdot \Gamma_{\mathrm{VH}} + 0.8922441 \cdot \Gamma_{\mathrm{VV}} \end{bmatrix}
\end{aligned}
\tag{2.43}
$$

Similar to the case with no co-pol gain mismatch, even though each $\mathbf{\Gamma}_{Meas}$ value modifying the signals for a given receive polarization (the pair Γ_{HH} and Γ_{HV}, and the pair Γ_{VH} and Γ_{VV}) have slightly different relative magnitudes, they are inseparable when the same waveform is used on both transmit polarizations simultaneously. Also similar to the no co-pol gain mismatch case, comparing the results of the alternating transmit case with co-pol gain mismatch in Eq. 2.41 with the simultaneous orthogonal transmit case with co-pol gain mismatch in Eq. 2.43, it is seen that the alternating transmit case results

Γ parameter	Alternating Transmit	Simultaneous Orthogonal Transmit
Γ_{HH}	$\frac{1}{0.1+0.1+0.01} = = 4.7619$	$\frac{1.0009441}{0.109441+0.10009441+0.0109441} = = 4.5399$
Γ_{HV}	$\frac{0.9441}{0.09441+0.009441+0.09441} = = 4.7619$	$\frac{0.9451}{0.10441+0.010441+0.09451} = = 4.5142$
Γ_{VH}	$\frac{0.9441}{0.09441+0.009441+0.09441} = = 4.7619$	$\frac{0.9449913}{0.09449913+0.0103323+0.103323} = = 4.5399$
Γ_{VV}	$\frac{0.8913}{0.008913+0.08913+0.08913} = = 4.7619$	$\frac{0.8922441}{0.0098571+0.0892241+0.098571} = = 4.5142$

Table 2.1: Γ Parameter Separability Through Ratio of Desired Γ Parameter to Sum of Other Γ Parameters for Example Alternating Transmit and Simultaneous Transmit Cases

in a slightly larger amplitude difference between the parameter of interest and all other parameters, as shown in Table 2.1.

Again, the alternating transmit case after matched filtering always results in a larger difference between the parameter of interest and the sum of the other parameters than the simultaneous orthogonal signal transmit case. However, the simultaneous orthogonal transmit case has a slightly improved difference for the signals transmitted on the channel with the larger gain and slightly more degraded difference for the signals transmitted on the channel with with the smaller gain. There is no real improvement (or serious degradation) to the scientific measurements with the use of orthogonal waveforms in simultaneous transmit mode on an antenna with a small co-pol mismatch versus the measurements with the use of orthogonal waveforms in simultaneous transmit mode on an antenna with no co-pol mismatch. Therefore, the same arguments presented previously for the use of orthogonal codes in simultaneous transmission versus alternating transmit for the co-pol gain matched case also apply to the co-pol gain mismatched case.

2.6 Analysis of Common Pulse Compression Waveforms and Their Utility as Pseudo-Orthogonal Waveform Sets

There exist several classes of codes that have been identified as having desirable pulse compression characteristics. Among these are Barker codes, Biphase MPS codes, and Polyphase Frank, P1, P2, P3, and P4 codes. These codes will be analyzed along with their potential utility as pseudo-orthogonal waveform sets. For this section, pseudo-orthogonality will be defined as having a maximum cross-correlation peak 40 dB lower than the autocorrelation peak. In order to compare waveform types with definite values, a global pulse length and bandwidth must be established. It is assumed for this section that all waveforms will be analyzed with a pulse length $T = 20\,\mu$s and a bandwidth of 80 MHz. Due to this exact combination of time and bandwidth not always being achievable for a given modulating waveform (code), it will be assumed that the pulse length of $20\,\mu$s is set and the bandwidth will be variable if a compromise on system parameters is to be made.

Barker sequences are coded waveforms that exhibit a peak sidelobe to mainlobe ratio of $\frac{1}{N}$, where N is the number of bits in the code. Although both biphase and polyphase variations of Barker codes exist, the term "Barker codes" commonly refers to biphase Barker codes unless otherwise specified.

Phase coded waveforms are assembled by concatenating N subpulses ("chips") of duration T_{chip}, where each chip (in a common constant modulus waveform) is a constant modulus pulse with a selected phase so that the phase

information stored in the individual chips of the final assembled waveform of duration T contains the desired N bits of information (the N length code to be transmitted). The -4 dB bandwidth B_{chip} of each chip is given by

$$B_{chip} \;=\; \frac{1}{T_{chip}} \tag{2.44}$$

and the energy in a phase-coded waveform is proportional to the total pulse duration $T \;=\; N\,T_{chip}$. Therefore, the time-bandwidth product of a phase-coded waveform TB is equal to the number of bits in the code, given by

$$TB \;=\; T\,B_{chip} \;=\; \frac{T}{T_{chip}} \;=\; N \tag{2.45}$$

Both biphase and polyphase Barker coded waveforms can be generated in a radar system through digital waveform generators [17], but there exists a clever method for the creation (as well as matched filter output assembly) of biphase codes that can be used to create biphase Barker codes. This method consists of utilizing a tapped delay line, where each tap spacing corresponds with a delay of T_{chip} and each tap imparts a phase shift of either 0 or π radians (corresponding with either $+1$ or -1 in the code, respectively). All tap outputs are then summed and processed through a filter matched to the chip duration T_{chip}. When an impulse is input into the delay line, the filtered summation of the tap outputs results in the creation of the biphase code as specified by the delay shifts of the individual taps. Similarly, the matched filter result of the received signal can be created by inputting the received signal into the delay line from the opposite end relative to the end used for initial waveform creation, effectively convolving the received signal with a time-reversed copy of the transmitted signal. Note that the matched filter result is the convolution of the received signal with the complex conjugate time-reversed copy of

the transmitted signal (see Eq. 2.24). Due to the transmitted signal being biphase, the lack of complex conjugate has no effect on the delay line generated matched filter results, but this does prevent the delay line matched filter method from being used on any polyphase code (where the complex conjugate would have an effect). An illustration of this tapped delay line method for generation and matched filtering of biphase coded waveforms is shown with a 13 bit Barker code implemented on pg. 351 of [18].

Barker codes are useful because their matched filter output has low predictable sidelobes, with a maximum sidelobe to main peak ratio of $\frac{1}{N}$, giving optimal peak sidelobe levels for a given number of bits. The downside of Barker codes is that very few of these codes have been discovered, with a maximum known code length of $N = 13$ for biphase Barker code and $N = 77$ for polyphase Barker code, corresponding with peak sidelobes of $-22.28\,\text{dB}$ and $-37.73\,\text{dB}$, respectively [24]. While Barker codes may result in the optimal peak sidelobe levels for a given length of code, the relatively short code lengths of the known Barker signals restricts their practical implementation in radar systems. Barker codes are also very Doppler intolerant, with a common design restraint on implemented biphase Barker codes that the Doppler phase rotation be limited to one-quarter cycle or less, requiring that the maximum expected Doppler shift and target velocity satisfy $F_{D,max}\,T \leq \frac{1}{4} \implies v_{max} \leq \frac{\lambda}{8T}$ as shown in [10], where $F_{D,max}$ is the maximum allowed Doppler frequency, v_{max} is the maximum allowed radial velocity, and λ is the wavelength of the carrier frequency.

There exists a combined, alternatively called "nested" or "compound," ap-

proach to generating combined Barker codes where the Kronecker product of two Barker sequences is used to create the combined code. The resulting combined Barker code has a larger time-bandwidth product than either of the Barker codes used to produce it, but the peak sidelobe to main peak ratio of the combined code is equal to the peak sidelobe to main peak ratio of the shorter of the two Barker codes used to produce the combined code. Therefore, the peak sidelobe to main peak ratio of a combined Barker code is still restricted to the relatively large ratios present in the standalone Barker codes, providing little help to radar systems when lower peak sidelobes for a given code length ($N > 13$) are desired. While both biphase and polyphase Barker codes are useful, the general consensus seems to be that the short code lengths available and Doppler intolerance limit their practical use in radar systems, and the lower sidelobes and better Doppler tolerance of polyphase codes (longer than known Barker codes) are desirable if the radar system is capable of generating them [1], [10], [11], [17], [18].

Polyphase coded waveforms can be physically generated in a radar system through digital waveform generators [17], and the final bandwidth of the transmitted signals can be calculated using Eq. 2.44. Polyphase Barker codes are found through complicated search algorithms, while Frank, P1, and P2 codes are derived from step approximations of an LFM waveform, and P3 and P4 codes are derived from LFM waveforms [11], [17], [24]–[26]. Therefore, polyphase Barker codes have a limited number of specific codes available, whereas Frank, P1, P2, P3, and P4 codes do not have an inherent maximum code length. The length of Frank, P1, and P2 codes must be a perfect square, with the requirement that P2 code length be the perfect square of an even

number for good sidelobe characteristics. The length of P3 and P4 codes are not limited to perfect squares.

While polyphase Barker codes exhibit very good peak sidelobe levels relative to the length of the code, the limited number of codes available limits the maximum sidelobe suppression possible. Polyphase Barker codes would be a practical choice for limited bandwidth applications where a set of pseudo-orthogonal waveforms is not needed. For the LFM derived polyphase codes, Frank codes have had success in low probability of intercept radars, and P4 codes have had success in modern radars including orthogonal netted radar systems and Multiple-Input-Multiple-Output (MIMO) radars [11], [27]–[29].

There are a limited number of polyphase Barker codes, with the three longest known codes being length 77, 76 and 72 [24]. The $T = 20\,\mu$s length 77, 76, and 72 polyphase Barker codes, with bandwidths of 3.85 MHz, 3.8 MHz, and 3.6 MHz respectively, have peak sidelobe levels that are suppressed by -37.73 dB, -37.62 dB, and -37.15 dB respectively as shown in Figure 2.5. Due to the desire to find a set of pseudo-orthogonal waveforms (defined as -40 dB cross-correlation), and seeing that even the longest available polyphase Barker is unable to achieve -40 dB autocorrelation sidelobe suppression, -40 dB cross-correlation suppression at all points between two polyphase Barker codes will probably not be feasible. In addition, because there is only one known code at each length, even if it were the case that two of the codes had good cross-correlation characteristics, if two versions of the same code were not being used then the transmitted pulse length would have to be different for the two codes so that the chip duration stays constant for processing (and main-

tains consistent bandwidth between the two codes), meaning that more energy would be transmitted on one code (and channel) than the other, making for a very strange system. However, for comparison's sake, the convolution of the three codes were computed for the regular convolution case, the case where one signal is time reversed, the case where one signal is complex conjugated, and the case where one signal is time reversed and complex conjugated (the traditional cross-correlation). These results, normalized by the magnitude of the longer convolved code's autocorrelation peak, are shown in Figure 2.5, Figure 2.6, Figure 2.7, and Figure 2.8, where the peak sidelobe level refers to the difference between the autocorrelation peak and the highest magnitude sidelobe for the autocorrelation case, and refers to the difference between the autocorrelation peak of the longer code and the highest magnitude point for the cross-correlation case. The combination with the best cross-correlation characteristics was the convolution of the length 77 code with itself, resulting in a maximum normalized magnitude $-15.34\,\mathrm{dB}$ lower than the autocorrelation peak. Overall, the known polyphase Barker codes have very poor cross-correlation characteristics and barring the discovery of future polyphase Barker codes they make a poor choice for the construction of a pseudo-orthogonal waveform set.

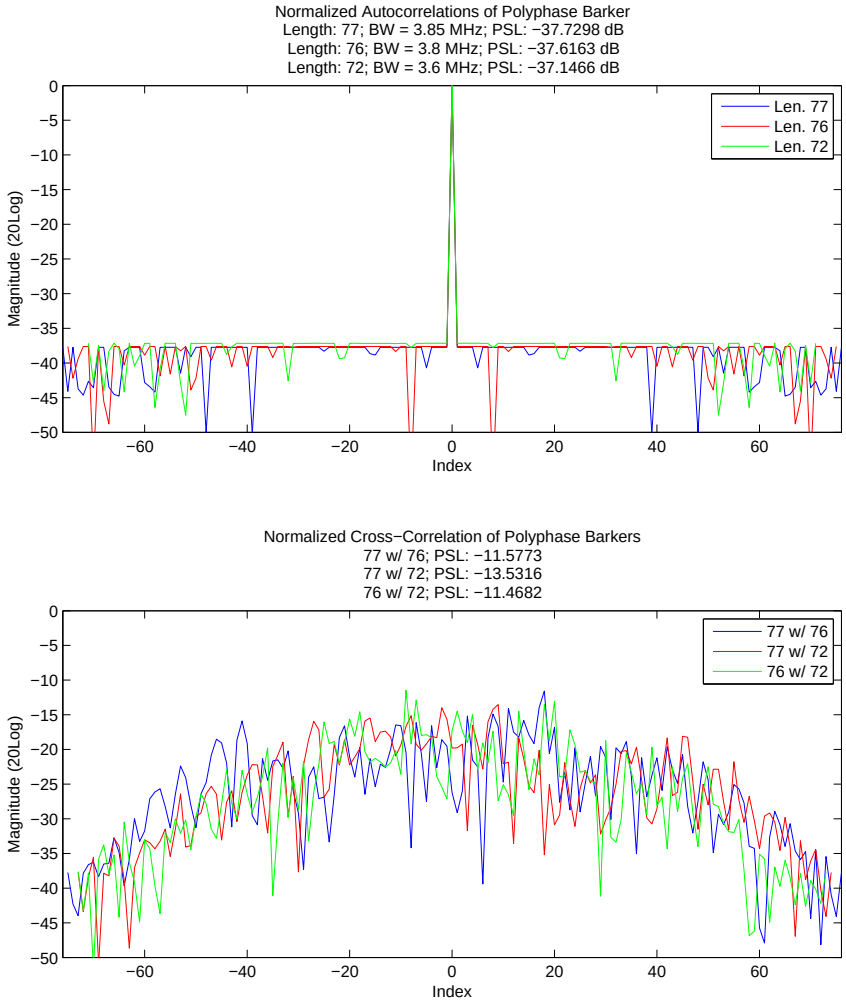


Figure 2.5: *Normalized Cross-Correlation Polyphase Barker Sequences*

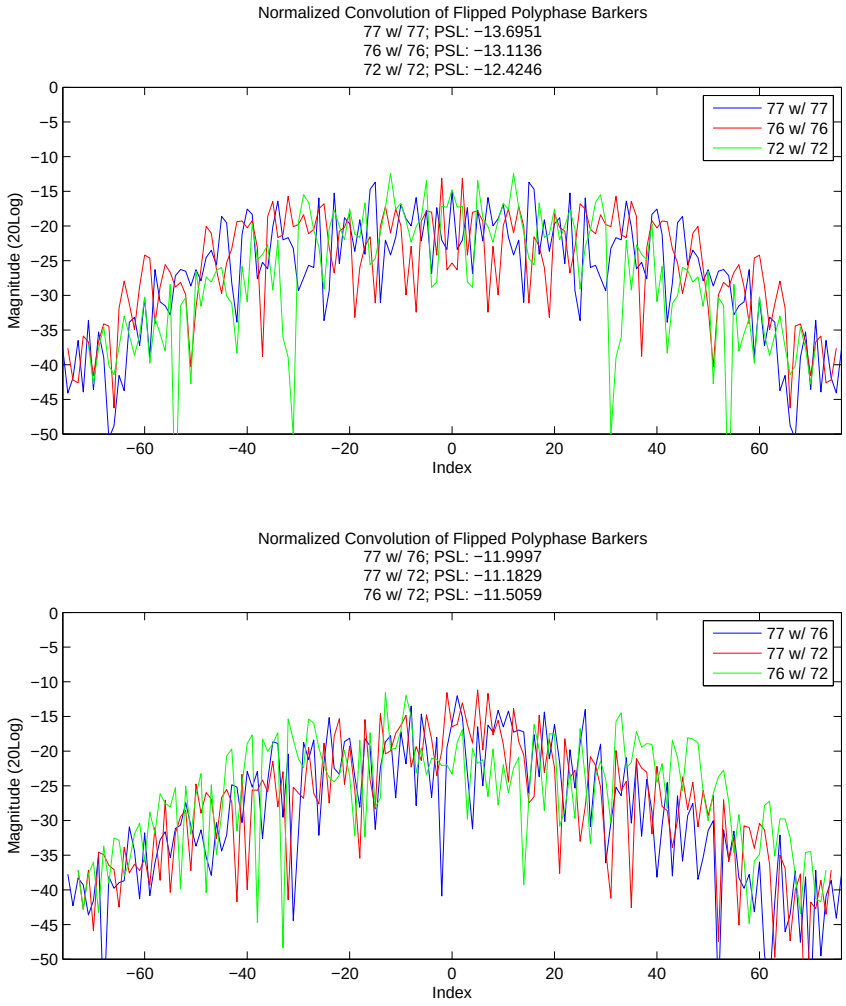


Figure 2.6: *Normalized Convolution of Time-Reversed Polyphase Barker Sequences*

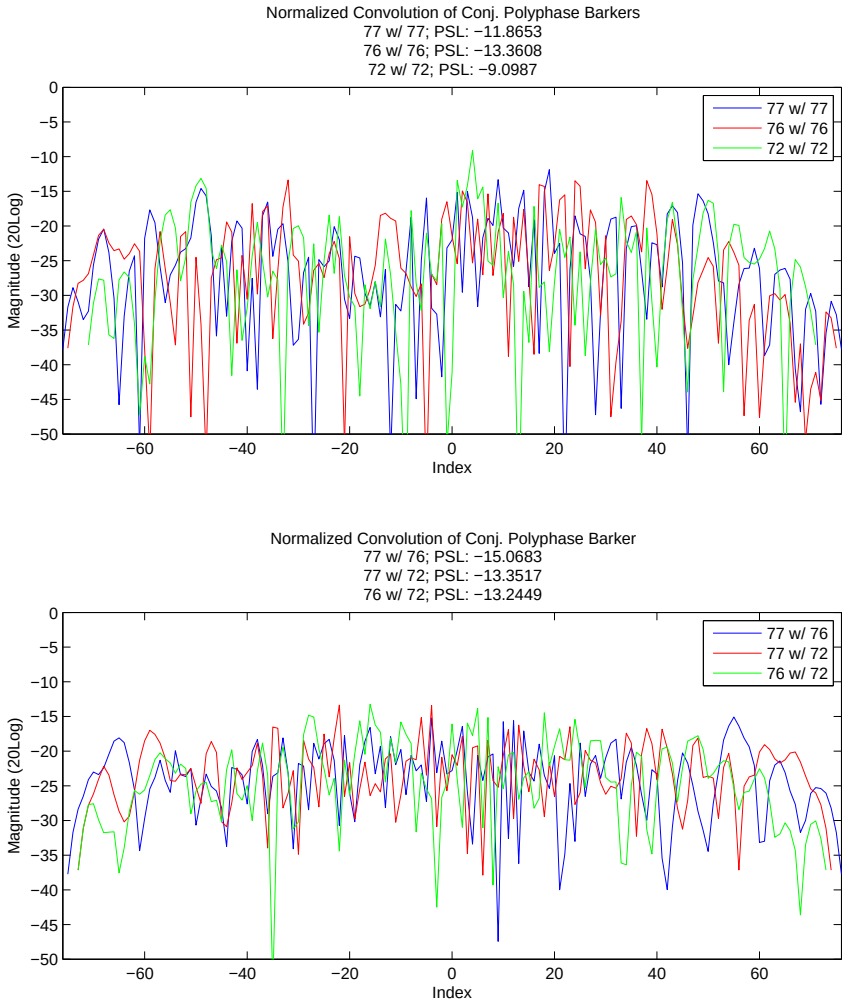


Figure 2.7: *Normalized Convolution of Complex Conjugated Polyphase Barker Sequences*

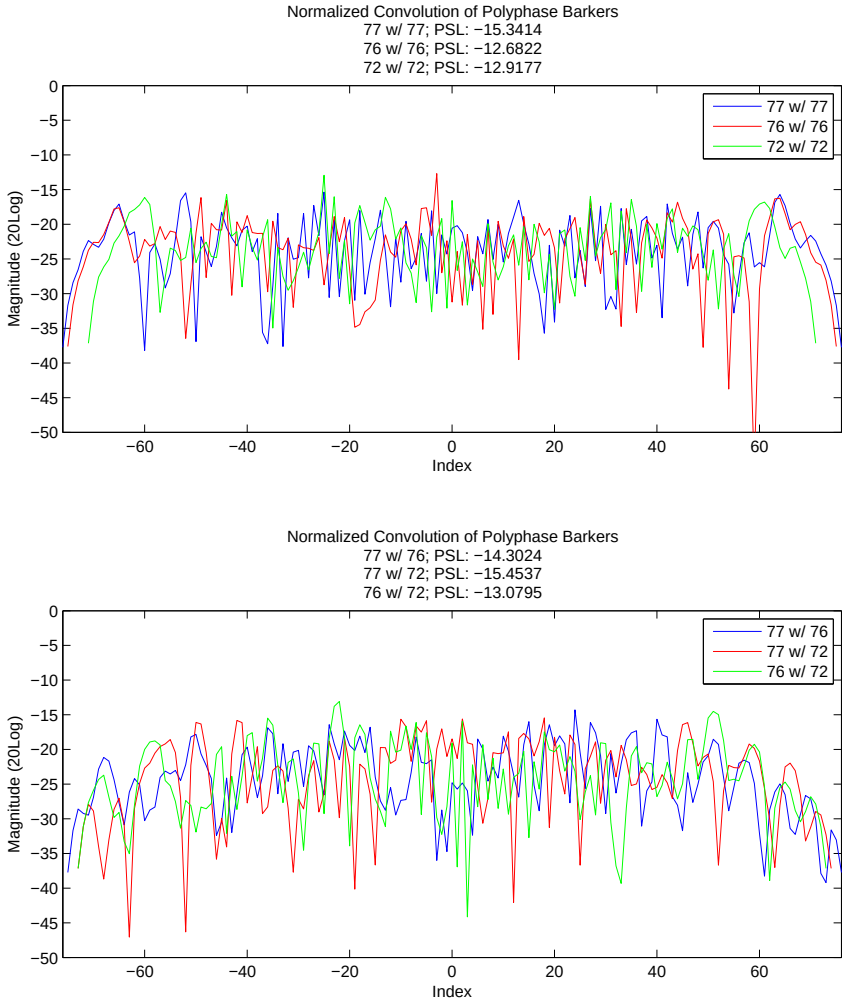


Figure 2.8: *Normalized Convolution of Polyphase Barker Sequences*

Given the requirement for a pulse length of $T = 20\,\mu$s, a maximum (-4 dB) bandwidth of $B = B_{chip} = 80$ MHz, and Eq. 2.44, the maximum number of allowed bits N_{max} can be shown as

$$N_{max} = \frac{T}{T_{chip}} = T \cdot B_{chip} = (20 \times 10^{-6}) \cdot (80 \times 10^{6}) = 1600 \quad (2.46)$$

For Frank, P1, P2, P3, and P4 polyphase codes, the codes' phases are determined by formulas, do not have an upper bound on the number of phases allowed, and 1600 phases (the calculated number of phases in Eq. 2.46 required to meet the desired system bandwidth) is a valid code length for all five code types. As a result, Frank, P1, P2, P3, and P4 codes with a length of 1600 will be analyzed.

From sec. 2.4, it is seen that while not truly orthogonal, an LFM upchirp and an LFM downchirp of the same frequency and bandwidth may be able to form a pseudo-orthogonal set if the right system parameters are met. Frank, P1, P2, P3, and P4 codes are all derived from LFM waveforms, therefore there are both upchirp and downchirp forms of these codes. The formulas dictating the phases of these waveforms given by Pace in [11] by default set Frank, P1, P3, and P4 codes as approximations of upchirps, with P2 being an approximation of a downchirp. The phases of the P1, P2, and P4 codes can be negated to give the opposite chirp case due to being approximations of a double sideband detected LFM chirp. Frank and P3 codes are approximations of single sideband detected LFM chirp, and due to having the same frequency characteristics and autocorrelation as their double sideband detected counterpart (P1 and P2 for Frank, and P4 for P3) as seen in Figure 2.9, the Frank and P3 codes can be ignored in analysis without loss of information or possible

solutions. Therefore the three codes to analyze are the upchirp and downchirp forms of the P1, P2, and P4 codes. For a code of length $N_c = M^2$, and letting i be the number of sample in a given frequency, and j is the number of frequency, the phase of the ith sample of the jth frequency of a P1 code $\phi_{P1;i,j}$ and of a P2 code $\phi_{P2;i,j}$ can be shown as

$$\phi_{P1;i,j} = \frac{-\pi}{M}[M - (2j - 1)][(j - 1)M + (i - 1)] \tag{2.47}$$

and

$$\phi_{P2;i,j} = \frac{-\pi}{2M}[2i - 1 - M][2j - 1 - M] \tag{2.48}$$

where $i = 1, 2, 3, ..., M$ and $j = 1, 2, 3, ..., M$, and where M must be even for the P2 code [11]. The phase of the ith sample of a P4 code $\phi_{P4;i}$ can be shown as

$$\phi_{P4;i} = \frac{\pi}{M^2}(i - 1)^2 - \pi(i - 1) \tag{2.49}$$

where $i = 1, 2, 3, ..., M^2$. For the Frank, P1, P2, P3, and P4 codes, the pulse compression ratio (alternatively called processing gain or pulse compression gain), defined as the ratio of SNR at the output of the matched filter to that prior to the filter, is M^2 [11], [17]. The P1 and P2 codes are step approximations of an LFM waveform, where the P2 waveform uses different starting phases at every frequency but has the same phase changes within each frequency, and the P2 waveform has the requirement that the codelength be the perfect square of an even number (for good autocorrelation behavior). The P4 waveform is an approximation of the quadratic phase in an LFM waveform, and has more continuous appearing phase and frequency changes than the P1

or P2 codes, as shown in Figure 2.10.

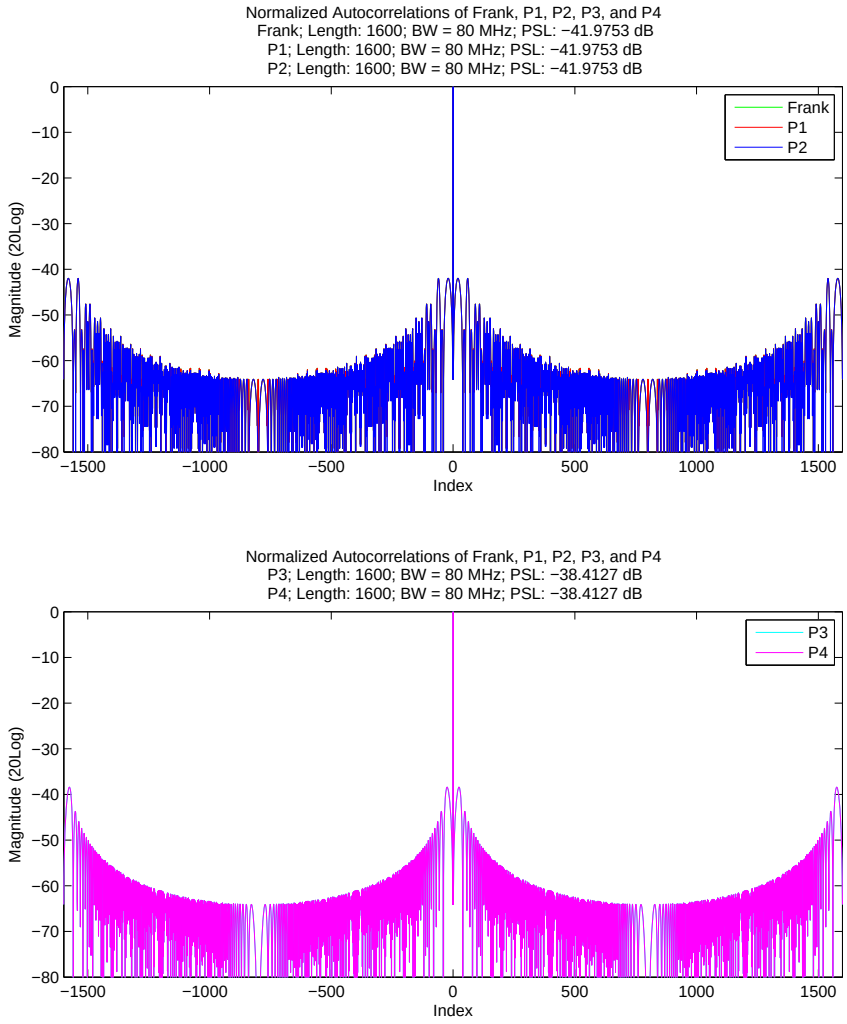


Figure 2.9: *Matching Autocorrelations for and Frank, P1, and P2 and Matching Autocorrelations for P3 and P4*

Due to the P1, P2, and P4 codes being double sideband detected LFM chirp approximations, taking the complex conjugate of the code switches the phase sign and effectively flips the chirp direction. When calculating the isolation between waveforms, the maximum magnitude of the cross-correlation is

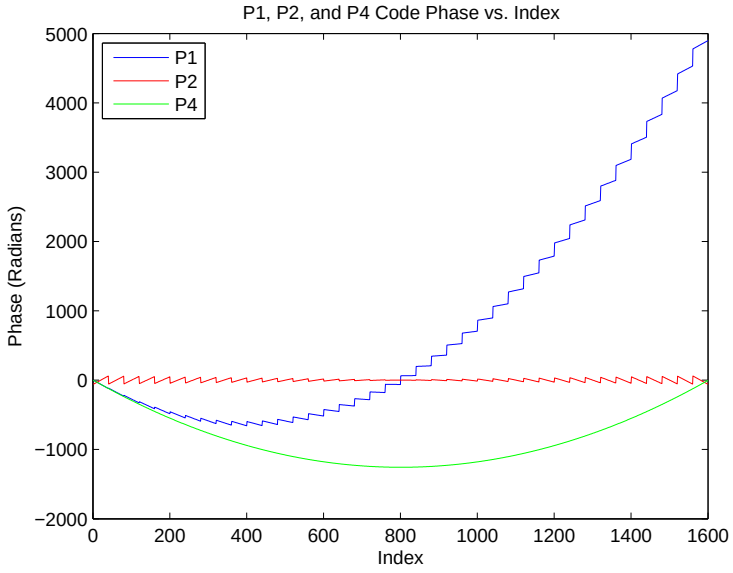


Figure 2.10: *Normalized Convolution of Polyphase Barker Sequences*

the determining factor, and it is desired to only calculate waveforms with opposite chirp directions to maximize isolation. Therefore comparing two codes with opposite chirp directions (ex: P1 up and P2 down) will yield the same magnitude results as those calculated when both codes' chirp directions are flipped (ex: P1 down and P2 up). Letting x_{up} represent a double sideband detected upchirp LFM approximation and letting y_{down} represent a double sideband detected downchirp LFM approximation, this can be shown as

$$|x_{up} \otimes y_{down}| = \sqrt{(x_{up} \otimes y_{down})(x_{up} \otimes y_{down})^*} = |(x_{up} \otimes y_{down})^*| = \\ = |x^*_{up} \otimes y^*_{down}| = |x_{down} \otimes y_{up}| \quad (2.50)$$

because $x^*_{up} = x_{down}$ and $y^*_{down} = y_{up}$ due to x and y being centered at complex baseband. Therefore, for the purpose of finding a pseudo-orthogonal set where the maximum magnitude of the cross-correlation is the determining factor, it is only necessary to calculate a pair of codes with one orientation of

opposite chirp directions.

For P1, P2, and P4 codes of pulse length $T = 20\,\mu$s, length 1600 (corresponding with -4 dB bandwidth of 80 MHz), the peak sidelobes of the autocorrelations are -41.98 dB, -41.98 dB, and -38.41 dB respectively. Due to the unbounded nature of these codes and the pulse length and bandwidth of the system, all three of these polyphase LFM approximation waveforms have lower autocorrelation sidelobes than the best known polyphase Barker case. The combination of codes with the best cross-correlation characteristics is the P2 code with an opposite chirp P4 code, where the maximum magnitude of the cross-correlation is 31.63 dB lower than the peak of the autocorrelation. For the cross-correlation case where the same code type is used with opposite chirp directions the P1 and P2 codes had practically equivalent 30.4 dB of suppression while the P4 code had 29.0 dB of suppression. These results are shown in Figure 2.11, Figure 2.12, and Figure 2.13. Although the cross-correlation of the P2 with the P4 code results in greater isolation by 1.2 dB, the peak sidelobe level of the P4 code is 3.6 dB higher than the peak sidelobe of the P1 or P2 code. This difference in sidelobe behavior, combined with different Doppler sensitivity between the P1 and P2 codes versus the P4 code [17], means that it would probably be wise to assemble a pseudo-orthogonal waveform set with opposite chirp directions of the same code so that both waveforms have very similar sidelobe, Doppler, and precompression band-limiting characteristics. For a system with limited precompression band-limiting and low Doppler tolerance expectations, either a set of P1 or P2 codes would be the best choice. For a system with more precompression band-limiting and/or larger Doppler tolerance expectations, the P4 code, with better tolerance for both of these

effects [17], may be a better choice even though its peak sidelobe level is 3.6 dB higher and its isolation is 1.4 dB less.

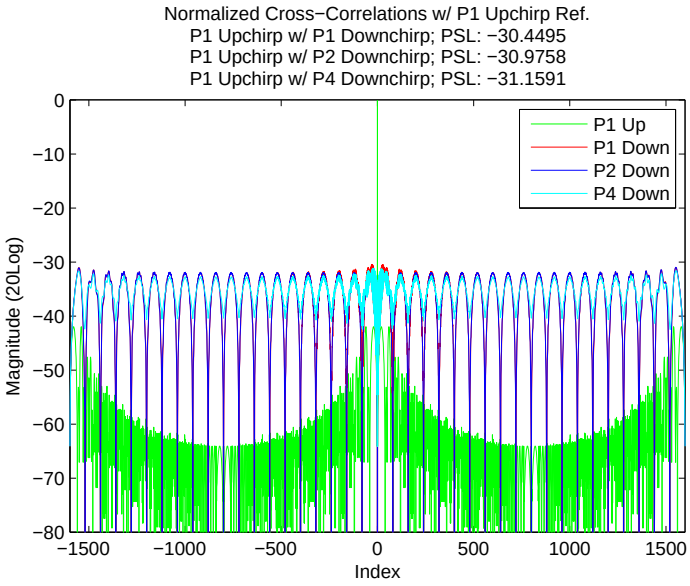


Figure 2.11: *Normalized Cross-Correlation of P1 Upchirp with P1, P2, and P4 Codes*

In order to achieve a truly pseudo-orthogonal waveform set with 40.0 dB of isolation in $T = 20\,\mu$s waveforms, the bandwidth must be increased drastically. It was found that the cross-correlation of the P2 and P4 codes are first to surpass 40.0 dB of isolation first at 562 MHz, and the cross-correlation of the P4 code was the first similar code pair (upchirp and downchirp) to surpass 40.0 dB of isolation at 595 MHz. These results are shown in Figure 2.14 and Figure 2.15 respectively. These bandwidths are not practical for most radar systems, and other modulation approaches will need to be examined to determine the practicality of a pseudo-orthogonal waveform set with the given system conditions.

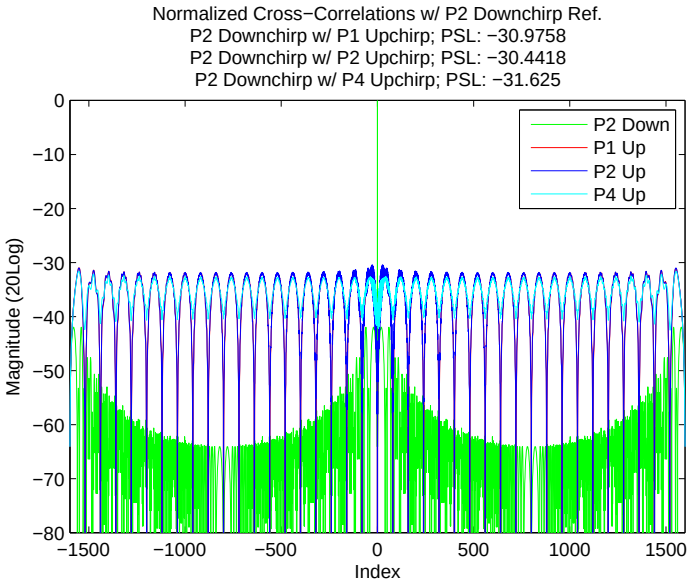


Figure 2.12: *Normalized Cross-Correlation of P2 Downchirp with P1, P2, and P4 Codes*

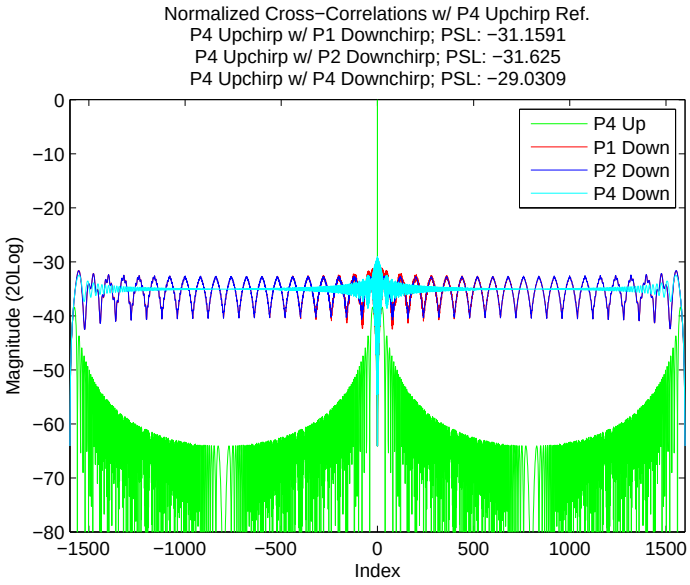


Figure 2.13: *Normalized Cross-Correlation of P4 Upchirp with P1, P2, and P4 Codes*

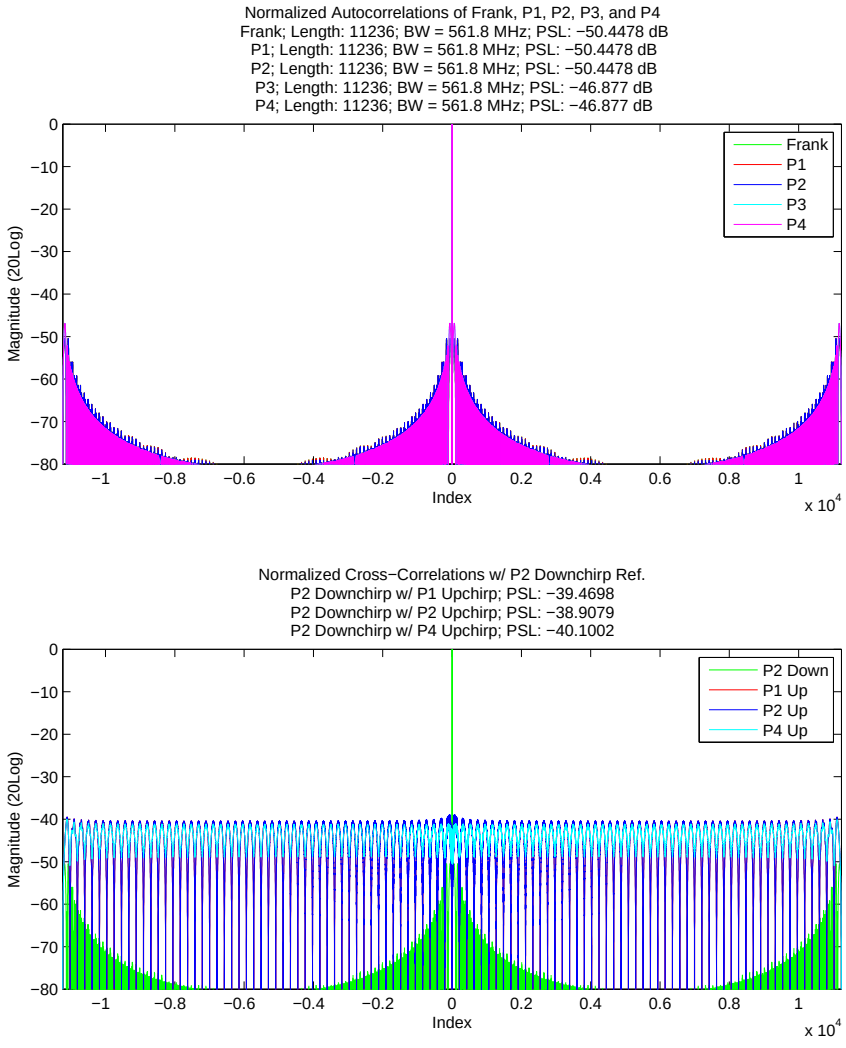


Figure 2.14: *Normalized Autocorrelations and Cross-Correlation of P2 Downchirp with P1, P2, and P4 Codes*

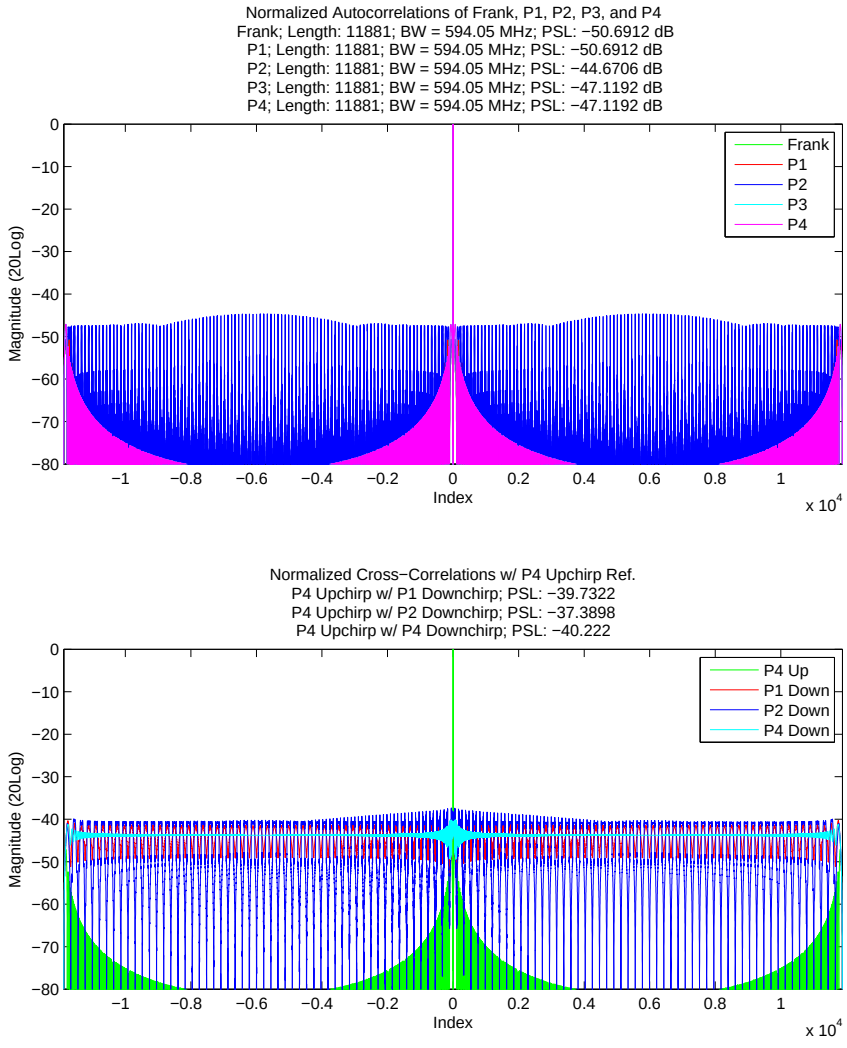


Figure 2.15: *Normalized Autocorrelations and Cross-Correlation of P4 Upchirp with P1, P2, and P4 Codes*

2.7 Low Sidelobe Pseudo-Orthogonal Code Sets Through Particle Swarm Optimization

As seen in Section 2.6, while the concept of a pseudo-orthogonal waveform set is easy to comprehend, an actual pseudo-orthogonal waveform set where all the waveforms are assumed to operate simultaneously over the same bandwidth is rather difficult to assemble. This difficulty stems from the dependence of pulse compression on a cross-correlation and auto-correlation based process. As a result, a direct optimization solution for pulse compressed waveforms has not yet been found. Therefore, iterative optimization methods must be introduced. This section proposes the use of particle swarm optimization for the purpose of finding pseudo-orthogonal waveform sets within a given desired set of system parameters. While particle swarm optimization has been previously utilized for antenna array optimization [30]–[32] and detection and identification of targets [33], [34], its application to the optimization of a variety of pseudo-orthogonal code sets has been relatively unexplored. This section closely follows the work presented by the author in [35] © 2016 IEEE.

2.7.1 Particle Swarm Optimization Background

The particle swarm methodology for the optimization of non-linear functions was first proposed as a biologically inspired algorithm [36]. In these early developments, researchers realized that the overall algorithm, originally designed to model the evolution of movement throughout flocks of birds or schools of fish, could be adapted to optimizing multi-dimensional non-linear problems through a process of intelligent progression of test points within an appropriate

state space. This is accomplished by creating an overall fitness function that is a function of all system variables, and that determines the desirability of the overall system output given the current variable values. The fitness function is then evaluated by a given number of particles, each at a different coordinates within the multi-variate space, at each iteration of the algorithm. After each iteration of the algorithm, the particles adjust their coordinates so that the overall swarm of particles approaches the coordinates giving the most desirable known fitness function result, all the while more closely evaluating as-yet untested coordinates close to the best known coordinates. This makes particle swarm optimization extremely effective at navigating large multi-variate state spaces and finding optimized solutions, whereas traditional techniques (e.g. Newton-Raphson) more easily suffer from limitations due to local minimization of an error function in non-convex problems.

At the initialization of the algorithm, a preset number of "particles," or fitness function evaluation points, are generated at random within the multi-variate space. In addition to randomly generated coordinates, each particle also has a randomly assigned "velocity," or preset rate of change for each variable dimension. The particles future positions are determined by their calculated velocity at each iteration, effectively giving the particles an inertia so that the overall swarm is not too easily swayed throughout evaluation of the iterations. All of the particles current states are then evaluated by the fitness function, and the lowest fitness function personal best seen by each individual particle (and its associated coordinates) are saved. Additionally, each particle also saves the coordinates giving the local best solution, which is the position giving the best solution within the nearest subset of particles,

where the subset size is a predetermined fraction of the total particles in the simulation. Each particle then evaluates its velocity vector, which determines its coordinates for the next iteration. The velocity vector is determined by summing a modifier based on the distance between the particles current coordinates and the particles personal best coordinates, a modifier based on the distance between the particles current coordinates and the particles local best coordinates, and a weighted version of the previous iterations velocity vector. The modifiers based on distance between coordinates each rely on the distance multiplied by random samples from a uniform distribution between zero and one, where the random sample for each modifier is regenerated every iteration.

For the iterations following the initial iteration, the coordinates of all the points are updated with their individually calculated velocities from the previous iteration. If any of the new points fall outside the preset allowable range of parameters, the violating coordinates are adjusted to satisfy the allowed range. The fitness function is then evaluated for all particle coordinates. For each particle, if its current coordinates result in a more desirable result than the previously saved personal best, then the personal best is overwritten with the current coordinates. Each particles local best is also reassessed, and the velocity vector for each particle is recalculated for the next iteration. The algorithm halts iterations either when the relative change in fitness function over several iterations has decreased to nearly zero, or when a preset program time limit has been reached.

2.7.2 Determining a Fitness Function

The actual execution of the particle swarm optimization algorithm lends itself to application to a vast array of non-linear optimization problems. Therefore, the main algorithm component that makes particle swarm optimization relevant to a specific problem is the fitness function. Fitness functions are evaluated such that lower values equate to more desirable system solutions. While some non-linear problems are relatively straightforward to determine the fitness function and are easy to visualize, such as finding the minimum of a polynomial based two dimensional surface, others are much more abstract and difficult to determine. For the purpose of finding pseudo-orthogonal waveform sets, the types of waveforms desired and waveform characteristics to be optimized must first be chosen. Next, the parameters needed to assemble the desired code types that only affect the chosen characteristics must be chosen before the fitness function can be determined. Possible fitness function characteristics to be evaluated and optimized for determining pseudo-orthogonal waveform sets can include maximizing main lobe power, minimizing beamwidth, minimizing peak sidelobe (PSL) levels, and minimizing cross-correlation levels with other codes' matched filters within the set.

It is not required for a fitness function to be convex, but a non-convex fitness function allows the possibility of the particles to coalesce around a coordinate representing a local minima within the available coordinate space that may not be the global minima. Therefore, it has been found to be beneficial to execute particle swarm optimization several times for a given optimization problem, saving the results for each overall optimization. The fitness function is then executed for each of the saved results, and the coordinates giving

the best overall result are then saved as the optimal solution. This multiple-optimization approach seems to be especially useful for non-convex fitness functions where the number of a coordinate dimensions approaches a noticeable fraction of the number of particles.

2.7.3 Optimized Polyphase Coded Pseudo-Orthogonal Waveform Sets

The first attempt at creating a pseudo-orthogonal waveform set revolved around creating a pair of length N constant modulus polyphase coded waveforms. Similar to a previous approach, each bit in the code was treated as an individual variable to be optimized [37], [38]. Each of the N bits was assigned a variable representing that particular bit's phase, with the final assembled waveforms shown as

$$R_{poly,1}\left[k\right] = e^{j\psi_1[k]} \tag{2.51}$$

and

$$R_{poly,2}\left[k\right] = e^{j\psi_2[k]} \tag{2.52}$$

where $1 \leq k \leq N$ and $0 \leq \psi_1\left[k\right], \psi_2\left[k\right] < 2$. The collection of all the phase variables compromised the coordinate space to be traversed by the particles. The fitness function F_{poly} was created by calculating the autocorrelation of both waveforms, as well as the cross-correlation between the two waveforms. The magnitude of the peak sidelobe levels from both autocorrelations were summed with the maximum magnitude present in the cross-correlation to yield

the fitness function, which is shown below

$$F_{poly} = |PSL\left(S_{11}\left(R_{poly,1}, R_{poly,1}\right)\right)| + |PSL\left(S_{22}\left(R_{poly,2}, R_{poly,2}\right)\right)| + max\left(|S_{12}\left(R_{poly,1}, R_{poly,2}\right)|\right) \quad (2.53)$$

where S_{xy} is defined as the discrete cross-correlation, shown as

$$S_{xy} = \sum_{-\infty}^{+\infty} x\left[n\right] y^{*}\left[n+k\right] \qquad -\infty < k < +\infty. \quad (2.54)$$

This simple fitness function encourages a desirable pseudo-orthogonal waveform set by equally penalizing high peak sidelobes from either autocorrelation as well as a high cross-correlation magnitude. This fitness function is not convex though, so the multiple-optimization approach should be used to identify as desirable a result as possible.

Using a multiple-optimization approach with 12 overall iterations, a pair of length 800 polyphase coded waveforms was generated. A length 800 code was chosen as this corresponds with a 20 μs pulse occupying a 40 MHz 4 dB bandwidth. It was seen that the resulting waveforms displayed PSLs of -26.8 dB and -25.9 dB respectively with a maximum cross-correlation response of -25.9 dB. These results are shown in Figure 2.16. While only a pair of polyphase coded waveforms were generated for this example, it should be noted that extending this approach to generate pseudo-orthogonal waveform sets containing more than two polyphase coded waveforms is relatively straightforward.

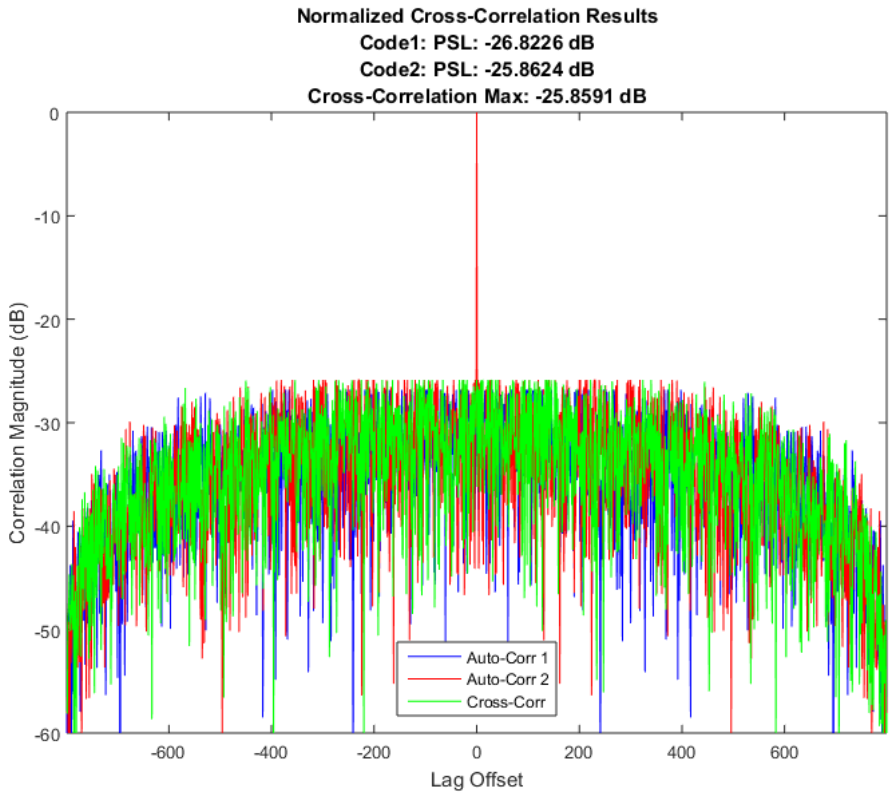


Figure 2.16: *Auto-Correlation and Cross-Correlation Results from Polyphase Coded Pseudo-Orthogonal Waveform Set, Reprinted from Dunn et al. (2016)* © *2016 IEEE*

2.7.4 Non-Linear Frequency Modulated Waveform Set

As addressed in Section 2.4.1, a common waveform set treated as "pseudo-orthogonal" is the pairing of an upchirp and downchirp Linear Frequency Modulated (LFM) waveform that each span the same bandwidth. It has been shown that Non-Linear Frequency Modulated (NLFM) waveforms can result in very low PSLs [1], [39]. It was hypothesized that an optimized pair of upchirp and downchirp NLFM waveforms could result in an improved pseudo-orthogonal set over the traditional LFM waveform pair. While the resulting waveform pair should also have improved pseudo-orthogonal characteristics

over a similarly optimized polyphase coded waveform set, by nature the approach of pairing of an upchirp with a downchirp is not easily modified to generate NLFM pseudo-orthogonal waveform sets containing more than two waveforms. Similar to a previous Genetic Algorithm-based approach [40], it was decided to create NLFM waveforms by shaping the instantaneous frequency with a spline function, where the points used to shape the spline were used as the parameters to be optimized by the particle swarm optimization method.

In order to minimize the number of variables needed to represent the instantaneous frequency curve and enforce certain qualities, a novel method of representing the spline points of an NLFM upchirp was devised. It was decided that the parameters to be optimized would not be the spline coordinates $(X_{sp}[i], Y_{sp}[i])$ themselves, but would be modifying factors $M[i]$ to be added to baseline coordinates $(X_{bl}[i], Y_{bl}[i])$. In order to restrict the modifying factors to a reasonable and repeatable range of possible values, the baseline coordinates are normalized in both the time and frequency domains to span from -1 to +1, and are multiplied back to their intended ranges after optimization has taken place. The baseline coordinates representing the points to be interpolated by the spline function to form the instantaneous frequency curve are normalized to span from -1 to +1 using p points, where $p = N + 3$ points and N, an even number, is the number of parameters to be optimized. The three additional points without associated modifying factors are due to fixing the starting and ending baseline coordinate points at $(X_{bl}[1], Y_{bl}[1]) = (-1, -1)$ and $(X_{bl}[p], Y_{bl}[p]) = (+1, +1)$ respectively, as well as fixing the middle point at $(X_{bl}[r], Y_{bl}[r]) = (0, 0)$ where $r = \frac{p}{2} + 0.5$. This ensures that the function

covers the full bandwidth range, and that the complex baseband center frequency occurs at the center of the waveform in the time domain. The other N baseline coordinates linearly interpolate between the three fixed points, leading to the creation of an LFM waveform when all the modifying factors are set equal to zero. The modifying factors themselves are distances from the baseline coordinates, such that the final spline coordinates are given by

$$(X_{sp}[i], Y_{sp}[i]) = (X_{bl}[i] - M[i], Y_{bl}[i] + M[i]). \tag{2.55}$$

Additionally, there is a restriction on the modifying factors' influence by ensuring that the instantaneous frequency curve acts as a function of time by preventing multiple possible frequencies for a given point in time. This is enforced by the conditional statement

if

$$X_{sp}[i] < (X_{sp}[i-1] + D_{buf}) \tag{2.56}$$

then

$$(X_{sp}[i], Y_{sp}[i]) = (X_{sp}[i-1] + D_{buf}, Y_{sp}[i-1] + 2\ D_{sp} - D_{buf}) \tag{2.57}$$

where D_{sp} is the horizontal spacing between adjacent baseline coordinate points, and D_{buf} is a user-determined distance buffer in the normalized space to prevent vertical segments in the instantaneous frequency plots.

Once the modifying factors have been found, a spline function is used to smoothly interpolate between the spline coordinates. The resulting spline is then renormalized in time to span the pulse length T, and the normalized

frequencies are multiplied by one half the bandwidth, effectively creating the waveform's true instantaneous frequency as a function of time $f_{inst}[t]$. This instantaneous frequency is then cumulatively summed and used as the phase terms of the final upchirp and downchirp waveforms, shown below respectively as

$$R_{NLFM,1}[t] = e^{j2\pi \sum_{l=\frac{-T}{2}}^{l=t} (f_{inst}[l])} \qquad \frac{-T}{2} \leq t \leq \frac{+T}{2} \tag{2.58}$$

and

$$R_{NLFM,2}[t] = e^{-j2\pi \sum_{l=\frac{-T}{2}}^{l=t} (f_{inst}[l])} \qquad \frac{-T}{2} \leq t \leq \frac{+T}{2}. \tag{2.59}$$

The fitness function is simply the maximum magnitude present in the cross-correlation summed with the PSL, where the PSL is the highest magnitude point outside the ideal main lobe. The ideal mainlobe width is determined by a Gaussian curve approximation as described in [41]. The fitness function for the NLFM particle swarm optimization is shown as

$$F_{NLFM} = \\ |PSL\left(S_{11}\left(R_{NLFM,1}, R_{NLFM,1}\right)\right)| + max\left(|S_{12}\left(R_{NLFM,1}, R_{NLFM,2}\right)|\right). \tag{2.60}$$

Using a multiple-optimization approach with 12 overall iterations and $N = 20$, a pair of 5 μs 10 MHz NLFM waveforms was generated. It was seen that the resulting waveforms display PSLs of -30.7 dB with a maximum cross-correlation response of -17.5 dB. These results are shown compared to a traditional LFM pairing in Figure 2.17, and it is seen that while the cross-correlation is only 0.05 dB lower than the traditional LFM case, the PSL is 17.2 dB lower in the presented NLFM waveform set. These results help to demonstrate the

viability of particle swarm optimization for the purpose of generating pseudo-orthogonal waveform sets within a given bandwidth and set of parameters that is much more desirable than the traditional LFM based waveform set.

2.7.5 Particle Swarm Conclusion

Particle swarm optimization offers a promising approach for generating pseudo-orthogonal waveform sets under various constraints for next-generation radar systems. This offers the possibility of creating waveform sets with optimal autocorrelation and cross-correlation characteristics while satisfying restrictive spectral requirements. This was demonstrated through a constant modulus polyphase coded example, as well as a constant modulus NLFM waveform created with a novel parametric methodology utilizing spline interpolation. Therefore, through the construction and assignment of a clever fitness function, pseudo-orthogonal waveform sets can be easily and efficiently assembled and utilized for MIMO, polarimetric, and other modern and emerging radar architectures.

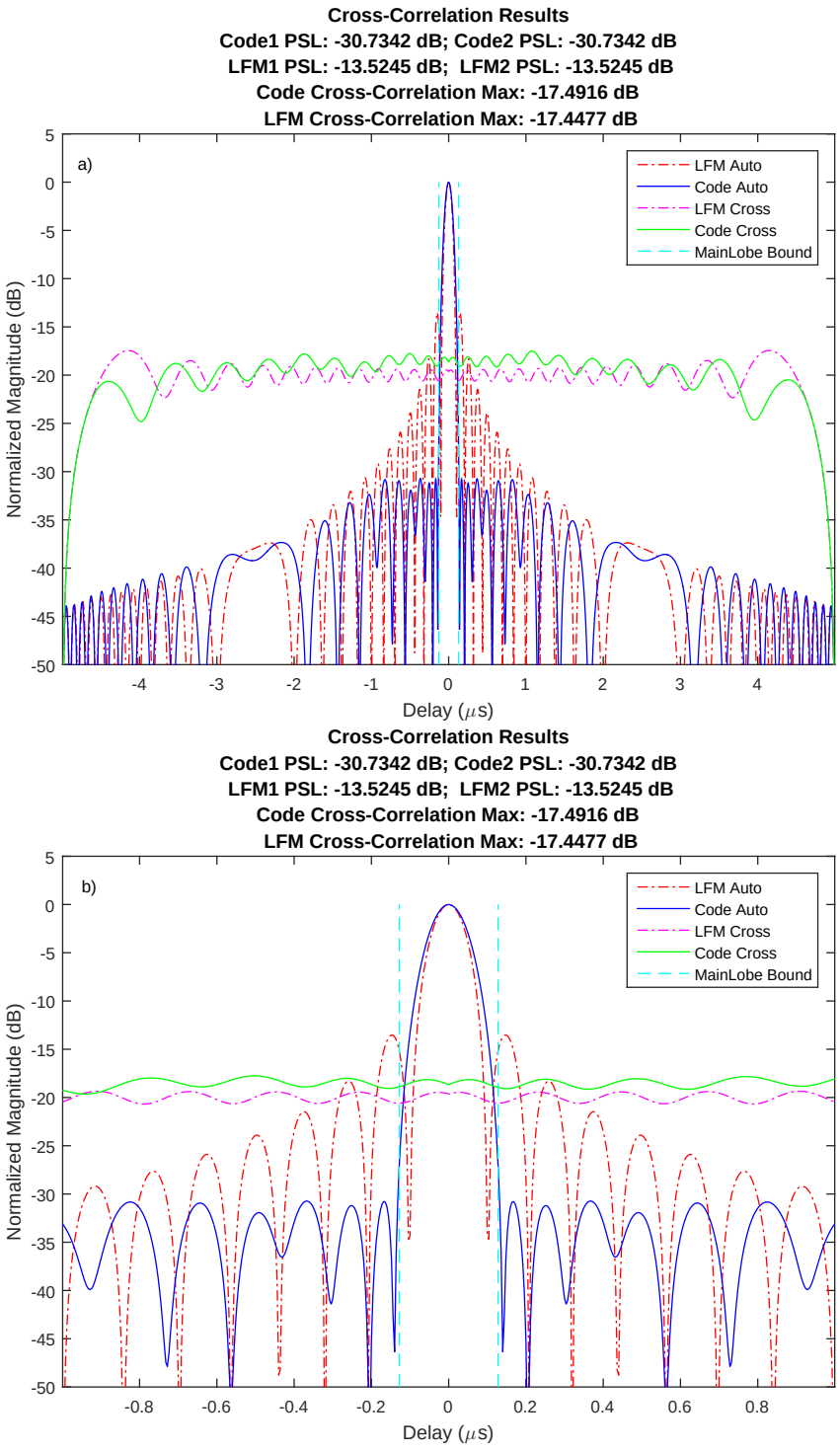


Figure 2.17: *Auto-Correlation and Cross-Correlation Results from NLFM Pseudo-Orthogonal Waveform Set Compared with LFM Waveform Set. a) Full View, b) Magnified View. Reprinted from Dunn et al. (2016) © 2016 IEEE*

2.8 Analysis of Range Resolution and Range Sidelobe Characteristics as a Function of Orthogonality Degradation

Using the mathematical basis established in sec. 2.2, the radar system depends upon both polarization orthogonality as well as coding orthogonality to recover the necessary scientific measurements by discriminating each $\mathbf{\Gamma}$ term individually. This results in the need to characterize resolution and range sidelobe characteristics for one receive channel's matched filter output (using one matched filter) as a function of two degrees of orthogonality degradation. The H channel's matched filter output (using the matched filter for the signal transmitted on the H channel) will be used as the orthogonal radar return to be analyzed.

As stated in sec. 2.2, the reflected signals are dependent upon the target's distribution in range, such that the reflected signal can be represented as a convolution of the transmitted signal $\mathbf{T}_{\text{trans}}(t)$ with an envelope $A(t)$ representing the magnitude of reflection at range. Using the generalized reflection envelope with Equations 2.2, 2.3, 2.4, 2.6, 2.7, 2.9, and 2.10 along with $[\,\cdot\,]_{\text{LPF}}$ denoting an applied lowpass filter, the received complex baseband signal $\mathbf{R}_{\text{CBB}}(t)$ can be shown as

$$\mathbf{R}_{\mathrm{CBB}}(t) \;=\; \left[\begin{array}{c} R_{\mathrm{CBB,H}}(t)\;\hat{\mathrm{H}} \\ R_{\mathrm{CBB,V}}(t)\;\hat{\mathrm{V}} \end{array}\right] \;=$$

$$=\; \left[\left(\mathbf{C}_{\mathrm{ant}}^{\mathrm{T}}\boldsymbol{\Gamma}\left[\left(\mathbf{C}_{\mathrm{ant}}\,\mathbf{T}_{\mathrm{ideal}}(t)\right)\otimes A(t)\right]\right)\,2e^{-j2\pi f_0 t}\right]_{\mathrm{LPF}} \;=$$

$$\left[\left(\left[\begin{array}{cc} 1 & \alpha \\ \alpha\,\beta & \beta \end{array}\right]\left[\begin{array}{cc} \Gamma_{\mathrm{HH}} & \Gamma_{\mathrm{HV}} \\ \Gamma_{\mathrm{VH}} & \Gamma_{\mathrm{VV}} \end{array}\right]\right.\right.$$

$$\left.\left.\left[\left(\left[\begin{array}{cc} 1 & \alpha\,\beta \\ \alpha & \beta \end{array}\right]\left[\begin{array}{c} |a_1(t)|\,cos(2\pi f_0 t\,+\,\theta_1(t))\;\hat{\mathrm{H}} \\ |a_2(t)|\,cos(2\pi f_0 t\,+\,\theta_2(t))\;\hat{\mathrm{V}} \end{array}\right]\right)\otimes A(t)\right]\right)\,2e^{-j2\pi f_0 t}\right]_{\mathrm{LPF}} \tag{2.61}$$

where $a_1(t),\ a_2(t)\ \in \mathbb{C}$ are the complex baseband modulation waveforms of the H and V channels, respectively, $a_1(t) = |a_1(t)|e^{j\,\theta_1(t)}$, $a_2(t) = |a_2(t)|e^{j\,\theta_2(t)}$, f_0 is the carrier frequency, and $\hat{\mathrm{H}}$ and $\hat{\mathrm{V}}$ are the basis vectors representing the independent channels. As explained in sec. 2.3, pulse compression is the convolution of the received (complex baseband) signal with the matched filter. The pulse compression output of the orthogonal radar return on the H channel using $h_1(t)$ as the matched filter for $a_1(t)$, $R_{\mathrm{PC,HH}}(t)$, is given by

$$R_{\mathrm{PC,HH}}(t) \;=\; R_{\mathrm{CBB,H}}(t)\otimes h_1(t) \tag{2.62}$$

For the point target case, the reflection envelope is given by

$$A(t) \;=\; \delta(t\;-\;\frac{2R}{c}) \tag{2.63}$$

and for the extended target (assuming constant return amplitude through range) the reflection envelope is given by

$$A(t) = \text{rect}\left(\frac{\left(t - \frac{2R}{c}\right)}{\frac{2L}{c}}\right) \tag{2.64}$$

where R is the range to the center of the target along the radial direction, L is the length of distributed target along the radial direction, c is the speed of light, $(\frac{2R}{c})$ is the round trip time delay between the monostatic radar and the center of the target along the radial direction, and the definition of rect (x) is given in Eq. 2.29.

For this problem there is assumed to be no co-pol gain mismatch (resulting in $\beta = 1$), and due to only wanting to examine pulse compression behavior and the $\mathbf{\Gamma}$ terms being separable with orthogonal receive channels and orthogonal coding as shown in sec. 2.2, the individual $\mathbf{\Gamma}$ terms themselves are not as important as the method of their retrieval. The α term is then treated as a variable representing polarization orthogonality with $\alpha = 0$ being total orthogonality, and $\alpha = 1$ being equal contribution from each "orthogonal" polarization (full orthogonality breakdown). In addition, the coding orthogonality degradation dictated by the pulse compression matched filter outputs must also be taken into account. It does not seem feasible to substitute generalized "normal-looking" matched filter outputs for analysis of orthogonality degradation when distributed targets are to be analyzed, as the matched filter output is the convolution of the matched filter with a summation of delayed and phase shifted returns. Examining the H channel while assuming the V channel is deactivated ($\alpha = \beta = 0$), no polarization or phase shift happening due to the target surface ($\Gamma_{HH} = 1$ and $\Gamma_{HV} = 0$), and an extended target as shown in Eq. 2.64 time centered to zero offset ($R = 0$), the H matched

filter output as shown in Eq. 2.61 and Eq. 2.62 collapses as shown below

$$
\begin{aligned}
R_{\mathrm{PC,HH}}(t) &= \left[\left(|a_1(t)|\, cos(2\pi f_0 t + \theta_1(t)) \otimes \mathrm{rect}\left(\frac{t}{\frac{2L}{c}}\right)\right) 2e^{-j2\pi f_0 t}\right]_{\mathrm{LPF}} \otimes h_1(t) = \\
&= \left[\left(\int_{-\infty}^{+\infty} |a_1(\tau)|\, cos(2\pi f_0 \tau + \theta_1(\tau)) \int_{-\frac{L}{c}}^{+\frac{L}{c}} \delta\left(t + x - \tau\right) \mathrm{d}x\, \mathrm{d}\tau\right) 2e^{-j2\pi f_0 t}\right]_{\mathrm{LPF}} \otimes h_1(t) = \\
&= \left[\left(\int_{-\frac{L}{c}}^{+\frac{L}{c}} |a_1(t+x)|\, cos(2\pi f_0 (t+x) + \theta_1(t+x))\, \mathrm{d}x\right) 2e^{-j2\pi f_0 t}\right]_{\mathrm{LPF}} \otimes h_1(t) = \\
&= \int_{-\frac{L}{c}}^{+\frac{L}{c}} \left[|a_1(t+x)|\, cos(2\pi f_0 (t+x) + \theta_1(t+x))\, 2e^{-j2\pi f_0 t}\right]_{\mathrm{LPF}} \mathrm{d}x \otimes h_1(t) = \\
&= \int_{-\frac{L}{c}}^{+\frac{L}{c}} \left[|a_1(t+x)| \left(\frac{e^{j(2\pi f_0 t + 2\pi f_0 x + \theta_1(t+x))}}{2} + \right.\right. \\
&\quad \left.\left. + \frac{e^{-j(2\pi f_0 t + 2\pi f_0 x + \theta_1(t+x))}}{2}\right) 2e^{-j2\pi f_0 t}\right]_{\mathrm{LPF}} \mathrm{d}x \otimes h_1(t) = \\
&= \int_{-\frac{L}{c}}^{+\frac{L}{c}} |a_1(t+x)|\, e^{j(2\pi f_0 x + \theta_1(t+x))}\, \mathrm{d}x \otimes h_1(t) = \int_{-\frac{L}{c}}^{+\frac{L}{c}} a_1(t+x)\, e^{j2\pi f_0 x}\, \mathrm{d}x \otimes h_1(t) = \\
&= \int_{-\infty}^{+\infty} \left(\int_{-\frac{L}{c}}^{+\frac{L}{c}} a_1(\tau + x)\, e^{j2\pi f_0 x}\, \mathrm{d}x\right) h_1(t - \tau)\, \mathrm{d}\tau = \\
&= \int_{-\frac{L}{c}}^{+\frac{L}{c}} e^{j2\pi f_0 x} \int_{-\infty}^{+\infty} a_1(\tau + x)\; h_1(t - \tau)\, \mathrm{d}\tau\, \mathrm{d}x \qquad (2.65)
\end{aligned}
$$

The final pair of manipulated equations shows that integrated time delayed returns with phase shifts due to target range differences are convolved with the matched filter. This result, unlike the autocorrelation and cross-correlation of received signals from a point target, does not have a readily identifiable expected shape of output. As a result the resolution and range sidelobe characteristics cannot be readily characterized without specifying the modulating waveforms $a_1(t)$ and $a_2(t)$ and the reflection envelope $A(t)$. Eq. 2.65 can be

generalized for the extended uniform target case and shown as

$$
\begin{aligned}
R_{\mathrm{PC,HH}}(t) \;&= \\
&= \int_{-\frac{L}{c}}^{+\frac{L}{c}} e^{j2\pi f_0(-2\frac{R}{c}+x)} \int_{-\infty}^{+\infty} \Big(\Gamma_{\mathrm{HH}} \left[a_1(\tau - \frac{2R}{c} + x) \;+\; \alpha\,\beta\, a_2(\tau - \frac{2R}{c} + x) \right] \;+ \\
&\qquad + \Gamma_{\mathrm{HV}} \left[\alpha\, a_1(\tau - \frac{2R}{c} + x) \;+\; \beta\, a_2(\tau - \frac{2R}{c} + x) \right] \;+ \\
&\qquad + \Gamma_{\mathrm{VH}} \left[\alpha\, a_1(\tau - \frac{2R}{c} + x) \;+\; \alpha^2\,\beta\, a_2(\tau - \frac{2R}{c} + x) \right] \;+ \\
&\qquad + \Gamma_{\mathrm{VV}} \left[\alpha^2\, a_1(\tau - \frac{2R}{c} + x) \;+\; \alpha\,\beta\, a_2(\tau - \frac{2R}{c} + x) \right] \Big)\; h_1(t - \tau)\mathrm{d}\tau\,\mathrm{d}x
\end{aligned}
\tag{2.66}
$$

This generalized equation can be used for the uniform distributed target case or for the point target case, where the point target case with target radial length $L = 0$ results in

$$
\begin{aligned}
R_{\mathrm{PC,HH}}(t) \;&= \\
&= e^{-j4\pi f_0 \frac{R}{c}} \int_{-\infty}^{+\infty} \Big(\Gamma_{\mathrm{HH}} \left[a_1(\tau - \frac{2R}{c}) \;+\; \alpha\,\beta\, a_2(\tau - \frac{2R}{c}) \right] \;+ \\
&\qquad + \Gamma_{\mathrm{HV}} \left[\alpha\, a_1(\tau - \frac{2R}{c}) \;+\; \beta\, a_2(\tau - \frac{2R}{c}) \right] \;+ \\
&\qquad + \Gamma_{\mathrm{VH}} \left[\alpha\, a_1(\tau - \frac{2R}{c}) \;+\; \alpha^2\,\beta\, a_2(\tau - \frac{2R}{c}) \right] \;+ \\
&\qquad + \Gamma_{\mathrm{VV}} \left[\alpha^2\, a_1(\tau - \frac{2R}{c}) \;+\; \alpha\,\beta\, a_2(\tau - \frac{2R}{c}) \right] \Big)\; h_1(t - \tau)\mathrm{d}\tau
\end{aligned}
\tag{2.67}
$$

In order to actually show the effect of orthogonality degradation on resolution and range sidelobe characteristics, the generalized Eq. 2.66 will be used in simulations for both the point target and distributed target cases.

Due to the pulse compression output characteristics being dependent upon the modulating waveform being used, it is more practical to examine some

specific cases rather than attempt to characterize an equation that is too generalized (Eq. 2.66). It was decided to examine polarization and coding orthogonality degradation for a point target and a distributed target for two cases with $T = 20\,\mu$s and $-4\,$dB bandwidths of 80 MHz, namely the LFM chirp pair case as shown in sec. 2.4 and the P2 chirp pair case as shown in sec. 2.6. In order to highlight the effects of orthogonality degradation in the pulse compression, all simulations were conducted with two targets of equal radial length in the target area where the near target has scattering parameters $\mathbf{\Gamma}_1$ and the far target has scattering parameters $\mathbf{\Gamma}_2$, as shown below.

$$\mathbf{\Gamma}_1 = \begin{bmatrix} 1 & 0 \\ 0 & 1 \end{bmatrix} \tag{2.68}$$

$$\mathbf{\Gamma}_2 = \begin{bmatrix} 0 & 1 \\ 1 & 0 \end{bmatrix} \tag{2.69}$$

These scattering parameters indicate that target 1 (the near target) only reflects polarized fields equal to the incident polarized fields, whereas target 2 (the far target) reflects all horizontally incident fields vertically and reflects all vertically incident fields horizontally. While these may not be realistic scattering matrices for real-world targets, they will highlight the effects of orthogonality degradation. It should also be noted that the center range between the targets was adjusted to zero for processing so that each target's center is equidistant from delay zero in the pulse compression output ($R = 0$ in Eq. 2.66 and Eq. 2.67). For simulations α was linearly varied between 0 and 1 to simulate polarization orthogonality breakdown, $a_2(t)$ was replaced with $d\,a_1(t) + (1-d)\,a_2(t)$ where d was varied linearly between 0 and 1 to simulate coding orthogonality breakdown, the two target centers were separated

by 600 m, and the carrier frequency was set to 400 MHz. Due to the the modulating waveform $a_1(t)$ and its matched filter $h_1(t)$ remaining unchanged as the othogonality of polarization and coding is altered, the resolution (width of the pulse compression peak) is expected to remain basically unchanged as the orthogonality is altered. For the point targets case, the resolution is expected to resemble the resolution present in the autocorrelation of $a_1(t)$. For the extended uniformly returning targets case where the target is longer than the distance traveled in one period of the carrier frequency (0.75 m for 400 MHz), the signal is expected to destructively interfere everywhere except the edges of the target, resulting in the appearance of two discrete targets rather than one continuous target, though the resolution of these "two" returns should still resemble the resolution present in the autocorrelation of $a_1(t)$.

For the point targets case with polarization orthogonality degradation, looking at Eq. 2.67 it is expected for the pulse compression output for both the LFM and the P2 waveforms to resemble the summation of the $a_1(t)$ autocorrelation with an offset convolution of $a_2(t)$ with $h_1(t)$ when the orthogonality is maximized, and to resemble the summation of the $a_1(t)$ autocorrelation with the convolution of $a_2(t)$ with $h_1(t)$ at both target locations (which will also result in a higher magnitude at each target peak) when the orthogonality is minimized. This is verified for the LFM case in Figure 2.18 and for the P2 case in Figure 2.19.

It is seen that the target return peak increased by approximately 6 dB while the general sidelobe level increased by approximately 11 dB at complete orthogonality loss. Additionally, the peak sidelobe behavior of the LFM waveform

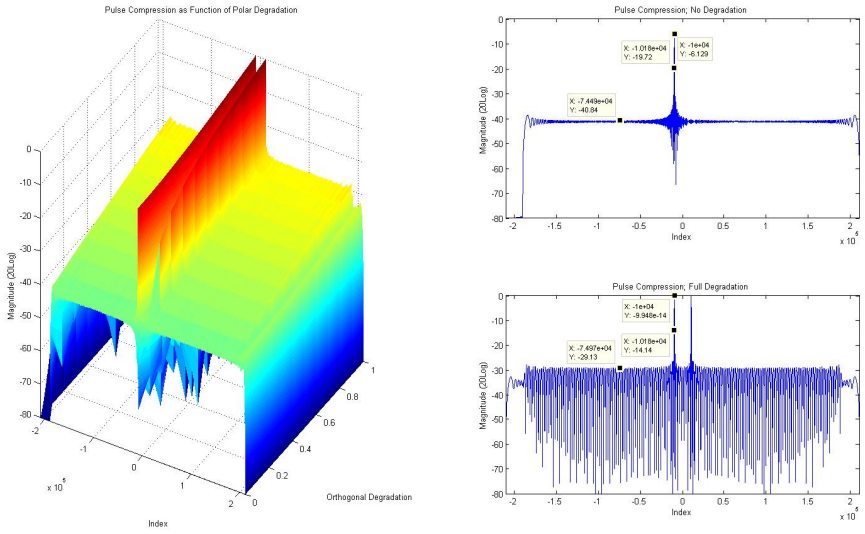


Figure 2.18: *Pulse Compression Output: LFM Waveform Orthogonal Polarization Degradation of Return from 2 Separated Point Targets*

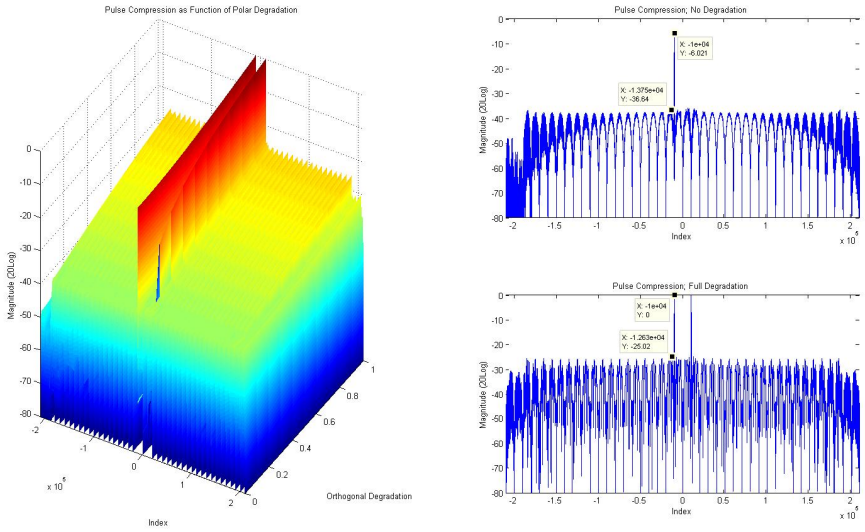


Figure 2.19: *Pulse Compression Output: P2 Coded Waveform Orthogonal Polarization Degradation of Return from 2 Separated Point Targets*

only decreased by 0.5 dB. As expected for the point target case, the resolution was virtually unchanged from that of the autocorrelation.

For the point targets case with coding orthogonality degradation and $\alpha = 0$, looking at Eq. 2.67 it is expected for the pulse compression output for both the LFM and the P2 waveforms to resemble the summation of the $a_1(t)$ autocorrelation with an offset convolution of $a_2(t)$ with $h_1(t)$ when the orthogonality is maximized, and to resemble the summation of the $a_1(t)$ autocorrelation at both target locations (which should result in a relatively unchanged magnitude at the first target peak) when the orthogonality is minimized. This is verified for the LFM case in Figure 2.20 and for the P2 case in Figure 2.21.

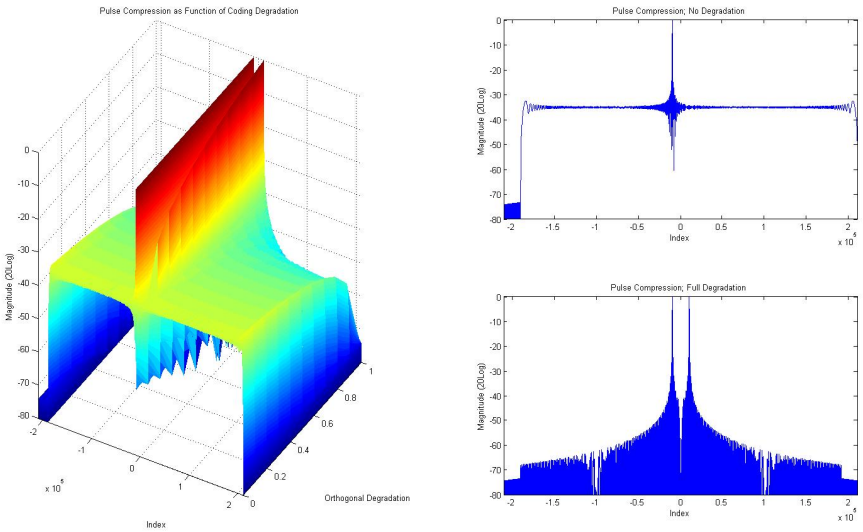


Figure 2.20: *Pulse Compression Output: LFM Waveform Orthogonal Coding Degradation of Return from 2 Separated Point Targets*

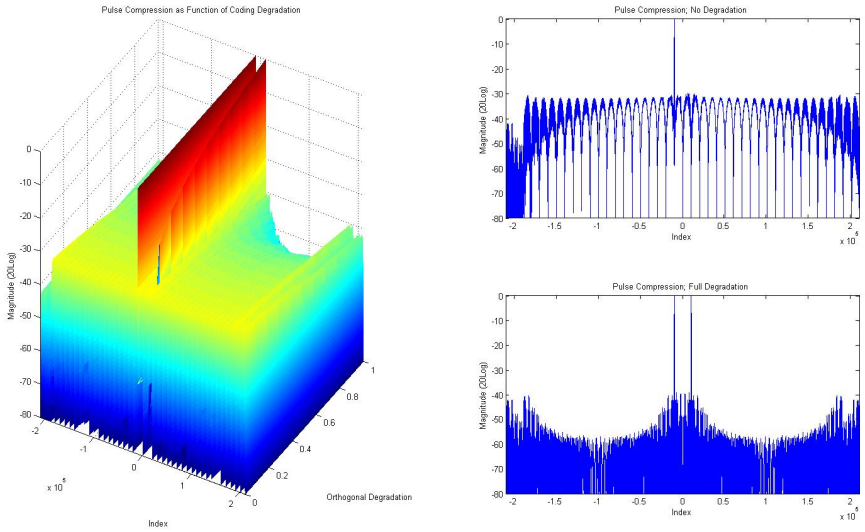


Figure 2.21: *Pulse Compression Output: P2 Coded Waveform Orthogonal Coding Degradation of Return from 2 Separated Point Targets*

It is seen that the target return peak for the first target had no appreciable change (lowering of 0.1 dB at full orthogonality loss), the peak sidelobe levels had no appreciable change (lowering of 0.3 dB at full orthogonality loss), and the general sidelobe level decreased and began to resemble the autocorrelation of $a_1(t)$ in shape due to the removal of the convolution of $a_2(t)$ with $h_1(t)$ at complete orthogonality loss. As expected for the point target case, the resolution was virtually unchanged from that of the autocorrelation.

For the 60 m extended targets case with polarization orthogonality degradation, looking at Eq. 2.66 it is expected for the pulse compression output for both the LFM and the P2 waveforms to resemble the summation of spread and distorted $a_1(t)$ convolved with $h_1(t)$ with an offset convolution of spread and distorted $a_2(t)$ with $h_1(t)$ when the orthogonality is maximized, and to resemble the summation of the spread and distorted $a_1(t)$ convolved with $h_1(t)$ with the convolution of spread and distorted $a_2(t)$ with $h_1(t)$ at both target locations (which will also result in a higher magnitude at each target peak) when the orthogonality is minimized. This is verified for the LFM case in Figure 2.22 and for the P2 case in Figure 2.23.

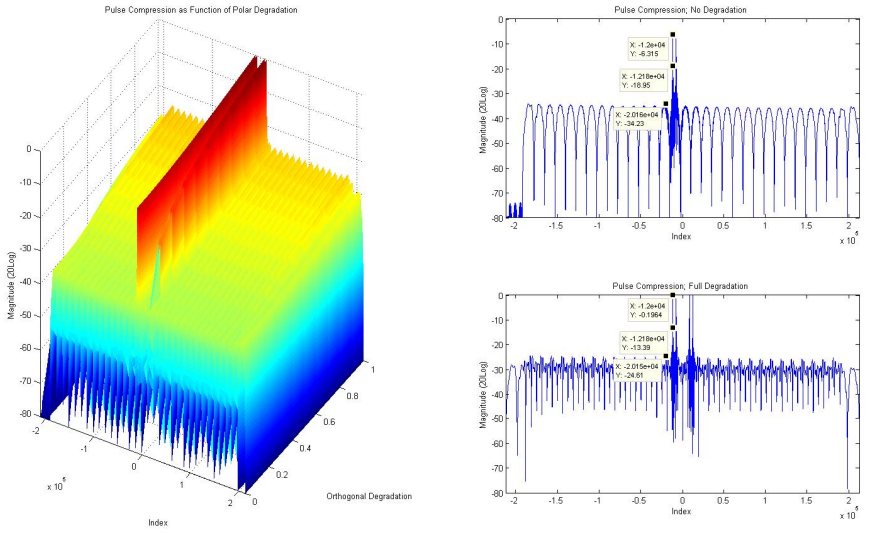


Figure 2.22: *Pulse Compression Output: LFM Waveform Orthogonal Polarization Degradation of Return from 2 Separated 60m Long Extended Targets*

It is seen that the target return peak increased by approximately 6 dB while the general sidelobe level increased by approximately 10 dB at complete

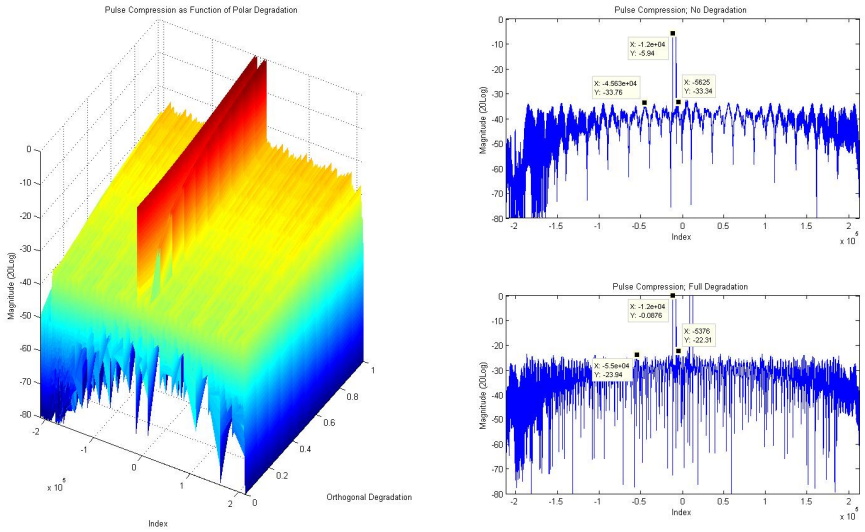


Figure 2.23: *Pulse Compression Output: P2 Coded Waveform Orthogonal Polarization Degradation of Return from 2 Separated 60m Long Extended Targets*

orthogonality loss. Additionally, the peak sidelobe behavior of the LFM waveform only decreased by 0.6 dB. As predicted for the extended target case, the peaks corresponding with the extended targets' locations resulted in the appearance of two separated peaks for each target, corresponding with the edges of the targets, where the edge peak's resolution was virtually unchanged from that of the autocorrelation and the magnitude between the edge peaks was much lower due to destructive interference of the uniformly returned signal.

For the 60 m extended targets case with coding orthogonality degradation, looking at Eq. 2.66 it is expected for the pulse compression output for both the LFM and the P2 waveforms to resemble the summation of spread and distorted $a_1(t)$ convolved with $h_1(t)$ with an offset convolution of spread and distorted $a_2(t)$ with $h_1(t)$ when the orthogonality is maximized, and to resemble the summation of the spread and distorted $a_1(t)$ convolved with $h_1(t)$ at both target locations (which should result in a relatively unchanged magnitude at the first target peak) when the orthogonality is minimized. This is verified for the LFM case in Figure 2.24 and for the P2 case in Figure 2.25.

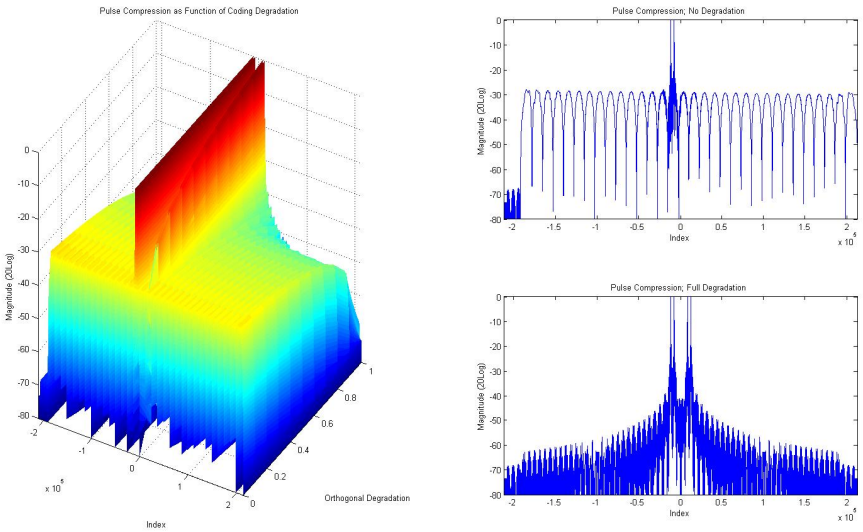


Figure 2.24: *Pulse Compression Output: LFM Waveform Orthogonal Coding Degradation of Return from 2 Separated 60m Long Extended Targets*

It is seen that the target return peak for the first target had negligible change, the peak sidelobe levels had no appreciable change (lowering of 0.4 dB at full orthogonality loss), and the general sidelobe level decreased and began to roughly resemble the autocorrelation of $a_1(t)$ in shape due to the removal

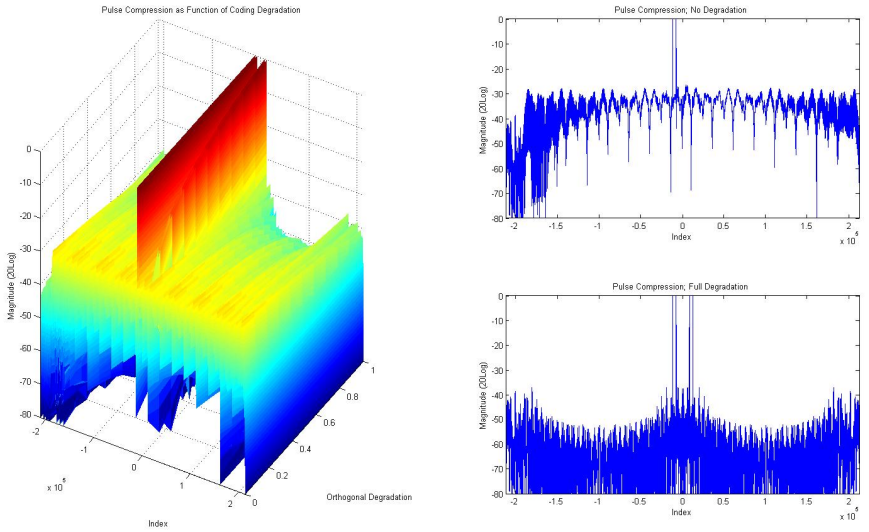


Figure 2.25: *Pulse Compression Output: P2 Coded Waveform Orthogonal Coding Degradation of Return from 2 Separated 60m Long Extended Targets*

of the convolution of the spread and distorted $a_2(t)$ with $h_1(t)$ at complete orthogonality loss. As predicted for the extended target case, the peaks corresponding with the extended targets' locations resulted in the appearance of two separated peaks for each target, corresponding with the edges of the targets, where the edge peak's resolution was virtually unchanged from that of the autocorrelation and the magnitude between the edge peaks was much lower due to destructive interference of the uniformly returned signal.

Overall it can be seen that the resolution is not appreciably affected by the loss of orthogonality of either the coding or the polarization. This makes sense as the resolution after pulse compression is determined by the waveform used and the matched filter, and since $a_1(t)$ is unchanged, the resolution as the orthogonality is altered does not change. The resolution for the constant magnitude reflection extended targets case does not produce a constant

high-magnitude return as would be expected, but instead produces two high magnitude peaks on each edge of the target with low magnitude return between the edges due to destructive interference. The resolution in the extended target case is not appreciably affected by loss of orthogonality either. For the unweighted LFM waveform the peak sidelobes remained relatively unchanged as the orthogonality of both parameters was altered, though the general shape of the sidelobes away from the peak would lower as the coding orthogonality was reduced (and polarization orthogonality was maintained), and the general shape of the sidelobes away from the peak would rise relative to the peak as polarization orthogonality was reduced. For the P2 waveform the general shape of the sidelobe behavior follows that of the LFM waveform, with the exception that the peak sidelobe behavior also follows the general sidelobe behavior as the orthogonality of both parameters was altered (rather than being relatively invariant as in the LFM case). From Eq. 2.66 and Figures 2.26, 2.27, 2.28, and 2.29 it is apparent that if both coding orthogonality and polarization orthogonality are lost simultaneously the result at full orthogonality loss is equivalent to the degraded coding orthogonality case with the total return magnitude increased.

While the resolution was basically unaffected and the sidelobe behavior was moderately affected by orthogonality breakdown, the recovery and separation of the individual $\mathbf{\Gamma}$ parameters suffers the most drastically as a degree of orthogonality is lost. From Eq. 2.66 it can be seen that the recovery and separation of the individual $\mathbf{\Gamma}$ parameters is completely based on the orthogonality of both the polarization and the coding. The separability is visualized in Figures 2.18 through 2.29 as the peak height of the targets, with target 1

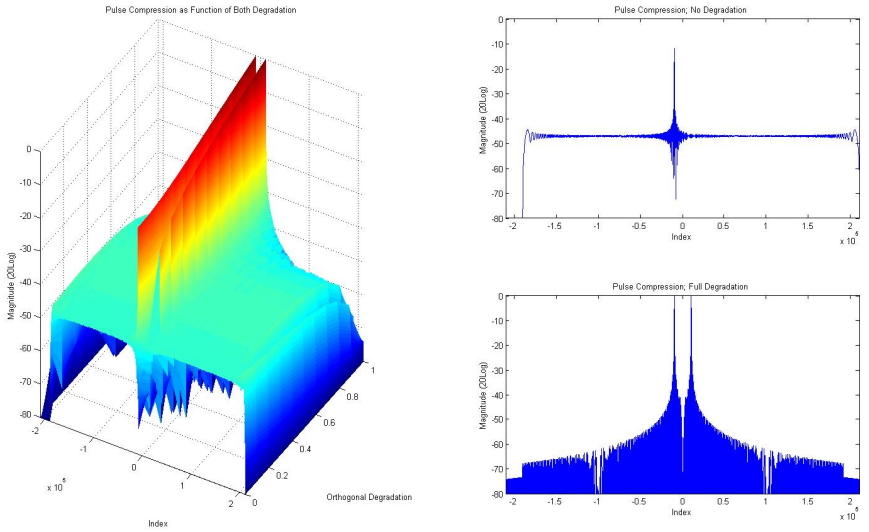


Figure 2.26: *Pulse Compression Output: LFM Waveform Orthogonal Polarization and Coding Degradation of Return from 2 Separated Point Targets*

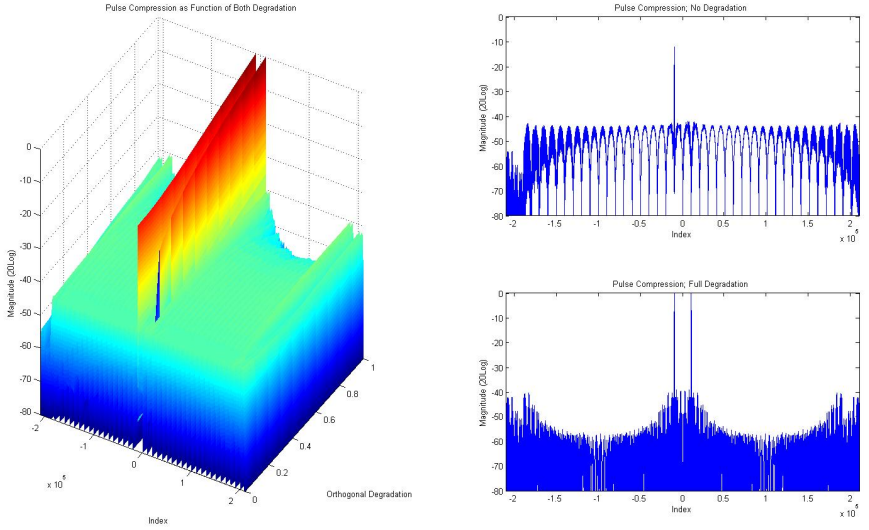


Figure 2.27: *Pulse Compression Output: P2 Coded Waveform Orthogonal Polarization and Coding Degradation of Return from 2 Separated Point Targets*

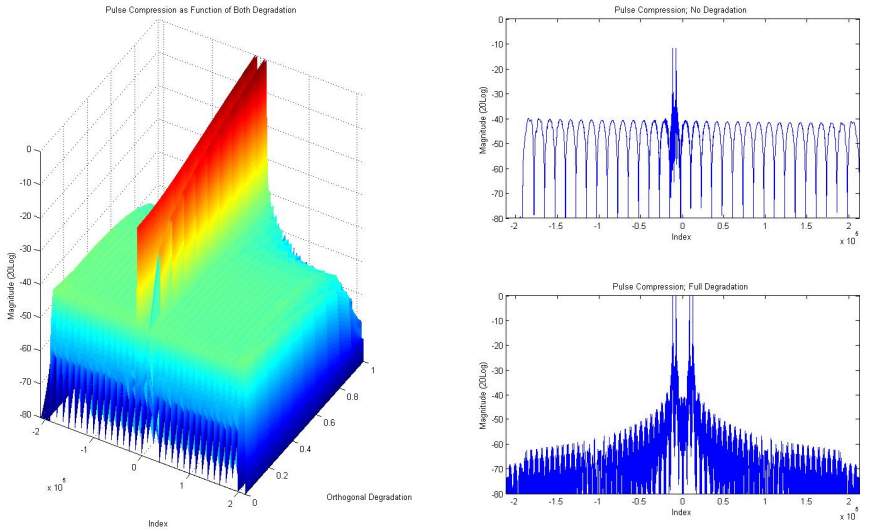


Figure 2.28: *Pulse Compression Output: LFM Waveform Orthogonal Polarization and Coding Degradation of Return from 2 Separated 60m Long Extended Targets*

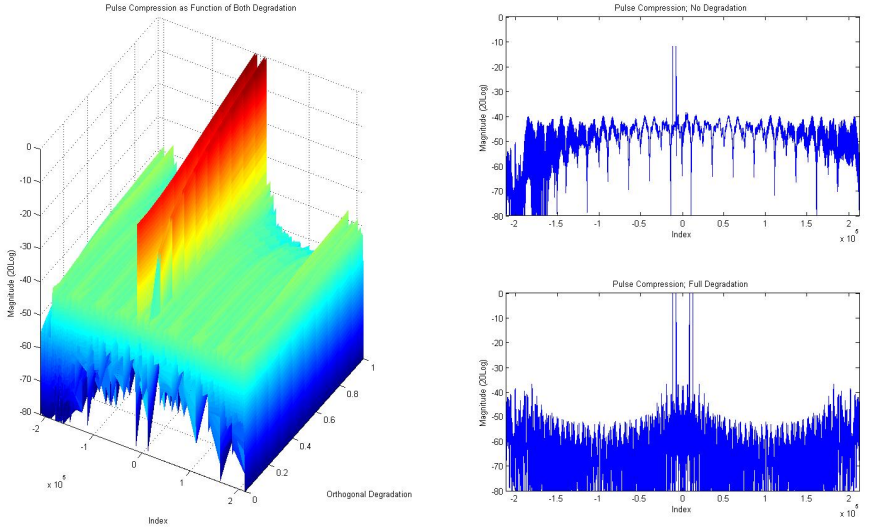


Figure 2.29: *Pulse Compression Output: P2 Coded Waveform Orthogonal Polarization and Coding Degradation of Return from 2 Separated 60m Long Extended Targets*

representing Γ_{HH} and target 2 representing Γ_{HV} due to Eq. 2.68 and Eq. 2.69 respectively and processing the H channel with matched filter $h_1(t)$. Note that in every simulation only target 1 had a pulse compression peak at no orthogonal degradation and the magnitude of the target 2 peak increased rapidly until both target 1 and target 2 had equal magnitude pulse compression peaks at full orthogonal degradation (of either variable). This shows that the $\mathbf{\Gamma}$ parameters are completely separable when orthogonality is maintained, but is completely lost when only one degree of orthogonality is lost. Therefore, in order to maintain a radar system that can make scientifically useful dual-polarization measurements it must be ensured that orthogonality of both coding and of polarization is maintained to a high degree.

2.9 Orthogonal Polarization Basis Transformation

As previously shown, polarization orthogonality is necessary for successful simultaneous transmit and simultaneous receive operation. This section serves to show that any orthonormal polarization basis can be mathematically transformed to serve as any other desired orthonormal polarization basis. This effectively allows a radar system with orthogonally polarized antenna elements in a given orthonormal polarization basis to be capable of transmitting an orthogonally polarized waveform set in any desired orthonormal polarization basis. Conversely, this also allows received radar data captured in a given orthonormal polarization basis to be processed and analyzed in any desired orthonormal polarization basis following a mathematical transformation of the captured data.

An orthogonal basis is defined as set of vectors in a domain where any two vectors are orthogonal to one another. If all vectors are of unit length in the set then it is an orthonormal basis. In addition, the number of vectors in the orthonormal set is equal to the order of the domain [19]. Therefore, because the plane spanned by the antenna is two dimensional, the orthogonal basis to describe polarization will be a set of two vectors. In addition, it is assumed that the basis vectors will be of unit length making the polarization basis an orthonormal set. The horizontal and vertical polarizations, H and V respectively, will be used as the base basis, as the channels and physical antennas on most common radar systems correspond with the physical H and V orientations.

Any polarization can be represented as an elliptical polarization, with linear and circular polarizations being special cases of elliptical polarizations. Therefore transformation from the H and V basis to any other orthogonal basis can be accomplished through use of a unitary generalized H and V to elliptical transformation matrix [42]. This generalized H and V to e_1 and e_2 (linear-to-elliptical) unitary transformation matrix $\mathbf{U}_{e,hv}$ is shown implemented on the orthogonal basis unit vectors as

$$\begin{bmatrix} \hat{e}_1 \\ \hat{e}_2 \end{bmatrix} = \mathbf{U}_{e,hv} \begin{bmatrix} \hat{h} \\ \hat{v} \end{bmatrix} \tag{2.70}$$

and is expanded as

$$\mathbf{U}_{e,hv} = \frac{1}{\sqrt{1 + \chi\chi^*}} \begin{bmatrix} e^{j\,\psi_1} & \chi\, e^{j\,\psi_1} \\ -\chi^*\, e^{j\,\psi_2} & e^{j\,\psi_2} \end{bmatrix} \tag{2.71}$$

where $[\,\cdot\,]^*$ denotes the complex conjugate, ψ_1 is the global phase shift added to the elliptical basis's first term, ψ_2 is the global phase shift added to the elliptical basis's second term , and χ is the complex polarization ratio, show below as

$$\chi \;=\; \frac{cos(\tau)\,sin(\psi) \;+\; j\,cos(\psi)\,sin(\tau)}{cos(\tau)\,cos(\psi) \;+\; j\,sin(\tau)\,sin(\psi)} \;=\; \frac{tan(\psi) \;+\; j\,tan(\tau)}{1 \;-\; j\,tan(\psi)\,tan(\tau)} \qquad (2.72)$$

where $\frac{-\pi}{2} \;\leq\; \psi \;\leq\; \frac{\pi}{2}$ is the angular offset (orientation angle) between the $\hat{H}$ axis and the major axis of the $\hat{e}_1$ ellipse, and $\frac{-\pi}{4} \;\leq\; \tau \;\leq\; \frac{\pi}{4}$ is the ellipticity angle, defined as the inverse tangent of the ratio of the ellipse minor to major axis. The ψ_1 and ψ_2 global phase shift terms affect the starting phase of each basis vector in the transformed basis, and while these values need to be chosen carefully if differential phases between different bases are to be compared, the recommended simplest values to use for consistency between results are $\psi_1 \;=\; \psi_2 \;=\; 0$ [42].

The transformation matrix $\mathbf{U}_{e,hv}$ as defined in Eq. 2.71 is unitary. It is important for the trasformation matrix to be unitary as a unitary transformation matrix preserves the inner product between two vectors as they are transformed between bases. This means that any polarization basis achieved through a unitary transformation from the H and V basis will also be orthonormal because the H and V basis is orthonormal. For a transformation matrix $\boldsymbol{\lambda}$ to be unitary (equivalent of orthogonal in the complex domain), $\boldsymbol{\lambda}^{\mathrm{H}} \;=\; \boldsymbol{\lambda}^{-1}$, therefore $\boldsymbol{\lambda}\,\boldsymbol{\lambda}^{\mathrm{H}} \;=\; I$, where I is the identity matrix and where $[\,\cdot\,]^{\mathrm{H}}$ denotes the transpose of the complex conjugate. Checking the generalized linear to elliptical transformation matrix $\mathbf{U}_{e,hv}$, it is shown that

$$\mathbf{U}_{e,hv}\,\mathbf{U}_{e,hv}^{\mathrm{H}} \;=\; \frac{1}{1\,+\,\chi\chi^{*}}\begin{bmatrix} e^{j\,\psi_1} & \chi\,e^{j\,\psi_1} \\ -\chi^{*}\,e^{j\,\psi_2} & e^{j\,\psi_2} \end{bmatrix}\begin{bmatrix} e^{-j\,\psi_1} & -\chi\,e^{-j\,\psi_2} \\ \chi^{*}\,e^{-j\,\psi_1} & e^{-j\,\psi_2} \end{bmatrix} =$$

$$= \frac{1}{1\,+\,\chi\chi^{*}}\begin{bmatrix} e^{0}\,+\,\chi\chi^{*}\,e^{0} & -\chi\,e^{j(\psi_1+\psi_2)}+\chi\,e^{j(\psi_1+\psi_2)} \\ -\chi^{*}\,e^{j(\psi_2-\psi_1)}\,+\,\chi^{*}\,e^{j(\psi_2-\psi_1)} & \chi\chi^{*}\,e^{0}\,+\,e^{0} \end{bmatrix} =$$

$$= \frac{1}{1\,+\,\chi\chi^{*}}\begin{bmatrix} 1\,+\,\chi\chi^{*} & 0 \\ 0 & \chi\chi^{*}\,+\,1 \end{bmatrix} = \begin{bmatrix} 1 & 0 \\ 0 & 1 \end{bmatrix} \quad (2.73)$$

which is expected with $\mathbf{U}_{e,hv}$ being a unitary matrix. Therefore, starting from the H and V orthonormal basis, any other orthonormal basis can be achieved by applying the applicable values of χ, ψ_1, and ψ_2 to the transform matrix $\mathbf{U}_{e,hv}$. Similarly, any orthonormal basis can be transformed back to the H and V basis by applying the applicable values of χ, ψ_1, and ψ_2 to $\mathbf{U}_{hv,e} = \mathbf{U}_{e,hv}^{\mathrm{T}}$. Therefore, any orthonormal basis can be transformed to any other orthonormal basis by the successive multiplication of two transforms (initial elliptical basis to H and V, then from H and V to final elliptical basis) as long as the applicable values of χ, ψ_1, and ψ_2 are known for both the initial basis and the final basis. This unitary basis transformation matrix approach also means that any modulating waveforms (amplitude and phase) known in any orthogonal basis can be converted to the appropriate modulating waveforms in any other orthogonal basis.

Using the unitary transformation matrix $\mathbf{U}_{e,hv}$ to obtain some example polarization bases from H and V may be beneficial, so five example cases are shown below.

For the unitary transformation matrix $\mathbf{U}_{hv,hv}$ from the linear H and V to linear H and V basis (no rotation), $\psi = 0$ and $\tau = 0$, giving $\chi = 0$. Setting the phase shifts $\psi_1 = \psi_2 = 0$, the basis transformation is shown as

$$\begin{bmatrix} \hat{l}_h \\ \hat{l}_v \end{bmatrix} = \mathbf{U}_{hv,hv} \begin{bmatrix} \hat{h} \\ \hat{v} \end{bmatrix} = \frac{1}{\sqrt{1 + \chi\chi^*}} \begin{bmatrix} e^{j\,\psi_1} & \chi\, e^{j\,\psi_1} \\ -\chi^*\, e^{j\,\psi_2} & e^{j\,\psi_2} \end{bmatrix} \begin{bmatrix} \hat{h} \\ \hat{v} \end{bmatrix} =$$
$$= \frac{1}{\sqrt{1 + 0}} \begin{bmatrix} e^0 & 0\, e^0 \\ -0\, e^0 & e^0 \end{bmatrix} \begin{bmatrix} \hat{h} \\ \hat{v} \end{bmatrix} = \begin{bmatrix} 1 & 0 \\ 0 & 1 \end{bmatrix} \begin{bmatrix} \hat{h} \\ \hat{v} \end{bmatrix} \quad (2.74)$$

This transformation matrix makes sense, as there should be no shift present, and appropriate values for χ, ψ_1, and ψ_2 result in the identity matrix. This basis transformation can be seen in Figure 2.30.

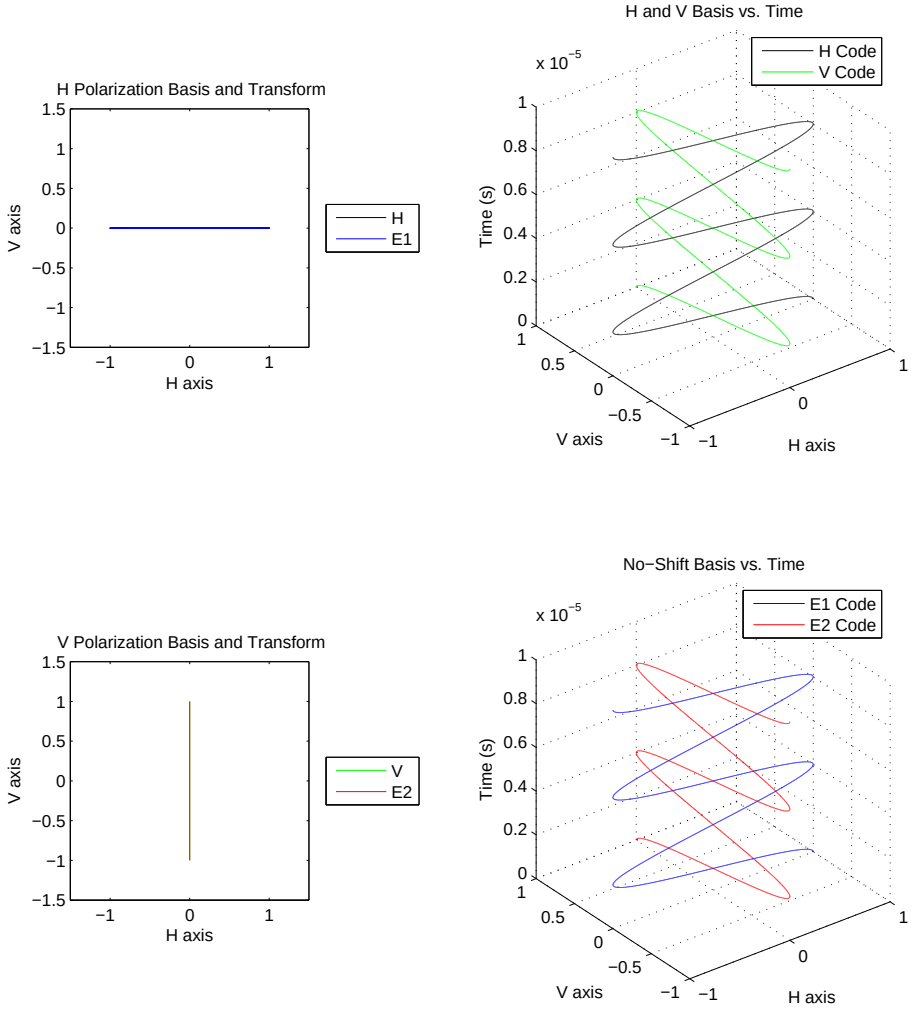


Figure 2.30: *Transformation from H and V Basis to H and V Basis*

For the unitary transformation matrix $\mathbf{U}_{45,hv}$ from the linear H and V to the linear slant 45 basis (rotation of $+45°$), $\psi = \frac{\pi}{4}$ and $\tau = 0$, giving $\chi = 1$. Setting the phase shifts $\psi_1 = \psi_2 = 0$, the basis transformation is shown as

$$\begin{bmatrix} \hat{l}_{+45} \\ \hat{l}_{-45} \end{bmatrix} = \mathbf{U}_{45,hv} \begin{bmatrix} \hat{h} \\ \hat{v} \end{bmatrix} = \frac{1}{\sqrt{1 + \chi\chi^*}} \begin{bmatrix} e^{j\,\psi_1} & \chi\, e^{j\,\psi_1} \\ -\chi^*\, e^{j\,\psi_2} & e^{j\,\psi_2} \end{bmatrix} \begin{bmatrix} \hat{h} \\ \hat{v} \end{bmatrix} =$$
$$= \frac{1}{\sqrt{1 + 1}} \begin{bmatrix} e^0 & 1\, e^0 \\ -1\, e^0 & e^0 \end{bmatrix} \begin{bmatrix} \hat{h} \\ \hat{v} \end{bmatrix} = \frac{1}{\sqrt{2}} \begin{bmatrix} 1 & 1 \\ -1 & 1 \end{bmatrix} \begin{bmatrix} \hat{h} \\ \hat{v} \end{bmatrix} \quad (2.75)$$

This transformation matrix makes sense, as the new basis should be a combination of equally weighted, equally phase shifted (zero phase shift selected) linear vectors, and appropriate values for χ, ψ_1, and ψ_2 result in a summation and difference of the original H and V basis. This basis transformation can be seen in Figure 2.31.

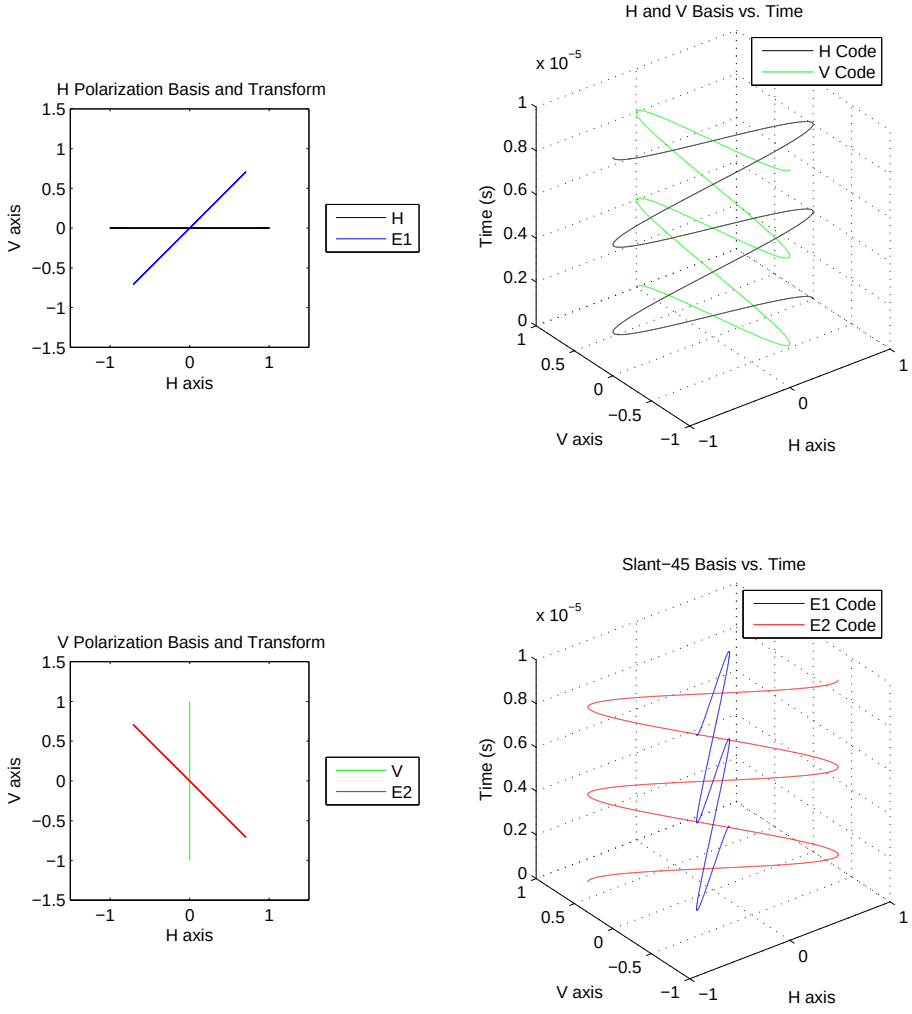


Figure 2.31: *Transformation from H and V Basis to Slant-45 Basis*

For the unitary transformation matrix $\mathbf{U}_{circ,hv}$ from the linear H and V to circular basis (right-hand circular and left-hand circular), $\psi = 0$ and $\tau = \frac{\pi}{4}$, giving $\chi = j$. Setting the phase shifts $\psi_1 = \psi_2 = 0$, the basis transformation is shown as

$$\begin{bmatrix} \hat{e}_{r,circ} \\ \hat{e}_{l,circ} \end{bmatrix} = \mathbf{U}_{circ,hv} \begin{bmatrix} \hat{h} \\ \hat{v} \end{bmatrix} = \frac{1}{\sqrt{1 + \chi\chi^*}} \begin{bmatrix} e^{j\,\psi_1} & \chi\, e^{j\,\psi_1} \\ -\chi^*\, e^{j\,\psi_2} & e^{j\,\psi_2} \end{bmatrix} \begin{bmatrix} \hat{h} \\ \hat{v} \end{bmatrix} =$$

$$= \frac{1}{\sqrt{1 + j(-j)}} \begin{bmatrix} e^0 & j\, e^0 \\ -(-j)\, e^0 & e^0 \end{bmatrix} \begin{bmatrix} \hat{h} \\ \hat{v} \end{bmatrix} = \frac{1}{\sqrt{2}} \begin{bmatrix} 1 & j \\ j & 1 \end{bmatrix} \begin{bmatrix} \hat{h} \\ \hat{v} \end{bmatrix} \quad (2.76)$$

This transformation matrix makes sense, as the new basis should be a combination of the equally weighted linear vectors where there is an equal magnitude opposite direction phase difference imparted between the two components. This basis transformation can be seen in Figure 2.32. It should be noted that by choosing $\psi_1 = \psi_2 = 0$ the right-circular base vector aligns with the H axis at time zero, and the left-circular base vector aligns with the V axis at time zero. Other slightly different H and V to circular unitary transformation matrices exist, but these only vary the starting position of the two circular basis vectors [42].

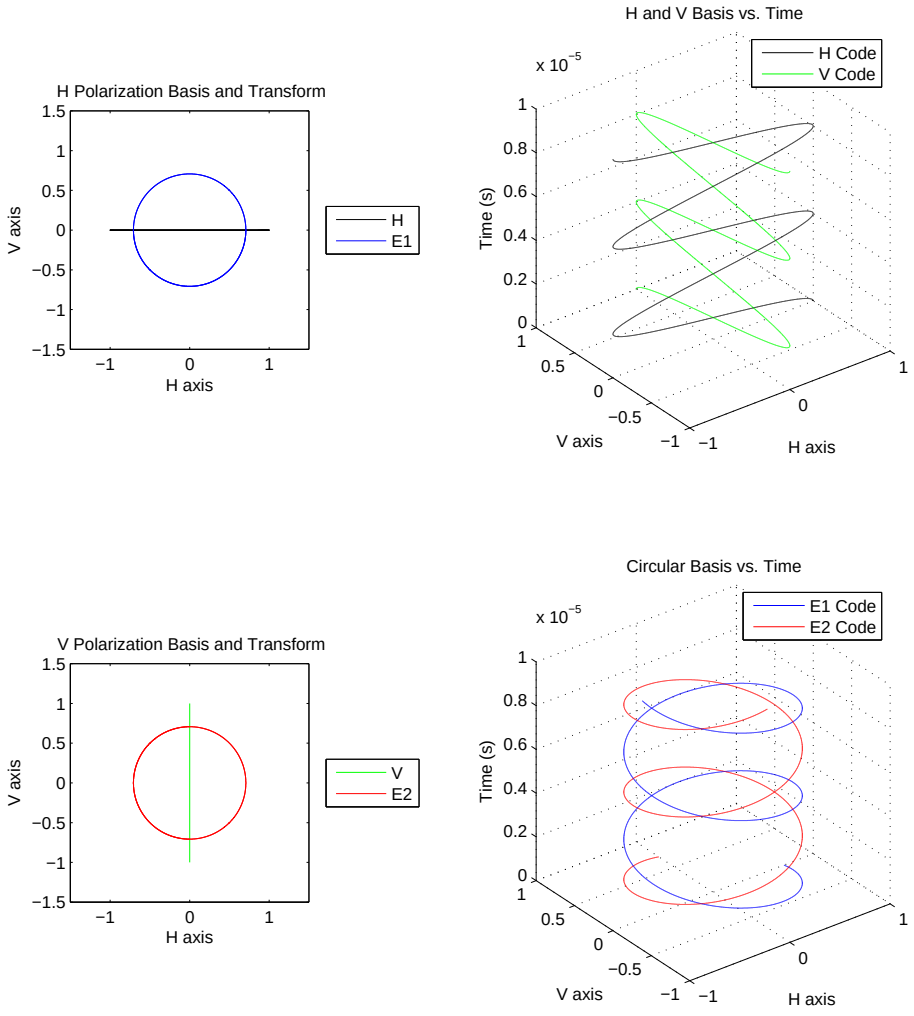


Figure 2.32: *Transformation from H and V Basis to Circular Basis*

For the unitary transformation matrix $\mathbf{U}_{ehv,hv}$ from the linear H and V to elliptical basis where the major axis of the two elliptical vectors are aligned with the original H and V basis (no major axis rotation) and the major axis has twice the magnitude of the minor axis, $\psi = 0$ and $\tau = tan(0.5) = 0.546$, giving $\chi = 0.608j$. Setting the phase shifts $\psi_1 = \psi_2 = 0$, the basis transformation is shown as

$$\begin{bmatrix} \hat{e}_h \\ \hat{e}_v \end{bmatrix} = \mathbf{U}_{ehv,hv} \begin{bmatrix} \hat{h} \\ \hat{v} \end{bmatrix} = \frac{1}{\sqrt{1 + \chi\chi^*}} \begin{bmatrix} e^{j\,\psi_1} & \chi\, e^{j\,\psi_1} \\ -\chi^*\, e^{j\,\psi_2} & e^{j\,\psi_2} \end{bmatrix} \begin{bmatrix} \hat{h} \\ \hat{v} \end{bmatrix} =$$

$$= \frac{1}{\sqrt{1 + (0.608j)(-0.608j)}} \begin{bmatrix} e^0 & 0.608j\, e^0 \\ -(-0.608j)\, e^0 & e^0 \end{bmatrix} \begin{bmatrix} \hat{h} \\ \hat{v} \end{bmatrix} =$$

$$= 0.73 \begin{bmatrix} 1 & 0.608j \\ 0.608j & 1 \end{bmatrix} \begin{bmatrix} \hat{h} \\ \hat{v} \end{bmatrix} \quad (2.77)$$

This transformation matrix makes sense, as the new basis should be a combination of the phase shifted unequally weighted linear vectors where there is an equal magnitude opposite direction phase difference imparted between the two components. This basis transformation can be seen in Figure 2.33.

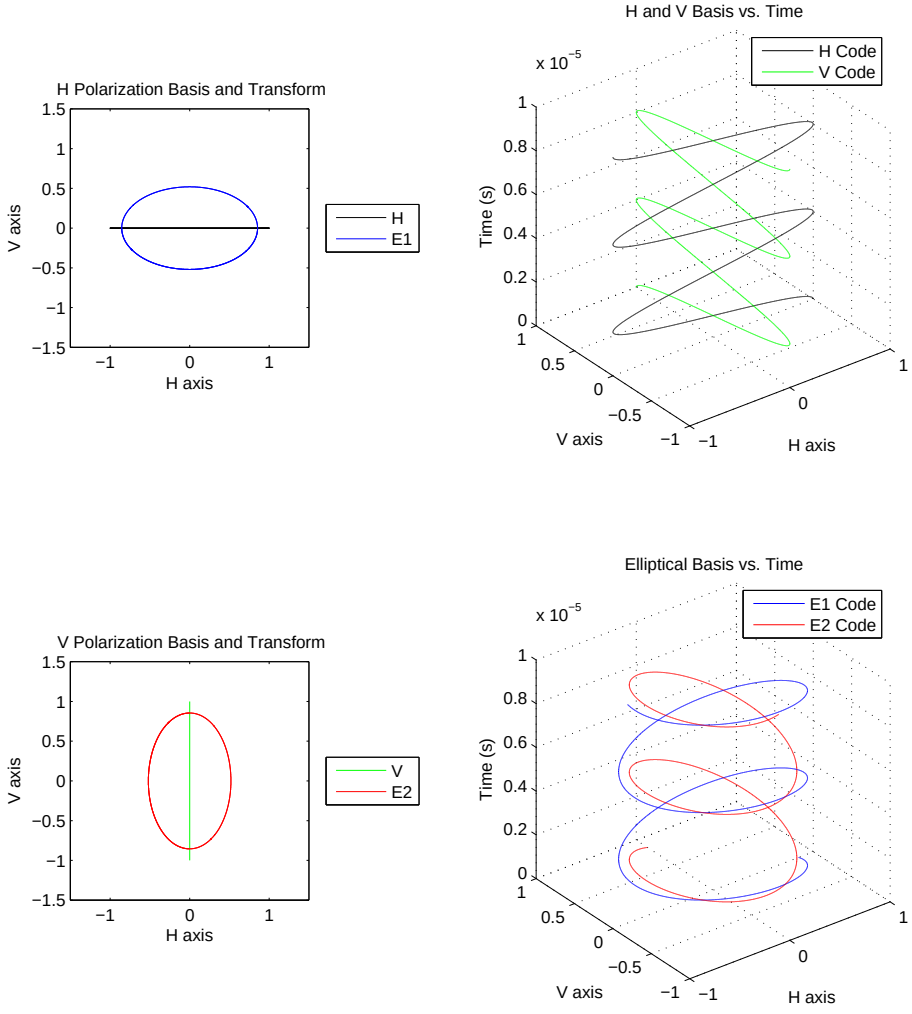


Figure 2.33: *Transformation from H and V Basis to Elliptical Basis*

For the unitary transformation matrix $\mathbf{U}_{e45,hv}$ from the linear H and V to elliptical basis where the major axis of the two elliptical vectors are aligned with a slant 45 basis (a $+45°$ major axis rotation) and the major axis has 1.618 times the magnitude of the minor axis, $\psi = \frac{\pi}{4}$ and $\tau = tan(\frac{1}{1.618}) = 0.711$, giving $\chi = 0.149 + 0.989j$ (Note for this case that $|\chi| = 1$). Setting the phase shifts $\psi_1 = \psi_2 = 0$, the basis transformation is shown as

$$\begin{bmatrix} \hat{e}_{+45} \\ \hat{e}_{-45} \end{bmatrix} = \mathbf{U}_{e45,hv} \begin{bmatrix} \hat{h} \\ \hat{v} \end{bmatrix} = \frac{1}{\sqrt{1 + \chi\chi^*}} \begin{bmatrix} e^{j\,\psi_1} & \chi\, e^{j\,\psi_1} \\ -\chi^*\, e^{j\,\psi_2} & e^{j\,\psi_2} \end{bmatrix} \begin{bmatrix} \hat{h} \\ \hat{v} \end{bmatrix} =$$

$$= \frac{1}{\sqrt{1 + (0.149 + 0.989j)(0.149 - 0.989j)}} \times$$

$$\times \begin{bmatrix} e^0 & (0.149 + 0.989j)\, e^0 \\ -(0.149 - 0.989j)\, e^0 & e^0 \end{bmatrix} \begin{bmatrix} \hat{h} \\ \hat{v} \end{bmatrix} =$$

$$= \frac{1}{\sqrt{2}} \begin{bmatrix} 1 & 0.149 + 0.989j \\ -0.149 + 0.989j & 1 \end{bmatrix} \begin{bmatrix} \hat{h} \\ \hat{v} \end{bmatrix} \quad (2.78)$$

This transformation matrix makes sense, as the new basis should be a combination of both phase shifted and non-phase shifted unequally weighted linear vectors where there is an equal magnitude opposite direction phase difference imparted between the two phase shifted components and the sum and difference of the non-phase shifted components in the new basis vectors. In addition it makes sense that there is equal magnitude contribution from each H and V basis vector ($|\chi| = 1$) in the creation of the new basis because $\psi = \frac{\pi}{4}$. This basis transformation can be seen in Figure 2.34.

The above examples were chosen to highlight the general use of $\mathbf{U}_{e,hv}$ to obtain some commonly used (and not-so-commonly used) basis transformations.

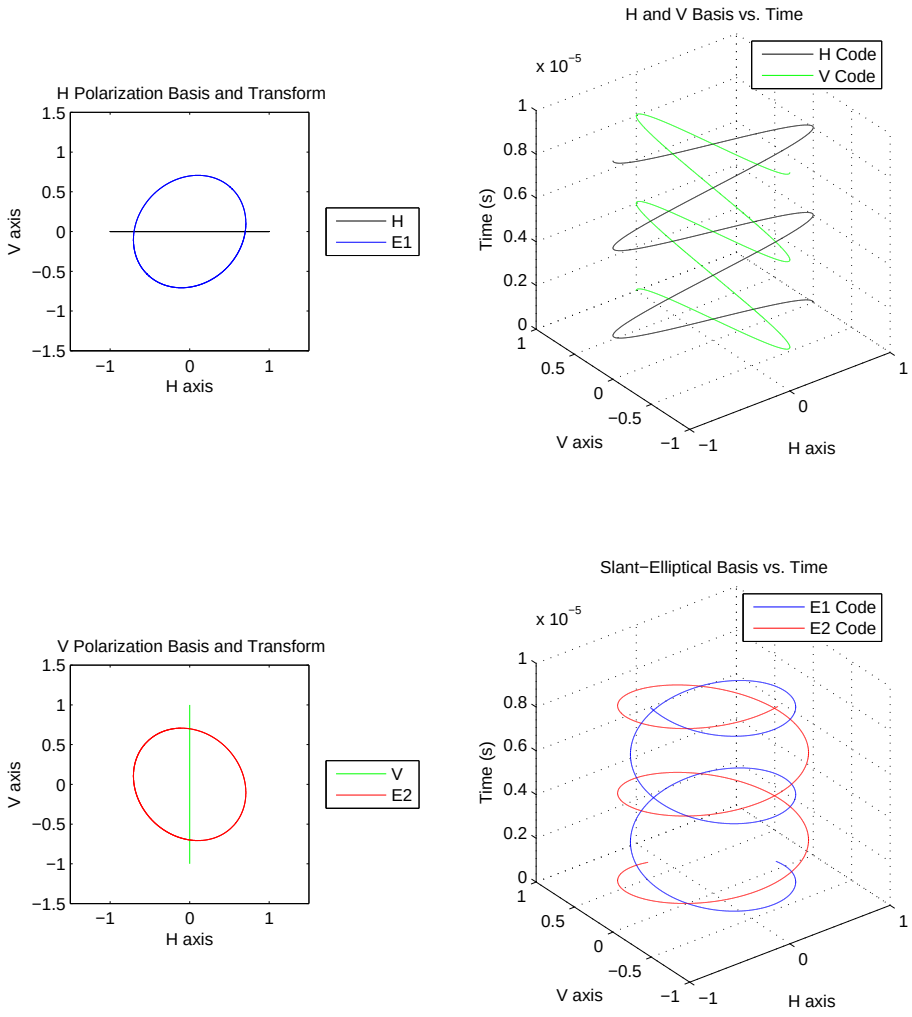


Figure 2.34: *Transformation from H and V Basis to Slant-Elliptical Basis*

Other transformations of vectors to (from) elliptical basis from (to) the H and V basis can be accomplished by using the unitary transformation matrix $\mathbf{U}_{e,hv}$ ($\mathbf{U}_{e,hv}^{\mathrm{T}}$ for elliptical to H and V) given in Eq. 2.71 with the appropriate values of χ, ψ_1, and ψ_2 for the ending (starting) basis.

2.10 Conclusion

In conclusion, from a scientific perspective, the high resolution measurement of a target's range and velocity and the simultaneous formation of the four-element polarimetric scattering matrix is desirable. This chapter established the mathematical basis for dual-polarimetric radar operation in a simultaneous transmit and simultaneous receive operational mode and demonstrated the importance of maintaining orthogonality in both polarization and in pulse compression waveform coding. Common pulse compression waveforms were analyzed for application in pseudo-orthogonal waveform sets before presenting a novel method for generating pseudo-orthogonal waveform sets utilizing particle swarm optimization. In the next two chapters, novel methods of digital predistortion are presented to force the chosen waveform for a given radar system to be linearly physically generated, ensuring that the measured results from the radar system will as closely match the desired theoretical performance as possible.

Chapter 3

Modeling and Digital Predistortion of Broadband Solid-State High Power Amplifiers

3.1 Introduction

As described and shown in the previous chapter, fully polarimetric radar operation with simultaneous transmit and simultaneous receive on both orthogonal polarizations is the preferred operation mode to gain the most scientifically valuable data capable of measuring the full polarimetric backscattering properties of the target area. The research contained in this dissertation is conducted in support of the NASA EcoSAR project, a proposed P-band digital beamforming polarimetric single pass interferometric synthetic aperture radar (SAR) testbed system that will be capable of wideband fully polarimetric simultaneous transmit and simultaneous receive operation. In order to support a wide range of advanced phased array techniques, such as wideband beamforming utilizing non-constant modulus waveforms, the EcoSAR employs a powerful and advanced architecture with an independent arbitrary waveform generator, analog to digital converter, and high power amplifier (HPA) for every antenna element in the system. It should be noted that this chapter

closely follows the work presented by the author in [43] © 2016 IEEE.

Increasingly stringent regulations on bandwidth allocation and management are at odds with growing expectations of future radar system capabilities [44], [45]. In radar systems such as EcoSAR utilizing coded waveforms with wide instantaneous bandwidths, the fidelity of the transmitted signal is crucial to the ultimate fidelity of the analyzed results of the received signal as well as the amount of spectral leakage present in the transmitted signal. With this in mind, the transmit chain of a radar system, specifically the main HPA, must be fully characterized so that the final transmitted waveform can be known relative to the desired output waveform. However, physical HPAs exhibit non-linear behavior over their input power range, which becomes more extreme as the amplifier nears its compression region where the power added efficiency of the amplifier is maximized [12]–[14]. In addition, this non-linear behavior also varies as a function of input frequency. As a result, HPA modeling can take several forms. The Volterra series is a convenient and "compact" mathematical model that is capable of modeling systems with both non-linear behavior and memory effects [46]–[51]. Non-linear variations over frequency can be viewed, and thus modeled, as a result of memory effects. With certain assumptions about the system to be modeled, even more compact forms of the Volterra model can be applied. One of these such models, convenient for use with non-linear and memory dependent systems with complex input and output data, is the memory polynomial (MP) model. Utilizing the MP model, it is possible to accurately model non-linear behavior and non-linear variation across input frequency.

While knowledge of the actual, distorted output waveform is useful in and of itself, it would be better to use this knowledge to alter the input waveform so that the final distorted output waveform is equal to the desired waveform. The inversion of the HPA model for the purpose of linearizing and equalizing the total system is known generically as predistortion [52]. Digital alteration of an input signal so that the output distorted signal of a system equals the true desired signal is known as digital predistortion (DPD). The model governing DPD for a given radar transmit chain is matched to each individual HPA. Seeing that the DPD must be a non-linear function of input power and input frequency, DPD can also be modeled with the MP model. DPD allows a given amplifier to output signals that appear to be linearly amplified with minimal distortion, even while the amplifier is operated in its compression region, thus maximizing power added efficiency and significantly reducing spectral regrowth.

Recent advancements in the fields of solid-state amplifiers have led to the practical implementation of the active array architecture [3]–[6], [53], [54] This is in contrast to traditional passive array architecture, where all of the antenna's elements are connected to one power amplifier. Therefore, with each antenna element having its own HPA, maximizing the utility and output of HPAs on an element-by-element basis is crucial to maximizing the capability of the overall wideband radar system. Digital predistortion would be ideal for use in this type of architecture, as allowing each amplifier to operate in its compression region without spectral spreading or distortion of the output waveform leads to the maximization of each amplifier's power added efficiency. This also allows the amplifier to give similar output characteristics of a larger amplifier

for waveforms requiring linear amplification. By utilizing smaller amplifiers to their full potential, the benefits of lower cost, lower weight, smaller hardware footprint, easier heat management, smaller and less expensive power supplies, and other associated hardware is quickly recognized. When these benefits are multiplied over the number of antenna elements and transmit chains in a given radar system, it can be seen that DPD can have a tremendous effect on the utility of the overall radar system without making drastic and expensive changes to the system's hardware to achieve similar performance.

While digital predistortion has been utilized in communication systems, as in [55]–[57], it does not have widespread use in radar applications. Whereas adaptive predistortion of unpredictable and constantly changing waveforms is not generally needed in radar systems, DPD in radar applications must apply over a much larger bandwidth at higher power levels in addition to complying with mandated lower sideband suppression than is common in communication systems [2]. This is especially true for wideband radar systems, such as EcoSAR. Radar systems typically have a finite number of waveforms to be used during operation, and the waveform to be transmitted is usually known prior to transmission. As a result, adaptive predistortion is not needed at every transmit pulse. Instead, the predistorted version of the input waveforms can be saved into memory to be played out during operation. The desired waveform is produced at the output of the amplifier even though this step only requires the same amount of computational power as playing the non-predistorted waveform from memory. With this in mind, it can be seen that while conservative implementation of DPD on an active phased array radar requires digital waveform creation, it does not require significant excess computational power. This

makes it attractive for modern and emerging architectures in environments where precise spectral usage is required [58], particularly for systems that can utilize non-constant modulus waveforms with broad instantaneous bandwidth, such as MIMO radar systems, Low-Probability of Intercept (LPI) radars, and SAR systems similar to EcoSAR utilizing wideband beamforming. An example of a non-constant modulus waveform for use in a wideband beamforming algorithm proposed by [7] is shown in Figure 3.1.

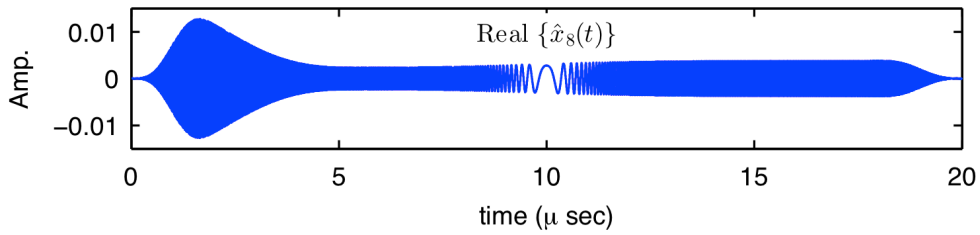


Figure 3.1: *Example of Non-Constant Modulus Waveform Single Channel Output of Wideband Beamforming Algorithm As Shown In [7], Reprinted from Dunn et al. (2016) © 2016 IEEE*

3.2 Technical Approach to Modeling Amplifier and Predistorter

3.2.1 Conceptual Approach to Digital Predistortion

As was previously stated, predistortion is effectively the inversion of a nonlinear HPA model for the purpose of linearizing the output power versus input power relation for the total system. To get a better understanding of what predistortion is actually doing, visual examples will be helpful. Output power versus input power graphs of simulated well-behaved narrowband and

measured wideband amplifier data with overlayed ideal outputs are shown in Figure 3.2 and Figure 3.3 respectively.

At its core, predistortion is essentially remapping a given input signal to a different input signal so that when altered by the HPA's non-linear distortion the desired ideal output signal is the result. This ideal output signal has a linear output power versus input power relation with a gain that matches the gain of the linear region of the measured amplifier, as well as a uniformly flat group delay response. Consider the simulated narrowband (i.e., single frequency) output power versus input power graph as shown in Figure 3.2. Predistortion effectively takes the ideal output power versus input power relationship and carefully and intentionally rescales the input power so that the new output power versus input power relationship matches the measured non-linear output power versus input power relationship of the amplifier. This process is relatively simple for the narrowband case, as for each ideal output power level, the same measured output power level corresponds with only one measured input power level. The non-linear equation that determines the particular horizontal stretch for a given input power is the predistortion model. Note that the maximum output power of the ideal signal is equal to the maximum output power of the measured signal. This means that the ideal input signal to be predistorted must have an upper power limit corresponding with the power that gives the maximum output power of the measured signal when the gain of the ideal output power versus input power relation is applied.

However, determining the predistortion model for a given amplifier is more complicated than it first appears due to the possibility of variation in non-linear

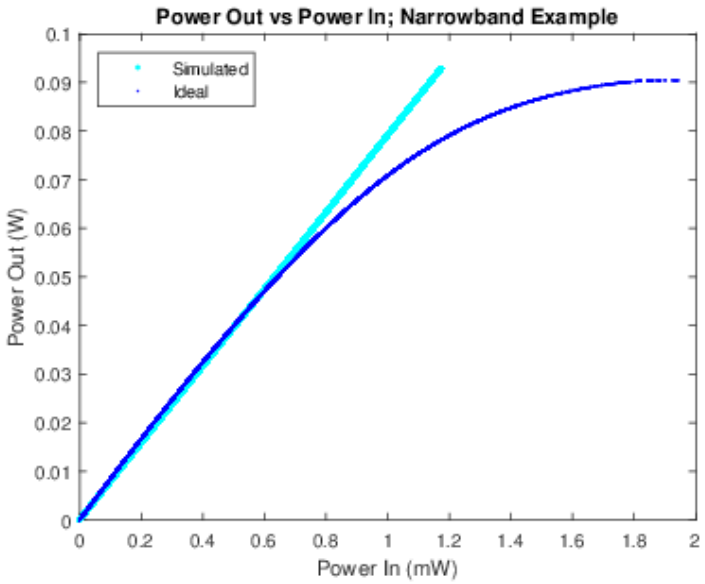


Figure 3.2: *Example of Power Out vs. Power In of Well-Behaved Narrowband and Ideal Amplified Signals, Reprinted from Dunn et al. (2016)* © *2016 IEEE*

behavior of the HPA over input frequency. The effect of this frequency dependence is readily apparent in the measured wideband case (40 MHz bandwidth), and can be seen in Figure 3.3 in the vertical width of the measured samples range for a given input power. The overall shape of the output power versus input power response samples can be thought of as the overlap of samples from numerous power sweeps at constant frequencies ranging the calibration data passband (this is not the case, but it is helpful to think of it this way for this example). Again, predistortion effectively takes the ideal input signal and rescales it so that the output power versus input power relationship matches the measured non-linear output power versus input power relationship of the amplifier. However, due to the wideband nature of the input signal and the frequency dependence of the amplifier, there is a measured input power level range that corresponds with any desired ideal output power level. The input power level range for a single output power is composed of a single sample

from each of the power sweeps at different frequencies. In order to map the ideal input signal to the correct measured input signal, the "instantaneous" frequency of the ideal input signal must be known. If frequency-based effects were ignored, the vertical width of the predistorted amplified signal would be largely unchanged from that of the measured samples. Note that in the wideband case, the maximum output power of the ideal signal is equal to the maximum vertical lower bound of the measured signal, which corresponds with the "worst-case" maximum power for all frequencies present in the signal. This ensures that the ideal output signal is possible to produce given the frequency effects present in the system. Furthermore, due to the fact that for a given ideal input signal sample at a given frequency there is only one correct measured input signal to which that point can be mapped, it is implied that the measured signal data from which the specific predistortion relation and model is derived must have a output power versus input power relation that is monotonically increasing.

It was previously stated that non-linear variations over frequency can be viewed, and thus modeled, as a result of memory effects. In the equations used to model both the non-linear distortion of the amplifier as well as the equations used to model the non-linear distortion of the predistorter, memory terms are simply terms of the causal polynomial that are functions of one or more delayed input signal samples. The presence of memory terms in a model's polynomial establishes effects within the output signal that are dependent upon the relation between input samples at fixed time interval differences (i.e., intervals of the sampling rate). The relation between input samples at fixed time interval differences can be interpreted as being frequency related,

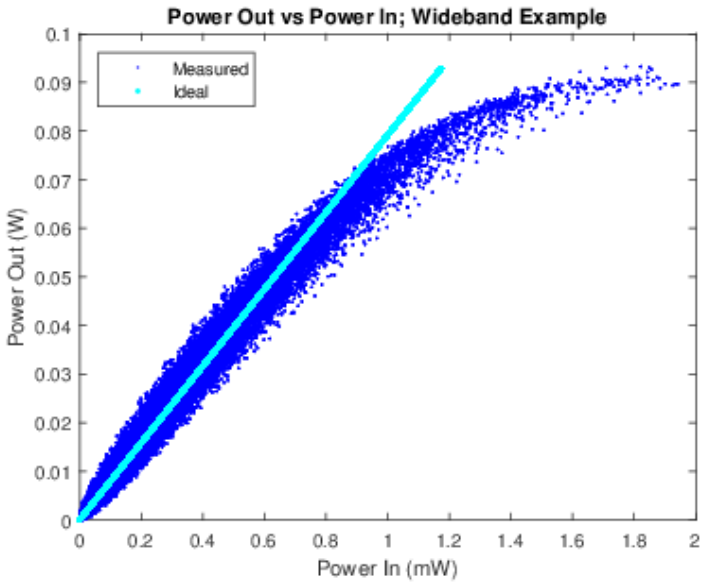


Figure 3.3: *Example of Power Out vs. Power In of Measured Wideband and Ideal Amplified Signals, Reprinted from Dunn et al. (2016) © 2016 IEEE*

and thus the introduction of memory terms allows frequency based effects to be reliably modeled.

3.2.2 Volterra Series and MP Model

The Volterra series is useful for modeling systems with both non-linearities and memory effects, and it is ideal for modeling the output of HPAs and their associated predistortion models. The general form of the discrete Volterra series is given by

$$y_V(n) = \sum_{k=1}^{K} y_k(n) \tag{3.1}$$

where

$$y_k(n) = \sum_{m_1}^{M-1} \cdots \sum_{m_k}^{M-1} h_k(m_1, \ldots, m_k) \prod_{l=1}^{k} x(n - m_l) \tag{3.2}$$

where $y_V(n)$ is the output sample, $x(n)$ is the input sample, K is the order of non-linearity of the system, M is the order of memory of the system, and $h_k(m_1, \ldots, m_k)$ is a coefficient with set values as a function of k and m_1 through m_k. The general form of the Volterra series is capable of modeling non-linear systems with memory effects due to the extensive number of coefficients paired with every combination of input sample and delayed input sample combinations within the bounds of the specified non-linear order and memory order of the model. The general form of the Volterra series is therefore able to model systems with both large non-linearities and significant memory effects, and higher precision and more accurate modeling can be provided by simply raising the non-linear and memory orders of the model. However, the number of coefficients, and thus computational complexity in calculating the coefficients, increases at a substantial rate as either the non-linear order or the memory order of the model is increased. With this in mind, many simplifications of the full Volterra model, with less coefficients and reduced complexity of calculation, have been devised and studied [59]–[61]. One of these simplified Volterra based models that has had previous success modeling physical amplifiers at complex baseband is the Memory Polynomial model [59], [62]–[65]. The MP model is given by

$$y(n) = \sum_{k=0}^{K-1} \sum_{m=0}^{M-1} h_{km} x(n - m)|x(n - m)|^k \tag{3.3}$$

where $y(n)$ is the output sample, $x(n)$ is the input sample, K is the order of non-linearity of the system, M is the order of memory of the system, and h_{km}

is a coefficient with set values as a function of k and m.

Due to the MP model being linear with respect to the coefficients, it can be represented efficiently in matrix form. This applies both to the amplifier model and its associated predistortion function. These matrix representations readily allow the coefficients to be determined for either case by using a set of measured input and output data, as detailed herein. Because the MP model is fundamentally composed of a summation of coefficients that are each paired with delayed powers of the input waveform, it can be represented efficiently in matrix form as $\mathbf{y} = \mathbf{X}\boldsymbol{\theta}_{MP}$. This matrix representation can be expanded to be shown as

$$\mathbf{y} = \begin{bmatrix} y(M) \\ \vdots \\ y(N) \end{bmatrix} = \mathbf{X} \begin{bmatrix} h_{00} \\ \vdots \\ h_{0m} \\ \vdots \\ h_{k0} \\ \vdots \\ h_{km} \end{bmatrix} \tag{3.4}$$

where the matrix $\mathbf{X} =$

$$\begin{bmatrix} x(M) \cdots & x(1) & \cdots & x(M)|x(M)|^k & \cdots & x(1)|x(1)|^k \\ \vdots & \vdots & & \vdots & & \vdots \\ x(N) \cdots & x(N-M+1) \cdots & x(N-M+1)|x(N-M+1)^k \cdots & & & x(N-M+1)|x(N-M+1)|^k \end{bmatrix}$$

where $\mathbf{X}$ is an $[A \times B]$ matrix called the delay matrix, $\mathbf{y}$ is an $[A \times 1]$ col-

umn vector containing the calculated outputs of the MP model, and $\boldsymbol{\theta}_{MP}$ is a $[B \times 1]$ column vector containing all the coefficients h_{km}. It should be noted that N is equal to the length of the input vector $\mathbf{x}$, B is equal to the number of coefficients for a given non-linear order and memory order of the MP model, while $A = N - (M - 1)$, which ensures that any generated output in $\mathbf{y}$ was calculated with populated values for the necessary delayed input terms. The delay matrix is composed of the varying combinations of input terms that are both delayed and not delayed associated with the B coefficients for each of the A output samples to be created. This means that the delay matrix can be created given only the input sample array and the order of non-linearity and memory order of the MP model to be used. The $[B \times 1]$ model coefficient column vector $\boldsymbol{\theta}_{MP}$ contains the unknown coefficients h_{km} that collectively capture HPA behavior over the power and frequency ranges of interest. High fidelity measurements of the amplifier output, excited by a strategically chosen and well known input signal, are required to estimate the coefficients in $\boldsymbol{\theta}_{MP}$. This pair of data is known as the calibration data, and it should be chosen so that the input signal excites across the entire bandwidth and power ranges over which the amplifier is to be modeled [66]. A good way to capture as much of the non-linearity effects and memory effects as possible is to generate a random signal spanning the desired power range before filtering the signal to the desired bandwidth. This random signal approach creates many combinations of input power and frequencies that help to excite the amplifier in as many different states as possible, leading to more behavior of the amplifier being recorded. As a result, when using the frequency filtered random signal approach to generating calibration data, the longer the signal is in time, the better the system will be characterized. With this in mind it is

useful to choose calibration data containing a large number of sample points, although the length of the calibration input signal is practically limited by the computational power needed to analyze the calibration data when calculating the MP model coefficients. Once a suitable calibration dataset is acquired for an HPA and the order of non-linearity and order of memory for the MP model is chosen, the coefficient column vector $\boldsymbol{\theta}_{MP}$ can be calculated. This is accomplished by minimizing the squared error with respect to the coefficient vector, where the error is defined as the difference between the calculated calibration output samples and the measured calibration output samples. This least-squares minimization problem is shown as

$$\begin{aligned} &\min_{\boldsymbol{\theta}_{MP}} \|\mathbf{y}_{cal} - \mathbf{X}_{cal}\boldsymbol{\theta}_{MP}\|^2 = \\ &= \min_{\boldsymbol{\theta}_{MP}} \left[\mathbf{y}_{cal}^{\mathrm{H}}\mathbf{y}_{cal} - \mathbf{y}_{cal}^{\mathrm{H}}\mathbf{X}_{cal}\boldsymbol{\theta}_{MP} - \boldsymbol{\theta}_{MP}^{\mathrm{H}}\,\mathbf{X}_{cal}^{\mathrm{H}}\mathbf{y}_{cal} + \boldsymbol{\theta}_{MP}^{\mathrm{H}}\mathbf{X}_{cal}^{\mathrm{H}}\mathbf{X}_{cal}\boldsymbol{\theta}_{MP}\right] \end{aligned} \quad (3.5)$$

where $\mathbf{y}_{cal}$ is the measured output signal column vector of the calibration data, $\mathbf{X}_{cal}$ is the delay matrix formed by the calibration data input signal $\mathbf{x}_{cal}$, and $[\,]^{\mathrm{H}}$ is the complex conjugate transpose operator. Setting the derivative of (3.5) equal to zero and solving for $\boldsymbol{\theta}_{MP}$ yields the least-squares solution, shown as

$$\boldsymbol{\theta}_{MP} = (\mathbf{X}_{cal}^{\mathrm{H}}\mathbf{X}_{cal})^{-1}\mathbf{X}_{cal}^{\mathrm{H}}\mathbf{y}_{cal}. \quad (3.6)$$

This well known solution is referred to as the Moore-Penrose pseudoinverse [67], [68]. See Appendix A for a more complete solution. Once the coefficients of the MP model have been found, if an adequate order of non-linearity and order of memory were selected, and the range of input power levels and range of frequencies present in an input signal array fall within those represented by the calibration data input signal, then the realistic output of the HPA can

be simulated. It should be noted that if $\boldsymbol{\theta}_{MP}$ remains unchanged throughout simulations following calibration, the method used to assemble the calibration data delay matrix given the calibration data's input signal should be used to assemble all future delay matrices given a desired input signal. This will ensure that the MP model coefficients for the given model are always correctly paired with their associated delayed and non-delayed input signal combinations.

It is desired not only to create a realistic model of a HPA, but also a model of an associated predistortion function that can be used in conjunction with the HPA to create an overall linearly behaving system. More specifically, when the DPD is paired with the HPA, the desired signal input into the DPD will be reproduced at the output of the HPA multiplied only by the gain corresponding with the linear region of the HPA. Therefore, the model of the DPD is basically an inverse of the model of the HPA. Due to the HPA exhibiting both non-linearities and memory effects, the DPD will need to account for both non-linearities and memory effects. However, because the HPA is successfully modeled by the MP model, this also means that the HPA's associated DPD can also be successfully modeled using the MP model, given by $\mathbf{y} = \mathbf{X}\boldsymbol{\theta}_{PD}$, where $\mathbf{y}$ is the DPD output signal column vector, $\mathbf{X}$ is the delay matrix formed by the DPD input signal, and $\boldsymbol{\theta}_{PD}$ is a column vector containing all the MP model coefficients of the DPD. The order of non-linearity and order of memory for the DPD may differ from the order of non-linearity and order of memory used in the model of the HPA. The coefficients of the MP model for the DPD can be calculated similarly to the method used to find $\boldsymbol{\theta}_{MP}$ using the Moore-Penrose pseudoinverse and a set of calibration data. In order to calculate the values of the coefficient column vector $\boldsymbol{\theta}_{PD}$ so that the DPD will be a match

with the given amplifier, the same set of calibration data is used, but it is scaled and used in reverse order. The calibration data input signal column vector $\mathbf{x}_{cal}$ remains unscaled, but the calibration data output signal $\mathbf{y}_{cal}$ is rescaled so that the maximum magnitude equals the magnitude that when multiplied by the HPA's linear region gain equals the maximum magnitude of the measured calibration data input signal. The Moore-Penrose pseudoinverse is executed and the coefficient column vector $\boldsymbol{\theta}_{PD}$ is found by

$$\boldsymbol{\theta}_{PD} = (\mathbf{Y}_{cal}^{\mathrm{H}}\mathbf{Y}_{cal})^{-1}\mathbf{Y}_{cal}^{\mathrm{H}}\mathbf{x}_{cal} \tag{3.7}$$

where $\mathbf{Y}_{cal}$ is the delay matrix formed by the rescaled calibration data output signal $\mathbf{y}_{cal}$. Once the coefficients of the MP model for the DPD have been found, if an adequate order of non-linearity and order of memory were selected, and the range of input power levels and range of frequencies present in the input signal array fall within those allowed by the calibration data, then the necessary predistorted signal can be simulated. It should be noted that the allowed range of frequencies for the input signal is equal to the range of frequencies represented by the calibration data. However the allowed range of amplitudes is limited by the maximum magnitude of the rescaled calibration data output signal $\mathbf{y}_{cal}$ that was used to solve for $\boldsymbol{\theta}_{PD}$, which was previously decided to be the magnitude that, when multiplied by the HPA's linear region gain, equals the maximum magnitude of the calibration data input signal. It should also be noted that in the way the DPD coefficient column vector $\boldsymbol{\theta}_{PD}$ was found, these coefficients are actually the necessary coefficients for a MP model post-inverse filter. However, due to the inherent quality of the Volterra series that the p^{th} order post-inverse of a Volterra series is equal to the p^{th} order pre-inverse of a Volterra series, the coefficients found for the post-inverse

model can be used as the coefficients of a pre-inverse model instead [69]. Therefore, by using two different realizations of the MP model simplification of the Volterra series and a single set of calibration data, it is possible to not only successfully model the output of a HPA given an input signal, but it is also possible to find the necessary DPD model that, when used in series with the HPA, will make the overall transmit chain behave as a linear system.

In summary, the DPD process requires a measured set of calibration data with a known linear region, pre-defined orders of non-linearity and memory for both the amplifier and DPD models, and a desired input signal. The DPD process results in the creation of the amplifier and DPD model coefficients, predistorted input waveform, simulated predistorted amplified output waveform, and the measured predistorted amplified output waveform. This process is visually summarized in Figure 3.4.

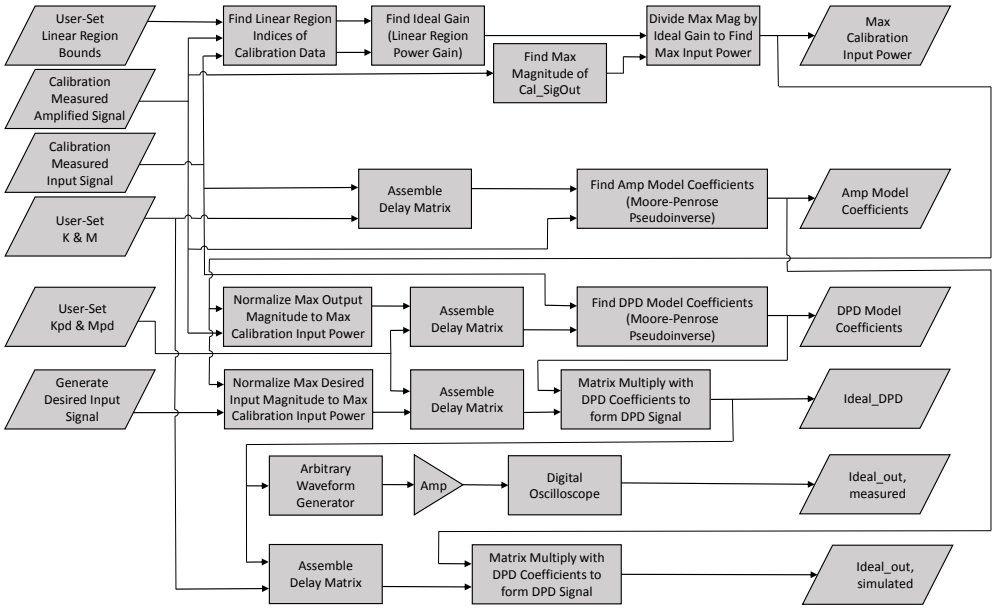


Figure 3.4: *Flow Chart Summary of Digital Predistortion Process, Reprinted from Dunn et al. (2016) © 2016 IEEE*

3.2.3 Weighting for Numerical Stability of Least-Squares Model Solution

When the specified order of non-linearity of the HPA or DPD model is large, numerical instabilities can begin to arise when solving for the model coefficients by executing the Moore-Penrose pseudoinverse. While other approaches have been proposed to make the pseudoinverse more numerically stable for large order polynomials by modifying the MP model itself [70], it was decided in this context to normalize the delay matrices of both the HPA model and the DPD model by dividing each individual term of the delay matrix by the maximum magnitude of the calibration input signal for that particular delay matrix to the power corresponding with the order of non-linearity of the particular term in the delay matrix. This can be represented by introducing a weighting matrix $\mathbf{W}$, substituting $\mathbf{X}_{\text{w}}$ for $\mathbf{X}$ in (3.4) and (3.6), where

$$\mathbf{X}_{\text{w}} = \mathbf{X}\mathbf{W}. \tag{3.8}$$

Similarly for (3.7), $\mathbf{Y}_{\text{cal,w}}$ is substituted for $\mathbf{Y}_{\text{cal}}$, where $\mathbf{Y}_{\text{cal,w}} = \mathbf{Y}_{\text{cal}}\mathbf{W}$. The elements $\mathbf{W}_{i,j}$ of the square weighting matrix $\mathbf{W}$ of dimensions $[B \times B]$ are represented by

$$\mathbf{W}_{i,j} = \begin{cases} \frac{1}{(x_{cal,max})^{K_j}} & \text{for } i = j \\ 0 & \text{for } i \neq j \end{cases} \tag{3.9}$$

where $x_{\text{cal,max}}$ is the maximum instantaneous magnitude present in the calibration data signal used to assemble the delay matrix, and K_j is the order of non-linearity associated with the jth coefficient term in the selected MP model.

This results in each individual term of the delay matrix being scaled so that, for a given input time signal, the range of typical values spanned by the varying non-linear terms is reduced by several orders of magnitude. As a result, when this normalized delay matrix is used in the Moore-Penrose pseudoinverse for finding the coefficients of the model, the least-squares solution for the coefficients is produced with a much more balanced importance being placed on each term as the order of non-linearity associated with that term changes. This normalization process effectively creates a weighted least-squares approach, with more accurate and numerically stable HPA simulation and DPD results than previous approaches, such as [51].

The stability of the Moore-Penrose pseudoinverse can be inspected quantitatively by the matrix condition number, more specifically the condition number of the delay matrix. The condition number is a common linear algebra tool for examining the sensitivity of a solution of a system of linear equations to error [71]–[73]. In the case of the amplifier MP model, the condition number can be thought of as the maximum ratio of the relative error in the coefficients divided by the relative error in the measured output signal. A matrix is said to be well conditioned if the condition number is close to 1, and said to be ill conditioned if the condition number is extremely large. Using a set of calibration data measured through a Specwave QBH-7-4012 amplifier, the condition number of the delay matrix was calculated using both the unweighted and weighted least-squares approaches. In order to examine various ranges of possible calibration data input values and their effect on the calculated condition number, the input and output calibration data was rescaled at decade incre-

ments from -30 dB to +30 dB. At each level of scaled calibration data, the delay matrix condition number was calculated for various model parameters, specifically for all permutations of models with order of nonlinearity equal to three, five, seven, or nine and with order of memory equal to one, three, or five. These calculations were made for both the amplifier and DPD delay matrices. The comparison between the weighted and unweighted approaches can be seen in Figure 3.5. It is observed that for both the amplifier and DPD cases the weighted least-squares based approach results in relatively low condition numbers that remain very stable as the magnitude of the calibration data is altered, whereas the unweighted least-squares based approach can have largely varying condition numbers result that are nearly always orders of magnitude larger than those computed with the weighted approach.

In general, for both the weighted and unweighted approaches, the matrix condition number increases as the number of coefficients in the MP model increases. Our successful measured results utilizing the weighted least-squares approach, presented later in Section 3, confirm our theoretical formulations.

3.2.4 Bayesian Analysis for Model Parameter Refinement and Slowly Changing Systems

While the Moore-Penrose pseudoinverse method of finding the least-squares solution is used in the previous sections for finding the coefficient values for both the amplifier model and the predistortion function, there are other methods available for calculating non-linear model parameters that offer benefits [74], [75]. One of these methods is Bayesian analysis utilizing Gibbs sampling,

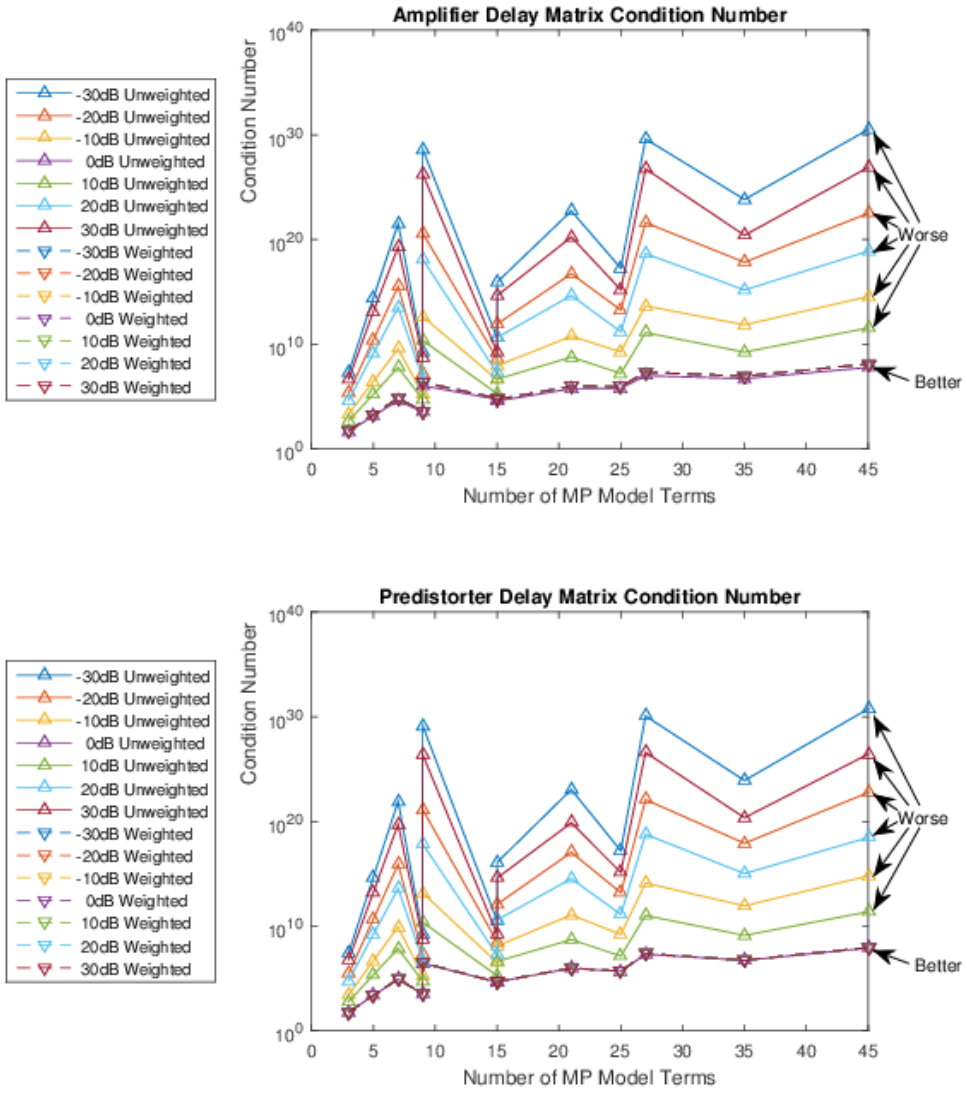


Figure 3.5: *Delay Matrix Condition Number for Amplifier and DPD MP Models As a Function of Number of Model Terms. Note that the condition numbers resulting from the weighted approach are more stable regardless of scaling. Reprinted from Dunn et al. (2016) © 2016 IEEE*

which is a form of Markov chain Monte Carlo (MCMC) algorithm that approximates the multivariate probability distribution of the model parameters. Whereas the Moore-Penrose least-squares solution uses all available measured calibration data each execution to find parameter values, Bayesian analysis

uses only the latest acquired calibration set of data in conjunction with a multivariate probability containing all prior knowledge of the system, known as a prior, to construct probabilities of the model parameters. Once the posterior conditional probabilities of the parameters are found, the mean of each is calculated to give point estimates for the parameters. Under the belief that the best model parameters are chosen when the greatest amount of calibration data is utilized, the Bayesian approach offers a significant computational advantage if the system continually acquires calibration data throughout operation. In addition, the Bayesian approach can result in parameters that are capable of accurately tracking the best underlying model in the presence of slowly varying system conditions [76]. The inherent ability of the Bayesian approach to correctly alter amplified non-linear model parameters as the system changes is in contrast to the previous least-squares only approach, such as [77], [78], that in a changing system environment with continuous training data acquisition can only result in a parameter set that is the least-squares solution to the system state that is essentially the average of all measured system states, rather than the current system state.

The model used for Bayesian analysis is based on the unweighted MP model shown in (3.3), but due to the Gibbs sampling program operating only on real numbers, the original complex MP model is converted into two real equations representing the real and imaginary components individually. These equations are shown as

$$\hat{y}_r[n] = \sum_{k=0}^{K-1} \sum_{m=0}^{M-1} \Big(\left(h_{km,r} x_{cal,r}[n-m] - h_{km,i} x_{cal,i}[n-m]\right) \times \times \sqrt{x_{cal,r}^2[n-m] + x_{cal,i}^2[n-m]}^{\,k} \Big) \quad (3.10)$$

and

$$\hat{y}_i[n] = \sum_{k=0}^{K-1} \sum_{m=0}^{M-1} \Big((h_{km,i} x_{cal,r}[n-m] + h_{km,r} x_{cal,i}[n-m]) \times \\ \times \sqrt{x_{cal,r}^2[n-m] + x_{cal,i}^2[n-m]}^{\,k} \Big) \quad (3.11)$$

where $\hat{y}[n]$ is the calculated MP model values with $\hat{y}[n] = \hat{y}_r[n] + \mathrm{j}\ \hat{y}_i[n]$, the measured input calibration signal $x_{cal}[n] = x_{cal,r}[n] + \mathrm{j}\ x_{cal,i}[n]$, and the complex MP model coefficients $h_{km} = h_{km,r} + \mathrm{j}\ h_{km,i}$. The measured output calibration signal is defined to be the result of a compound Normal distribution, shown as

$$y_{cal,r}[n] \sim \mathrm{N}(\mu = \hat{y}_r[n], \tau = \tau_{y,r}) \quad (3.12)$$

and

$$y_{cal,i}[n] \sim \mathrm{N}(\mu = \hat{y}_i[n], \tau = \tau_{y,i}) \quad (3.13)$$

where the measured output calibration signal $y_{cal}[n] = y_{cal,r}[n] + \mathrm{j}\ y_{cal,i}[n]$, the distribution's mean is the MP model value $\hat{y}[n]$ calculated using the measured input calibration signal, and the distribution's precision τ is a model variable itself. Once the multivariate posterior probability distribution of the model's variables has been calculated, the point estimate of each conditional probability is calculated, giving the MP model coefficient estimates as well as the precision of the compound Normal distribution approximating the model about the measured data. The distribution approximating the model output is compound Normally distributed due to the precision itself being an unknown distribution.

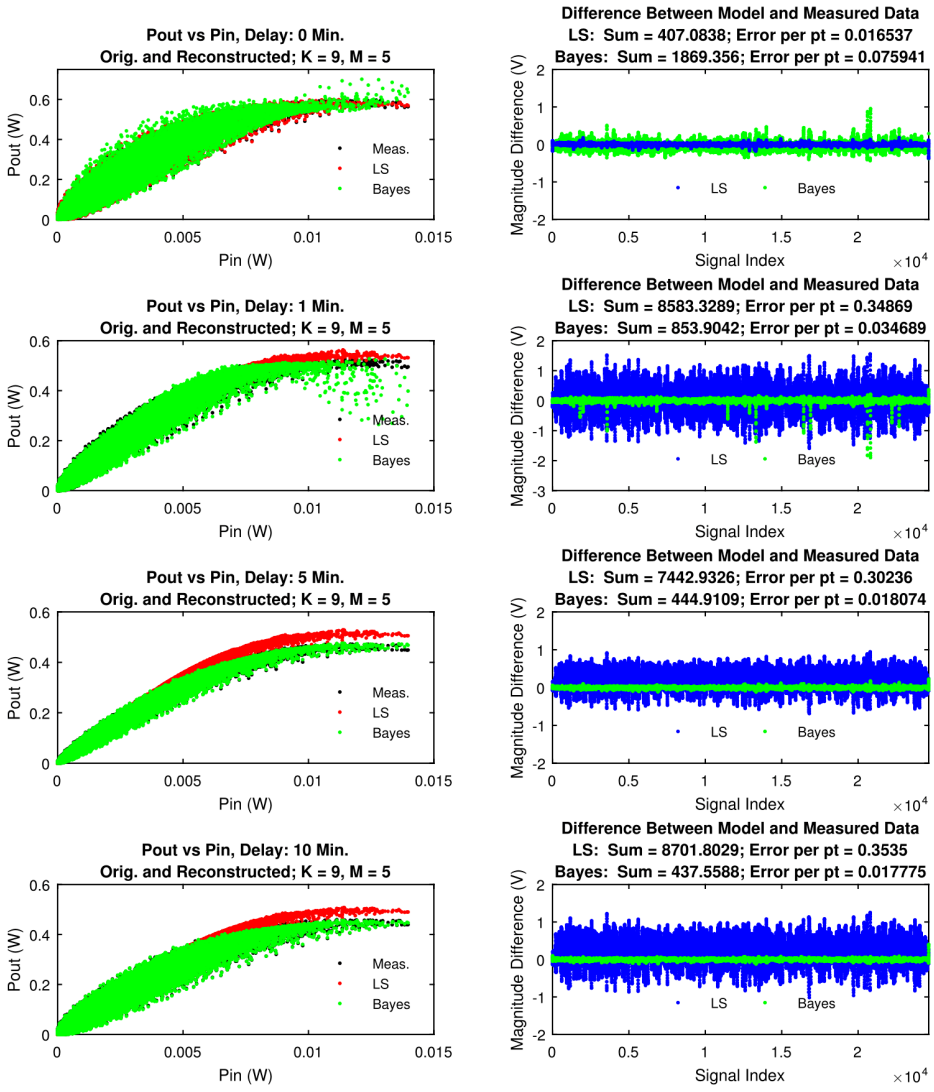


Figure 3.6: *Measured Amplifier Data versus Least-Squares and Bayesian Model Results, Reprinted from Dunn et al. (2016) © 2016 IEEE*

A single set of calibration data with a bandwidth of 40 MHz was used, implying the underlying assumption of a completely steady-state system. Additionally, all parameters for the Bayesian algorithm were initialized with uninformative priors, and it was found that the weighted least-squares approach

generated model parameters that had slightly better results than those generated by the Bayesian generated coefficients. This resulted in amplifier models with results closer to measured values and DPD models that resulted in less spectral spreading. However, when amplifier characteristics changed due to changing unmodeled system parameters, such as the temperature of the amplifier, the Bayesian generated coefficients gave much more satisfactory results as the system was able to track with the changes while still incorporating and adding to historical data about the amplifier. These results are seen in Figure 3.6, which shows the $K = 9$, $M = 5$ amplifier models generated by both the least-squares and Bayesian analysis approaches as the amplifier undergoes a temperature shift, with each subsequent row representing a progression in amplifier state. The predicted output power versus input power for both approaches is plotted in addition to the current measured amplifier output power versus input power in the left column of Figure 3.6. The difference between both modeled amplifier output powers and the current measured amplifier output power is plotted in the right column of Figure 3.6. It can be easily seen that the difference between the measured and modeled results is less for the least-squares approach when the system is stable, but is less for the Bayesian generated approach as the system changes. The calibration data was formed by concatenating four calibration data sets that were each recorded during the warm-up period of a Specwave QBH-7-4012 amplifier, with the four 40 MHz bandwidth measurements taken at delays of zero, one, five, and ten minutes after amplifier activation, respectively.

3.3 Predistortion of Digitally Coded Waveforms

Simulations and tests were conducted on a representative non-constant modulus waveform that spans the power and bandwidth of a possible wideband radar waveform, as well as a constant modulus constrained coded waveform typical of a wideband radar. The P4 coded waveform was chosen to represent a typical wideband constant modulus radar waveform, as it is a polyphase code with broad instantaneous bandwidth. Although polyphase codes have been known for some time, P4 codes have gained in popularity over the last several years as they are efficient to digitally synthesize and have unique applications in modern radars, for example [27]–[29] and others. New classes of good polyphase code sets can be generated using pieces of P4 polyphase codes, and these code sets are suited for many applications including orthogonal netted radar systems (ONRS) and MIMO radars [28]. Under the cross-correlation elimination (CCE) condition many monostatic radar waveforms can be directly used in the MIMO radar system, such as P4 codes [27]. As noted by Lewis and Kretschmer [79], the P4 polyphase pulse compression code is very Doppler tolerant, can provide large pulse compression ratios, and is tolerant of precompression bandwidth limitations. Therefore, the P4 code and its results represent any typical wideband constant modulus radar waveform with wide instantaneous bandwidth, including but not limited to Frank, P1, P2, P3, biphase, or polyphase modulated waveforms.

The non-constant modulus waveform chosen to represent any possible wideband radar waveform within the system's filtered bandwidth range consists of a randomly generated complex baseband signal filtered to the bandwidth that

the system is to be characterized. Although the available test setup hardware limited the calibration waveform to a relative bandwidth that was not overly large, the chosen bandwidth was sufficient to capture wideband effects of the amplifier. This is demonstrated by the large vertical width of the output power for a single input power as seen in Section 3.3.4. Therefore, this randomly generated code and its results represent any radar waveform with wide instantaneous bandwidth and non-constant modulus. Waveforms with these attributes could be encountered in more specialized and advanced radar system roles, such as MIMO systems, LPI radars, and SAR wideband beamforming applications. Due to the assumption of a steady-state system, these waveforms were predistorted utilizing the weighted least-squares based method described in Section III, and the simulated and measured results were compared to the respective non-predistorted cases. This was done to test the ability of the DPD to match the final distorted output waveform to the desired output waveform in a steady-state system, and to quantify the effect on spectral spreading behavior while the amplifier is operating in its compression region. Through trial and error, it was found that $K = 9$ and $M = 5$ for the MP DPD orders provided optimal performance for the given test datasets.

For both the constant modulus and non-constant modulus waveforms tests, it was expected that the simulated predistorted results would have slightly better suppressed spectral spreading than their physically measured counterparts. This is due to the fact that the predistorted and non-predistorted signal in a physically measured test is being applied to a real system with nonlinear characteristics, rather than a known model approximating a system with nonlinear characterisitics. Therefore, when a simulation is executed, the exact nonlinear

behavior of the simulated amplifier is already known, whereas the measured test will have some element of noise or unmodeled and unaccounted for effect present simply due to the fact that a physical amplifier's nonlinear behavior cannot be perfectly known. This expectation was confirmed, and for both the constant modulus and non-constant modulus waveform tests, the magnitude of the spectral spreading was slightly lower for the simulated case than for the respective physically measured case.

3.3.1 P4 Waveform Simulation

A simulated system was analyzed using calibration data measured through a Specwave QBH-7-4012 amplifier and a constant modulus 20 MHz P4 coded waveform filtered to a bandwidth of 40 MHz. A 40 MHz filter was chosen in order to capture the null-to-null waveform information. The waveforms had a pulse width of 84 μs and a maximum input voltage equal to the maximum allowed magnitude as specified by analysis of the calibration data. Using an HPA model with $K = 9$ and $M = 5$, it was seen that the digitally predistorted signal was nearly an exact match to the desired output signal. The non-predistorted signal, which was equal to the DPD input signal and scaled so that its maximum magnitude corresponded with the predistorted signal's maximum magnitude, experienced non-linear distortion and compression across the span of the waveform. The spectral spreading of the non-predistorted output signal was much larger than that of the predistorted signal after being distorted by the HPA. This is seen in Figure 3.7. With these results in mind, it can be seen that using the DPD model on the input waveform leads to a much more desirable simulated result, closely matching the ideal output signal, and with

a much smaller degree of spectral spreading than would be present without digital predistortion.

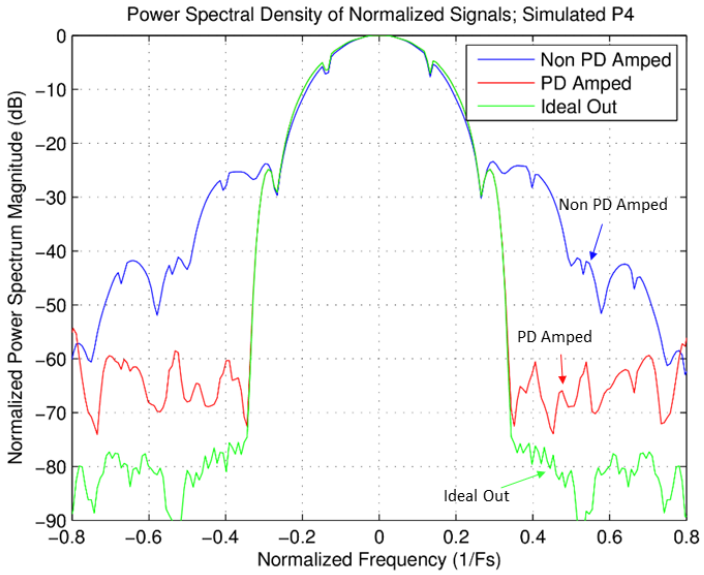


Figure 3.7: *Power Spectral Density of Simulated Predistorted and Non-Predistorted P4 Coded Waveforms after HPA Distortion, Reprinted from Dunn et al. (2016) © 2016 IEEE*

3.3.2 P4 Waveform Test in Hardware

The same P4 coded waveform used in simulation was generated with a center frequency of 1.2 GHz and amplified through a Specwave QBH-7-4012 amplifier and tested both with and without DPD. Using a pulse width of 84 μs and a maximum input voltage equal to the maximum allowed magnitude as specified by analysis of the calibration data, it is seen in Figure 3.8 that the digitally predistorted signal had much lower measured spectral spreading than the non-predistorted signal. This demonstrates DPD's potential impact on modern wideband radar signals, where high gain systems utilizing waveforms with

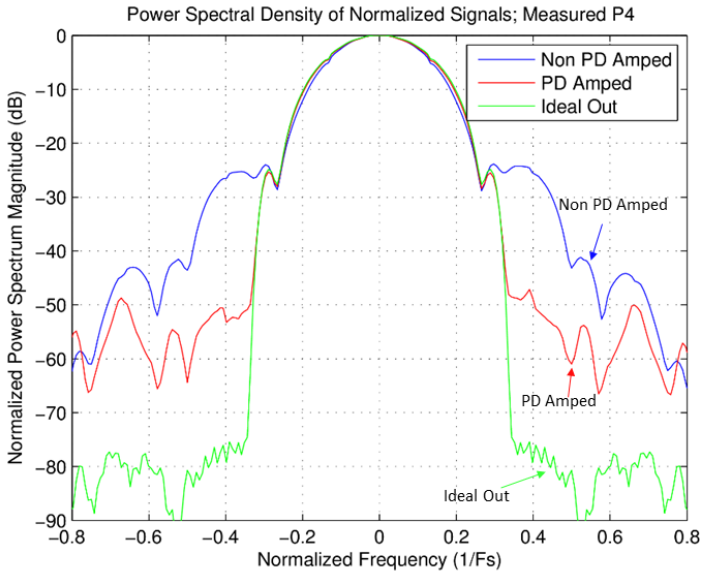


Figure 3.8: *Power Spectral Density of Measured Predistorted and Non-Predistorted P4 Coded Waveforms after HPA Distortion, Reprinted from Dunn et al. (2016) © 2016 IEEE*

broad instantaneous frequency can be predistorted to have much improved spectral characteristics.

3.3.3 Non-Constant Modulus Waveform Simulation

A simulated system was analyzed using calibration data measured through a Specwave QBH-7-4012 amplifier and a representative non-constant modulus test signal composed of a randomly generated complex baseband signal filtered to a bandwidth of 40 MHz, a pulse width of 25 μs, and a maximum input voltage equal to the maximum allowed magnitude as specified by analysis of the calibration data. Using an HPA model with $K = 9$ and $M = 5$, it was seen that the digitally predistorted signal was nearly an exact match to the desired output signal. However, the non-predistorted signal, which was equal to the

DPD input signal and scaled so that its maximum magnitude corresponded with the predistorted signal's maximum magnitude, experienced non-linear distortion and compression across the span of the waveform. It was also seen that the spectral spreading of the non-predistorted output signal was much larger than that of the predistorted signal after being distorted by the HPA. This is seen in Figure 3.9. With these results in mind, it can be seen once again that using the DPD model on the input waveform leads to a much more desirable simulated result, closely matching the ideal output signal, and with a much smaller degree of spectral spreading than would be present without digital predistortion.

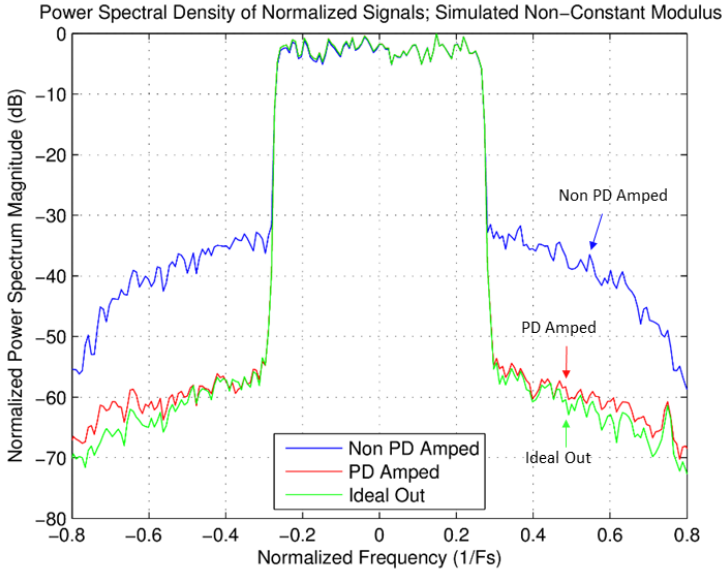


Figure 3.9: *Power Spectral Density of Simulated Predistorted and Non-Predistorted Signals after HPA Distortion, Reprinted from Dunn et al. (2016) © 2016 IEEE*

3.3.4 Non-Constant Modulus Waveform Test in Hardware

The same non-constant modulus representative test signal used in simulation was generated with a center frequency of 1.2 GHz and amplified through a Specwave QBH-7-4012 amplifier and tested both with and without DPD. Using a pulse width of 25 μs and a maximum input voltage equal to the maximum allowed magnitude as specified by analysis of the calibration data, it is seen in Figure 3.10 that the digitally predistorted signal had much lower measured spectral spreading than the non-predistorted signal.

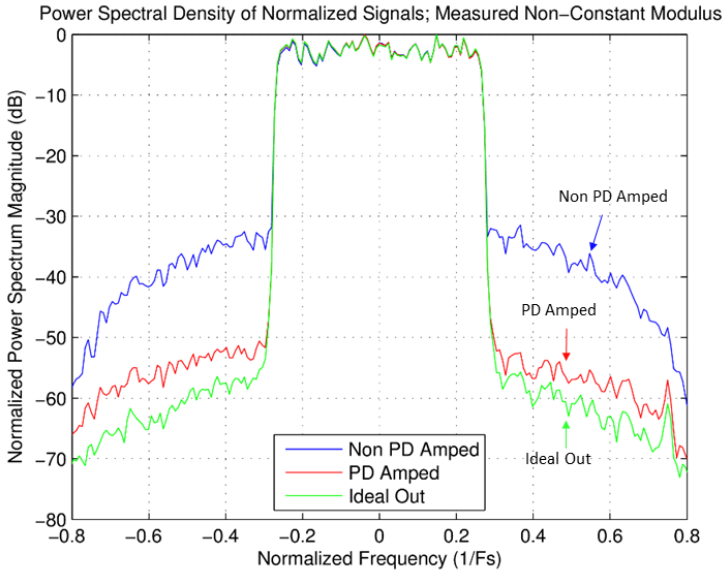


Figure 3.10: *Power Spectral Density of Measured Predistorted and Non-Predistorted Signals after HPA Distortion, Reprinted from Dunn et al. (2016) © 2016 IEEE*

It can be seen in Figure 3.11 that the measured predistorted signal closely matches the ideal linear gain across the output power range. The large vertical width of the measured non-predistorted signal for a given input power is due to the wideband nature of the waveform in conjunction with the frequency

dependency of the amplifier. The vertical narrowing of the predistorted signal is due to frequency dependency correction, demonstrating that the order of memory chosen for the model is sufficient to correct the system's wideband effects. This frequency dependency correction is also apparent when comparing the passband group delay of the measured digitally predistorted signal to that of the measured non-predistorted signal, as seen in Figure 3.12.

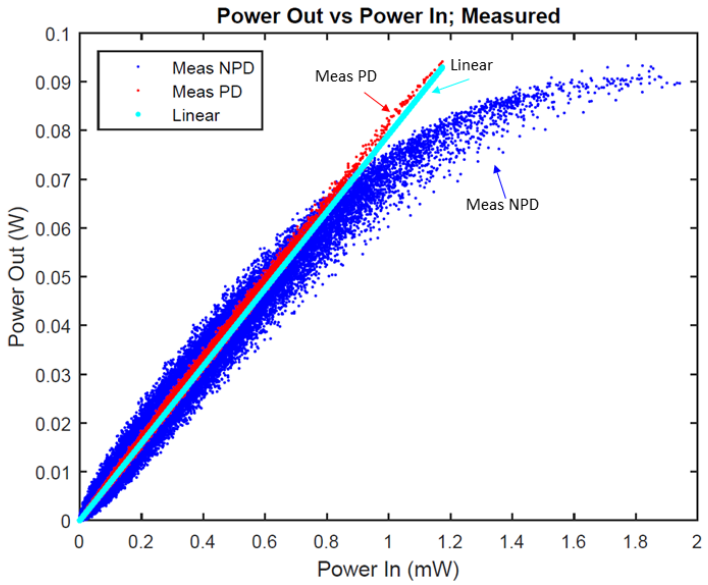


Figure 3.11: *Power Out vs. Power In of Measured Predistorted and Non-Predistorted Signals after HPA Distortion, Reprinted from Dunn et al. (2016) © 2016 IEEE*

While the particular amplifier under test had an overall relatively flat group delay response over the given frequency range, there was still a fair amount of variance present. The predistorted signal maintained the overall flat group delay response in addition to significantly suppressing the variance throughout the passband, thus significantly improving the accuracy of the overall predistorted system. By producing a linear power out versus power in response, as well as a flat group delay response in the passband, the predistortion ap-

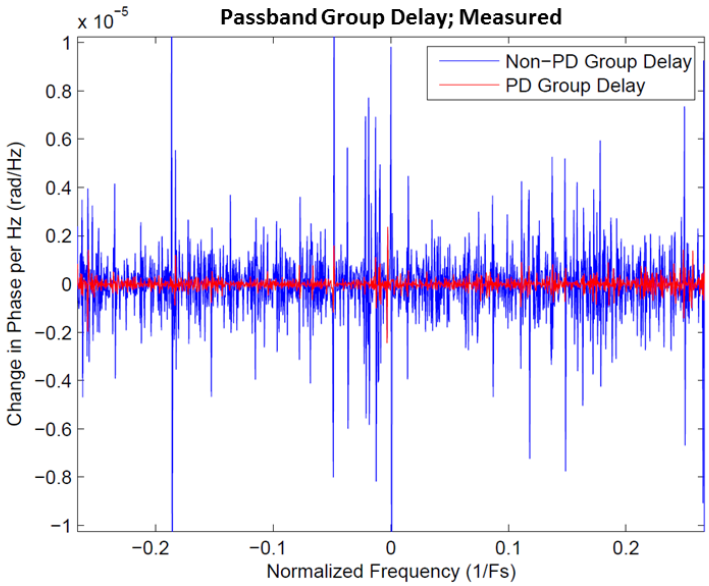


Figure 3.12: *Passband Group Delay of Measured Predistorted and Non-Predistorted Signals after HPA Distortion, Reprinted from Dunn et al. (2016) © 2016 IEEE*

proach presented is shown to be able to accurately reproduce a desired complex baseband waveform. These results found using a wideband non-constant modulus waveform with broad instantaneous bandwidth verify that the DPD approach presented is not constrained to the traditional constant modulus class of radar waveforms. This opens the possibility of significantly improved generated signal fidelity and greatly reduced spectral leakage in modern and emerging broadband radar systems that may be dependent upon non-constant modulus waveforms, such as MIMO radar systems, LPI radars, and SAR systems utilizing wideband beamforming.

3.4 Conclusion

In conclusion, it has been shown that the Volterra series, more specifically the MP model, is able to accurately model the non-linear effects and memory effects of both high power amplifiers and their associated predistortion models in wideband radar systems. The predistortion model can be implemented digitally in a system and shows potential for significant improvements in radar spectral performance and overall waveform fidelity. These improvements have significant potential impact when used in conjunction with phased array radar architectures utilizing solid-state amplifiers and waveform generators at every antenna element. In the past, least-squares approaches have been shown to be useful to solve DPD model parameters, primarily within the communication community. The newly presented weighted least-squares approach for predistortion and modeling of wider band radar signals is more numerically stable than previous approaches. In addition, for the first time, a Bayesian approach is proposed that allows the models to track with slowly changing system parameters to maintain the best current model. Laboratory testing has confirmed the efficacy of this approach. When system data is continuously recorded for system characterization the Bayesian approach offers long-term computational benefits. DPD allows the radar system to linearly amplify and transmit waveforms over the entire HPA's output power range, maximizing power added efficiency, minimizing spectral spreading, and have an overall performance similar to that of a much larger and more costly radar system that does not utilize digital predistortion. These qualities make DPD a strong contender not only for EcoSAR, but also for modern phased array radar systems that require high fidelity generation of eccentric or non-constant

modulus waveforms, such as MIMO radar systems, LPI radars, and SAR systems utilizing wideband beamforming.

In the next chapter, several sets of proposed wideband beamforming waveforms for EcoSAR are introduced with both alternating transmit simultaneous receive and simultaneous transmit simultaneous receive operation modes in mind. In addition to their method of generation and simulated ideal combined beam-pattern, the calculated beam-pattern is also shown for the cases where each waveform is physically generated, amplified, and measured, as well as digitally predistorted using the previously described approaches, physically generated, amplified, and measured. The calculated beam-patterns generated from the non-predistorted and predistorted measured waveforms are then analyzed for suitability of application in EcoSAR.

Chapter 4

An Impedance Dependent Memory Polynomial Model for Wideband Digital Predistortion of Solid-State Radar Amplifiers

4.1 Introduction

Modern and emerging radar systems are increasingly utilizing wideband waveforms in active array architectures, in which each individual antenna element is associated with its own unique high power amplifier (HPA) and transmit and receive chain [3], [4]. In addition to phased array radar systems, active array architectures will solve unique problems in high-traffic next-generation communication systems, such as the 5G wireless network [80]–[84]. In addition to the benefits of traditional phased arrays, such as rapid beamsteering and graceful degradation, an active array architecture also allows for the execution of unique radar operational schemes, such as multi-beam transmit and receive, the use of designed wideband waveform sets that result in frequency-invariant beampatterns, and simultaneous multi-mode operation [5]–[8]. These operational modes are often dependent on the use of non-constant modulus waveforms, and the success of the operational scheme often hinges on the accurate

generation of these very specifically defined waveform sets, both in their output power versus input power relationships as well as in their spectral footprint. It is well documented that HPAs operate non-linearly over their input power range, as well as that their highest power added efficiency occurs well into the non-linear region [12]–[14]. The non-linear behavior exhibited by amplifiers results in an effect known as spectral spreading, where the intended signal's spectral shape is corrupted by the addition of power outside the intended band of usage. Increasingly stringent requirements imposed on bandwidth allocation and management in conjunction with the high fidelity waveform creation required in next-generation active array radar systems necessitates that a system's HPAs linearly reproduce the system's intended signals. In order for a HPA to linearly reproduce its input signal, the input signal must be restricted to a constant modulus, the input signal's power level must remain well below the maximum input power of the amplifier to coincide with the linear region of the HPA and operate at a sub-optimal power added efficiency, or the input signal should be predistorted so that the non-linear effects of the amplifier ultimately result in a linearly amplified signal over the full output power range of the amplifer. Digital alteration of an input signal so that a system's distorted output signal equals the true desired signal is known as digital predistortion (DPD). Due to active array architectures containing a HPA at each antenna element, the cost incurred through requiring larger and more powerful amplifiers, along with the larger associated heat management and power system requirements, in order to operate the amplifiers at less than maximum input power would be unreasonable and would linearly increase with the number of number of antenna elements. As a result, it is much more desirable to utilize a form of DPD to maximize the effectiveness of the HPAs in a given system.

It is well documented that in addition to amplifiers exhibiting non-linear characteristics over their input power range, amplifiers also exhibit non-linearities over their input frequency range. In order for modern radar systems to accurately predistort non-constant modulus wideband waveforms in each transmit/receive chain, the amplifier must be carefully characterized as a function of both input power and input frequency. The memory polynomial (MP) model has been shown to be capable of successfully modeling non-linear and memory dependent systems with complex input and output data [59], [62]–[65]. In previous work, the MP model has been shown to produce satisfactory results when applied to wideband digital predistortion of radar amplifiers [77], [78]. It should be noted that non-linear variations over frequency can be viewed, and thus modeled, as a result of memory effects.

In addition to HPA performance being a function of the input power and frequency, HPA behavior is also affected by the complex load impedance experienced at the output port of the amplifier [85], [86]. This is important in active phased array architectures as the complex load impedance experienced by the HPA at each antenna element will vary as a function of scan angle [1], [15]. This change in impedance as a function of scan angle is aptly known as scan impedance. This work differs from previous radar-centric wideband digital predistortion research in that it is desired to not only predistort HPAs as a function of input power and input frequency, but also as a function of the load impedance experienced by the HPA. This is accomplished through the proposal of a novel modified MP model, henceforth referred to as the impedance dependent memory polynomial (IDMP) model. While digital pre-

distortion has been utilized in communication systems, as in [55]–[57], it does not have widespread use in radar applications. While adaptive predistortion of unpredictable and constantly changing waveforms is not generally needed in radar systems, DPD in radar applications must apply over a much larger bandwidth at higher power levels in addition to complying with mandated lower sideband suppression than is common in communication systems [2]. Modern and emerging radar systems typically utilize a finite number of pre-known wideband waveforms to be used during operation. Therefore, adaptive predistortion is not required at every transmit pulse. Instead the predistorted versions of the input waveforms can be saved into memory as a function of scan angle to be recalled during operation. In active phased array architectures, this method of generating pre-saved waveforms requires the same computational power as generating non-predistorted waveforms. This makes digital predistortion utilizing the IDMP model desirable for modern and emerging radar systems, especially for beamsteering systems that may require the usage of wideband non-constant modulus waveforms, such as in MIMO radar systems, Low-Probability of Intercept (LPI) radars, SAR systems utilizing wideband beamforming, and systems executing simultaneous multi-mode operation. This chapter closely follows the work presented by the author in [87] © 2017 IEEE.

4.2 Technical Approach to Modeling Amplifier and Predistorter

4.2.1 Mutual Coupling and Scan Impedance in Phased Arrays

When antennas are transmitting near each other in an array, radiated energy from each antenna invariably ends up at every other transmitting antenna element to some extent. This unwanted energy can be absorbed, rescattered, or reradiated, again slightly affecting all other antenna elements in the array. This effect of unintentionally trading energy throughout an antenna array through secondary transmission effects is known as mutual coupling [88]. Energy absorbed through mutual coupling between antenna elements can lead to effectively changing the antenna element's impedance. Changing an antenna element's impedance is the same as changing its reflection coefficient. For the generalized example case of a two-dimensional uniform array, the array scan reflection coefficient Γ for the 00 antenna element can be represented as

$$\Gamma = \sum_{p}^{P-1} \sum_{q}^{Q-1} S_{00,pq} \frac{A_{pq}}{A_{00}} \tag{4.1}$$

where P is the number of rows of elements in the array, Q is the number of columns of elements in the array, S is the s-parameter between the 00 element and the pq element, and A_{pq} is the complex excitation coefficient of the pq element [89]. While the coupling coefficient is determined from the impedance matrix, the excitation coefficient is set by the radar system's intended scan

angle. Therefore, due to the mutual coupling, reflection coefficient, and effective antenna impedance being dependent upon all the other active antenna elements and the radar system's intended scan angle, the effective antenna impedance for a given element is called the scan impedance. Scan impedance effects are widely recognized in phased array systems [1], [88]–[90]. For an array that has matched elements at broadside the array can be expected to experience a voltage standing wave ratio (VSWR) of at least 2:1 over a normal operational scanning range, which corresponds with a scan reflection coefficient that does not produce a loss exceeding -10 dB. [1]. Additionally, due to being a function of frequency and the chosen transmit beamsteering direction, the scan impedance characteristics remain consistent for a given antenna array. This means that during initial calibration of the radar system the scan impedance characteristics of the antenna array can be related as a function of excitation frequency and beamsteering angle, thus allowing the creation of a method for the direct mapping of an individual antenna element's, and thus individual HPA's, load impedance to the desired beamsteering angle. For the remainder of this chapter only the HPA load impedance will be addressed for modeling purposes, and it will be assumed that the scan impedance is known versus scan angle and that the array is well-characterized enough that the scan impedance for a given scan angle is consistent across all antenna elements. The primary purpose of this chapter is to demonstrate that wideband impedance-dependent corrections are possible and effective on the testbed scale. Future research goals involve expanding and applying the presented DPD approach to a larger array, as well as successfully mapping the intended transmit beamsteering angle to HPA load impedance for each antenna element in a finite phased array antenna.

4.2.2 Conceptual Approach to Impedance Dependent Digital Predistortion

As was previously stated, digital predistortion is the digital alteration of an input signal so that a system's distorted output signal equals the ideal output signal. The ideal output signal is defined as being the input signal multiplied only by a linear gain. Alternatively, the ideal output to input relation is that of a linear output power versus input power relation, a gain matching that of the linear region of the amplifier, and a uniformly flat group delay response. Consider the narrowband impedance matched case of amplifier predistortion, where the measured non-linear output power versus input power relationship is fairly straightforward as there is only one output power for any given input power. For the narrowband case, predistortion is relatively intuitive, as it simply consists of carefully and intentionally rescaling the input power so that the ideal output power versus input power relation is remapped to the measured non-linear output power versus input power relation. The equation governing the rescaling of the input power is the predistortion model. Note that in order for the ideal output power versus input power relation to be successfully remapped to the measured output power versus input power relation, the maximum output power must be equal in both cases.

Consider the wideband impedance matched case of amplifier predistortion, where the measured non-linear output power versus input power relationship has an added level of complexity as the non-linear output power versus input

power relationship of the amplifier is also dependent upon frequency. This means that for a wideband input signal, multiple output powers correspond with any given input power. Therefore in order to map the ideal input signal to the correct measured input signal, the frequency based effects must be taken into account. A more in-depth analysis of wideband digital predistortion in impedance matched radar systems can be found in [43], [77], [78].

In addition to having output power versus input power relationships as a function of input power and input frequency, a high power amplifier's output characteristics are also a function of their complex load impedance. For the wideband load impedance varying case of amplifier predistortion, the non-linear output power versus input power relationship, with multiple output powers corresponding with any given input power due to frequency dependent effects, as a whole changes non-linearly as a function of load impedance. As an example, the average of the highest 5% magnitude samples per impedance measurement from a MACOM MAAP-010171 high power amplifier are shown in Figure 4.1 with the magnitude plotted as a function of the impedance's resulting complex reflection coefficient. It can be easily seen that a high power amplifier's load impedance does indeed affect the amplifier's output characteristics. Whereas the wideband matched impedance case's predistortion model only requires a time-dependent input signal, the impedance dependent model requires the addition of another parameter to address the extra dimension based on the amplifier's load impedance. This parameter can be the amplifier's load impedance, the complex reflection coefficient calculated using the system's characteristic impedance, the complex voltage standing wave ratio (VSWR), or any other parameter that results in a one-to-one mapping from

the complex load impedance. Note that in order for the ideal output power versus input power relation to be successfully remapped to the ideal output power versus input power for the impedance dependent case, the maximum output power of the ideal output must equal the maximum lower bound of the measured output power over all the possible load impedances. By ensuring that the maximum ideal output signal does not exceed the lowest maximum power for all frequencies and load impedances that can be experienced by the system, this ensures that it will be possible to recreate the ideal output signal. Alternatively, if the highest output power at each scan angle is desired at the expense of uniform output power across scan angles, then the same model could be utilized in conjunction with a maximum ideal output power that is a function of load impedance. For the remainder of this chapter it is desired that the output power be uniform across input power, frequency, and load impedance, therefore the ideal output power for a given HPA will be assumed to be a constant.

4.2.3 Memory Polynomial Model and Impedance Dependent Memory Polynomial Model

As previously stated, the memory polynomial model, itself a simplification of the Volterra series [59], has been shown to produce satisfactory results when applied to complex baseband modeling of physical amplifiers. The MP model is given by

$$y(n) = \sum_{k=0}^{K-1} \sum_{m=0}^{M-1} h_{km} x(n-m)|x(n-m)|^k \tag{4.2}$$

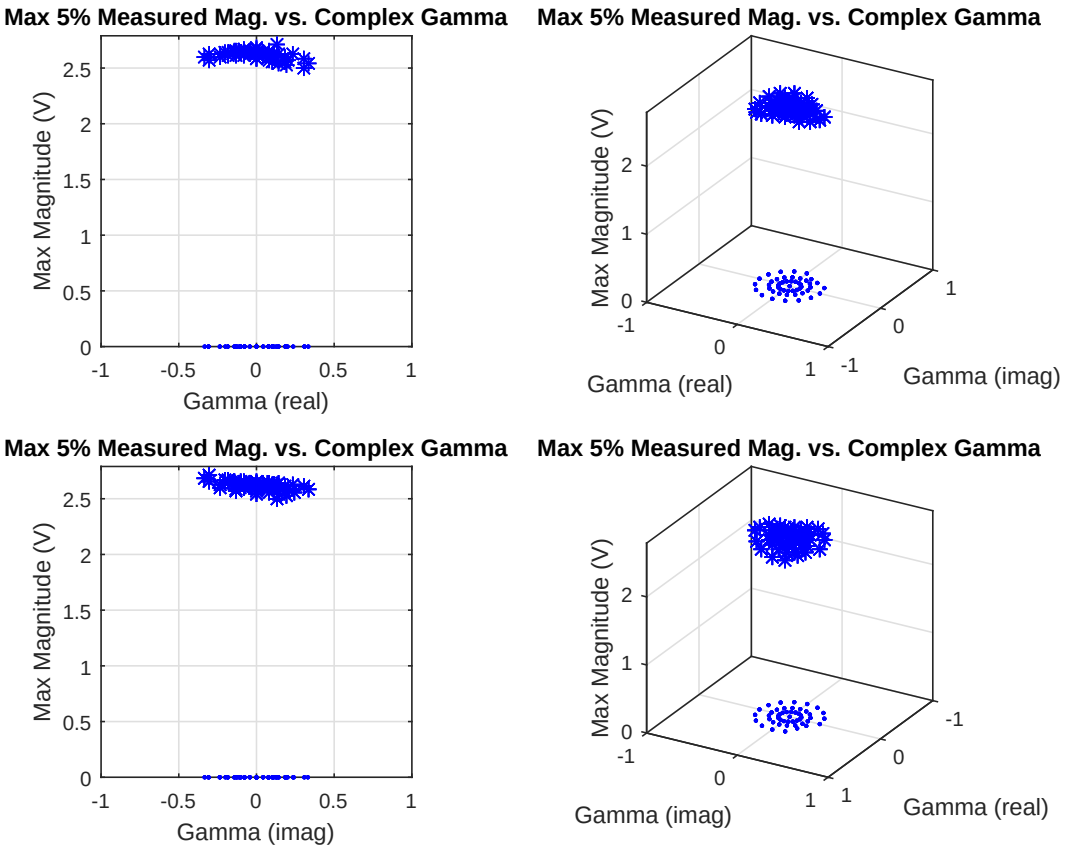


Figure 4.1: *Various Perspectives of Mean of Top 5% Maximum Magnitudes per Load Impedance vs. Complex Reflection Coefficient, Reprinted from Dunn et al. (2017) © 2017 IEEE*

where $y(n)$ is the output sample, $x(n)$ is the input sample, K is the order of non-linearity of the system, M is the order of memory of the system, and h_{km} is a coefficient with set values as a function of k and m.

When the specified order of non-linearity or order of memory is large in a DPD model, numerical instabilities can begin to arise when solving for the coefficients of the model. While approaches have been proposed to mitigate instabilities by modifying the MP model itself [70], previous work by the authors found success through normalizing the terms of the MP model. This

normalization was executed through weighting by dividing each term of the MP model by the maximum magnitude of the calibration input signal for the particular modeling scenario to the power corresponding with the current order of non-linearity for that particular model term. Therefore, the weighted memory polynomial model can be fully represented as

$$y(n) = \sum_{k=0}^{K-1} \sum_{m=0}^{M-1} h_{km} x(n-m)|x(n-m)|^k \frac{1}{(x_{cal,max})^{k+1}} \tag{4.3}$$

where $x_{\text{cal,max}}$ is the maximum instantaneous magnitude present in the calibration data signal used for the model. This weighted MP model was demonstrated to accurately model a wideband radar amplifier and its associated DPD model for a matched impedance system while remaining stable relative to changes in model size [43].

This chapter expands previous work through the inclusion of load impedance dependent effects. As mentioned previously, the formation of a load impedance dependent non-linear model requires the addition of another parameter to address the extra dimension due to the inclusion of the amplifier's load impedance's effect on the model. Using the weighted memory polynomial model as the starting point, a satisfactory impedance dependent memory polynomial (IDMP) model was developed by this research that could model the necessary DPD function at complex baseband. This IDMP model can be shown as

$$\begin{aligned} y(n) = \sum_{k=0}^{K-1} \sum_{m=0}^{M-1} \sum_{p=0}^{C-1} \sum_{a=0}^{C-1} \big(& \Phi_{kmpa} x(n-m)|x(n-m)|^k \lambda_R \lambda_I + \\ & j\Psi_{kmpa} x(n-m)|x(n-m)|^k \lambda_R \lambda_I \big) \frac{1}{(x_{cal,max})^{k+1} \Gamma_{max}^{p+a}} \end{aligned} \tag{4.4}$$

where

$$\lambda_R = \begin{cases} 1 & \text{for } p = 0 \\ \Gamma_R[n]\,|\Gamma_R[n]\,|^{p-1} & \text{for } p > 0 \end{cases} \tag{4.5}$$

and

$$\lambda_I = \begin{cases} 1 & \text{for } a = 0 \\ \Gamma_I[n]\,|\Gamma_I[n]\,|^{a-1} & \text{for } a > 0 \end{cases} \tag{4.6}$$

where C is the user selected order of impedance dependency and Φ_{kmpa} and Ψ_{kmpa} are complex coefficients with set values as a function of k, m, p, and a. All impedances present in the calibration dataset are used to compute all the corresponding complex reflection coefficients $\Gamma[n] = \Gamma_R[n] + j\Gamma_I[n]$ using a standard characteristic impedance of 50 Ω. The complex term Γ_{max} is given by $\Gamma_{max} = \max(|\mathrm{Re}\{\Gamma[n]\}|) + j\max(|\mathrm{Im}\{\Gamma[n]\}|)$, where "max( )" returns the maximum of the input vector, "| |" denotes the magnitude operator, "Re {}" denotes the real component, and "Im {}" denotes the imaginary component. The proposed IDMP model captures the complex relations between the complex input signal and the complex reflection coefficient, as well as all the complex cross terms resulting from a non-linear function of $\Gamma[n]$ by manually separating the real and imaginary components of the resulting $\Gamma[n]$ cross terms. This manual separation of the complex equation results in a model with $2 \times K \times M \times C^2$ coefficients overall.

Due to the IDMP model being linear with respect to the coefficients, it can be represented efficiently in matrix form as $\mathbf{y} = \mathbf{X}\boldsymbol{\theta}_{IDMP}$. This matrix

representation can be expanded to be shown as

$$\mathbf{y} = \begin{bmatrix} y(M) \\ \vdots \\ y(N) \end{bmatrix} = \mathbf{X} \begin{bmatrix} \Phi_{0000} \\ \vdots \\ \Phi_{kmpa} \\ \vdots \\ \Psi_{0000} \\ \vdots \\ \Psi_{kmpa} \end{bmatrix} \tag{4.7}$$

where the $[A \times B]$ matrix $\mathbf{X}$ is called the delay matrix, and is best represented as the result of submatrices, shown as $\mathbf{X} = [\mathbf{X}_R\mathbf{W}\ j\mathbf{X}_R\mathbf{W}]$. It should be noted that N is equal to the length of the input vector $\mathbf{x}$ and $B = 2KMC^2$ is equal to the total number of coefficients for a given order of non-linearity K, order of memory M, and order of impedance dependence C. Therefore the complex coefficients Φ_{kmpa} and Ψ_{kmpa} are both of size $\left[\frac{B}{2} \times 1\right]$. The length of the output vector is given by $A = N - (M-1)$ to ensure that any generated output in $\mathbf{y}$ is calculated with populated values for all of the needed delay terms. The $\left[A \times \frac{B}{2}\right]$ submatrix $\mathbf{X}_R$ can be partially expanded to be shown as

$$\mathbf{X}_R = \begin{bmatrix} x(M)\cdots & x(1)|x(1)|^k\Gamma_R|\Gamma_R|^{C-1}\Gamma_I|\Gamma_I|^{C-1} \\ \vdots & \vdots \\ x(N)\cdots\ x(N-M+1) & |x(N-M+1)|^k\Gamma_R|\Gamma_R|^{C-1}\Gamma_I|\Gamma_I|^{C-1} \end{bmatrix} \tag{4.8}$$

and the $\left[\frac{B}{2} \times \frac{B}{2}\right]$ square submatrix $\mathbf{W}$ handles the model weighting for nu-

merical stability, shown as

$$\mathbf{W}_{i,j} = \begin{cases} \frac{1}{(x_{cal,max})^{k_j} \ \Gamma_{max}^{p_j+a_j}} & \text{for } i = j \\ 0 & \text{for } i \neq j \end{cases} \tag{4.9}$$

where k_j is the order of non-linearity, p_j is the order of impedance dependency on the real term of the complex reflection coefficient, and a_j is the order of impedance dependency on the imaginary term of the complex reflection coefficient associated with the j^{th} coefficient term in the selected IDMP model.

It can now be seen that the delay matrix $\mathbf{X}$ is composed of varying combinations of the input vector $\mathbf{x}$ that are both delayed and not delayed, multiplied by the appropriate Γ values, to be associated with the B coefficients used to create the A output samples in $\mathbf{y}$. Therefore $\mathbf{X}$ can be assembled given only the input sample array, the load impedance state associated with each input sample, and the specified orders of non-linearity, memory, and impedance dependence for the given IDMP model to be used. As a result, the only DPD model component that is not specifically set or determined by the user is the $[B \times 1]$ model coefficient column vector $\boldsymbol{\theta}_{IDMP}$ that embodies the non-linear characteristics of the system over the desired input power, input frequency, and load impedance ranges. In order to estimate the coefficient vector $\boldsymbol{\theta}_{IDMP}$, high precision output measurements through the device to be characterized or predistorted must be acquired using a well known excitation signal. The excitation signal should be strategically chosen to excite the device over the desired input power and frequency ranges, and the measurements of the excitation signal should be taken throughout the expected range of load impedances using

an appropriate test setup. This pair of input and measured signals is known as the calibration signal. One method of capturing as much of the non-linear behavior as possible with a single excitation waveform is to generate a complex baseband waveform that is randomly generated in time and phase, and then to filter the waveform so that it occupies the desired bandwidth. This helps to generate as many random combinations of input power and frequency as possible in a given pulse length to excite the amplifier. This filtered waveform can then be used to assemble a bank of amplifier measurements with the amplifier's load impedance varied across the range it is to be characterized. This bank of input and amplified measured waveforms are then concatenated into two identical dimension vectors containing all of the measured input waveforms and all of the measured amplified waveforms, respectively. Additionally, a third vector is created with a length equal to the total number of samples in one of the first two vectors, and each element of the vector contains the load impedance experienced by the amplifier at that same index in the amplified measured output vector. These three vectors together form a calibration dataset that captures enough of the amplifier's non-linearities across the ranges of interest of input power, frequency, and load impedance to model the system or the system's DPD model to a satisfactory degree.

Once a satisfactory calibration dataset has been acquired and the desired order of non-linearity, order of memory, and order of load impedance have been chosen, the IDMP model coefficient vector $\boldsymbol{\theta}_{IDMP}$ can be calculated. The DPD model coefficients are found using a method similar to that used to solve for the MP model coefficient vector in [43], [51], [77], [78], where the calibration data is used to solve for the coefficients of a post-inverse filter for

the system's HPA. Due to the IDMP model being formed from the Volterra series, the Volterra series property that any system's p^{th} order post-inverse filter is equivalent to the same system's pre-inverse filter still holds true [69]. This property is visualized for a simplified one-to-one linearization case in Figure 4.2.

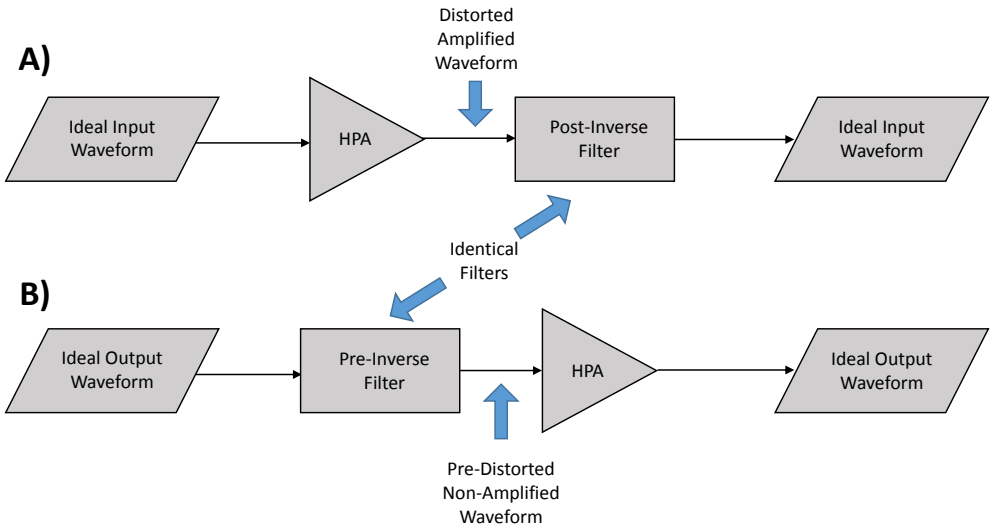


Figure 4.2: *Visualization of Volterra Series Post-Inverse A) to Pre-Inverse B) Equivalency Property, Reprinted from Dunn et al. (2017) © 2017 IEEE*

In practice, it is desired for the DPD to be implemented as a pre-inverse filter, with the pre-inverse filter and HPA pair itself being treated as a black-box amplifier with ideal linear amplification. In order for the pre-inverse filter to remove the non-linear effects of the HPA without removing the desired gain from the HPA, the coefficients of the post-inverse filter (used in practice as the pre-inverse filter) must be solved using the calibration data where the measured output calibration waveform has been rescaled so that its maximum magnitude does not exceed the system's maximum allowed input magnitude. The maximum allowed input magnitude is the magnitude that, when multiplied by the linear region gain of the HPA, equals the maximum magnitude

of the measured calibration data output signal. This method of pairing the DPD and the HPA as a black-box ideal amplifier is shown in Figure 4.3 where subplot A) helps visualize the system non-linearities compensated by the solution of the post-inverse filter, subplot B) helps visualize that the system's post-inverse filter is equivalent to the system's pre-inverse filter, and subplot C) helps visualize the implementation of the pre-inverse filter in practice.

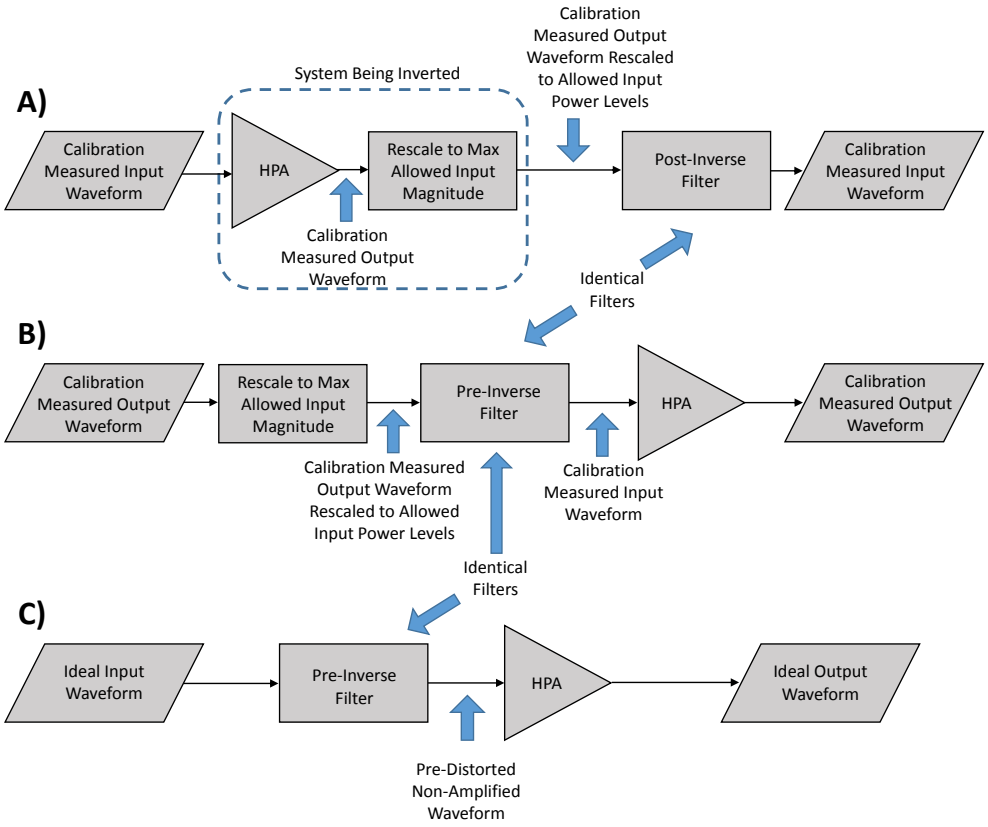


Figure 4.3: *Visualization of Calibration Post-Inverse A) to Calibration Pre-Inverse B) and Implemented Pre-Inverse C) Equivalency Property in Black-Box Linear Amplifier Method, Reprinted from Dunn et al. (2017)* © *2017 IEEE*

Utilizing the matrix representations of the IDMP model shown in Equations 4.7 through 4.9, the least-squares solution to the IDMP model coefficient vector $\boldsymbol{\theta}_{IDMP}$ characterizing the post-inverse filter for a given HPA is found

through the Moore-Penrose pseudoinverse [67], [68], shown as

$$\boldsymbol{\theta}_{IDMP} = (\mathbf{X}_{cal}^{\mathrm{H}}\mathbf{X}_{cal})^{-1}\mathbf{X}_{cal}^{\mathrm{H}}\mathbf{y}_{cal} \tag{4.10}$$

where $\mathbf{y}_{cal}$ is the measured input signal column vector of the calibration data, $\mathbf{X}_{cal}$ is the delay matrix formed by the rescaled calibration data output signal $\mathbf{x}_{cal}$, and $[\,]^{\mathrm{H}}$ is the complex conjugate transpose operator. See Appendix A for a more complete solution of the Moore-Penrose pseudoinverse. Once the post-inverse (DPD model) coefficients have been found, if adequate model orders have been chosen and the desired system input signal is within the input power, input frequency, and load impedance ranges characterized by the calibration dataset, then properly predistorted signals for that particular system can be created. It should be noted that the input power range is limited to the maximum magnitude of the rescaled calibration output signal used to create the delay matrix used in the Moore-Penrose pseudoinverse, but the frequency range and load impedance range coincide with those encountered during calibration data acquisition.

In summary, the DPD process utilizing the IDMP model requires a measured set of calibration data including load impedance information, user-defined orders of non-linearity, memory, and impedance dependency, and a desired ideal input signal and amplifier load impedance in order to create a properly predistorted input signal for the system that will result in a linearly amplified version of the desired ideal input signal at the system output. A high-level flowchart of the implemented DPD process for the IDMP model is shown in Figure 4.4, and an overview of the process for implementing DPD using the IDMP model is listed below.

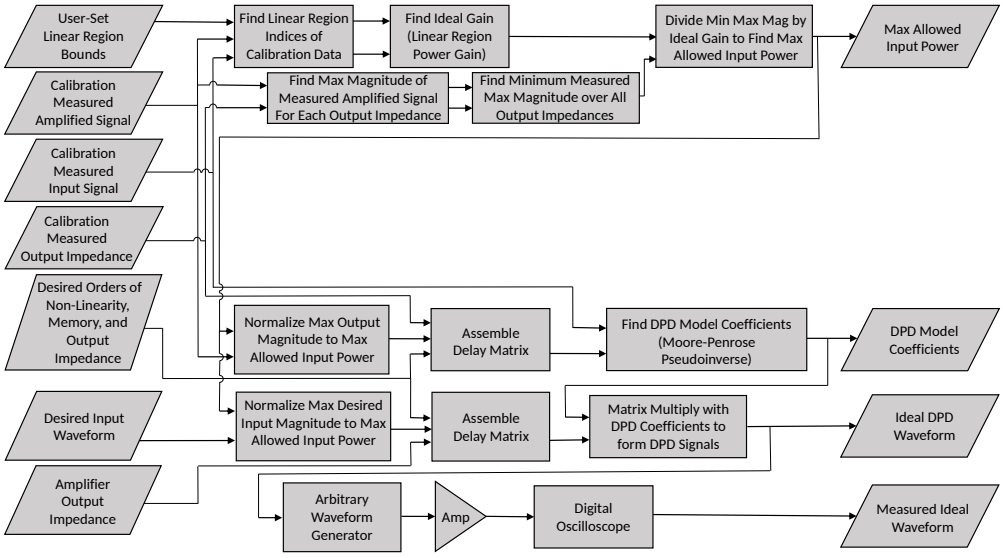


Figure 4.4: *Flowchart Summary of Impedance Dependent Digital Predistortion Process, Reprinted from Dunn et al. (2017) © 2017 IEEE*

Steps for Practical Implementation of DPD Using the IDMP Model

1. Create non-constant modulus wideband calibration excitation waveform that will encompass desired ranges of input power and operating frequency.

2. Set load impedance of HPA to desired complex impedance.

3. Generate calibration waveform at arbitrary waveform generator and measure resulting non-amplified and amplified calibration data at the selected HPA load impedance.

4. Repeat steps 2-3 over sufficiently dense grid of output impedances to characterize the desired range of load impedances.

5. Find maximum magnitude of measured amplified calibration signal for each measured load impedance case.

6. Concatenate measured non-amplified calibration signals into a single data vector, concatenate measured amplified calibration signals into a single data vector, and concatenate load impedance per sample point into a single vector so that the full calibration dataset is represented as three vectors.

7. Examine output power versus input power relation of the calibration dataset and select output power threshold for defining the linear region of the amplifier.

8. Use least-squares regression to calculate the linear region gain of the amplifier using only calibration data corresponding with the linear region of the amplifier as determined by the selected output power threshold.

9. Find minimum value of the previously calculated maximum magnitudes for each load impedance, convert minimum of the maximum magnitudes to units of power, and divide by calculated linear region gain of amplifier to obtain the maximum allowed input power level.

10. Select order of non-linearity K, order of memory M, and order of impedance dependence C to use in the desired IDMP model.

11. Scale measured amplified calibration signal vector so that the maximum magnitude matches the maximum allowed input power.

12. Use rescaled calibration data vector and the tested load impedances vector to assemble the delay matrix X_{cal} in accordance with Equations 4.4 through 4.9 and the selected orders of non-linearity, memory, and impedance dependency.

13. Execute Moore-Penrose pseudoinverse using the measured non-amplified calibration signal vector and X_{cal} in accordance with Equation 4.10 to assemble the IDMP model coefficient vector $\boldsymbol{\theta}_{IDMP}$.

14. Create desired excitation waveform to be used in the system (within the input power and operating frequency ranges characterized by the calibration dataset).

15. Determine expected HPA load impedance for the desired beamsteering angle.

16. Rescale desired excitation waveform so that its maximum magnitude corresponds with the maximum allowed input power.

17. Use rescaled desired waveform and the expected HPA load impedance for the desired beamsteering angle to assemble the delay matrix X in accordance with Equations 4.4 through 4.9 and the selected orders of non-linearity, memory, and impedance dependency.

18. Matrix multiply delay matrix X with the IDMP model coefficient vector $\boldsymbol{\theta}_{IDMP}$ in accordance with Equation 4.7 to obtain the predistorted waveform.

19. The predistorted waveform is now ready for generation in the characterized system.

4.3 Predistortion of Digitally Coded Waveforms

Tests were conducted on a representative non-constant modulus waveform spanning the power and bandwidth of a possible radar waveform. This representative waveform was tested on an amplifier with a varying load impedance, where the impedance range resulted in a range of VSWR's that could be reasonably expected due to scan impedance effects in a well matched active array radar antenna (e.g. 2:1 VSWR). Digital predistortion was executed on the ideal input signal using the IDMP method described in Section 4.2.3, DPD was executed on the ideal input signal using the 50 Ω matched impedance independent MP model utilized in [43], and a non-predistorted ideal input signal was used as a control.

A testbed was constructed consisting of a Tektronix AWG7122C Arbitrary Waveform Generator capable of generating samples at 12 GS/s and a Tektronix DPO70604 Digital Phosphor Oscilloscope with a 25 GHz sampling rate. A two-stage pre-amplifier was assembled, consisting of a Mini-Circuits ZX60-V82-S+ wideband amplifier feeding a Spanawave SSA-26034 general purpose amplifier. The two-stage pre-amplifier chain was assembled to ensure that an extremely linear reproduction of the desired input signal was produced at the necessary power level at the input to the HPA, a MACOM MAAP-010171 2-stage, 8 W saturated S-band amplifier. The HPA amplifier required pulsed power on the drain pin during operation, and this was accomplished with the use of a pulsed power board produced in-house. This pulsed power board can be seen being held close to the HPA by the adjustable circuit board mount in Figure 4.6. Both the arbitrary waveform generator and the pulsed power

board were remotely triggered by a Stanford Research Systems DG535 Digital Delay Generator to ensure that the amplifier was sufficiently powered when the modulated waveforms were to be amplified. All amplifiers and equipment have a characteristic impedance of 50 Ω. A Weinschel Engineering DS-109 double-stub tuner was placed at the output of the HPA, and a large attenuator and load were placed on the opposite end of the double-stub tuner. Double-stub tuning is a common and basic method of impedance matching circuits [91], but in this case the double-stub tuner allows the amplifier's load impedance mismatch to be carefully and specifically set through a calibration with S_{11} measurements on a network analyzer. Two directional couplers were placed in the system chain, with one preceding the first pre-amplifier, and the second in-line between the HPA output and the double-stub tuner input. These two directional couplers give the measured input signal and the measured amplified output signal. A directional coupler ensures that the amplified signal being captured is due primarily to the amplifier's output characteristics and not an unweighted combination of the amplified and reflected signals due to the double-stub tuner's impedance mismatch. A high-level flowchart of the experimental test setup used is shown in Figure 4.5 and a photograph is shown in Figure 4.6.

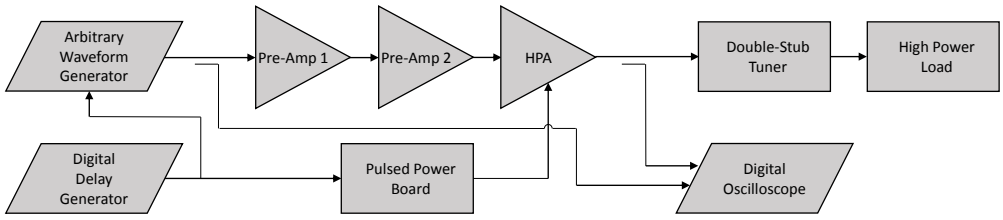


Figure 4.5: *Flowchart of Experimental Testbed Utilized, Reprinted from Dunn et al. (2017) © 2017 IEEE*

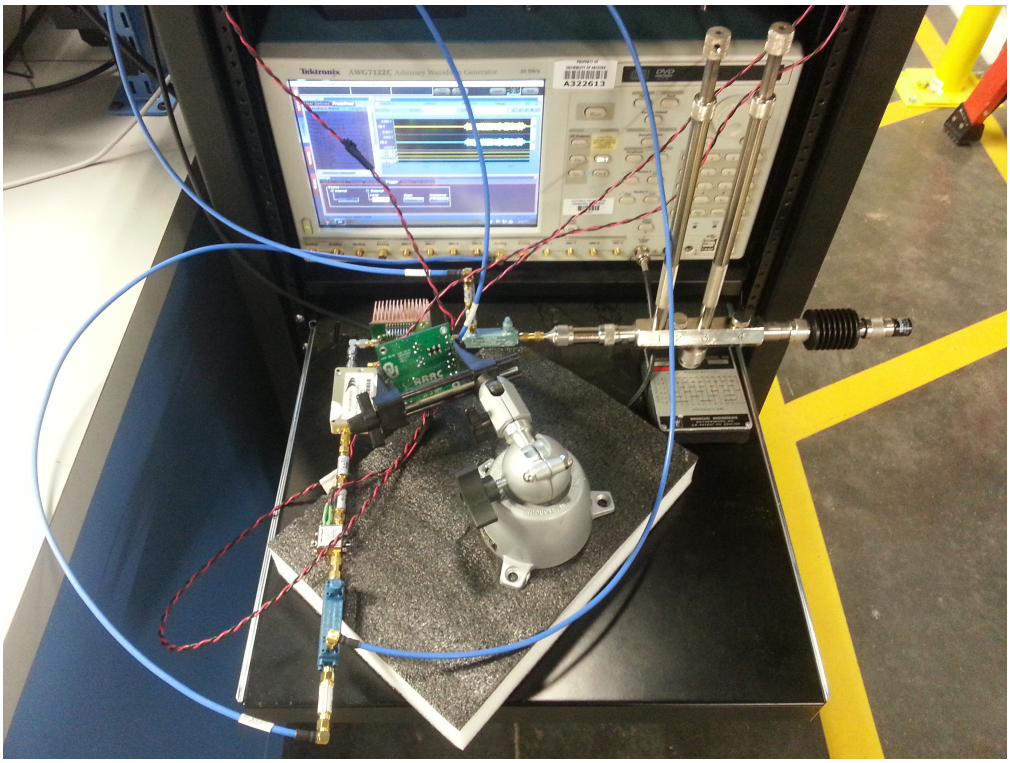


Figure 4.6: *Photograph of Experimental Testbed Utilized, Reprinted from Dunn et al. (2017) © 2017 IEEE*

A waveform generator sample generation frequency of 12 GHz was selected along with a digital oscilloscope sampling rate of 25 GHz. Additionally, an "Analyze" frequency of 1.0 GHz was selected for the actual processing and calculations of the measured and predistorted waveforms in order to help minimize required computational resources by reducing the needed number of computed points for a given pulse length. Another parameter, an integer referred to as the delay-multiple, was used in processing to help minimize required computational resources by spacing the delayed samples to be used as the delayed memory terms in the IDMP model. Representing the delay-multiple with d, this is equivalent to replacing m and M in Equations 4.4 through 4.8 with dm and dM, respectively. The delay-multiple allows a wide range of frequency characteristics within the complex baseband to be modeled using a smaller

number of delay terms than would be necessary if every sample between the zero-delay term and the maximum time-delayed term were also used. A 40 MHz waveform was randomly generated using the method described in Section 4.2.3, and a center frequency of 2.7 GHz was selected. An IDMP model was assigned a delay-multiple of 7, along with an order of non-linearity of 9, an order of memory of 5, and an order of impedance dependency of 3. The impedance independent MP model was assigned the same parameters (with the exception of the order of impedance dependency).

A calibration dataset was compiled utilizing the method described in Section 4.2.3. The 40 MHz randomly generated waveform was measured in the system with the double-stub tuner pre-set to a variety of impedances, and the calibration dataset was compiled by concatenating the waveform measurements from each of the different impedance settings. The impedances were chosen so that, in addition to the 50 Ω matched case giving a VSWR of 1:1, VSWRs of 1.25:1, 1.5:1, and 2.0:1 would result at phase angles of $\frac{q\pi}{8}$ for $q = 0$ to 15. Two exceptions to this pattern occurred at the points corresponding with VSWR = 2:1 and phase angles $\frac{\pi}{4}$ and $\frac{3\pi}{8}$ where the double-stub tuner was unable to create the desired impedance. As a result, the impedances resulting in VSWRs of 1.75:1 and 1.7:1 were used at phase angles $\frac{\pi}{4}$ and $\frac{3\pi}{8}$ respectively. The test waveform was measured at twelve random impedances of roughly equal distribution within the 2:1 VSWR circle on the Smith chart. Four of the evaluation impedances were randomly chosen to coincide with impedances used in assembling the calibration dataset, and eight of the evaluation impedances did not coincide with the calibration points. A depiction of the impedances used in assembling the calibration dataset and the evaluation

dataset is shown in Figure 4.7. A depiction of the impedance-based effects on the maximum 5% of magnitudes for each impedance measurement point in the calibration dataset can be seen in Figure 4.1. Note that the magnitudes roughly trend as an inclined plane with an overlayed parabolic-like effect across the measured region. The impedance independent MP model was calculated using only the calibration data acquired when the double-stub tuner was set

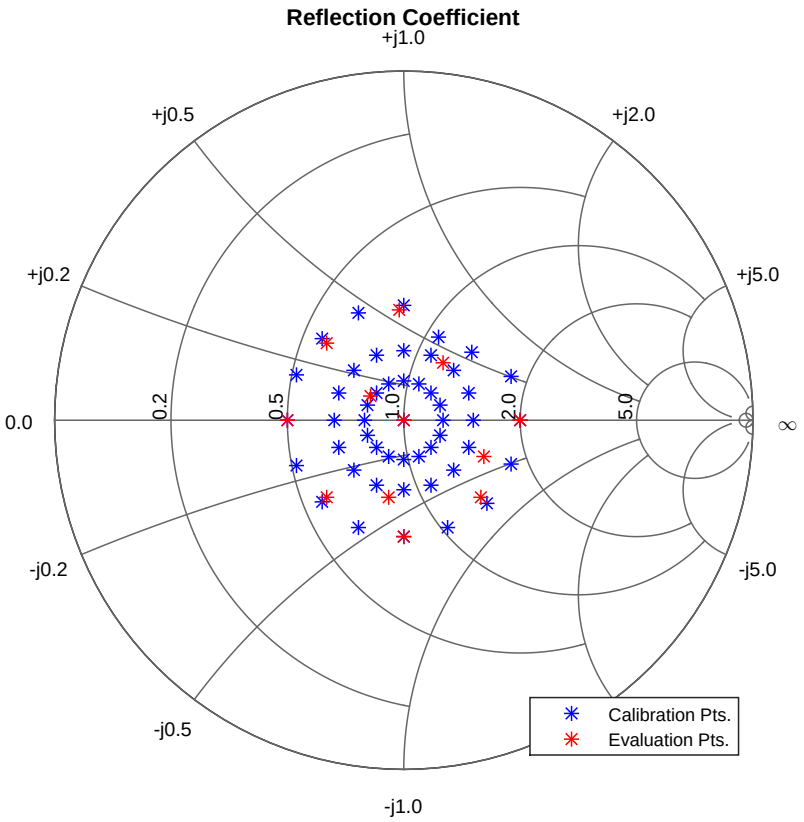


Figure 4.7: *Calibration Dataset and Evaluation Dataset Impedance Test Points, Reprinted from Dunn et al. (2017) © 2017 IEEE*

The resulting power spectral densities from the measured waveforms can be seen in Figure 4.8. Both the IDMP DPD method and the 50 Ω MP method result in very similar reductions in spectral spreading, with the MP method

giving 8.2 dB of suppression and the IDMP method giving 8.5 dB of suppression. Both methods still result in waveforms with spectral spreading that is approximately 3.5 dB greater than the ideal (non-amplified) waveform's power spectral level outside the waveform's intended bandwidth. The real improvement of the IDMP method over the MP method can be easily seen in the output power versus input power graph shown in Figure 4.9. It is easily seen that the 50 Ω matched MP model still provides a drastically more linear output than results from the non-predistorted output, but the IDMP DPD model provides a significantly more linear output than that resulting from the impedance independent MP model (see more details in the following paragraph). It should be noted that when comparing the relative linearity of the output power versus input power relation resulting from the IDMP DPD model outputs does not appear as "tightly" linear as previous impedance independent MP DPD model outputs in a system with stationary load impedance, such as in [43], [77], [78]. This slightly divergent behavior is to be expected as the IDMP model incorporates an extra dimension of dependency, thus attributing to greater compounding errors overall throughout the measurement process. This compounding error could be theoretically combated by assembling a much greater calibration dataset for a given model size so that random errors would destructively interfere when solving for the model coefficients, but the additional time and processing requirements needed to acquire and utilize a significantly larger dataset in exchange for a minor increase in model performance was deemed an inefficient use of time and resources for the purposes of this chapter.

The improvement of the IDMP DPD model over the MP DPD model

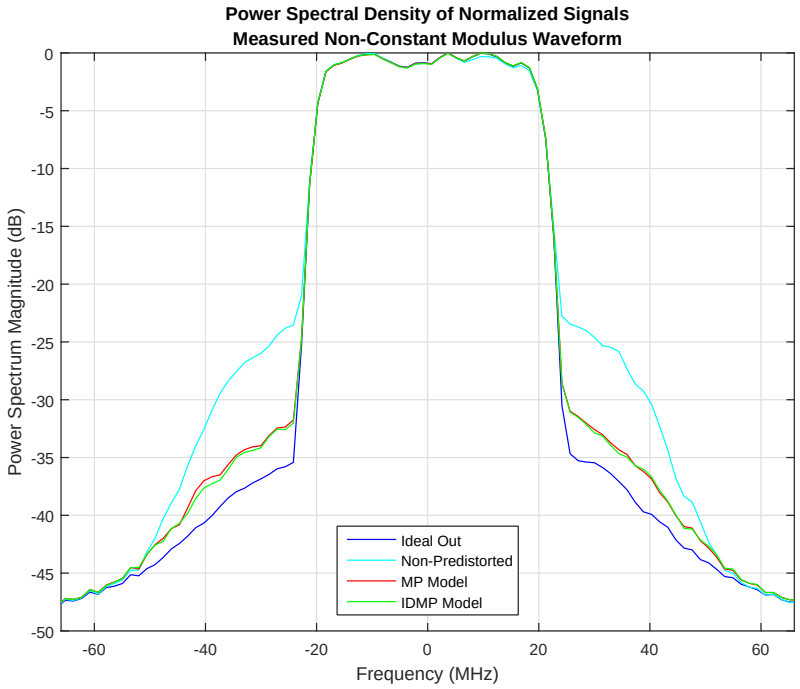


Figure 4.8: *Power Spectral Density of Measured Non-Predistorted, Predistorted, and Ideal Waveforms, Reprinted from Dunn et al. (2017) © 2017 IEEE*

is reinforced by examining the calculated error for the non-predistorted, the MP DPD model, and the IDMP DPD model outputs as seen in Figure 4.10. The calculated voltage error per point for the non-predistorted, the MP DPD model, and the IDMP DPD model was also calculated for the measurement samples over various thresholds of the normalized input power. These voltage error per point calculations demonstrate that the IDMP DPD model provides notable improvement over the MP DPD model, and the IDMP DPD model's output demonstrates increasingly better accuracy performance over the MP model as the average input magnitude of the calculated samples is increased. These voltage errors per calculated power level threshold for the three different measured cases are shown in Figure 4.11. Therefore it is seen that the IDMP DPD model is capable in practice of successfully linearizing the wideband out-

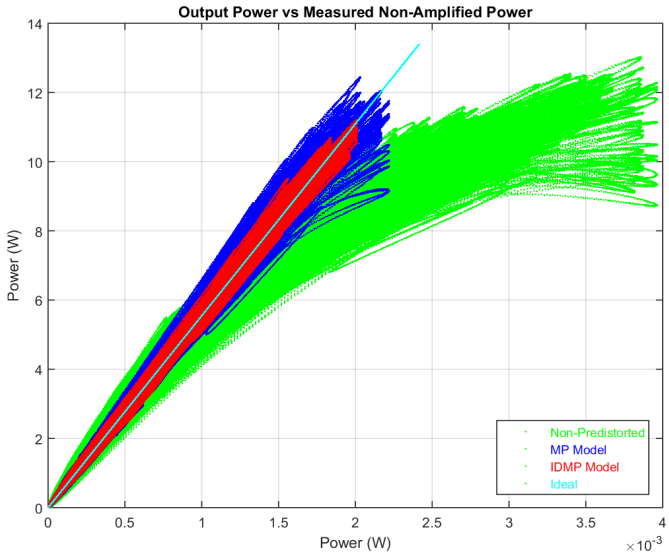


Figure 4.9: *Output Power Versus Input Power of Measured Non-Predistorted, Predistorted, and Ideal Waveforms, Reprinted from Dunn et al. (2017) © 2017 IEEE*

put of a HPA with varying load impedance, providing much more satisfactory results than those generated using previous load impedance independent DPD methods.

4.4 Conclusion

In conclusion, the newly introduced impedance dependent memory polynomial model has been developed and demonstrated as a feasible method of digitally predistorting wideband waveforms in a high power amplifier experiencing load impedance mismatches that would be typical of beamsteering-induced scan impedance effects experienced in an active phased array architecture. While the IDMP DPD model and the MP DPD model result in similar suppression

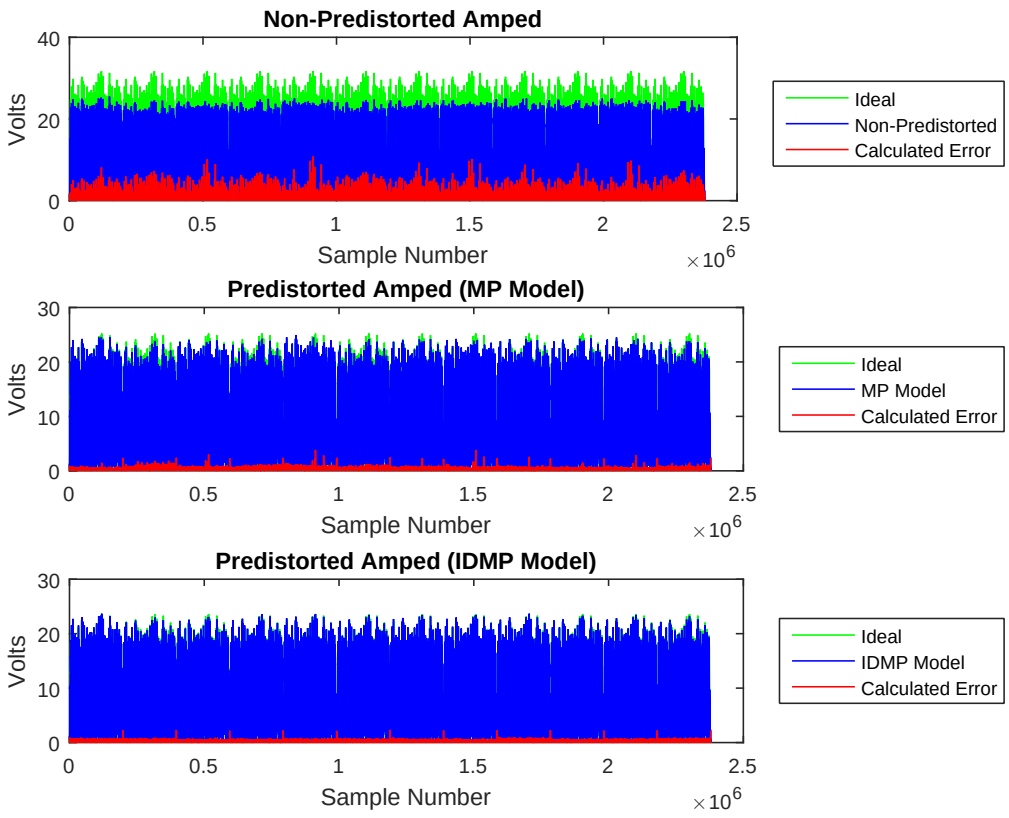


Figure 4.10: *Ideal, Measured, and Calculated Errors for Measured Non-Predistorted and Predistorted Waveforms, Reprinted from Dunn et al. (2017) © 2017 IEEE*

of spectral spreading, it can be easily seen that the output power versus input power relation of the system utilizing IDMP is significantly more linear than that produced by the impedance independent method presented previously. Reduced resultant mean error per sample point is verified in the implemented IDMP DPD model versus the implemented MP DPD model. Versus non-predistorted systems, the IDMP DPD model stands to provide greatly improved transmission characteristics through reduced spectral spreading and consistent amplified linear behavior while still operating at maximum power added efficiency when implemented in modern and emerging active phased array radar systems. Possible future extensions of this research involve testing

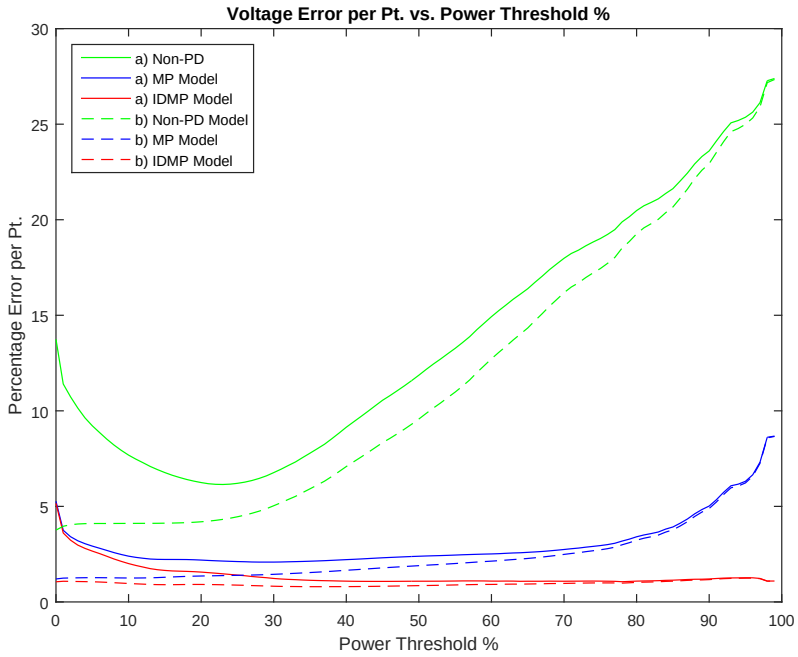


Figure 4.11: *Voltage Errors per Point Calculated on Point-by-Point Basis a) and Versus Maximum Measured Magnitude Basis b) for All Samples over Normalized Input Signal Power Threshold, Reprinted from Dunn et al. (2017) © 2017 IEEE*

the presented IDMP model on larger arrays, testing the IDMP DPD model over wider ranges of VSWR, quantifying the effects of IDMP DPD on common radar waveform ambiguity functions, comparing and contrasting the IDMP DPD method versus phased array applicable adaptive DPD methods common in communication systems, and mapping the intended transmit beamsteering angle to the amplifier load impedance on an element by element basis for finite phased array antennas.

Chapter 5

Conclusion

Overall, this dissertation has served to help provide some necessary framework for next-generation radar systems so that they can maximize their potential impact by providing high fidelity scientific data while operating within strict operational and budgetary guidelines. Chapter 2 demonstrated the necessity of maintaining a high degree of orthogonality in order to successfully recover quality scientific information within a simultaneous transmit and simultaneous receive operational mode. This began with a generalized matrix-based mathematical expansion of the expected received complex baseband waveforms for a dual-polarimetric radar system in Section 2.2. A brief background on cross-correlation and pulse compression was provided in Section 2.3 before explaining the application of pseudo-orthogonality in waveform sets in Section 2.4 and computing an example case in Section 2.5. While common pulse compression waveforms were analyzed for their suitability as pseudo-orthogonal waveforms in Section 2.6, Section 2.7 presented a unique method for designing specific pseudo-orthogonal waveforms sets utilizing particle swarm optimization. It was demonstrated that particle swarm optimization could be utilized to create polyphase coded pseudo-orthogonal waveform sets of arbitrary size, as well as a pseudo-orthogonal waveform set consisting of a pair of non-linear

frequency modulated waveforms utilizing a novel parameterization method. Chapter 2 maintained a focus on the importance of maintaining orthogonality, and Section 2.8 provided analysis on pulse compression characteristics in a few common pseudo-orthogonal waveform sets as a function of both polarization orthogonality degradation and of waveform coding orthogonality degradation. Chapter 2 was ended with Section 2.9 providing the mathematical transformations necessary to convert from any orthonormal polarization basis to any other orthonormal polarization basis, which helps to broaden the potential utility of any radar system utilizing independent arbitrary waveform generators in orthogonal polarizations.

Chapter 3 presented a method for digitally predistorting a desired wideband waveform for solid-state high power radar amplifiers utilizing the memory polynomial model. Digital predistortion allows a radar system to maximize its implemented utility by forcing the physically transmitted waveform to match the ideal transmitted waveform while still operating at the high power amplifier's maximum power added efficiency. A conceptual approach to both narrowband and wideband predistortion was provided prior to a presentation of the math background and utilization of the memory polynomial model in Section 3.2. A weighting approach for enhancing the numerical stability of the memory polynomial approach was also provided in Section 3.2.3. Additionally, a novel Bayesian approach for digital predistortion of slowly changing systems and supporting simulated results was also provided in Section 3.2.4. Simulated and measured results verifying the success of the memory polynomial digital predistortion approach for both a P4 polyphase coded waveform and a non-constant modulus instantaneously wideband waveform were provided

in Section 3.3. As a whole, Chapter 3 serves to provide the necessary background and processes necessary to successfully digitally predistort wideband waveforms for use in a radar system with a high power amplifier and digital waveform creation at each channel.

Chapter 4 expanded upon the wideband digital predistortion method provided in Chapter 3 by also taking into account amplifier non-linear effects due to changing amplifier load impedances that would likely be experienced due to scan impedances in an active phased array architecture. A brief background on mutual coupling and scan impedance characteristics of active phased array architectures was provided in Section 4.2.1 before a conceptual approach to impedance dependent wideband predistortion was provided in Section 4.2.2. The expansion of the memory polynomial model into the novel impedance dependent memory polynomial model, as well as the mathematical techniques needed for solving and implementing the model, was provided in Section 4.2.3. Measured results verifying the success of the impedance dependent memory polynomial digital predistortion approach were provided in Section 4.3. As a whole, Chapter 4 serves to provide the background and novel processes necessary to successfully digitally predistort wideband waveforms for use in radar systems utilizing electronic beamsteering in active phased array architectures where varying load impedances will be experienced by the high power amplifiers at each channel.

Altogether, this dissertation's aim is to help provide some of the necessary framework for next-generation radar systems so that they can maximize their potential impact by providing high fidelity scientific data while operating

within strict operational and budgetary guidelines. Mathematical analysis of expected radar operational modes and unique processes for helping analyze, design, and intelligently modify potential wideband waveform sets were provided to this end. While this research should be very helpful in the design and implementation of next-generation radar systems in its own right, future work always remains. Possible future extensions of the presented research include:

- Expanding the particle swarm optimization waveform design method to design and compare varying waveform types for a given set of system parameters before returning an optimal pseudo-orthogonal waveform set.

- Expanding the analysis of pulse compression characteristics as a function of orthogonality degradation to address non-uniform extended targets, such as those that may be encountered in synthetic aperture radar operation.

- Modifying the memory polynomial digital predistortion model presented in Chapter 3 and the impedance dependent memory polynomial digital predistortion model presented in Chapter 4 to address non-linear amplifier effects as a function of temperature.

- Changing the impedance dependent memory polynomial model's maximum allowed power from a single value to a function of load impedance, effectively trading uniform linearly amplified waveform outputs across beamsteering angles in exchange for the maximum linearly amplified waveform output at each beamsteering angle.

- Developing a method for mapping the intended beamsteering angles to the experienced load impedances at each antenna element for infinite and finite active phased array antennas.

- Testing the memory polynomial and impedance dependent memory polynomial digital predistortion methods implemented on larger active phased array radar systems and quantifying the results.
- Testing the impedance dependent memory polynomial model over an increased range of VSWR.

References

[1] M. Skolnik, *Radar Handbook, Third Ed.* New York: McGraw-Hill, 2008.

[2] *Manual of regulations and procedures for federal radio frequency management*, National Telecommunications and Information Administration (NTIA), 2014.

[3] U. K. Revankar, K. Sreenivasulu, K. M. Veerabhadra, K. S. Beenamole, and D. Kumar, "An experimental active aperture array for l-band high power active phased array radar", in *IEEE International Symposium on Phased Array Systems and Technology*, 2003, pp. 289–294.

[4] M. Yeary, D. Conway, J. Herd, M. Fosberry, M. Harger, and K. Hondl, "A method of improving cross-pol isolation based on the use of auxilary elements", in *Proc. IEEE International Symposium on Phased Array Systems and Technology*, Oct. 2013.

[5] A. Zaghloul, O. Kilic, and E. Kohls, "System aspects and transmission impairments of active phased arrays for satellite communications", *IEEE Transactions on Aerospace and Electronic Systems*, vol. 43, pp. 176–186, Jan. 2007.

[6] W. Chappell and C. Fulton, "Digital array radar panel development", in *Proc. IEEE International Symposium on Phased Array Systems and Technology (ARRAY)*, Oct. 2010, pp. 50–60.

[7] F. Uysal, M. Yeary, N. Goodman, R. Rincon, and B. Osmanoglu, "Waveform design for wideband beampattern and beamforming", in *Proc. IEEE International Radar Conference*, Arlington, VA, May 2015.

[8] F. Uysal, Z. Dunn, M. Yeary, and R. F. Rincon, "Application of waveform weighting for a frequency invariant transmit beampattern", *In Revision by IEEE Aerospace & Electronic Systems Magazine*,

[9] R. Doviak and D. Zrnic, *Doppler Radar and Weather Observations, Second Ed.* Mineola, NY: Dover, 2006.

[10] M. Richards, *Fundamentals of radar signal processing*. New York: McGraw-Hill, 2005.

[11] P. Pace, *Detecting and Classifying Low Probability of Intercept Radar, Second Ed.* Norwood, MA: Artech House, 2009.

[12] M. Yeary, "An efficient intermodulation product computing technique for broadband active transmit systems", *IEEE Trans. on Instrumentation and Measurement*, vol. 57, no. 2, pp. 438–443, Feb. 2008.

[13] J. Li and Q. Liu, "Psk communications systems using fully saturated power amplifiers", *IEEE Transactions on Aerospace and Electronic Systems*, vol. 42, no. 2, pp. 464–477, Apr. 2006.

[14] D. M. Snider, "A theoretical analysis and experimental confirmation of the optimally loaded and overdriven rf power amplifier", *IEEE Trans. Electron Devices*, vol. ED-14, no. 12, pp. 851–857, Dec. 1967.

[15] S. Edelberg and A. Oliner, "Mutual coupling effects in large antenna arrays: Part 1–slot arrays", *IRE Transactions on Antennas and Propagation*, vol. 8, no. 3, pp. 286–297, May 1960.

[16] R. Raney, "A perspective on compact polarimetry", *IEEE Geoscience and Remote Sensing Newsletter*, vol. 160, pp. 12–18, Sep. 2011.

[17] M. Richards, *Principles of Modern Radar*. Edison, NJ: SciTech, 2010.

[18] M. Skolnik, *Introduction to Radar Systems, Third Ed.* New York: McGraw-Hill, 2001.

[19] D. H. B. Kolman, *Elementary Linear Algebra with Applications, Ninth Ed.* Upper Saddle River, NJ: Pearson Education, 2008.

[20] A. W. A. Oppenheim, *Signals & Systems, Second Ed.* Upper Saddle River, NJ: Pearson, 1997.

[21] S. Mitra, *Digital Signal Processing: A Computer-Based Approach, Fourth Ed.* New York: McGraw-Hill, 2011.

[22] J. Klauder, A. Price, S. Darlington, and W. Albersheim, "The theory and design of chirp radars", *The Bell System Technical Journal*, vol. 39, no. 4, pp. 745–808, Jul. 1960.

[23] J. Weideman, "Computation of the complex error function", *Society for Industrial and Applied Mathematics*, vol. 31, no. 5, pp. 1497–1518, Oct. 1994.

[24] C. Nunn and G. Coxson, "Polyphase pulse compression codes with optimal peak and integrated sidelobes", *IEEE Transactions on Aerospace and Electronic Systems*, vol. 45, no. 2, pp. 775–781, 2009.

[25] M. Friese, "Polyphase barker sequences up to length 31", *Electronics Letters*, vol. 30, no. 23, pp. 1930–1931, Nov. 1994.

[26] A. Brenner, "Polyphase barker sequences up to length 45 with small alphabets", *Electronics Letters*, vol. 34, no. 16, pp. 1576–1577, Aug. 1998.

[27] X. Song, S. Zhou, and P. Willett, "Enhanced multistatic radar resolution via stc", in *IEEE Radar Conference*, May 2009, pp. 1–6.

[28] F. Qazi and A. Fam, "Doppler detection capable good polyphase code sets based on piecewise linear fm", in *IEEE Radar Conference*, May 2014, pp. 212–217.

[29] F. Gross and J. Connor, "Comparison of detectability of radar compression waveforms in classic passive receivers", *IEEE Transactions on Aerospace and Electronic Systems*, vol. 43, no. 2, pp. 789–795, Apr. 2007.

[30] D. Gies and Y. Rahmat-Samii, "Particle swarm optimization (pso) for reflector antenna shaping", in *IEEE Antennas and Propagation Society International Symposium 2004*, vol. 3, Jun. 2004, pp. 2289–2292.

[31] P. J. Kajenski, "Particle swarm optimization of antenna elements for foliage penetrating radar", in *Radar Conference, 2007 IEEE*, Apr. 2007, pp. 449–450.

[32] H. Cao, T. Jiang, and X. Chen, "Array optimization for mimo radar by particle swarm algorithm", in *IEEE CIE International Conference on Radar 2011*, vol. 1, Oct. 2011, pp. 99–103.

[33] R. G. Farias, V. Dmitriev, and e. R. M. de Oliveira, "Application of particle swarm optimization to ultra-wideband multistatic radar used for protection of indoor environment", in *SBMO/IEEE MTT-S International Microwave and Optoelectronics Conference 2007*, Oct. 2007, pp. 822–826.

[34] J. G. Warner and J. W. Middour, "Radar transmitter geolocation via novel observation technique and particle swarm optimization", in *IEEE Aerospace Conference 2012*, Mar. 2012, pp. 1–9.

[35] Z. Dunn, M. Yeary, F. Uysal, and C. Fulton, "Low sidelobe pseudo-orthogonal code sets through particle swarm optimization", in *IEEE Radar Conference*, 2016.

[36] J. Kennedy and R. Eberhart, "Particle swarm optimization", in *Neural Networks, 1995. Proceedings., IEEE International Conference on*, vol. 4, Nov. 1995, pp. 1942–1948.

[37] B. R. Reddy and M. U. Kumari, "Polyphase orthogonal waveform using modified particle swarm optimization algorithm for mimo radar", in *IEEE International Conference on Signal Processing Computing and Control (ISPCC) 2012*, Mar. 2012, pp. 1–6.

[38] P. J., N. Balaji, and C. D. Naidu, "Optimal coded sequence design for radar using fractional oppositional particle swarm optimization", in *Recent Advances and Innovations in Engineering (ICRAIE) 2014*, May 2014, pp. 1–6.

[39] E. D. Witte and H. D. Griffiths, "Improved ultra-low range sidelobe pulse compression waveform design", *Electronics Letters*, vol. 40, no. 22, pp. 1448–1450, Oct. 2004.

[40] J. M. Kurdzo, B. L. Cheong, R. D. Palmer, and G. Zhang, "Optimized nlfm pulse compression waveforms for high-sensitivity radar observations", in *International Radar Conference 2014*, Oct. 2014, pp. 1–6.

[41] *Obtaining low sidelobes using non-linear fm pulse compression*, MIT Lincoln Laboratory, 1994.

[42] V. Bringi and V. Chandrasekar, *Polarimetric Doppler Weather Radar Principles and Applications*. New York: Cambridge University Press, 2001.

[43] Z. Dunn, M. Yeary, C. Fulton, and N. Goodman, "Wideband digital predistortion of solid-state radar amplifiers", *In Revision by IEEE Transactions on Aerospace and Electronic Systems*, 2016.

[44] M. Davis, "Frequency allocation challenges for ultra-wideband radars", *IEEE Aerospace and Electronic Systems Magazine*, vol. 28, no. 7, pp. 12–18, Jul. 2013.

[45] C. Nunn and L. Moyer, "Spectrally-compliant waveforms for wideband radar", *IEEE Aerospace and Electronic Systems Magazine*, vol. 27, no. 8, pp. 11–15, Aug. 2012.

[46] M. Tummla, M. T. Donovan, B. E. Watkins, and R. North, "Volterra series based modeling and compensation of nonlinearities in high power amplifiers", in *Proc. IEEE ICASSP*, Apr. 1997, pp. 2417–2420.

[47] S. Benedetto, E. Biglieri, and R. Daffara, "Modeling and performance evaluation of nonlinear satellite links-a volterra series approach", *IEEE Transactions on Aerospace and Electronic Systems*, vol. AES-15, no. 4, pp. 494–507, Jul. 1979.

[48] C. Siviero, P. Lavrador, and J. Pedro, "A frequency domain extraction procedure of low-pass equivalent behavioural models of microwave pas", in *European Microwave Integrated Circuits Conference*, Sep. 2006, pp. 253–256.

[49] A. Javed, P. A. Goud, and B. Syrett, "Analysis of a microwave feedforward amplifier using volterra series representation", *IEEE Transactions on Communications*, vol. 25, no. 3, pp. 355–360, Mar. 1997.

[50] S. Narayanan, "Transistor distortion analysis using volterra series representation", *The Bell System Technical Journal*, vol. 46, no. 5, pp. 991–1024, May 1967.

[51] Z. Dunn, M. Yeary, and C. Fulton, "Frequency-dependent power amplifier modeling and correction for distortion in wideband radar transmissions", in *IEEE International Midwest Symposium on Circuits and Systems (MWSCAS)*, Aug. 2014.

[52] M. Faulkner and M. Johansson, "Adaptive linearization using predistortion - experimental results", *IEEE Transactions on Vehicular Technology*, vol. 43, pp. 323–332, May 1994.

[53] E. D. Cohen, "Active electronically scanned arrays", in *Proc. IEEE National Telesystems Conference*, May 1994, pp. 3–6.

[54] W. P. H. Jr. and R. D. Nordmeyer, "Active-element, phased-array radar: Affordable performance for the 1990s", in *Proc. National Telesystems Conference*, Mar. 1991, pp. 193–197.

[55] A. D'Andrea, V. Lottici, and R. Reggiannini, "Efficient digital predistortion in radio relay links with nonlinear power amplifiers", in *Proc. IEE Proceedings on Communications*, Jun. 2000, pp. 175–179.

[56] J. Lee, S. Jeon, J. Kim, H. J. Ryu, Y. Suh, H. Mok, and M. Kim, "An improved lut based dpd technique for nonlinear hpa in atsc dtv system", in *Proc. IEEE International Symposium on Broadband Multimedia Systems and Broadcasting (BMSB)*, Mar. 2010, pp. 1–4.

[57] D. Han and T. Hwang, "An adaptive pre-distorter for the compensation of hpa nonlinearity", *IEEE Transactions on Broadcasting*, vol. 46, pp. 152–157, Feb. 2000.

[58] M. Wicks, E. Mokole, S. Blunt, R. Schneible, and V. Amuso, *Principles of Waveform Diversity and Design*. Raleigh, NC: SciTech Publishing, Inc., 2010.

[59] D. Morgan, M. Zhengxiang, K. Jaehyeong, M. Zierdt, and J. Pastalan, "A generalized mp model for digital predistortion of rf power amplifiers", *IEEE Transactions on Signal Processing*, vol. 54, no. 10, pp. 3852–3860, Oct. 2006.

[60] H. W. Kang, Y. S. Cho, and D. H. Youn, "Adaptive precompensation of wiener systems", *IEEE Transactions on Signal Processing*, vol. 46, no. 10, pp. 2825–2829, Oct. 1998.

[61] K. Narendra and P. Gallman, "An iterative method for the identification of nonlinear systems using a hammerstein model", *IEEE Transactions on Automatic Control*, vol. 11, no. 3, pp. 546–550, Jul. 1966.

[62] J. Zhai, L. Zhang, J. Xia, J. Zhou, X. Zhu, and W. Hong, "Combined memory polynomial model for doherty power amplifiers with memory effects", *International Conference on Microwave and Millimeter Wave Technology (ICMMT)*, vol. 2, pp. 1–3, May 2012.

[63] L. Ding, G. T. Zhou, D. R. Morgan, Z. Ma, J. S. Kenney, J. Kim, and C. R. Giardina, "A robust digital baseband predistorter constructed using memory polynomials", *IEEE Transactions on Communications*, vol. 52, no. 1, pp. 159–165, Jan. 2004.

[64] J. Kim and K. Konstantinou, "Digital predistortion of wideband signals based on power amplifier model with memory", *Electronics Letters*, vol. 37, no. 23, pp. 1417–1418, Nov. 2001.

[65] X. Yu and H. Jiang, "Digital predistortion using adaptive basis functions", *IEEE Transactions on Circuits and Systems I: Regular Papers*, vol. 60, no. 12, pp. 3317–3327, Dec. 2013.

[66] A. Zhu, J. Dooley, and T. Brazil, "Simplified volterra series based behavioral modeling of rf power amplifiers using deviation-reduction", in *IEEE MTT-S International Microwave Symposium Digest*, Jun. 2006, pp. 1113–1116.

[67] A. Albert, *Regression and the Moore-Penrose Pseudoinverse*. New York: Academic Press, 1972.

[68] P. Courrieu, "Fast computation of moore-penrose inverse matrices", *Neural Information Processing*, vol. 8, no. 2, pp. 25–29, Aug. 2005.

[69] M. Schetzen, *The Volterra and Wiener Theories of Nonlinear Systems*. New York: Wiley, 1980.

[70] R. Raich, H. Qian, and G. T. Zhou, "Digital baseband predistortion of nonlinear power amplifiers using orthogonal polynomials", in *IEEE International Conference on Acoustics, Speech, and Signal Processing (ICASSP)*, vol. 6, Apr. 2003, pp. 689–692.

[71] A. Cline, C. Moler, G. Stewart, and J. Wilkinson, "An estimate for the condition number of a matrix", *SIAM J. Numer. Anal.*, vol. 16, pp. 368–375, 1979.

[72] V. Vu and T. Tao, "The condition number of a randomly perturbed matrix", in *Proceedings of the thirty-ninth annual ACM symposium on Theory of Computing*, 2007, pp. 248–255.

[73] R. Varga, *Matrix Iterative Analysis, 2nd Edition*. Springer-Verlag, 2000.

[74] Y. Zhai and M. Yeary, "Implementing particle filters with metropolis-hastings algorithms", in *IEEE Region 5 Conference*, Apr. 2004, pp. 149–152.

[75] J. Kruschke, *Doing Bayesian Data Analysis, A Tutorial with R and BUGS*. Burlington, MA: Academic Press, 2010.

[76] B. Ristic, A. Farina, D. Benvenuti, and M. Arulampalam, "Performance bounds and comparison of nonlinear filters for tracking a ballistic object on re-entry", *IEE Proceedings on Radar, Sonar, and Navigation*, vol. 150, no. 2, pp. 65–70, Apr. 2003.

[77] Z. Dunn, M. Yeary, C. Fulton, and N. Goodman, "Wideband solid-state power amplifier modeling and predistortion for radar transmissions", in *NATO Science and Technology Organization SET-204 Specialists' Meeting on Waveform Diversity*, Sep. 2014.

[78] ——, "Memory polynomial model for digital predistortion of broadband solid-state radar amplifiers", in *IEEE Radar Conference*, 2015, pp. 1482–1486.

[79] B. Lewis and F. Kretschmer, "Linear frequency modulation derived polyphase pulse compression codes", *IEEE Transactions on Aerospace and Electronic Systems*, vol. 18, no. 5, pp. 637–641, Sep. 1982.

[80] E. G. Larsson, O. Edfors, F. Tufvesson, and T. L. Marzetta, "Massive MIMO for next generation wireless systems", *IEEE Communications Magazine*, vol. 52, no. 2, pp. 186–195, Feb. 2014.

[81] W. Roh, J. Y. Seol, J. Park, B. Lee, J. Lee, Y. Kim, J. Cho, K. Cheun, and F. Aryanfar, "Millimeter-wave beamforming as an enabling technology for 5G cellular communications: Theoretical feasibility and prototype results", *IEEE Communications Magazine*, vol. 52, no. 2, pp. 106–113, Feb. 2014.

[82] P. Pirinen, "A brief overview of 5G research activities", in *1st International Conference on 5G for Ubiquitous Connectivity 2014*, Nov. 2014, pp. 17–22.

[83] V. Jungnickel, K. Manolakis, W. Zirwas, B. Panzner, V. Braun, M. Lossow, M. Sternad, R. Apelfrojd, and T. Svensson, "The role of small cells,

coordinated multipoint, and massive MIMO in 5G", *IEEE Communications Magazine*, vol. 52, no. 5, pp. 44–51, May 2014.

[84] D. Kapetanovic, G. Zheng, and F. Rusek, "Physical layer security for massive MIMO: An overview on passive eavesdropping and active attacks", *IEEE Communications Magazine*, vol. 53, no. 6, pp. 21–27, Jun. 2015.

[85] A. Tirado-Mendez, H. Jardon-Aguilar, E. Andrade-Gonzalez, and M. Reyes-Ayala, "A novel active load linearizer for HBT low noise amplifier at 2.4 GHz", in *IEEE 18th International Symposium on Personal, Indoor and Mobile Radio Communications, 2007.*, Sep. 2007, pp. 1–3.

[86] M. Fellows, C. Baylis, L. Cohen, and R. J. M. Ii, "Real-time load impedance optimization for radar spectral mask compliance and power efficiency", *IEEE Transactions on Aerospace and Electronic Systems*, vol. 51, no. 1, pp. 591–599, Jan. 2015.

[87] Z. Dunn, M. Yeary, C. Fulton, and R. Rincon, "Impedance dependent wideband digital predistortion of solid-state radar amplifiers", *In Revision by IEEE Transactions on Aerospace and Electronic Systems*, 2017.

[88] C. Balanis, *Antenna Theory, Third Edition*. Hoboken, New Jersey: John Wiley & Sons, Inc., 2005.

[89] R. Hansen, *Phased Array Antennas*. Hoboken, New Jersey: John Wiley & Sons, Inc., 2009.

[90] R. C. V. Wagoner and R. C. Hansen, "Measurement of phased array scan impedance by load pull", *Electronics Letters*, vol. 39, no. 15, pp. 1101–1102, Jul. 2003.

[91] D. Pozar, *Microwave Engineering, 4th Edition*. John Wiley & Sons, Inc., 2012.

Appendix A

Moore-Penrose Pseudoinverse as Least-Squares Solution

It is commonly known that the Moore-Penrose Pseudoinverse is the least-squares (or minimum Euclidean norm) solution to a system of linear equations. This section aims to explain this commonly accepted truth. The system of linear equations can be represented as

$$\mathbf{y} = \mathbf{X}\mathbf{A} \tag{A.1}$$

and using this notation, the classic Moore-Penrose Pseudoinverse is defined as

$$\mathbf{A} = \left(\mathbf{X}^{\mathrm{H}}\mathbf{X}\right)^{-1}\mathbf{X}^{\mathrm{H}}\mathbf{y} \tag{A.2}$$

where $\mathbf{y}$ is a $[N \times 1]$ matrix, $\mathbf{X}$ is a $[N \times C]$ matrix, and $\mathbf{A}$ is a $[C \times 1]$ matrix. For the common case of $\mathbf{y}$ as the output vector of a system model, $\mathbf{X}$ as the expanded input values matrix, and $\mathbf{A}$ as the vector containing the coefficients of the model, the least-squares difference between the predicted model values and the measured values is shown as

$$\min_{\mathbf{A}} \|\mathbf{y} - \mathbf{X}\mathbf{A}\|^2 \tag{A.3}$$

The Euclidean norm can be expanded as

$$\|\mathbf{y}-\mathbf{XA}\|^{\,2} = \sqrt{(\mathbf{y}-\mathbf{XA})^{\mathrm{H}}(\mathbf{y}-\mathbf{XA})}^{2} =$$
$$= \mathbf{y}^{\mathrm{H}}\mathbf{y} - \mathbf{y}^{\mathrm{H}}\mathbf{XA} - \mathbf{A}^{\mathrm{H}}\,\mathbf{X}^{\mathrm{H}}\mathbf{y} + \mathbf{A}^{\mathrm{H}}\mathbf{X}^{\mathrm{H}}\mathbf{XA} \quad \text{(A.4)}$$

where $[\,]^{\mathrm{H}}$ represents the complex conjugate transpose operator.

The least-square difference is desired, so the derivative of Equation A.4 with respect to the vector $\mathbf{A}$ is needed. Assuming the denominator layout matrix convention, remember the following properties

$$\tfrac{d}{d\mathbf{A}}\mathbf{CA} = \mathbf{C}^{\mathrm{H}} \quad \text{and} \quad \tfrac{d}{d\mathbf{A}}\mathbf{A}^{\mathrm{H}}\mathbf{C} = \mathbf{C} \qquad \text{(A.5)}$$

where $\mathbf{C}$ is not a function of $\mathbf{A}$ and $[\,]^{\mathrm{H}}$ represents the complex-conjugate transpose operator.

Using the properties expressed in Equation A.5, the least-squares solution can be found by setting the derivative of Equation A.4 with respect to vector $\mathbf{A}$ equal to zero. This is shown below.

$$\frac{d}{d\mathbf{A}}\left[\mathbf{y}^{\mathrm{H}}\mathbf{y} - \mathbf{y}^{\mathrm{H}}\mathbf{XA} - \mathbf{A}^{\mathrm{H}}\,\mathbf{X}^{\mathrm{H}}\mathbf{y} + \mathbf{A}^{\mathrm{H}}\mathbf{X}^{\mathrm{H}}\mathbf{XA}\right] = 0 =$$
$$= 0 - \mathbf{X}^{\mathrm{H}}\mathbf{y} - \mathbf{X}^{\mathrm{H}}\mathbf{y} + \left[\mathbf{X}^{\mathrm{H}}\mathbf{XA} + \mathbf{X}^{\mathrm{H}}\mathbf{XA}\right] = -\mathbf{2}\mathbf{X}^{\mathrm{H}}\mathbf{y} + \mathbf{2}\mathbf{X}^{\mathrm{H}}\mathbf{XA} \quad \text{(A.6)}$$

Rearranging the result from Equation A.6, the matrix $\mathbf{A}$ giving the least-squares solution can be shown as

$$2\mathbf{X}^{\mathrm{H}}\mathbf{X}\mathbf{A} = \mathbf{2}\mathbf{X}^{\mathrm{H}}\mathbf{y}$$

$$\Rightarrow \mathbf{X}^{\mathrm{H}}\mathbf{X}\mathbf{A} = \mathbf{X}^{\mathrm{H}}\mathbf{y}$$

$$\Rightarrow \mathbf{A} = \left(\mathbf{X}^{\mathrm{H}}\mathbf{X}\right)^{-1}\mathbf{X}^{\mathrm{H}}\mathbf{y} \quad \text{(A.7)}$$

where $[\,]^{-1}$ represents the inverse of a matrix. Note that the result of Equation A.7 exactly matches the definition of the Moore-Penrose Pseudoinverse as shown in Equation A.2. Therefore, the Moore-Penrose Pseudoinverse has been demonstrated to give the least-squares solution to a system of linear equations.

Appendix B

Matlab Code for Digital Predistortion

B.1 Digital Predistortion Utilizing Memory Polynomial Model

Due to the excessive length of the generalized digital predistortion Matlab code, a pseudo-code consisting of explanations and selected highlights of the code utilized are given in this section instead.

The implemented digital predistortion process is began by acquiring a set of calibration data as described in Section 3.2.2. The column vectors containing the measured non-amplified signal and the measured amplified signal, which have been time aligned with each other and resampled to the arbitrary waveform generator's sampling rate, are given by the variables "siginresam" and "sigoutresam" respectively. The maximum allowed input power "PLimIn" is then found using the following code:

```
% Find gain of linear region of amplifier, using measured data
% upper threshold for determining the linear region
% of the measured amplifier
```

```
LinGainCutoffH = 0.5;
% lower threshold for determining the linear region
% of the measured amplifier
LinGainCutoffL = 0.1;
GainInd = (((abs(sigoutresam).^2)<...
(LinGainCutoffH*max(abs(sigoutresam).^2)))&...
((abs(sigoutresam).^2)>...
(LinGainCutoffL*max(abs(sigoutresam).^2))));

% Max Power Input to Amp (W)
PMaxIn = (max(abs(siginresam)).^2)/(2*Z0);
% Max Power Output of Amp (W);
PMaxOut = (max(abs(sigoutresam)).^2)/(2*Z0);

% Find LMS regression solution for linear region
% w/ forced 0 intercept
Glin = ((abs(siginresam(GainInd).^2)/(2*Z0)))\...
(abs(sigoutresam(GainInd).^2)/(2*Z0));

% Calculate Limit for Power in to not exceed
% training data range
PLimScaleDown = 1.0;
PLimIn = PLimScaleDown*(PMaxOut)/Glin; % Max Power in (W)
```

The amplifier model coefficient vector $\boldsymbol{\theta}_{MP}$ and the amplifier digital predistortion coefficient vector $\boldsymbol{\theta}_{PD}$ can then be calculated (represented by "AmpCoeffs" and "PDCoeffs", respectively) according to Equations 3.6 and 3.7,

respectively. Note that calculation of the model coefficient vectors requires consistent assembly of the delay matrix, therefore the separate Matlab function "MPDelayMatrixGenerator" was created to ensure consistent assembly of the memory polynomial delay matrix. The Matlab function "MPDelayMatrixGenerator" is given in its entirety in Section B.2. The code that solves for the model coefficients is given below:

```
% Find Amplifier and DPD Model Coefficients
CaliSignal = siginresam;
CaliOutputSignal = sigoutresam;

AmpMaxNormMag = max(abs(CaliSignal));
AmpCalDelayMatrix = ...
DelayMatrixGenerator02(CaliSignal,K,M,...
AmpMaxNormMag,DelayMultiple);
AmpCoeffs = ...
((AmpCalDelayMatrix')*AmpCalDelayMatrix)\...
((AmpCalDelayMatrix')*CaliOutputSignal(...
(DelayMultiple*(M-1)+1):end));

PDMaxNormMag = ...
sqrt(PLimIn/PMaxOut)*max(abs(CaliOutputSignal));
PDCalDelayMatrix = ...
DelayMatrixGenerator02(sqrt(PLimIn/PMaxOut)*...
CaliOutputSignal,KPD,MPD,PDMaxNormMag,DelayMultiple);
PDCoeffs = ...
```

```
((PDCalDelayMatrix')*PDCalDelayMatrix)\...
((PDCalDelayMatrix')*CaliSignal(...
(DelayMultiple*(MPD-1)+1):end));
```

Once the digital predistortion coefficient vector has been found, the digitally predistorted version of the ideal input waveform can be created. Given an ideal input waveform "FSSigInFreqAnalyze" that has a maximum magnitude less than or equal to the maximum magnitude of "siginresam", a correctly digitally predistorted input waveform "FSPDSigInFreqAnalyze" is created by the code below:

```
PDDelayMatrix = ...
DelayMatrixGenerator02(sqrt(PLimIn/PMaxIn)*...
FSSigInFreqAnalyze,KPD,MPD,...
PDMaxNormMag,DelayMultiple);
FSPDSigInFreqAnalyze = (PDDelayMatrix*PDCoeffs);
```

Following resampling to the waveform generator's sampling rate and mixing from complex baseband to the carrier frequency, the predistorted waveform is ready for generation by the arbitrary waveform generator.

B.2 Memory Polynomial Delay Matrix Formation Function

The function "MPDelayMatrixGenerator" returns the memory polynomial delay matrix as seen in Equation 3.4. The variable "tempInput" is a column vector of the complex signal from which the delay matrix is to be formed. The variables "tempK" and "tempM" are the chosen orders of non-linearity

and memory, respectively. The variable "MaxNormMag" is the selected maximum magnitude of the input signal, as seen in Equation 3.9. The variable "DelayMultiple" is the delay-multiple, as described in Section 4.3. While the variables "MaxNormMag" and "DelayMultiple" are optional, all other input variables are required for delay matrix formation.

```
function [DelayMatrix] = MPDelayMatrixGenerator(tempInput,tempK,tempM,...
    MaxNormMag,DelayMultiple)

    % If MaxNormMag value not given, assume unweighted calculation
    if nargin == 3
        MaxNormMag = 1;
        DelayMultiple = 1;
    elseif nargin == 4
        DelayMultiple = 1;
    elseif nargin ~= 5
        error('Incorrect Input Values for Delay Matrix Generation');
    end

    tempDelayMatrix = ...
        zeros(length(tempInput((DelayMultiple*(tempM-1)+1):end)),...
        tempK*tempM);
    for ctK = 0:(tempK-1)
        for ctM = 0:(tempM-1)
            MDelay = ctM*DelayMultiple;
            MIndStart = DelayMultiple*(tempM-1) + 1;
```

```
            tempDelayMatrix(:,ctK*tempM+ctM+1) = ...
                (tempInput((MIndStart-MDelay):(end-MDelay))...
                .*abs(tempInput((MIndStart-MDelay):(end-MDelay))).^ctK)...
                ./(MaxNormMag^(ctK+1));
        end
    end

    DelayMatrix = tempDelayMatrix;
end
```

B.3 Digital Predistortion Utilizing Impedance Dependent Memory Polynomial Model

Due to the excessive length of the generalized impedance dependent digital predistortion Matlab code, a pseudo-code consisting of explanations and selected highlights of the code utilized are given in this section instead.

The implemented digital predistortion process is began by acquiring a set of calibration data as described in Section 4.2.3. The calibration data consists of a pair of column vectors from each tested load impedance, where each pair contains the measured non-amplified signal and the measured amplified signal which have been time aligned with each other, resampled to the arbitrary waveform generator's sampling rate, and converted to complex baseband. In each measured load impedance dataset, the signals resulting from the non-amplified and the amplified measurements are "CaliNonAmpedFreqSamCBB" and "CaliAmpedFreqSamCBB", respectively. The impedance dependent memory polynomial model uses the concatenation of all the measured

load impedance cases to form the three vectors comprising the calibration dataset. These three vectors are the non-amplified complex baseband measured signal resampled to the waveform generator's sampling rate, the amplified complex baseband measured signal resampled to the waveform generator's sampling rate, and the vector containing the amplifier load impedance corresponding with the instantaneous load impedance at each sample, represented by "siginresamCon", "sigoutresamCon", and "sigZ0Con", respectively. The Matlab code used for assembly of the calibration dataset, given the cell array "ImportFiles" containing the file names of all the measured load impedance cases, is shown below:

```
%%
tempIndOffset_1 = ones(1,length(ImportFiles));


siginresamCell = [];
sigoutresamCell = [];
sigZ0 = [];


for ctLoad = 1:length(ImportFiles)
    tempName = ImportFiles{ctLoad};
    tempImportData = load(tempName);


    CaliNonAmpedFreqSamCBB = tempImportData.CaliNonAmpedFreqSamCBB;
    CaliAmpedFreqSamCBB = tempImportData.CaliAmpedFreqSamCBB;
    tempZ0 = tempImportData.Z0;


    if ctLoad == 1
```

```
        CaliSignalExportCBB = tempImportData.CaliSignalExportCBB;
    end



    tempCorr = xcorr(CaliNonAmpedFreqSamCBB,CaliSignalExportCBB);
    tempIndOffset = ...
        fix(length(tempCorr)/2 - find(abs(tempCorr)==...
        max(abs(tempCorr))));
    tempInd = (1:length(CaliSignalExportCBB))-tempIndOffset;


    siginresamCell{ctLoad} = ...
        CaliNonAmpedFreqSamCBB(tempInd-tempIndOffset_1(ctLoad));
    sigoutresamCell{ctLoad} = ...
        CaliAmpedFreqSamCBB(tempInd-tempIndOffset_1(ctLoad));
    sigZ0Cell{ctLoad} = tempZ0*ones(1,length(tempInd));


    clear CaliNonAmpedFreqSamCBB CaliAmpedFreqSamCBB
    clear tempImportData tempZ0
end


%%
% Initialize concatenated calibration data vectors
siginresamCon = [];
sigoutresamCon = [];
sigZ0Con = [];
```

```
for ctC = 1:length(siginresamCell)
    siginresamCon = [siginresamCon siginresamCell{ctC}];
    sigoutresamCon = [sigoutresamCon sigoutresamCell{ctC}];
    sigZ0Con = [sigZ0Con sigZ0Cell{ctC}];
end
```

Once the impedance dependent calibration dataset is formed, the maximum allowed input power "PLimIn" is then found using the following code:

```
    % set calibration scaled, resampled signals
    siginresam = siginresamCon;
    sigoutresam = sigoutresamCon;

    siginresam = siginresam(:);
    sigoutresam = sigoutresam(:);

    % Find gain of linear region of amplifier, using measured data
    % upper threshold for determining the linear region
        % of the measured amplifier
    LinGainCutoffH = 0.5;
    % lower threshold for determining the linear region
        % of the measured amplifier
    LinGainCutoffL = 0.1;
    GainInd = ...
        (((abs(sigoutresam).^2)<...
        (LinGainCutoffH*max(abs(sigoutresam).^2)))&...
        ((abs(sigoutresam).^2)>...
```

```
    (LinGainCutoffL*max(abs(sigoutresam).^2))));

% Rescale to not exceed lowest max magnitude
    % for load impedance/frequency combination
PMaxOutInputScaledown = 0.925;

% Find PMaxIn and PMaxOut for lowest case based on Z0
PMaxIn = [];
PMaxOut = [];
tmpPMaxInBest = max(abs(siginresam)).^2/(2*Z0_orig);
tmpPMaxOutBest = max(abs(sigoutresam)).^2/(2*Z0_orig);
for ctF = 1:length(sigZ0unique)
    tmpPMaxIn = ...
        (max(abs(siginresam(sigZ0Con==sigZ0unique(ctF))))...
        .^2)/(2*Z0_orig); % Max Power Input to Amp (W)
    tmpPMaxOut = ...
        (max(abs(sigoutresam(sigZ0Con==sigZ0unique(ctF))))...
        .^2)/(2*Z0_orig);  % Max Power Output of Amp (W)

    if tmpPMaxIn < tmpPMaxInBest
        tmpPMaxInBest = tmpPMaxIn;
    end
    if tmpPMaxOut < tmpPMaxOutBest
        tmpPMaxOutBest = tmpPMaxOut;
    end
end
```

```
PMaxIn = tmpPMaxInBest;
PMaxOut = PMaxOutInputScaledown*tmpPMaxOutBest;

% Find LMS regression solution for linear region
    % w/ forced 0 intercept
Glin = ...
    ((abs(siginresam(GainInd).^2)/(2*Z0_orig)))\...
    (abs(sigoutresam(GainInd).^2)/(2*Z0_orig));

% Calculate Limit for Power in to not exceed training data range
PLimScaleDown = 1.0;
PLimIn = PLimScaleDown*(PMaxOut)/Glin; % Max Power in (W)
```

The amplifier digital predistortion coefficient vector $\boldsymbol{\theta}_{IDMP}$, represented by "PDCoeffs", can then be calculated according to Equation 4.10. Note that calculation of the model coefficient vectors requires consistent assembly of the delay matrix, therefore the separate Matlab function "IDMPDelayMatrixGenerator" was created to ensure consistent assembly of the memory polynomial delay matrix. The Matlab function "IDMPDelayMatrixGenerator" is given in its entirety in Section B.4. The code that solves for the digital predistortion model coefficients is given below:

```
% Find Amplifier Model Coefficients (at FreqAnalyze)
% Resample to FreqAnalyze
temp_tSam = (0:1:(length(siginresam)-1))*(1/FreqSam).';
temp_tAnalyze = (0:(1/FreqAnalyze):max(temp_tSam)).';
CaliSignal = ...
```

```
interp1(temp_tSam,real(siginresam),temp_tAnalyze) +...
1i*interp1(temp_tSam,imag(siginresam),temp_tAnalyze);
CaliOutputSignal = ...
interp1(temp_tSam,real(sigoutresam),temp_tAnalyze) +...
1i*interp1(temp_tSam,imag(sigoutresam),temp_tAnalyze);
sigZ0FreqAnalyze = ...
interp1(temp_tSam,real(sigZ0Con),temp_tAnalyze) +...
1i*interp1(temp_tSam,imag(sigZ0Con),temp_tAnalyze);
% Convert load impedance to reflection coefficient
GammaFreqAnalyze = ...
(sigZ0FreqAnalyze - Z0_orig*ones(size(sigZ0FreqAnalyze)))...
./(sigZ0FreqAnalyze + Z0_orig*ones(size(sigZ0FreqAnalyze)));

% Assemble maximum gamma for calibration dataset
PDMaxGamma_r = AmpMaxGamma_r;
PDMaxGamma_i = AmpMaxGamma_i;
PDMaxGamma = PDMaxGamma_r + 1i*PDMaxGamma_i;

sigZ0unique = unique(sigZ0Con.','rows','stable');
PDMaxNormZ = max(abs(sigZ0unique));
PDMaxNormMag = sqrt(PLimIn/PMaxOut)*max(abs(CaliOutputSignal));

PDCalDelayMatrix = ...
IDMPDelayMatrixGenerator(sqrt(PLimIn/PMaxOut)*...
CaliOutputSignal,GammaFreqAnalyze,ZPD,KPD,MPD,...
PDMaxNormMag,PDMaxGamma,DelayMultiple);
```

```
PDCoeffs = [];
PDCoeffs = ...
((PDCalDelayMatrix')*PDCalDelayMatrix)\...
((PDCalDelayMatrix')*CaliSignal(...
(DelayMultiple*(MPD-1)+1):end));
clear PDCalDelayMatrix
```

Once the digital predistortion coefficient vector has been found, the digitally predistorted version of the ideal input waveform can be created. Given an amplifier load impedance associated with the desired array beamsteering angle and an ideal input waveform "FSSigInFreqAnalyze" that has a maximum magnitude less than or equal to the magnitude corresponding with "PMaxIn", a correctly digitally predistorted input waveform "FSPDSigInFreqAnalyze" is created by the code below. The variable "FSPDSigInFreqAnalyze" is then resampled to the arbitrary waveform generator's sampling rate and mixed from complex baseband to the carrier frequency in variable "txPDrpreRef", which is ready for generation by the arbitrary waveform generator:

```
InputScaledown = 1.0;
PDScaledInputSignal = sqrt(PLimIn/PMaxIn)*FSSigInFreqAnalyze;
PDDelayMatrix = ...
IDMPDelayMatrixGenerator(...
PDScaledInputSignal,...
((Z0-Z0_orig)/(Z0+Z0_orig))*...
ones(size(PDScaledInputSignal)),...
ZPD,KPD,MPD,PDMaxNormMag,...
PDMaxGamma,DelayMultiple);
```

```
FSPDSigInFreqAnalyze = (PDDelayMatrix*PDCoeffs);


% Convert from FreqAnalyze to FreqSam while at CBB
tFreqAnalyze = ...
0:(1/FreqAnalyze):...
((length(FSPDSigInFreqAnalyze)-1)/FreqAnalyze);
tFreqSam = ...
min(tFreqAnalyze):(1/FreqSam):max(tFreqAnalyze);


FSPDSigIn = ...
interp1(tFreqAnalyze(:),...
real(FSPDSigInFreqAnalyze(:)),...
tFreqSam(:)) + ...
1i*interp1(tFreqAnalyze(:),...
imag(FSPDSigInFreqAnalyze(:)),tFreqSam(:));


tPD = (0:(1/FreqSam):((length(FSPDSigIn)-1)/FreqSam)).';
txPDrpreRef = real(FSPDSigIn.*exp(1i*2*pi*FreqCarrier*tPD));
```

B.4 Impedance Dependent Memory Polynomial Delay Matrix Formation Function

The function "IDMPDelayMatrixGenerator" returns the impedance dependent memory polynomial delay matrix as seen in Equation 4.7. The variable "tempInput" is a column vector of the complex signal from which the delay matrix is to be formed, and the variable "tempInputGamma" is a column vector of the complex reflection coefficient due to the load impedance

experienced by the amplifier at each sample point. The variables "tempZ", "tempK", and "tempM" are the chosen orders of impedance dependency, nonlinearity, and memory, respectively. The variable "MaxNormMag" is the selected maximum magnitude of the input signal, as seen in Equation 4.9. The variable "MaxGamma" is the selected maximum complex reflection coefficient Γ_{max} as discussed in Section 4.2.3. The variable "DelayMultiple" is the delay-multiple, as described in Section 4.3. While the variables "MaxNormMag", "MaxGamma", and "DelayMultiple" are optional, all other input variables are required for delay matrix formation.

```
function [DelayMatrix] = IDMPDelayMatrixGenerator(...
    tempInput,tempInputGamma,tempZ,tempK,tempM,MaxNormMag,...
    MaxGamma,DelayMultiple)

    % If MaxNormMag value not given, assume unweighted calculation
    if nargin == 5
        MaxNormMag = 1;
        MaxGamma = 1;
        DelayMultiple = 1;
    elseif nargin == 6
        MaxGamma = 1;
        DelayMultiple = 1;
    elseif nargin == 7
        DelayMultiple = 1;
    elseif nargin ~= 8
        error('Incorrect Input Values for Delay Matrix Generation');
```

```
end


tempDelayMatrix = ...
    zeros(length(tempInput((DelayMultiple*(tempM-1)+1):end)),...
    2*tempZ^2*tempK*tempM)*NaN;
    for ctGR = 0:(tempZ-1)
        for ctGI = 0:(tempZ-1)
            for ctK = 0:(tempK-1)
                for ctM = 0:(tempM-1)
                    MDelay = ctM*DelayMultiple;
                    MIndStart = DelayMultiple*(tempM-1) + 1;
                    % Complex Reflection Coefficient parameterization
                    if ctGR == 0
                        tempGR = 1;
                    else
                        tempGR = ...
                            real(tempInputGamma(...
                            (MIndStart-MDelay):(end-MDelay)))...
                            .*(abs(real(tempInputGamma(...
                            (MIndStart-MDelay):(end-MDelay))))...
                            .^(ctGR-1));
                    end


                    if ctGI == 0
                        tempGI = 1;
                    else
```

```
    tempGI = ...
        imag(tempInputGamma(...
        (MIndStart-MDelay):(end-MDelay)))...
        .*(abs(imag(tempInputGamma(...
        (MIndStart-MDelay):(end-MDelay))))...
        .^(ctGI-1));
end


tempDelayMatrix(:,...
    ctGR*tempZ*tempK*tempM+...
    ctGI*tempK*tempM+ctK*tempM+ctM+1) = ...
    ((tempInput(...
    (MIndStart-MDelay):(end-MDelay)))...
    .*abs(tempInput(...
    (MIndStart-MDelay):(end-MDelay)))...
    .^ctK).*(tempGR.*tempGI)...
    ./(MaxNormMag^(ctK+1)...
    *MaxGamma^(ctGR+ctGI)); % Real Component
tempDelayMatrix(:,...
    tempZ^2*tempK*tempM + ...
    ctGR*tempZ*tempK*tempM+...
    ctGI*tempK*tempM+ctK*tempM+ctM+1) = ...
    ((tempInput(...
    (MIndStart-MDelay):(end-MDelay)))...
    .*abs(tempInput(...
    (MIndStart-MDelay):(end-MDelay)))...
```

```
                                .^ctK).*(1i*tempGR.*tempGI)...
                                ./(MaxNormMag^(ctK+1)...
                                *MaxGamma^(ctGR+ctGI)); % Imag Component
                            end
                        end
                    end
                end
            DelayMatrix = tempDelayMatrix;
        end
```

Appendix C

Author's Previous Publications

Journal Papers:

[1] Z. Dunn, M. Yeary, C. Fulton, and R. Rincon, "An Impedance Dependent Memory Polynomial Model for Wideband Digital Predistortion of Solid-State Radar Amplifiers", Submitted with *IEEE Transactions on Aerospace and Electronic Systems.*

[2] F. Uysal, Z. Dunn, M. Yeary, and R. Rincon, "Application of Waveform Weighting for A Frequency Invariant Transmit Beampattern", Pending second-level review with *IEEE Aerospace and Electronic Systems Magazine Special Issue on Waveform Diversity.*

[3] Z. Dunn, M. Yeary, C. Fulton, and N. Goodman, "Wideband Digital Predistortion of Solid-State Radar Amplifiers", Pending second-level review with *IEEE Transactions on Aerospace and Electronic Systems.*

Conference Papers:

[1] Z.Dunn, M. Yeary, F. Uysal, and C. Fulton, "Low Sidelobe Pseudo-Orthogonal Code Sets Through Particle Swarm Optimization", Accepted in *IEEE Radar Conference*, 2016.

[2] Z. Dunn, M. Yeary, C. Fulton, N. Goodman, and R. Rincon, "Effects of Cross-Correlated Waveforms on Polarimetric Scattering Parameter Recovery", Poster # 78 presented at *AMS* 37^{th} *Conference on Radar Meteorology*, 2015.

[3] Z.Dunn, M. Yeary, C. Fulton, and N. Goodman, "Memory polynomial model for digital predistortion of broadband solid-state radar amplifiers", in *IEEE Radar Conference*, 2015, pp. 1482-1486.

[4] Z. Dunn, M. Yeary, C. Fulton, and N. Goodman, "Wideband solid-state power amplifier modeling and predistortion for airborne radar", in *NATO Science and Technology Organization SET-204 Specialists' Meeting on Waveform Diversity*, 2014.

[5] Z. Dunn, M. Yeary, and C. Fulton, "Frequency-dependent power amplifier modeling and correction for distortion in wideband radar transmissions", in *IEEE* 57^{th} *International Midwest Symposium on Circuits and Systems*, 2014, pp. 61-64.

[6] Z. Dunn, C. Fulton, N. Goodman, R. Rincon, and M. Yeary, "Orthogonal Coding in a MIMO Polarimetric Radar System as a Method to Recover

Full Polarimetric Data", Poster # 331 presented at *AMS* 36^{th} *Conference on Radar Meteorology*, 2013.

[7] Z. Dunn, "Atmospheric Studies and Spectral Monitoring in the High Frequency (HF) Band", Poster presented at *SACNAS National Conference*, 2012.

[8] Z. Dunn, M. Yeary, "Practical considerations for laboratory based spectral monitoring in the High Frequency (HF) band", in *IEEE International Instrumentation and Measurement Technology Conference*, 2012, pp. 134-137.

[9] Z. Dunn, "HF Oblique Incident Sounding for Calibration of an Over-The-Horizon Radar (OTHR) System", Poster presented at *AISES National Conference*, 2011.